buildings

Special Issue Reprint

Structural Analysis of Underground Space Construction

Edited by
Yong Fang, Zhigang Yao, Zhongtian Chen and Zhen Wei

mdpi.com/journal/buildings

MDPI

Structural Analysis of Underground Space Construction

Structural Analysis of Underground Space Construction

Guest Editors

Yong Fang
Zhigang Yao
Zhongtian Chen
Zhen Wei

MDPI

Basel • Beijing • Wuhan • Barcelona • Belgrade • Novi Sad • Cluj • Manchester

Guest Editors

Yong Fang
Department of Tunnel and Underground Engineering
Southwest Jiaotong University
Chengdu
China

Zhigang Yao
Key Laboratory of Transportation Tunnel Engineering
Southwest Jiaotong University
Chengdu
China

Zhongtian Chen
Faculty of Engineering and Architecture
Ghent University
Ghent
Belgium

Zhen Wei
School of Civil Engineering
Lanzhou University of Technology
Lanzhou
China

Editorial Office
MDPI AG
Grosspeteranlage 5
4052 Basel, Switzerland

This is a reprint of the Special Issue, published open access by the journal *Buildings* (ISSN 2075-5309), freely accessible at: https://www.mdpi.com/journal/buildings/special_issues/UM0HZ314EF.

For citation purposes, cite each article independently as indicated on the article page online and as indicated below:

Lastname, A.A.; Lastname, B.B. Article Title. *Journal Name* **Year**, *Volume Number*, Page Range.

ISBN 978-3-7258-4627-6 (Hbk)
ISBN 978-3-7258-4628-3 (PDF)
https://doi.org/10.3390/books978-3-7258-4628-3

Contents

Fenglan Li, Pengcheng Si, Yintao He, Hui Wang, Zhixiao Zhang and Shunbo Zhao
Numerical Analysis of the Single-Directionally Misaligned Segment Behavior of Hydraulic TBM Tunnel
Reprinted from: *Buildings* **2024**, *14*, 2198, https://doi.org/10.3390/buildings14072198 . . . . . . **1**

Bowen Wu, Jucai Chang, Xiangyu Wang, Wenbao Shi, Chuanming Li and Dingchao Chen
Research on the Mechanism and Application of High Pre-Tension on the Crack-Arresting Effect of Rockbolt Anchorage
Reprinted from: *Buildings* **2024**, *14*, 2584, https://doi.org/10.3390/buildings14082584 . . . . . . **15**

Tao Yu, Junfeng Sun, Jianfeng Wang, Jianping Feng, Liangjun Chen, Guofeng Su, et al.
Study on the Propagation Law and Waveform Characteristics of a Blasting Shock Wave in a Highway Tunnel with the Bench Method
Reprinted from: *Buildings* **2024**, *14*, 2802, https://doi.org/10.3390/buildings14092802 . . . . . . **33**

Yongjun He, Jian Cheng, Zengli Shi, Bin Zhang, Li Chen, Xi Li, et al.
Research on Axial Stress and Strain Characteristics of Reinforced-Concrete Curved Pipe Jacking in Power Tunnels
Reprinted from: *Buildings* **2024**, *14*, 3030, https://doi.org/10.3390/buildings14093030 . . . . . . **49**

Jian Cui, Zhigang Yao, Tao Yu, Jianfeng Wang, Kaichen Ying, Bo Liu, et al.
Soil Displacement of Slurry Shield Tunnelling in Sandy Pebble Soil Based on Field Monitoring and Numerical Simulation
Reprinted from: *Buildings* **2024**, *14*, 3043, https://doi.org/10.3390/buildings14103043 . . . . . . **59**

Gang Liu, Dongwei Wang, Shengxuan Wang, Yonglong Zan, Qiqi Zhang, Zhitao Yang, et al.
Effect of Sandstone Pore Morphology on Mechanics, Acoustic Emission, and Energy Evolution
Reprinted from: *Buildings* **2024**, *14*, 3503, https://doi.org/10.3390/buildings14113503 . . . . . . **79**

Yongli Liu, Lei Tao, Shenglei Zhao, Weixin Chen and Yaozu Ni
Technology for Treatment and Reinforcement of Soft Rock Tunnel Floor Using Sealing Material
Reprinted from: *Buildings* **2024**, *14*, 4004, https://doi.org/10.3390/buildings14124004 . . . . . . **99**

Lu Ma, Luyi Xing, Chang Liu, Tongyuan Cui, Xi Qiao, Wang Miao and Peng Kong
Research on the Instability Mechanism and Control Technology of Gob-Side Entry in Deep Mines with Soft Rock
Reprinted from: *Buildings* **2025**, *15*, 19, https://doi.org/10.3390/buildings15010019 . . . . **115**

Xuewen Rong, Mingze Li, Hongjian Liao, Ao Zhang, Tao Dang, Hangzhou Li and Zheng Wu
Influence of Groundwater Level Rising on Mechanical Properties of Pile Foundations Under a Metro Depot in Loess Areas
Reprinted from: *Buildings* **2025**, *15*, 1341, https://doi.org/10.3390/buildings15081341 . . . . . . **134**

Bafeng Ren, Shengbin Hu, Min Hu, Zhi Chen and Hang Lin
Safety Risk Assessment of Double-Line Tunnel Crossings Beneath Existing Tunnels in Complex Strata
Reprinted from: *Buildings* **2025**, *15*, 2103, https://doi.org/10.3390/buildings15122103 . . . . . . **160**

buildings

MDPI

Article

Numerical Analysis of the Single-Directionally Misaligned Segment Behavior of Hydraulic TBM Tunnel

Fenglan Li [1,2,*], Pengcheng Si [2], Yintao He [3], Hui Wang [2], Zhixiao Zhang [3] and Shunbo Zhao [2,*]

1 Xuchang Innovation Center of Intelligent Construction and Building Industrialization Technology, Zhongyuan Institute of Science and Technology, Zhengzhou 451400, China
2 Collaborative Innovation Center for Efficient Utilization of Water Resources, North China University of Water Resources and Electric Power, Zhengzhou 450046, China; pengcheng772@163.com (P.S.); wh@ncwu.edu.cn (H.W.)
3 Anyang Zhongzhou Water Supply Co., Ltd., Anyang 455000, China; hyt_1988@163.com (Y.H.); zzxayzz@163.com (Z.Z.)
* Correspondence: lifl64@ncwu.edu.cn (F.L.); sbzhao@ncwu.edu.cn (S.Z.)

Abstract: The misalignment of segments in installation is a common issue in the construction of TBM tunnels. This raises a question of whether misalignment affects the operation safety of a hydraulic TBM tunnel. Using a water transfer engineering project as an example, this paper built a three-dimensional finite element model composited with segment, grout layer and surrounding rock for the numerical analysis of the behavior of single-directionally misaligned segments. The crown or invert segment was separately misaligned towards to the center of segment ring in a value of 5 mm, 10 mm, 20 mm, 30 mm or 40 mm. The strength grade of the segment concrete was C50. A weaker surrounding rock composed of V-class rock was considered for the tunnel. The results indicate that the misalignment of the crown or invert segment, respectively, creates the tensile stress in the inner surface of the corresponding segment, the tensile stress will be over the limit of C50 concrete when the misalignment is over 30 mm, indicating a risk of concrete cracking. The contact surfaces of the segment ring basically remain in compression, and the locating pins between the segment rings exhibit an evident increase in tensile stress at misaligned positions. The key points that can be obtained from this study are that a special supervision is needed to ensure the accuracy of segment installation, and strengthening measures are needed for existing misaligned segments.

Keywords: hydraulic shield tunnel; segment lining; misalignment defect; stress; displacement

1. Introduction

In contemporary social development, long-distance hydraulic tunnels are indispensable for managing and distributing water resources for dwellings, industry and agriculture [1,2]. In regions characterized by mountainous terrain, the construction of hydraulic tunnels often encounters intricate geological conditions which surpasses the capabilities of traditional methods, thereby necessitating the employment of sophisticated tunnel boring machine (TBM) technology [3–5]. This raises doubt about the TBM's efficiency, which is hinged significantly on the structural reliability and stability of the tunnels. Due to the complexity of construction conditions, the impact factors not only come from the TBM itself, including the cutterhead wear, excavating attitude and thrust and jack compression on segments, but also come from surrounding conditions, including rock, underground water, adjacent structures and labor technics [6]. A common phenomenon is concerned about the misalignment between adjacent segments, which is normally caused by manufacturing discrepancies, assembly errors and the unavoidable initial misalignment in the shield process. Although the misalignment does not immediately threaten construction safety, it may adversely affect the operational safety of the tunnel, due to the alterations in the loading and unloading of the surrounding rock, nearby excavations or other activities [7,8].

This leads to the escalation of complexity and the increase in financial burden associated with the maintenance and repair of shield tunnels [9].

Numerical and experimental research has been performed on the load-bearing characteristics of hydraulic tunnels under external stresses. A half-plane time-domain boundary element method was applied to obtain the seismic ground response of tunnels [10,11]. An integrated model was formulated for a small-diameter hydraulic tunnel, which included surrounding rock, grouting and segments [12,13]; the results indicated that the stress and deformation of the segment lining are minimal during construction, with primary stresses concentrated near the joints. A semi-analytical solution was proposed to determine the ultimate load-bearing capacity of directly spliced tunnel linings [14], concentrating on the stress and deformation experienced by the linings under various vertical load cases. An analytical model was introduced, which aimed to assess the mechanical responses of shield tunnels subjected to ground fault displacements, while a large-scale model test was conducted to investigate the deformation and failure modes of tunnel structures amidst fault ruptures [15]. A full-scale test model was conducted to study the deformation and failure patterns of tunnel structures under extreme loading conditions [16]. A comprehensive three-dimensional model was developed to analyze portal structures in hydraulic tunnels, identifying potential damage modes and exploring their mechanisms [17]. In fact, a finite element model (FEM) has been specified in codes for the design and analysis of non-rods structures, including massive concrete structures and shield tunnels [18,19].

The statistical analyses have highlighted the fact that deviations in segment assembly are primary contributors to tunnel damage before construction is completed [20,21]. Common defects identified during the installation of tunnel linings are misalignments and gaps between segments [22]. Using full-scale model tests to examine the initial deformation of a tunnel [23], convergence changes were measured to gain insights into the lateral mechanical response of a misaligned shield tunnel that was impacted by unloading from neighboring excavation sites. The investigations into cracks and misalignments in the tunnel segments revealed that these issues predominantly arise from delays in backfilling with peastone grouting after installation [24]. These prevalent misalignments, classified into longitudinal and ring joint types, not only cause localized problems such as longitudinal cracks, corner drop-offs and water leakage but also change the internal force distribution within the entire tunnel ring, resulting in stress concentrations [25–27]. The stress concentration has significant implications on the failure mode of the tunnel lining, critically affecting the structure's safety and durability [28]. From a mechanical standpoint, when identifying the causes of segment misalignment, the buoyancy exerted by synchronous grouting fluid around the segments is a frequent factor; the misalignment commonly occurs at the crown and the invert segments [29]. The statistical analysis of segment misalignment during construction showed that misalignments significantly affect structural stress and primarily cause longitudinal cracking [30]. From the study of shield tunnels with segment misalignment, significant alterations in the internal forces of structure were found following the initial segment misalignment [31]. Full-scale tests and simulations revealed that excessive bolt pressure and asymmetrical stress in misaligned tunnel segments led to joint damage and distinct crack patterns under various support conditions [32,33]. This highlights the importance of investigating the effects of misalignment on the load-bearing capacities of hydraulic tunnel structures.

Therefore, tunnel segment misalignment is an issue that should be researched to identify the causes and types of misalignments, along with examining the local mechanical properties of the affected segments. Despite the above efforts reported in the literatures, there is a lack of a comprehensive analysis of a single-directionally misaligned segment on the structural load-bearing performance of the tunnel. In this respect, this study aims to bridge this gap by employing three-dimensional (3D) FEM to investigate the effects of prevalent misalignment forms on the load-bearing capacities of tunnel structures. In view of the fact that weak rock exerts significant surrounding pressure on segment lining, the V-class surrounding rock was considered in this study. The circumferential stress of segments, the segment contact stress and the locating pin stress were analyzed to identify the worst status of segment lining. The results provide an examination of the mechanical properties of segment lining with misalignment defects and valuable guidance for controlling the construction quality of the segment lining of hydraulic tunnels.

2. 3D FEM for Numerical Analysis

2.1. Composition of Segment Lining

According to the design document for the hydraulic tunnel for Anyang City's West Route of the South-to-North Water Diversion Project, the segments of shield tunnel are made of C50W8F100 concrete. Figure 1 illustrates the segment assembly of the tunnel. Each ring of the segment lining consists of four hexagonal honeycomb-shaped segments, and the adjacent segments are connected by two locating pins in the ring joints. No protrusions are used on the contact surfaces of the ring and the longitudinal joints of the segments.

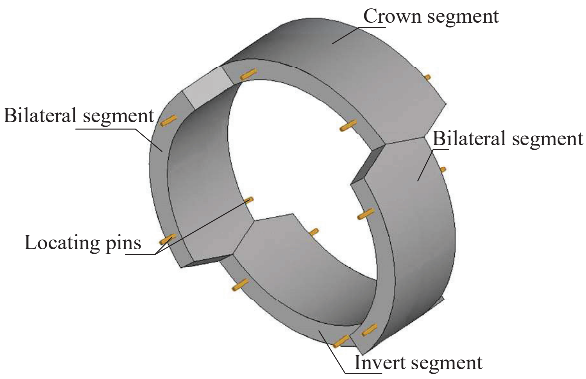

Figure 1. A ring of segment lining of the tunnel.

2.2. Composition of Segment Lining

With the aid of ANSYS 17.0 finite-element software, the coordinates of the 3D FEM of the segment lining were set as the X-axis for the transverse horizontal direction of the tunnel section, the Y-axis for the transverse vertical direction of the tunnel section and the Z-axis for the longitudinal direction along the tunnel. The boundary was determined with a distance from the lining no less than 8–10 times that of the tunnel diameter [34,35]. As shown in Figure 2a, the entire 3D FEM was built with the origin coordinate being the sectional center of the tunnel. The vertical boundary and the bottom boundary were 44 m from the center. The top boundary was the ground surface, which was selected at a poor geological condition with V-class rock, and the average burial depth was 87 m for the tunnel.

To build the 3D FEM, the mesh of the surrounding rock was first divided to simulate the initial excavation to achieve a stress equilibrium. Then, the peastone grouting, the segment lining and the locating pins were successively established, as shown in Figure 2b. The normal constraints were set on the vertical boundaries, and the fixed constraints were set in all three directions at the bottom boundary. Because this study involves quasi-static analysis, seven segment rings were established to eliminate boundary effects. The middle ring of segments was intended to give the analytical results. The segments, peastone grouting and surrounding rocks were simulated using SOLID45 elements, while the locating pins were simulated using BEAM188 elements. To achieve higher accuracy when analyzing complex geometries, all meshes were divided using mapped hexahedral elements. The surrounding rock within a 4 m radius of the tunnel was more finely meshed to ensure precise computational results. The misalignment defects of the segments were simulated by applying enforced displacement to the segments. The gaps generated by the enforced displacement were managed using element management options, ensuring that the gaps were filled with peastone grouting. The grooves between the segment contacts were simplified to planar contacts with an applied friction coefficient to simulate the behavior of the contact surfaces. The contact was established using TARGE170 target elements, which described the 3D target surfaces for contact with the CONTA173 elements. The CONTA173 contact elements were 4-node surface-to-surface contact elements, which described the contact and sliding conditions between the TARGE170 target elements and the deformable surfaces defined by these elements [36–38].

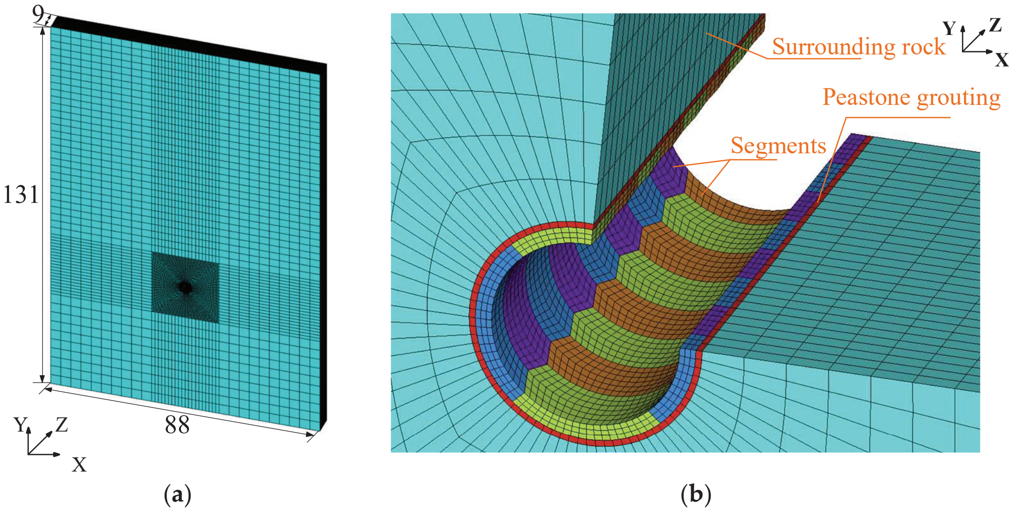

Figure 2. View of the 3D FEM of the shield tunnel for numerical analysis. (**a**) Surrounding rock model. (**b**) Detail model.

2.3. Constitutive Relationships

The constitutive relationships among the segment concrete, peastone grouting and locating pins were set as the linear elastic, with the main parameters shown in Table 1. The Mohr–Coulomb constitutive model was used for the surrounding rock, with the main parameters shown in Table 2. The interfaces between the segments and the surrounding rock and those between the segments were set as face-to-face contacts, which complied with Coulomb's law of friction along the tangent direction. When the tangential stress reached a critical value, a slipping was created with a friction coefficient of 0.5 [39]. A hard contact was applied to the normal direction of the interfaces, which was allowed to separate.

Table 1. Main physical and mechanical parameters of the segment lining materials.

Type of Material	Compressive Strength (MPa)	Tensile Strength (MPa)	Deformation Modulus (GPa)	Poisson's Ratio	Density (kg/m^3)
C50 concrete	32.4	2.64	34.5	0.1	2450
Peastone grouting	8.0	-	3.0	0.27	1700
Locating pin	-	310	210	0.3	7800

Table 2. Main physical and mechanical parameters of the surrounding rock.

Type of Surrounding Rock	Density (kg/m^3)	Internal Friction Angle (°)	Cohesion (MPa)	Deformation Modulus (GPa)	Poisson's Ratio
V	2000	20	0.08	0.5	0.40

2.4. Working Conditions

Based on empirical knowledge and findings from the related literature on segment misalignment [29,30], the most prevalent forms of segment misalignment during the installation process were crown or invert segment misalignments. These are classified as single-directionally misaligned segments, as depicted in Figure 3.

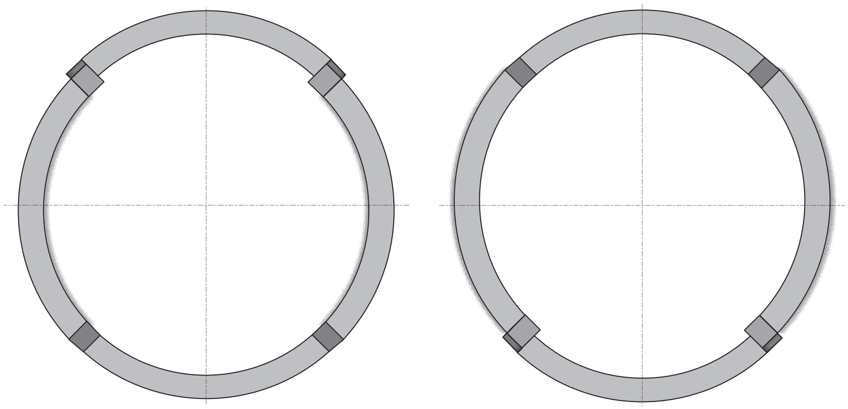

(a) (b)

Figure 3. Misalignment types of the segment lining. (**a**) Misaligned crown segment. (**b**) Misaligned invert segment.

In the acceptance reports for these two types of segment misalignments, the maximum misalignment was found to be 30 mm. Due to the complexity and unpredictability of tunnel structures, segment misalignments may exceed the acceptance criteria. To explore the stress variation trends in misaligned segment structures, the maximum segment misalignment was set as 40 mm. To investigate the effects of different amounts of misalignment, the single-directional misalignment was set as 5 mm, 10 mm, 20 mm, 30 mm or 40 mm, along with a no-defect case as a comparison. The specific conditions are shown in Table 3.

Table 3. Working conditions of the shield tunnel with segment misalignment defects.

Working Condition	Defect Type	Segment Misalignment Size (mm)
1	No defect	0
2	Misaligned crown segment	5
3		10
4		20
5		30
6		40
7	Misaligned invert segment	5
8		10
9		20
10		30
11		40

2.5. Analytical Locations of the Segment Lining

When a misalignment exists in a segment lining, the failure of the segment lining will occur if the compressive stress is over the compressive strength of the segment concrete or the misalignment enlarges to break away from the contact of the segments. Otherwise, cracks may appear on segments if the tensile stress is over the tensile strength of the segment concrete. Because the shield tunnel mainly bears the vertical load of the surrounding rock, in order to reduce the influence of boundary effects on the analytical results, the middle ring of the segment lining along the longitudinal direction of the 3D FEM was selected as the analytical object after the misalignment defects were exerted. The middle cross-section of the middle ring segment was selected to analyze the circumferential stress, from which 360 pairs of circumferential stresses were extracted at different angles. The contact surfaces of the misaligned segment were selected to analyze the contact performance, which were numbered 1 to 4, as shown in Figure 4a. Meanwhile, the locating pins numbered 1 to 8, as shown in Figure 4b, were selected to analyze the bearing performance of the locating pins.

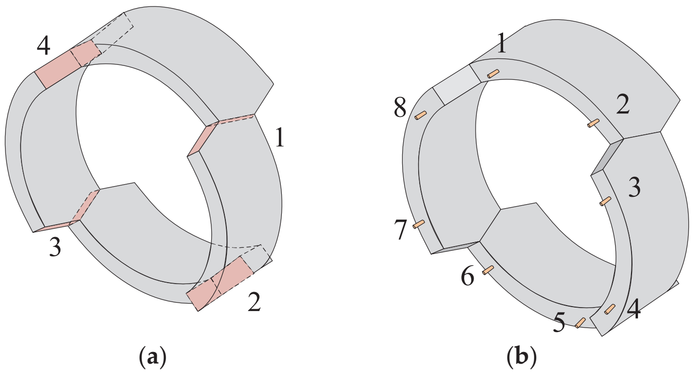

Figure 4. Analytical location of the middle ring for 3D FEM segment lining. (**a**) Misalignment defect surfaces. (**b**) Locating pins of the middle segment ring.

3. Results, Analysis and Discussion

3.1. Misaligned Crown Segment

3.1.1. Circumferential Stress of Segment

The circumferential stresses on the inner and outer layers of the middle cross-section of the misaligned ring segment are depicted in Figure 5a. It is defined that the direction toward the center of the segment is tensile stress (positive), and the outward direction is compressive stress (negative). The peak values of circumferential stress on the inner and outer layers are illustrated in Figure 5b. In the case of no defect, the stress and deformation of the segment ring is similar to existing studies [6,12], with the inner layer of both crown and invert segments experiencing tension and the inner layer of the invert segment experiencing the highest tensile stress. This demonstrates the reliability of the FEM analytical results of this study. Because the V-class rock is lower in strength, which mainly produces vertical pressure transmitted through the grout layer on the crown segment, it causes a bending effect on the crown and invert segments, with the character of outer side compression and inner side tension.

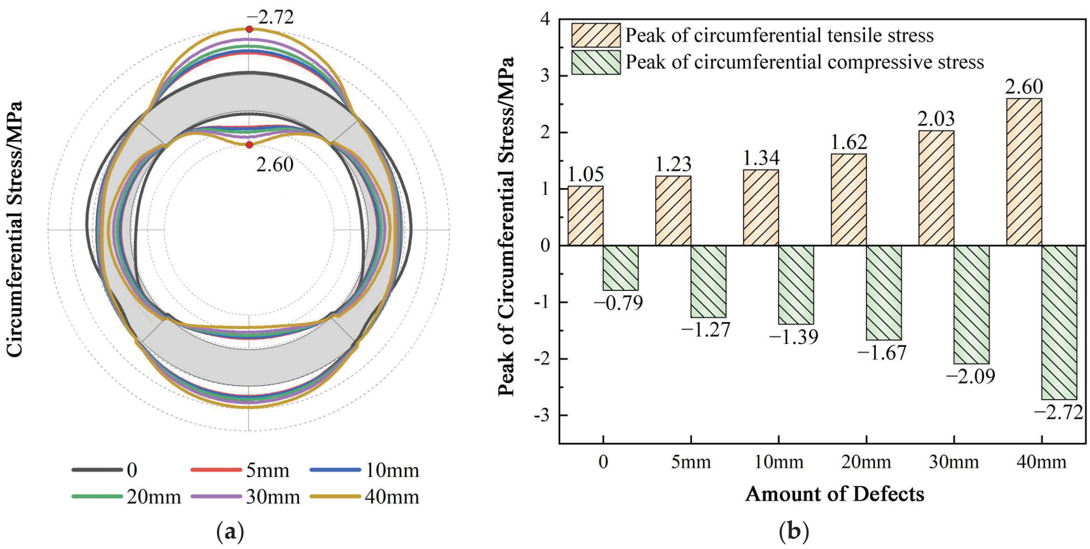

Figure 5. Circumferential stress distribution on the middle ring of the segment lining with the misaligned crown segment. (**a**) Circumferential stress of the outer and inner layers. (**b**) Peak stress.

With the increase in the misalignment of the crown segment, both the inner circumferential tensile stress and the outer circumferential compressive stress at the crown position exhibit a continuous increase tendency. The peak values of these stresses across the entire ring segment are consistently found at the middle of the crown of the misaligned segment ring. As shown in Figure 5b, the maximum tensile and compressive stresses of segment ring without misalignment are 1.05 MPa and −0.79 MPa, respectively. With a 40 mm misalignment of the crown segment, these stresses respectively escalate to 2.60 MPa and −2.72 MPa. The increments in maximum tensile stress under various conditions are 17%, 9%, 22%, 25% and 28%, while those for maximum compressive stress are 61%, 9%, 20%, 25% and 30%, respectively. Considering that the tensile stress limit of C50 concrete is 0.85 times that of the tensile strength, i.e., 0.85×2.64 MPa = 2.24 MPa [18], the tensile stress of 2.60 MPa is over the limit at the maximum crown segment misalignment. This means a substantial risk of cracking. Notably, the tensile stress of 2.03 MPa at a 30 mm segment misalignment also reaches 90.6% of the limit stress, indicating a high potential for cracking. Therefore, the segment lining exhibits a higher tolerance for compressive stresses, while tensile stress emerges as a critical factor in the potential for structural failure with the presence of crown segment misalignment.

3.1.2. Segment Contact Stress

Given the symmetrical assembly of the tunnel segments in this study, the contact stresses are likewise symmetrical. Thus, the analysis is confined to the right-hand contact surfaces, namely, contact surfaces 1 and 2. Figures 6 and 7 illustrate the contact surface stress distribution on contact surfaces 1 and 2 in the cases of different crown segment misalignments.

The FEM analysis of contact stresses on the segments without misalignment defects reveals that all joint surfaces are in normal contact, with the contact surfaces primarily transmitting compressive forces. The invert segment must endure the load transferred from the above segments, resulting in higher compressive stress on contact surface 2 than on contact surface 1. The peak compressive stresses on contact surfaces 1 and 2 are 0.62 MPa and 0.78 MPa, respectively.

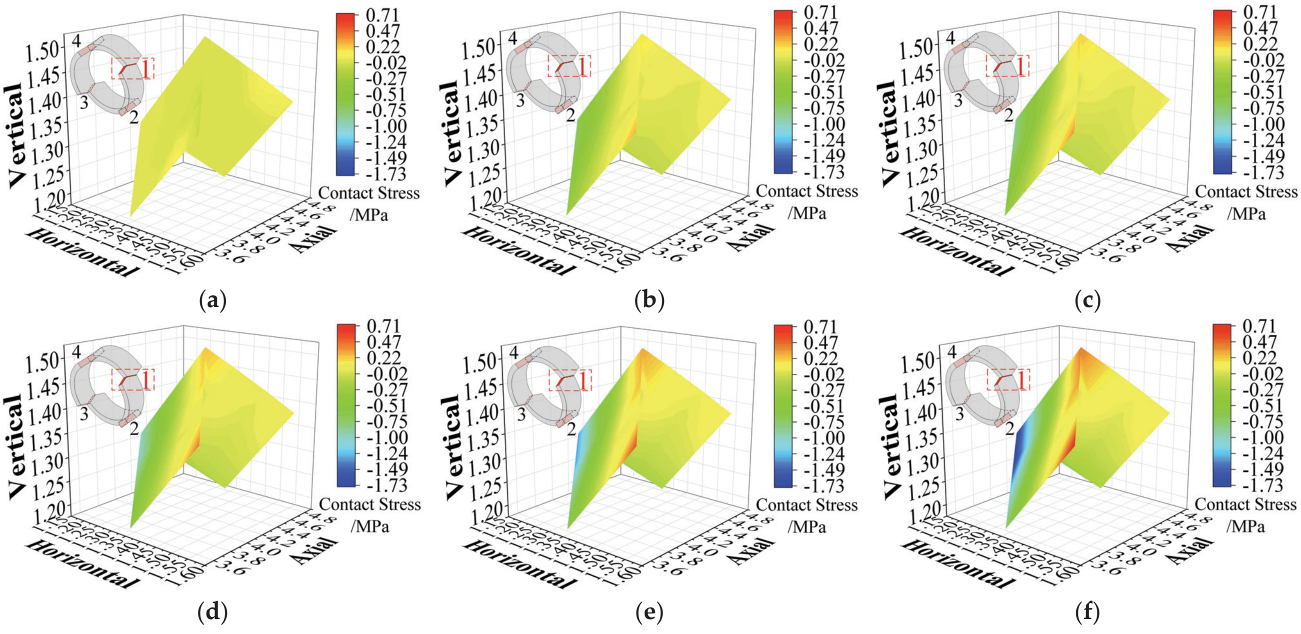

Figure 6. Contact stress on contact surface 1 of the segment ring with a misaligned crown segment: (**a**) 0, (**b**) 5 mm, (**c**) 10 mm, (**d**) 20 mm, (**e**) 30 mm and (**f**) 40 mm.

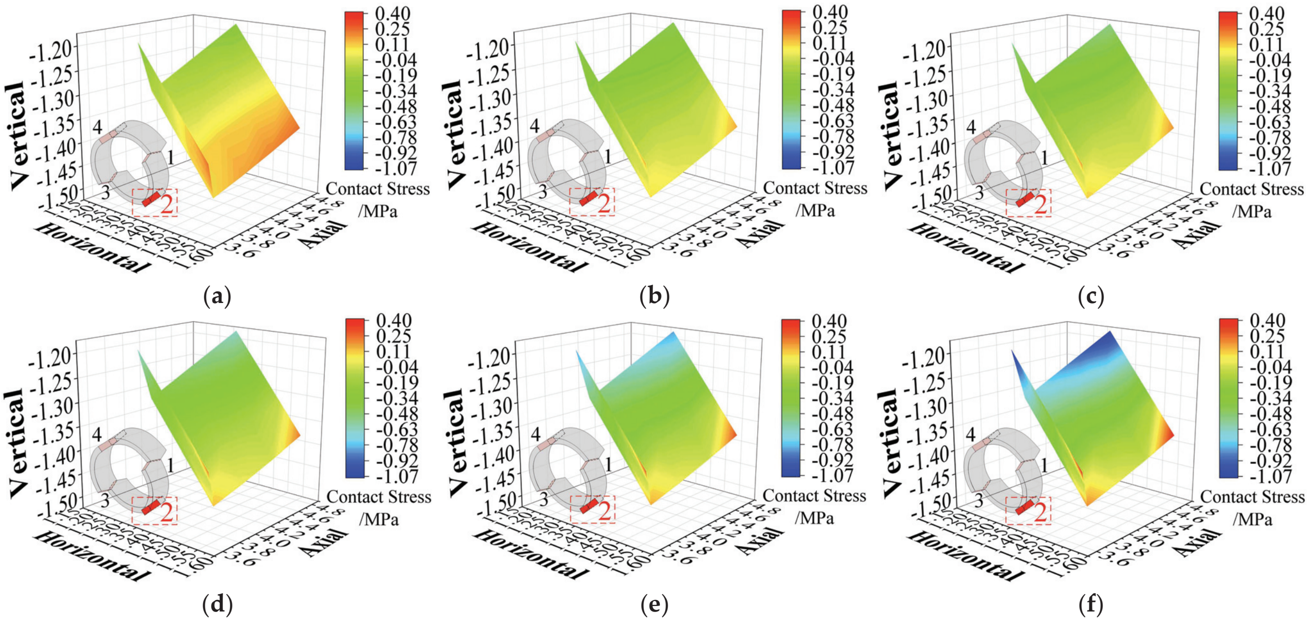

Figure 7. Contact stress on contact surface 2 of the segment ring with a misaligned crown segment: (**a**) 0, (**b**) 5 mm, (**c**) 10 mm, (**d**) 20 mm, (**e**) 30 mm and (**f**) 40 mm.

When a crown segment misalignment defect occurs, the crown segment fails to properly align with the adjacent side segments, resulting in an uneven force distribution at the site of the misalignment. As the misalignment level increases, the pressure on contact surface 1 also escalates. These defects primarily transfer loads from the interior of the segment to the invert segment, thereby increasing the pressure on contact surface 2 as the misalignment intensifies. At the maximum misalignment of 40 mm, the peak tensile stress on contact surface 1 reaches 0.71 MPa, while the maximum compressive stress reaches −1.73 MPa. Similarly, on contact surface 2, the peak tensile stress is 0.40 MPa, and the maximum compressive stress is −1.07 MPa. Despite these stress increases, the stresses on the contact surfaces remain within the design standard values, and no failure phenomenon is observed, indicating that the structure maintains its integrity even under such conditions.

3.1.3. Stress of Locating Pins

This section examines the eight locating pins positioned on the middle ring segment lining under V-class surrounding rock. Figure 8 displays the tensile stress of each locating pin under different working conditions.

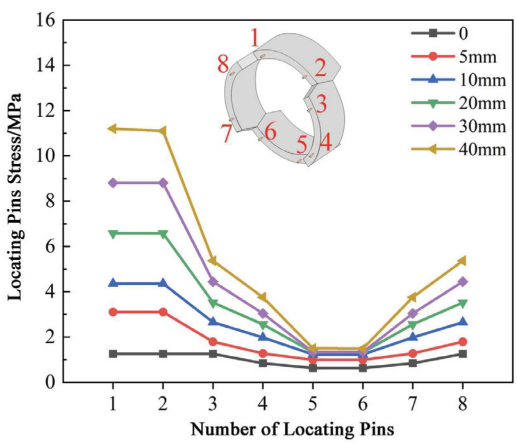

Figure 8. Stress of locating pins with a misaligned crown segment.

In the case of no misalignment defect, the vertical pressure of surrounding rock is transmitted from the crown segment through the side segments to the invert segment. This results in the greatest deformation to raise a maximum tensile stress in the crown segment; the value is 1.10 MPa. With the increase in the crown segment misalignment, the maximum stress continues to be concentrated at the crown position. The positioning pins, designed to minimize the gaps between the segment rings, enable the structure to handle increased loads. Consequently, with greater misalignment, the tensile stress of the crown's locating pins becomes more pronounced. At positions 1 and 2, the maximum tensile stress of the pins can reach 11.20 MPa. However, this underscores the critical role of maintaining the structural integrity of the tunnel under varying working conditions.

3.2. Misaligned Invert Segment

3.2.1. Circumferential Stress of Segment

Figure 9 exhibits the maximum circumferential stress distributions and the peak values of the circumferential stresses on the inner and outer surfaces of the middle cross-section of the middle ring segment with V-class surrounding rock.

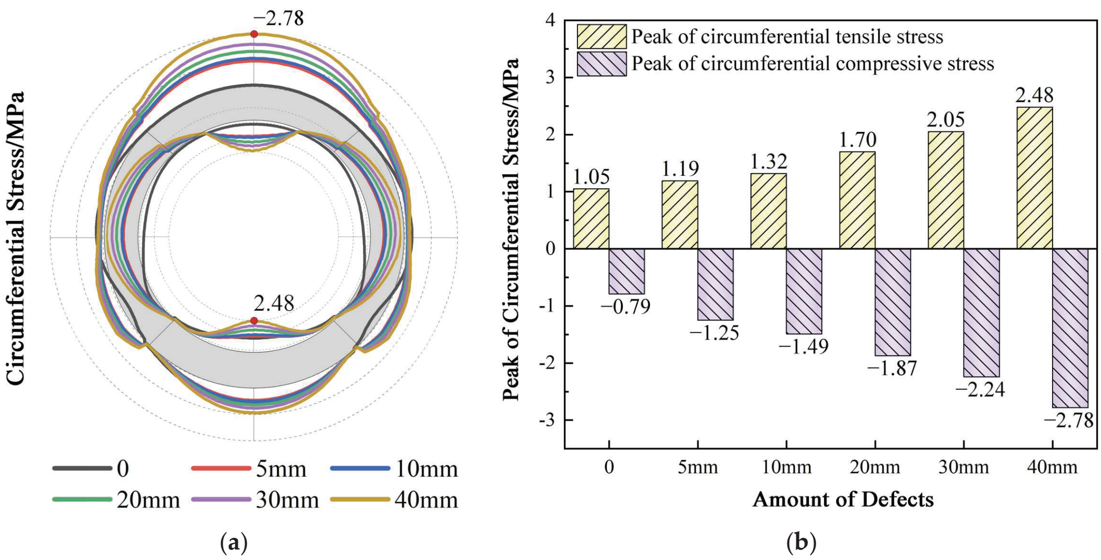

Figure 9. Distribution of the circumferential stress of the segment lining with the misaligned invert segment. (**a**) Circumferential stress of the outer and inner layers. (**b**) Peak stress.

As the misalignment of the invert segment increases, the fluctuations in the tensile and compressive stresses at the crown and invert of the arch become more significant. The peak values of circumferential tensile stress are located at the middle of the arch invert of the misaligned ring, while the peak values of compressive stress are found at the middle of the crown segment. As shown in Figure 9b, with a 40 mm misalignment, the maximum tensile and compressive stresses in the segment ring reach 2.48 MPa and −2.78 MPa, respectively. The increments in maximum tensile stress under various conditions are 13%, 11%, 29%, 21% and 17%, while the increments in maximum compressive stress are 58%, 19%, 26%, 20% and 24%. Considering the tensile stress limit is 2.24 MPa for C50 concrete [18], the tensile stress of 2.48 MPa indicates the cracking of the concrete at the maximum crown segment misalignment. Meanwhile, the tensile stress of 2.05 MPa at a 30 mm segment misalignment reaches 91.5% of the limit stress, indicating a high potential for cracking.

Therefore, the segment lining presents greater resilience to compressive stresses, while the presence of an invert segment misalignment renders tensile stress a critical factor in evaluating the risk of structural failure.

3.2.2. Segment Contact Stress

This section examines the variations in contact stress between segments at different misalignments of invert segments. Figures 10 and 11 illustrate the contact surface stress distribution of contact surfaces 1 and 2 for each invert segment misalignment.

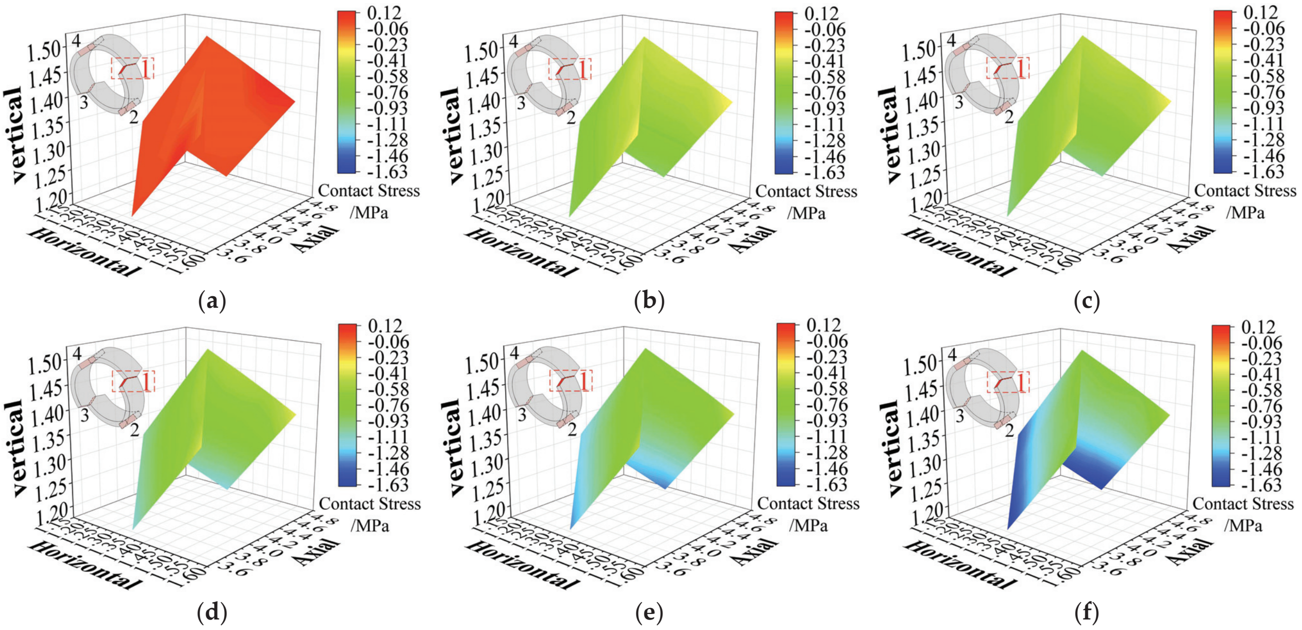

Figure 10. Contact stress on contact surface 1 of the segment ring with a misaligned invert segment: (**a**) 0, (**b**) 5 mm, (**c**) 10 mm, (**d**) 20 mm, (**e**) 30 mm and (**f**) 40 mm.

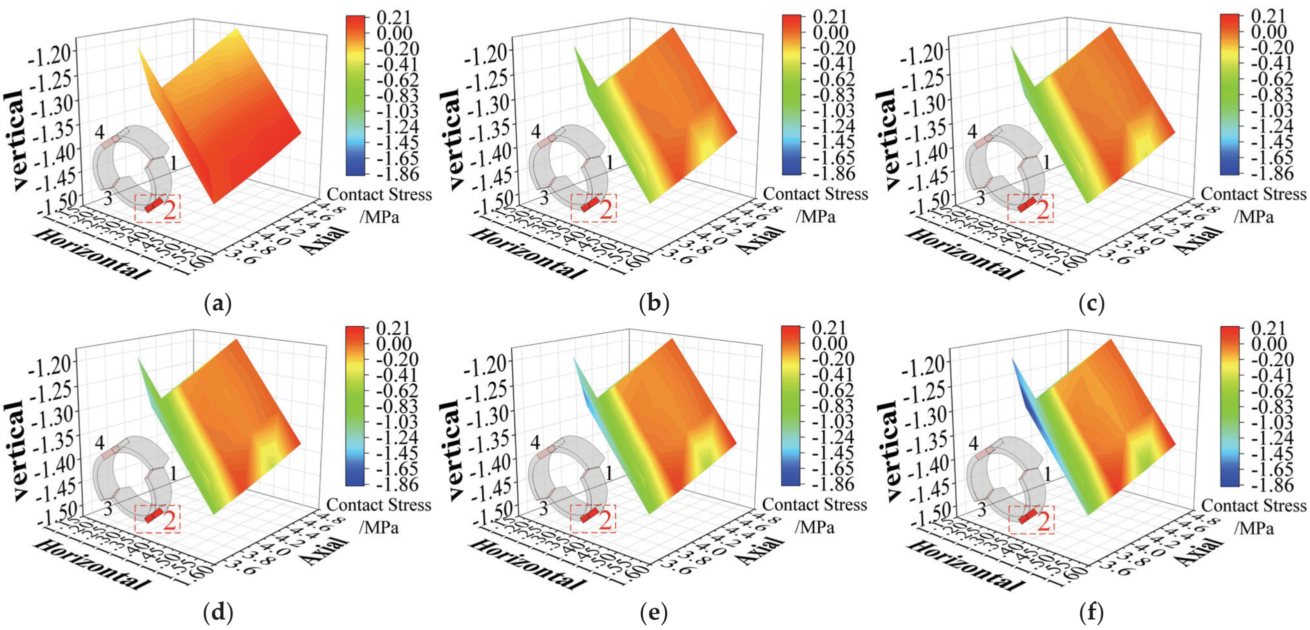

Figure 11. Contact stress on contact surface 2 of the segment ring with a misaligned invert segment: (**a**) 0, (**b**) 5 mm, (**c**) 10 mm, (**d**) 20 mm, (**e**) 30 mm and (**f**) 40 mm.

The invert segment misalignment defect in the segment lining results in an uneven force distribution at the misalignment site. This causes notable changes in the compressive stress on the contact surface between the misaligned invert segment and the adjacent side segments. As the defect increases, contact surface 1 predominantly experiences an increase in compressive stress; the contact stress between the adjacent rings on contact surface 2 shows minimal variation, while the contact stress between the misaligned invert segment and the side segments continuously escalates with the size of the defect. At the maximum defect level, the peak tensile stress on contact surface 1 is recorded at 0.12 MPa, and the peak compressive stress reaches −1.63 MPa. On contact surface 2, the peak tensile stress is 0.21 MPa, and the peak compressive stress is −1.86 MPa. Notably, in all cases, the stresses on the contact surfaces remain within the prescribed design standard values, and no failure phenomenon is observed, indicating that the structure maintains its integrity even under significant misalignment conditions.

3.2.3. Stress of Locating Pins

Figure 12 illustrates the tensile stress of each positioning pin under different conditions. It can be seen that the stress variations in the positioning pins near the invert segment intensify with the increasing misalignment of the invert segment. In the case of no defect, the positioning pins at the crown experience the maximum tensile stress. With the increase in defect degree, the structural stress gradually redistributes, with the highest stress shifting to the ring segment at the invert. The positioning pins are designed to prevent gaps between segment rings, thereby enabling them to handle increased loads. Consequently, as the defect enlarges, the tensile stress on the positioning pins at the arch invert becomes more pronounced. The maximum tensile stress on these positioning pins, particularly at positions 5 and 6, reaches a substantial 10.8 MPa.

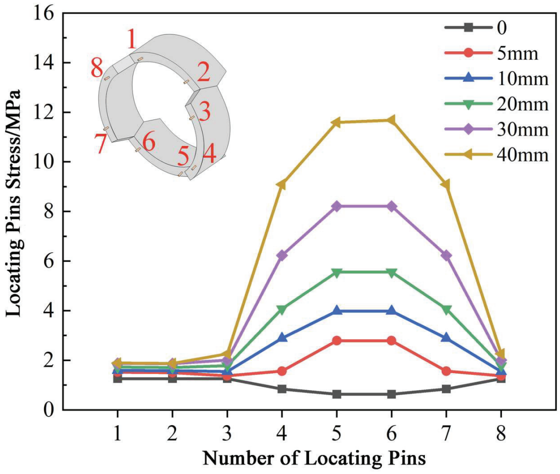

Figure 12. Stress of locating pins with the misaligned invert segment.

4. Conclusions

This paper presents a numerical simulation study on the stress characteristics of segment linings at a burial depth of 87 m, focusing on both crown and invert segment misalignment. The study yields the following conclusions:

(1) Under the influence of crown or invert segment misalignment defects, the trend of tensile stress becomes more pronounced at the corresponding crown or invert segment, identified as the structure's weak point in such cases. With a 40 mm misalignment, the maximum tensile stress of 2.60 MPa on a misaligned crown segment or 2.48 MPa on a misaligned invert segment is over the tensile stress limit for C50 concrete of 2.24 MPa, indicating a substantial risk of cracking. At a 30 mm misalignment, the tensile stress of 2.03 MPa on the misaligned crown segment or 2.05 MPa on the misaligned invert segment, respectively, reaches 90.6% and 91.5% of the limit stress, indicating a high potential for cracking.

(2) With a single-directional misalignment of segment linings, an increased tensile stress is created on the misaligned segment at the crown or invert. With the weaker surrounding rock in V-class, when the misalignment is over 30 mm, the misaligned segment will face a risk of cracking. Therefore, it is crucial to control misalignment defects during

the installation of segment lining. Due to the deformation of segment lining being directly related to the modulus of elasticity of the concrete, the segment with a lower strength of concrete will create a larger deformation, facing the issue of cracking. Therefore, a high-strength concrete should be applied to increase its cracking resistance when the misalignment is over 30 mm. In this aspect, the threshold of misalignment will change with the different strength of the concrete.

(3) The contact surfaces primarily endure compressive stress, especially at the points where the segments are misaligned; however, the stress does not pose an identifiable safety risk. The locating pins show an evident increase in tensile stress at misaligned positions, with a maximum tensile stress of 10.8–11.2 MPa, which is only 3.5%–3.6% of the 310 MPa tensile strength of steel. This indicates that the stress on each locating pin is lower than the tensile strength. Therefore, no countermeasure needs to be applied to strengthen the pins or mitigate the tensile stress.

(4) This study only researched the effect of single-directionally misaligned segments on the mechanical properties of segment lining. However, multidirectional misalignment also exists in practical engineering, which can produce an influence on the load-bearing performance of the tunnel. Future research should further explore the impact of multidirectional misalignment under different types of surrounding rock to fully assess its impact on structural safety.

Author Contributions: Methodology, F.L. and S.Z.; conceptualization, P.S. and H.W.; validation and data curation, Y.H., P.S. and Z.Z.; writing—original draft preparation, P.S. and Y.H.; writing—review and editing, Z.Z., H.W. and F.L.; supervision and funding acquisition, S.Z. All authors have read and agreed to the published version of the manuscript.

Funding: This work was supported by the Fund for First-Class Discipline Innovation Team of Henan, China (grant no. CXTDPY-6).

Data Availability Statement: The data used and/or analyzed in this study are available from the corresponding author upon reasonable request.

Conflicts of Interest: Authors Yitao He and Zhixiao Zhang were employed by the company Anyang Zhongzhou Water Supply Co., Ltd. The remaining authors declare that the research was conducted in the absence of any commercial or financial relationships that could be construed as a potential conflict of interest.

References

1. Li, X.; Cao, G.; Yao, G.; Yan, Z.; Ding, X.; Zhao, S. Optimization of anchor groove and its forming techniques with permanent formwork for prestressed concrete lining of high-pressure water conveyance tunnel. *J. North China Univ. Water Resour. Electr. Power* **2022**, *43*, 13–18.
2. Wang, X.; Behbahani, S.; Iseley, T.; Azimi, M.; Wei, X.; Wei, G.; Shi, Y. Vertical tunneling in China—A case study of a hydraulic tunnel in Beihai. *Tunn. Undergr. Space Technol.* **2021**, *107*, 103650. [CrossRef]
3. Deng, M.; Tan, Z. Study on boring indexes and key issues of tunnel boring machine cluster construction of super-long tunnels. *Tunn. Constr.* **2021**, *41*, 1809–1826.
4. Sun, W.; Shi, M.; Zhang, C.; Zhao, J.; Song, X. Dynamic load prediction of tunnel boring machine (TBM) based on heterogeneous in-situ data. *Autom. Constr.* **2018**, *92*, 23–34. [CrossRef]
5. Huang, X.; Liu, W.; Zhang, Z.; Zhuang, Q.; Zhu, Y.; Wang, Q.; Kwok, C.Y.; Wang, S. Structural behavior of segmental tunnel linings for a large stormwater storage tunnel: Insight from full-scale loading tests. *Tunn. Undergr. Space Technol.* **2020**, *99*, 103376. [CrossRef]
6. Zhang, Z.; Wang, B.; Wang, X.; He, Y.; Wang, H.; Zhao, S. Safety risk assessment of TBM tunnel construction based on fuzzy evidence reasoning. *Processes* **2022**, *10*, 2597. [CrossRef]
7. Su, A.; Wang, S.; He, C.; Lu, D.; Fang, R. Disease characteristics and causes analysis of segments of shield tunnels in composite stratum during construction. *Chin. J. Geotech. Eng.* **2019**, *67*, 683–692.
8. Li, X.; Lin, X.; Zhu, H.; Wang, X.; Liu, Z. Condition assessment of shield tunnel using a new indicator: The tunnel serviceability index. *Tunn. Undergr. Space Technol.* **2017**, *67*, 98–106. [CrossRef]
9. Yao, Z.; Xiong, Y.; Fu, L.; Quan, Y.; Niu, W.; Hu, L. Failure mechanism and support technology of surrounding rocks in lithologic interface area of deep-buried tunnel bored by tunnel boring machine. *Tunn. Constr.* **2023**, *43*, 102–111.

10. Panji, M.; Mojtabazadeh-Hasanlouei, S. On subsurface box-shaped lined tunnel under incident SH-wave propagation. *Front. Struct. Civ. Eng.* **2021**, *15*, 948–960. [CrossRef]
11. Panji, M.; Mojtabazadeh-Hasanlouei, S. Seismic ground response by twin lined tunnels with different cross sections. *SN Appl. Sci.* **2021**, *3*, 787. [CrossRef]
12. Su, K.; Zhou, X.; Wu, H.; Mao, W.; Geng, B. Structure characteristics of parallelogram segment lining in deep-buried tunnel under hydraulic pressure. *Water Resour. Power* **2019**, *37*, 45–48.
13. Su, K.; Zhao, X.; Yang, F.; Geng, B.; Wang, M. Structure characteristics of a new kind of parallelogram segment lining in TBM tunnel. *Eng. J. Wuhan Univ.* **2020**, *53*, 471–482.
14. Li, H.; Li, X.; Liu, H. Deformation and failure mechanism of metro shield tunnel subjected to buried fault dislocation. *Eng. Fail. Anal.* **2023**, *15*, 107551. [CrossRef]
15. Li, H.; Li, X.; Liu, H. Analytical solution for evaluating the effects of buried fault dislocation on segmental tunnel considering the plastic yield behavior of circumferential joints. *Alex. Eng. J.* **2024**, *97*, 319–332. [CrossRef]
16. Liu, X.; Bai, Y.; Yuan, Y.; Mang, H. Experimental investigation of the ultimate bearing capacity of continuously jointed segmental tunnel linings. *Struct. Infrastruct. Eng.* **2015**, *12*, 1364–1379. [CrossRef]
17. Wang, X.; Chen, J.; Zhang, Y.; Xiao, M. Seismic responses and damage mechanisms of the structure in the portal section of a hydraulic tunnel in rock. *Soil Dyn. Earthq. Eng.* **2019**, *123*, 205–216. [CrossRef]
18. *SL 191-2008*; Design Code for Hydraulic Concrete Structures. China Hydropower Press: Beijing, China, 2008.
19. *GB/T 51438-2021*; Standard for Design of Shield Tunnel Engineering. China Standard Press: Beijing, China, 2021.
20. Sharghi, M.; Chakeri, H.; Afshin, H.; Dias, D. Analysis of the possible cracking and damages of tunnel lining segments during installing stage. *Soil Mech. Found. Eng.* **2021**, *58*, 287–294. [CrossRef]
21. Sharghi, M.; Afshin, H.; Dias, D.; Jeong, H. 3D numerical study of the joint dislocation and spacing impacts on the damage of tunnel segmental linings. *Structures* **2023**, *56*, 104878. [CrossRef]
22. Cavalaro, S.; Blom, C.; Aguado, A.; Walraven, J. New design method for the production tolerances of concrete tunnel segments. *J. Perform. Constr. Facil.* **2012**, *26*, 824–834. [CrossRef]
23. Wei, G.; Feng, F.; Cui, Y.; Wang, X.; Diao, H.; Wu, Y. Research on the influence of foundation pit excavation on the lateral force and deformation of side shield tunnels based on full-scale experiments. *Tunn. Undergr. Space Technol.* **2023**, *140*, 105236. [CrossRef]
24. Li, W.; Xu, J.; Han, L. Analysis on reason of cracks and translocation in 6# tunnel of general trunk line leading Yellow river. *Water Resour. Hydropower Eng.* **2002**, *33*, 13–14.
25. Qin, J.; Zhu, W.; Chen, J. Study of dislocation of duct pieces and crack problems caused by shield attitude control. *Constr. Technol.* **2004**, *33*, 25–27.
26. Xu, X.; Li, Z.; Wang, K.; He, H. Structural scheme of metro station constructed by enlarging large diameter shield tunnel and stress and deformation of its key joints. *China Railw. Sci.* **2021**, *42*, 66–76.
27. Jin, Y.; Ding, W.; Xiao, M.; Sun, W.; Wu, W.; Ye, M.; Tu, X. Experimental research on sealing behavior of segmental joints of Sutong GIL utility tunnel under ultra-high water pressure. *Tunn. Constr.* **2020**, *40*, 538–544.
28. Nabipour, M.; Rezapour, S.; Mohajeri, S. A parametric study on friction-loss in water conveyance tunnels considering misalignment of precast concrete segments. *Tunn. Undergr. Space Technol.* **2020**, *96*, 103221. [CrossRef]
29. Ding, E.; Wei, Y.; Wang, Y.; Kang, G. Analysis of causes of tunnel segment misplacement and prevention and control measures from the perspective of mechanics. In Proceedings of the National Civil Engineering Construction Technology Exchange Meeting, Beijing, China, 21 December 2020.
30. Chen, W.; Li, S.; Zhang, Z. Segment cracking analysis of double shield TBM tunnel in construction stage. *Tunn. Constr.* **2020**, *40*, 50–57.
31. Wang, G.; Wang, Y.; Mu, J.; Sun, F. Seismic performance analysis of shield tunnel considering segment misalignment. *J. Railw. Eng. Soc.* **2021**, *38*, 93–101.
32. Sun, W.; Li, X.; Cheng, K.; Jia, W.; Liu, H. Analysis on the influence of large diameter intercity railway tunnel under passing the main canal of the middle route of South-to-North Water Diversion Project. *J. North China Univ. Water Resour. Electr. Power* **2020**, *40*, 46–52.
33. Meda, A.; Rinaldi, Z.; Caratelli, A.; Cignitti, F. Experimental investigation on precast tunnel segments under TBM thrust action. *Eng. Struct.* **2016**, *119*, 174–185. [CrossRef]
34. Ding, W.; Wu, Y.; Zhang, X.; Qiao, Y. Effect of dislocation on flexural behavior of longitudinal segmental joint for shield tunnel. *China J. Highw. Transp.* **2023**, *36*, 256–265.
35. Wang, H.; Chen, Z.; Ma, S.; Li, X.; Liu, S.; Zhao, S. Seismic performance analysis of shallow-buried large-scale three-box-section segment-connected pipeline structure under multiple actions. *Sci. Rep.* **2023**, *13*, 2584. [CrossRef] [PubMed]
36. Wang, X.; Li, Y.; Xu, H. *ANSYS Structural Analysis Unit and Application*, 1st ed.; China Communications Press: Beijing, China, 2011; pp. 375–406.
37. Chen, Z.; Zhao, S. *Structural Finite Element Analysis Principle and Engineering Examples*; Machine Industry Press: Beijing, China, 2024.

38. Chen, Z.; Li, X.; Yang, Y.; Zhao, S.; Fu, Z. Experimental and numerical investigation of the effect of temperature patterns on behaviour of large scale silo. *Eng. Fail. Anal.* **2018**, *91*, 543–553. [CrossRef]
39. Cao, Y.; Wang, P.; Jin, X.; Wang, J.; Yang, Y. Tunnel structure analysis using the multi-scale modeling method. *Tunn. Undergr. Space Technol.* **2012**, *28*, 124–134. [CrossRef]

buildings

MDPI

Article

Research on the Mechanism and Application of High Pre-Tension on the Crack-Arresting Effect of Rockbolt Anchorage

Bowen Wu [1,*], Jucai Chang [1], Xiangyu Wang [2], Wenbao Shi [1], Chuanming Li [1] and Dingchao Chen [2]

[1] School of Mining Engineering, Anhui University of Science and Technology, Huainan 232001, China; cjcminecoal@163.com (J.C.); 2014070@aust.edu.cn (W.S.); chuanmingliaust@163.com (C.L.)

[2] School of Mines, China University of Mining and Technology, Xuzhou 221116, China; wangxiangyu@cumt.edu.cn (X.W.); tb23020002a41ld@cumt.edu.cn (D.C.)

* Correspondence: 2022013@aust.edu.cn; Tel.: +86-18252430278

Abstract: In order to investigate the effect of pre-tension on the anchoring and crack-arresting effect of rockbolts, a theoretical model of stress intensity factor at the crack tip in anchored surrounding rock was established using fracture mechanics theory. An expression for the difference in stress intensity factor due to axial force on the rockbolt was derived, exploring the influence of pre-tension on the stress intensity factor of cracks. A numerical model of anchored crack specimens was developed using UDEC (V6.0) software to simulate and analyze the mechanical performance and damage characteristics of specimens anchored with different pre-tension. The results indicate that the difference in stress intensity factor of cracks is positively correlated with pre-tension. High-pre-tensioned rockbolts can effectively reduce the stress intensity factor of cracks. Prestressed rockbolts can alter the failure mode of rock masses from shear failure along pre-existing cracks to tensile splitting failure. The application of high pre-tension significantly enhances the strength of the rock mass, reducing both the damage degree and the number of internal cracks. After anchoring with high-pre-tensioned rockbolts, the peak strength and elastic modulus of the crack specimens increased by 22.5% and 31.9%, respectively, while damage degree decreased by 17.4%, the number of shear cracks decreased by 22.6%, and the number of tensile cracks decreased by 42.9%. The pre-tensioned rockbolt method proposed in this study was applied to the support of roadway widening. Field monitoring data indicated that the axial force of the rockbolts in the test section generally exceeded 60 kN, effectively controlling the deformation of the roadway surrounding the rock. The convergence of the two sides decreased by 22%, and borehole inspections showed a significant reduction in internal cracks. The research results provide a theoretical basis for controlling the discontinuous deformation of deep broken surrounding rock roadways.

Keywords: rockbolt support; strength factor; crack propagation; pre-tension; crack-arresting effect

1. Introduction

As one of the crucial reinforcement techniques in underground engineering, rockbolt support has been widely applied in the control of surrounding rock in coal mine roadways in China [1–3]. High-prestressed, high-strength, and high-elongation rockbolt support is an effective method for controlling the deformation of surrounding rock. By actively applying high pre-tension, a high-strength prestressed rockbolt can fully mobilize the inherent stability of the surrounding rock [4,5]. With the increasing depth of coal resource extraction, the support objects in deep roadways are often fractured rock masses containing cracks. The continuous propagation of these internal cracks in the surrounding rock is a major cause of anchor instability [6]. Therefore, it is necessary to conduct research on the crack-arresting effect of high-pre-tensioned rockbolts to effectively control the discontinuous deformation of fractured surrounding rocks.

The instability of fractured rock masses is primarily driven by slippage along weak planes, and rockbolts exert their anchoring effect through mechanisms such as toughening, slip resistance, and axial compression [7,8]. Scholars have conducted extensive research on the mechanical properties of bolted jointed rock masses and the crack-arresting mechanisms of rockbolts. Liu et al. [9] and Liu et al. [10,11] found that high-pre-tensioned rockbolts can significantly increase the cohesion and internal friction angle of joint surfaces, effectively enhancing the shear stiffness of jointed rock masses and inhibiting rock deformation. Zhou et al. [12] found that as the angle of rockbolts changes, the ultimate tensile strength of the bolted body first increases and then decreases. Wang et al. [13] concluded that full-length anchoring and extended anchoring can effectively control the deformation of jointed surrounding rock in roadways. Shi et al. [14] posited that the stability of the support structure is determined by the bond damage at the rockbolt–rock interface. Based on the uniaxial compression and CT scan results of bolted rock samples, Teng et al. [15] concluded that the crack-arresting effect of rockbolts is due to the weakening, cutting, and arresting of cracks within the bolted zone. Experimental results of Zhao et al. [16] indicated that rockbolts can enhance the cracking strength, elastic modulus, and peak strain ratio of jointed rocks. The simulation analysis results of Wang et al. [17] indicated that prestressed rockbolts crossing joints can effectively increase the compressive stress on crack surfaces. Wu et al. [18] believed that the reinforcement mechanism of rockbolts can be divided into two aspects: one is to share the load, and the other is to inhibit crack propagation. Zu et al. [19] discovered that high-pre-tensioned rockbolts could still exert crack-arresting effects under impact loads, significantly enhancing the fracture toughness of rock masses and delaying the initiation and development of cracks. Zhang et al. [20] concluded that the axial force of the rockbolts, combined with the expansive stress of the grout, acts synergistically on the fractured rock mass, thereby improving its stress situation. Li and Ge [21,22] identified the “axial compression” and “dowel” effects as the primary mechanisms by which rockbolts control internal cracks in rock masses. Through acoustic emission and stress monitoring in uniaxial failure tests, Wang et al. [23] demonstrated that within the effective anchoring range, rockbolts can delay the initiation of primary cracks and increase the strength of cracked specimens. Yuan et al. [24] simulated and analyzed rockbolts from a microscopic perspective, concluding that rockbolts increase the cohesion of cracks within rock masses. Zhou et al. [25] found that prestressed rockbolts not only enhance the mechanical properties of rock masses, but also restrict crack formation and alter crack propagation modes. Chen et al. [26] and Wu et al. [27] discovered that rockbolts could effectively reduce the number of cracks within the fill body and increase its load-bearing capacity.

Based on the previous research conclusions, it can be found that rockbolts can delay the initiation time and development speed of cracks, reduce the number of cracks in the rock body, and improve the shear stiffness and compressive strength of the rock mass by increasing parameters such as crack cohesion, internal friction angle, and initiation strength in the anchorage zone, thereby achieving stability of the fractured rock mass. However, the crack-arresting effect of rockbolts on cracks in rock masses is the result of multiple factors, such as pre-tension, anchoring method, anchoring zone range, and rockbolts–rock interface damage. The mechanism by which pre-tension affects the crack-arresting effect of rockbolts is still unclear. Therefore, this article conducts relevant research on the factor of pre-tension. Firstly, based on the theory of fracture mechanics, a theoretical model of the stress intensity factor at the crack tip of the anchored rock mass in deep roadways was established. The relationship between the pre-tension and the stress intensity factor of the crack was clarified, and it was proven that high-pre-tensioned rockbolts can suppress the initiation of internal cracks in the rock mass. Subsequently, numerical simulation methods were used to study the mechanical and damage characteristics of the anchorage body, analyzing the strength, number of cracks, and degree in damage of the anchorage body under different pre-tension, and elucidating the mechanism by which pre-tension affects the crack-arresting effect of rockbolts. Finally, effective reinforcement methods were proposed based on the research results and actual on-site conditions.

2. Engineering Profile

2.1. Engineering Background

The Ji-15-23090 headgate of Pingmei No. 4 Mine is located in the Ji-15 coal seam at a depth of 900 m. The coal seam exhibits blocky structures with an average thickness of 1.5 m and an average dip of 9.6°. The immediate roof consists of a composite roof composed of 4.5 m of fine sandstone and 0.25 m of Ji-15 coal, while the main roof is 3.0 m of fine sandy mudstone. The immediate floor comprises 1.6 m of mudstone, and the main floor is 7.5 m of fine sandy mudstone.

The roadway is driven along the roof of the coal seam, with a net width of 5.4 m and a height of 3.4 m, utilizing anchor and mesh support. The specifications for the side rockbolts are Φ22 × 2400 mm, with five rockbolts in the upper side and four rockbolts in the lower side, spaced at intervals of 750 × 800 mm. The rockbolts are torqued to 300 N·m. The support parameters are illustrated in Figure 1a, and the field deformations are depicted in Figure 1b.

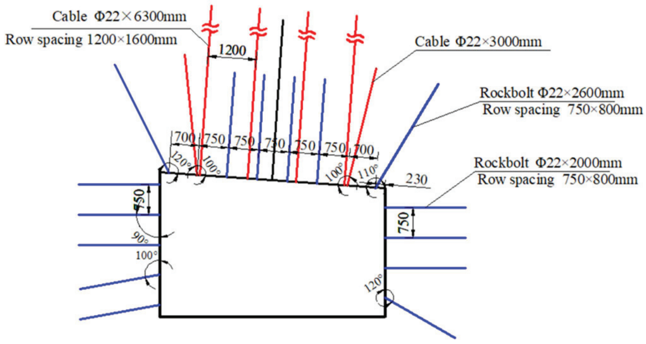

(**a**)

(**b**)

Figure 1. Original support scheme and deformation of roadway. (**a**) Original roadway support scheme. (**b**) Roadway deformation situation.

2.2. Analysis of Peeping Results

During the mining period, influenced by high in situ stress and mining-induced stress at depth, the surrounding rock of the Ji-15-23090 headgate has become fragmented. In order to view the broken surrounding rock of the roadway, boreholes are arranged in the side of the roadway for peeping. Figure 2 shows the arrangement and observation of boreholes. The blue circle in this Figure shows five boreholes, and five photos show the observation of each borehole.

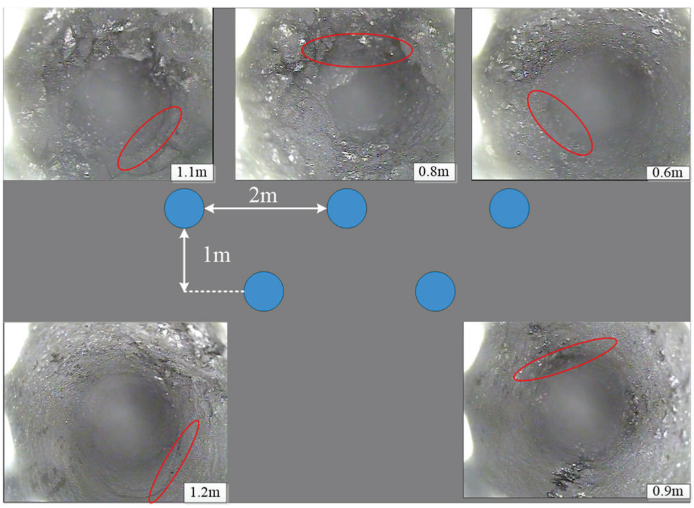

Figure 2. Peeping results of roadway side.

In adjacent boreholes at a depth of approximately 1 m, there are evident circumferential cracks, and the boreholes are considerably fractured. This indicates that at around 1 m depth, there are extensive primary cracks with numerous secondary cracks, leading to significant extrusion of the roadway sides and an average reduction in cross-sectional width to 3.5 m. To ensure safe production, it is necessary to carry out roadway expansion operations.

2.3. Current Issues

From the field observation results, it can be seen that the torque rockbolt has a poor control effect on the deformation of the surrounding rock of the deep roadway due to the low pre-tension, and it is difficult to effectively control the crack development inside the surrounding rock, resulting in the fragmentation of the roadway surrounding the rock and causing the large deformation of the roadway. In response to this situation, this manuscript adopts the methods of theoretical analysis and numerical simulation to carry out relevant research on the crack-arrest effect of high-pre-tension rockbolt, analyzes the mechanism of high-pre-tension affecting the crack-arrest effect of rockbolts, and puts forward effective support methods applied to the field in order to solve the problem of difficult maintenance of deep fractured rock roadways.

3. Theoretical Analysis of Crack-Arresting Effect of Prestressed Rockbolts

Rockbolts primarily inhibit crack propagation through the shear stiffness of the rod and the application of axial force. This study focuses on the axial force of rockbolts, and based on the stress conditions of the surrounding rock in deep roadways and fracture mechanics theory, establishes the theoretical model of the stress intensity factor at the crack tip in anchored surrounding rock, as shown in Figure 3a. This model is used to explore the influence of pre-tension on the crack-arresting effect of rockbolts.

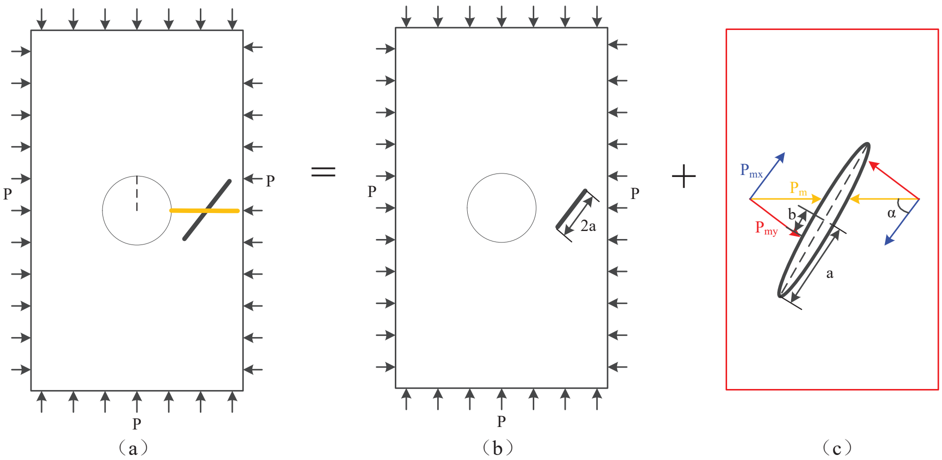

Figure 3. Theoretical analysis model. (**a**) Theoretical model of the stress intensity factor at the crack tip in anchored surrounding rock; (**b**) in situ stress influence model; (**c**) rockbolt axial force influence model.

3.1. Stress Intensity Factor Model for Cracks in Anchored Surrounding Rock

Assume the surrounding rock is a homogeneous elastic body under hydrostatic pressure, and ignore the influence of the crack on the stress field distribution [28,29]. The angle between the rockbolt (represented by yellow lines) and the crack is α, and the crack length is 2a. In linear elasticity problems, the stress fields generated by each load can be calculated linearly. Therefore, the model can be decomposed into the in situ stress influence model (Figure 3b) and the rockbolt axial force influence model (Figure 3c).

The intrinsic characteristics of internal cracks in the surrounding rock of deep mine roadways and their stress environment are relatively fixed. The main goal of rockbolt support is to reduce the stress intensity factor of the cracks, thus preventing them from reaching the fracture toughness. In the in situ stress influence model, the calculation of the stress intensity factor follows the problem of crack initiation under compressive and shear stresses. Hence, this study focuses on calculating and analyzing the stress intensity factor in the rockbolt axial force influence model.

3.2. Expression for the Stress Intensity Factor of Cracks under Axial Force of Rockbolt

Under compressive and shear forces, crack initiation is influenced by the decomposed axial force parallel to its surface. Therefore, the rockbolt axial force influence model can be converted into a model of a crack in an infinite plate subjected to a concentrated shear force (Figure 4).

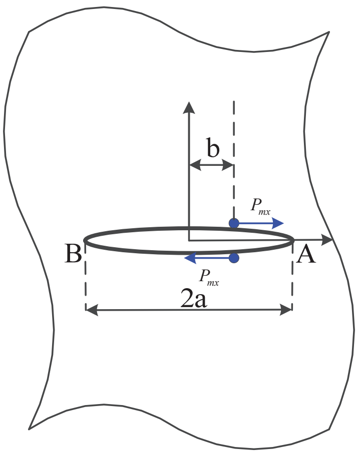

Figure 4. Concentrated shear force model of cracks in an infinite plate.

From Figure 3c, the expression for P_{mx} is obtained as follows:

$$\left.\begin{array}{l} P_{my} = P_m \sin\alpha \\ P_{mx} = P_m \cos\alpha \end{array}\right\} \tag{1}$$

where P_{mx} is the decomposed force parallel to the crack surface, kN, and P_{my} is the decomposed force perpendicular to the crack surface, kN.

In the full-length anchoring method, the relationship between the axial force and the pre-tension of rockbolt is given by [30]:

$$P_m = P_t e^{-\frac{tz^2}{2}} \tag{2}$$

where $t = \frac{1}{(1+\mu)(3-2\mu)d^2}\left(\frac{E}{E_m}\right)$; P_m is the axial force of rockbolt, kN; P_t is the tensile stress at the end of the rockbolt, kN; μ is the Poisson's ratio of the rock mass; d is the radius of the rockbolt, mm; E is the elastic modulus of the rock mass, GPa; E_m is the elastic modulus of the rockbolt, GPa; and z is the distance from the hole mouth, m.

When the rockbolt does not penetrate the crack perpendicularly and $b \neq 0$, the stress intensity factors generated by the concentrated shear stress at both ends of the crack are different. The stress intensity factor at the closer point to the anchor point is selected as the crack-tip stress intensity factor. Based on the Westergard stress function method, the expression for the stress intensity factor at point A is [31]:

$$\begin{aligned} K_{\mathrm{II}A} &= \lim_{|z'|\to 0} \sqrt{2\pi z'} Z_{\mathrm{II}}(z') \\ &= \lim_{|z'|\to 0} \sqrt{2\pi z'} \frac{P_{mx}\sqrt{a^2-b^2}}{\pi(z'+a-b)\sqrt{z'(z'+2a)}} \\ &= \frac{P_{mx}}{\sqrt{\pi a}}\sqrt{\frac{a+b}{a-b}} \end{aligned} \tag{3}$$

Establishing the geometric relationship between b and the semi-minor axis of the ellipse (c), as shown in Figure 5, and the relationship between the two is as follows:

$$b = \frac{c \tan \alpha}{1 + \tan^2 \alpha} \tag{4}$$

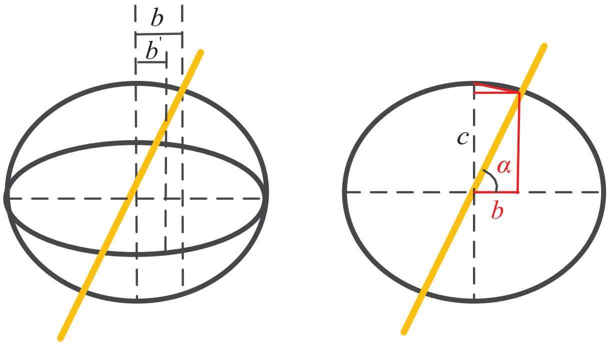

Figure 5. Diagram of value b change and its relation with semi-minor axis of ellipse (c) (The yellow line represents the rockbolts).

The semi-minor axis of the ellipse (c) is controlled by the normal stress generated on the crack surface by the axial force of the rockbolt (P_{my}). Therefore, it is necessary to clarify the relationship between the normal stress on the crack surface (P_{my}) and the semi-minor axis (c).

Based on the fracture constituent elements, a model is established, as shown in Figure 6, to analyze the relationship between the normal stress on the crack surface and the crack opening, assuming that the crack is subjected to a uniformly distributed normal stress (P_{my}), denoted as σ_z, the crack opening is c_m, where c_m = 2c, and the elastic constants of the crack are λ_c and G_c. The normal stiffness of the crack is K_{nc}, and the shear stiffness is K_{sc}.

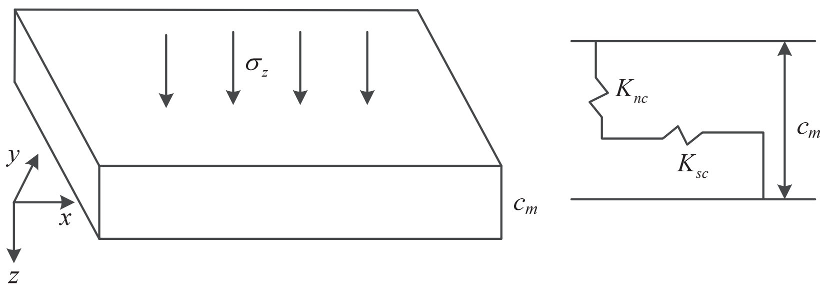

Figure 6. Calculation model of relationship between crack opening and normal stress.

According to the generalized Hooke's law:

$$\begin{Bmatrix} d\sigma_z \\ d\tau_{xz} \\ d\tau_{zy} \end{Bmatrix} = \begin{bmatrix} K_{nc} & 0 & 0 \\ 0 & K_{sc} & 0 \\ 0 & 0 & K_{sc} \end{bmatrix} \begin{Bmatrix} dU_z \\ dU_x \\ dU_y \end{Bmatrix} \tag{5}$$

where $K_{nc} = \frac{\lambda_c + 2G_c}{c_m - U_z}$, $K_{sc} = \frac{G_c}{c_m - U_z}$.

From Equation (5), the expression for the deformation of the crack under compression (U_z) is:

$$U_z = c_{\mathrm{m}} \left(1 - e^{-\frac{\sigma_z}{\lambda + 2G}}\right) \tag{6}$$

Therefore, the crack opening after compression (c'_m) is:

$$c'_m = c_m - U_z = c_m e^{-\frac{P_{my}}{K_{nc} \cdot c_m}} \tag{7}$$

Since c_m = 2c, the evolution relationship for b can be derived as:

$$b = \frac{2ce^{-\frac{P_{my}}{2K_{nc}\cdot c}}\tan\alpha}{1+\tan^2\alpha} \tag{8}$$

Letting K_{nc} = 200 GPa/m, α = 60°, c = 0.1 m, the evolution curve for b can be calculated by substituting these values into Equation (8), as shown in Figure 7. The trend indicates that the anchor point of the rockbolt shifts towards the center of the crack as the pre-tension increases.

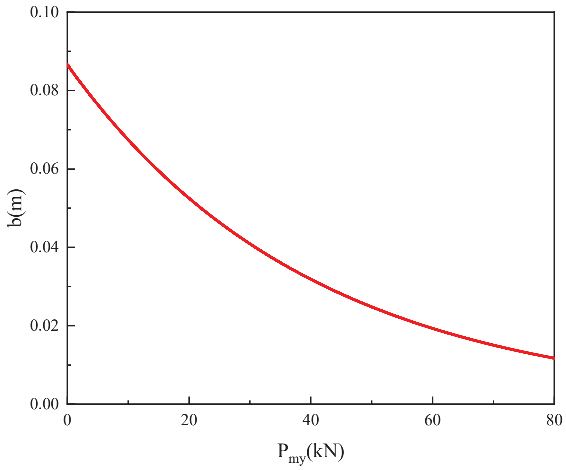

Figure 7. Relationship between b value and normal stress.

Combining Equations (2)–(4) and (8), the expression for the stress intensity factor of the crack under axial force is:

$$K_{\mathrm{II}m} = \frac{P_t e^{-\frac{tz^2}{2}}\cos\alpha}{\sqrt{\pi a}}\sqrt{\frac{a\left(1+\tan^2\alpha\right)+2ce^{-\frac{P_t e^{-\frac{tz^2}{2}}\sin\alpha}{2K_{nc}\cdot c}}\tan\alpha}{a\left(1+\tan^2\alpha\right)-2ce^{-\frac{P_t e^{-\frac{tz^2}{2}}\sin\alpha}{2K_{nc}\cdot c}}\tan\alpha}} \tag{9}$$

According to fracture mechanics theory, under compressive and shear conditions, the damage and failure of the cracked rock mass are still caused by the propagation of tensile cracks [32]. Therefore, the expression for the mode II crack stress intensity factor obtained from Equation (9) needs to be converted into an expression for the mode I crack stress intensity factor:

$$\begin{aligned} K_{\mathrm{I}m} &= \frac{2}{\sqrt{3}}K_{\mathrm{II}m} \\ &= \frac{2}{\sqrt{3}}\left[\frac{P_t e^{-\frac{tz^2}{2}}\cos\alpha}{\sqrt{\pi a}}\sqrt{\frac{a\left(1+\tan^2\alpha\right)+ce^{-\frac{P_t e^{-\frac{tz^2}{2}}\sin\alpha}{K_{nc}\cdot c}}\tan\alpha}{a\left(1+\tan^2\alpha\right)-ce^{-\frac{P_t e^{-\frac{tz^2}{2}}\sin\alpha}{K_{nc}\cdot c}}\tan\alpha}}\right] \end{aligned} \tag{10}$$

3.3. Influence Mechanism of Pre-Tension on Crack Stress Intensity Factor

The difference in stress intensity factor before and after anchoring represents the stress intensity factor generated by the axial force of the rockbolt, denoted as $\Delta K_{\mathrm{I}m} = K_{\mathrm{I}m}$. Based on Equation (10), we programmed this relationship in Matlab (V2016) and used the data from Table 1 for calculations, generating the evolution curve of the stress intensity factor difference under the influence of pre-tension, as shown in Figure 8.

Table 1. General parameter assignment of intensity factor difference analysis.

General Parameters	Value
Elastic modulus of rockbolt/GPa	200
Elastic modulus of rock/GPa	1.8
Poisson's ratio of rock	0.25
Radius of rockbolt/mm	11
Length of rockbolt/m	2.8
Angle between rockbolt and crack/°	60
Normal stiffness of crack/(GPa·m^{-1})	200
Shear strength of crack/MPa	2
Friction angle of crack/(°)	30
Cohesion of crack/MPa	1
Short semi-axis of crack/m	0.1
Distance from hole mouth/m	0.1
Long semi-axis of crack/m	0.2

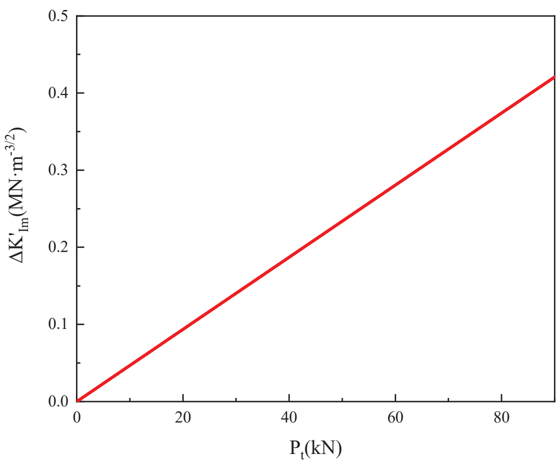

Figure 8. The evolution curve of strength factor difference under different pre-tension.

From Figure 8, it can be observed that the pre-tension of rockbolt is positively correlated with the stress intensity factor difference. As the pre-tension of rockbolt increases, the stress intensity factor difference also increases. Therefore, high-pre-tensioned rockbolts can effectively reduce the stress intensity factor of cracks, preventing them from reaching the fracture toughness and inhibiting crack initiation and propagation. This conclusion is consistent with the results calculated in the literature [33].

In this section, the theoretical analysis method is used to clarify the relationship between the pre-tension and the crack stress intensity factor, and it is proved that increasing the pre-tension can inhibit the crack initiation inside the rock mass. In the next section, the numerical simulation method will be used to analyze the crack development and mechanical parameter changes in the anchorage body under different pre-tension, and to clarify the crack-arrest mechanism of the high-pre-tension rockbolts.

4. Numerical Analysis of the Crack-Arresting Effect of Prestressed Rockbolts

The above analysis elucidates the evolution trend in the stress intensity factor for cracks under different pre-tension. To further analyze the influence of pre-tension on the crack-arresting effect of rockbolts, this section utilizes the discrete element software UDEC (V6.0) for numerical simulation and analysis.

4.1. Establishment of the Numerical Model

To explore the crack-arresting effect of prestressed rockbolts, a model is established, as shown in Figure 9. The dimensions of the model are 1 m in width and 2 m in height. The block and contact surfaces in the model adopt the strain-softening model and the coulomb slip model, respectively. The rockbolt is modeled using the 'Rockbolt element', with a full-length anchoring. The simulated rockbolt specifications are Φ22 mm × 2000 mm. The horizontal displacement at the bottom boundary of the model is fixed, and stress is applied to the upper boundary of the model at a loading rate of 0.02 m/s. The crack in the model is located at the center of the rock, with a length of 1.0 m and an angle of 60°. The rockbolt is arranged to pass through the center of the crack, and pre-tension is applied to the rockbolt by loading at the node. Black lines represent cracks, and yellow lines represent rockbolts.

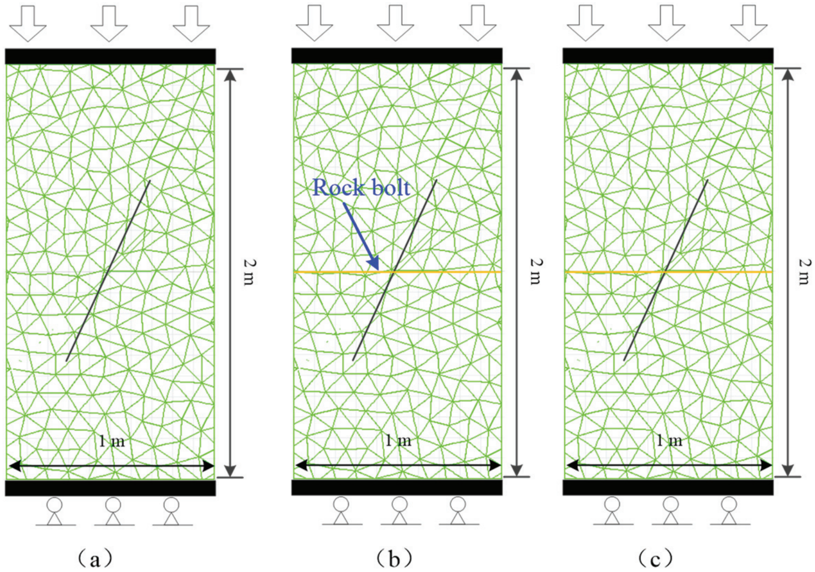

Figure 9. Numerical calculation model (**a**) without anchoring; (**b**) pre-tension 40 kN; (**c**) pre-tension 90 kN.

At present, pre-tension is typically applied to rockbolts through torque in underground construction. A pre-tension torque of 300–400 N·m corresponds to a pre-tension of approximately 30–40 kN [34]. This study uses 40 kN, equivalent to a load of 0.105 MPa. For HRB335 left-hand threaded steel rockbolts with a diameter of 22 mm, 70% of the yield strength is approximately 90 kN. This value is used in this study as the high pre-tension application value, which translates to a load of 0.237 MPa. To analyze the crack-arresting effect of rockbolts under different pre-tension, three groups of comparative simulations are set up: uniaxial compression of a crack sample without anchoring, uniaxial compression of a crack sample with low-pre-tensioned rockbolt anchoring, and uniaxial compression of a crack sample with high-pre-tensioned rockbolt anchoring (Table 2).

Table 2. Simulation scheme.

Group	Pre-Tension (Load)/MPa	Loading Speed/($m \cdot s^{-1}$)
1	0 (without rockbolt)	0.02
2	0.105	
3	0.237	

In the simulation, a FISH language statistical program is independently written to monitor the total length of contact surfaces, and the length and number of shear and tensile cracks within the specimen. The damage degree of the specimen is defined as the ratio of the crack length to the total length of the contact surfaces. The changes in damage degree and crack number before and after anchoring reflect the crack-arresting effect of the rockbolts.

The damage degree of the specimen is as follows:

$$D = \frac{L_S + L_T}{L_C} \times 100\% \tag{11}$$

where L_C is the total length of the contact surfaces, L_S is the total length of shear cracks, and L_T is the total length of tensile cracks.

4.2. Calibration of Model Parameters

4.2.1. Calibration of Rock Parameters

A 1 m × 2 m model is established in UDEC for calibration. The block and contact surfaces adopt the strain-softening model and coulomb slip model, respectively. The bottom of the model is fixed, and a vertical load is applied to the top at a rate of 0.02 m/s. The trial-and-error method is used to continuously calibrate the model parameters. The calibration results are shown in Figure 10. The uniaxial compressive strength of the rock specimen measured by the laboratory is 12.1 MPa, and the elastic modulus is 1.8 GPa. Numerical simulation shows that the uniaxial compressive strength of the rock specimen is 11.9 MPa, and the elastic modulus is 1.8 GPa. The data error between the two is within 2%. Therefore, it can be considered that there is a high degree of agreement between the stress–strain curve of the calibrated numerical model and the experimental test results. The final rock simulation parameters determined are listed in Table 3.

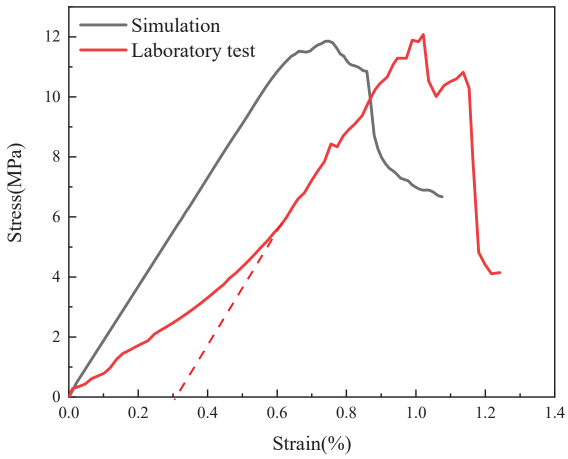

Figure 10. Correction results of rock parameters.

Table 3. Simulation parameters of rock.

Category	Density/ (kg·m^{-3})	Bulk Modulus/ GPa	Shear Modulus/GPa	Cohesion/ MPa	Friction Angle/(°)	Tensile Strength/MPa
Block	1800	1.2	0.72	6.3 (ε_p = 0) 4.9 (ε_p = 0.002) 0.2 (ε_p = 0.005)	26	1.2
Contact surface	Normal stiffness/ (GPa·m^{-1}) 216	Tangential stiffness/ (GPa·m^{-1}) 86.4	Cohesion /MPa 3.8	Friction angle/(°) 17	Tensile strength/MPa 1.2	

4.2.2. Calibration of Rockbolt Element Parameters

To obtain specific parameters for the rockbolt, a pull-out test was conducted using a LW-1000 horizontal tension testing machine in the laboratory on a Φ22 mm × 2000 mm HRB335 left-hand thread steel rockbolt.

In UDEC, a numerical model for the rockbolt pull-out test was established, as shown in Figure 11. The model employs full-length anchoring to embed the rockbolt into the rock sample. The rock parameters used are calibrated rock parameters. A rockbolt element simulating a Φ22 mm × 2000 mm rockbolt is utilized. The model dimensions are set as width × height = 1 m × 2 m. The test involves setting up 17 nodes along the rockbolt, with nodes 1 to 15 embedded within the rock sample, node 16 near the surface of the sample, and node 17 outside the sample. A speed of 0.08 m/s is applied to node 17 for the pull-out test, with the model's upper surface fixed during computation. FISH language is used to monitor axial load and displacement of the rockbolt.

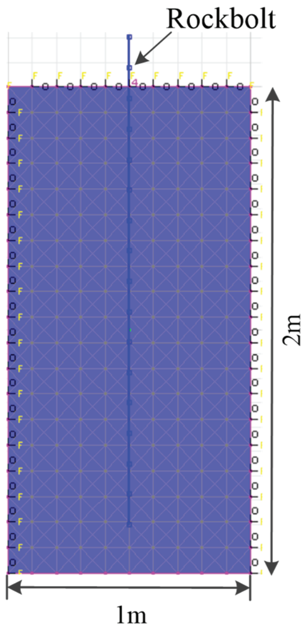

Figure 11. Numerical model diagram of rockbolt drawing.

Rockbolt unit parameters include parameters for the rockbolt and parameters for anchoring. Table 4 presents the simulation parameters for the rockbolt and anchoring obtained based on laboratory pull-out test data.

Table 4. Rockbolts and anchoring parameters.

	Cross-sectional area/(m^2)	**Elastic modulus/GPa**	**Yield limit/ kN**		**Moment of inertia of the cross-section/(m^4)**		**Failure strain limit**
Rockbolt	3.8×10^{-4}	200	128		1.2×10^{-8}		0.15
	Exposed perimeter/m	**Cohesive strength of tangential coupling spring/MPa**	**Stiffness of tangential coupling spring/ (GPa·m^{-1})**	**Friction angle of tangential coupling spring/(°)**	**Cohesive strength of normal coupling spring/MPa**	**Stiffness of normal coupling spring/ (GPa·m^{-1})**	**Friction angle of normal coupling spring/(°)**
Anchoring parameters	0.07	1	8	45	200	20	0

As shown in Figure 12, the simulation curve's slope in the elastic stage, failure load, and corresponding displacement parameters match well with the test curve, indicating a reasonable calibration of the parameters.

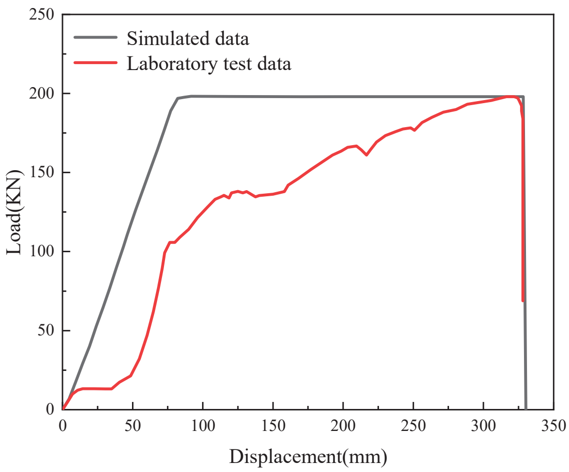

Figure 12. Correction results of rockbolt element parameters.

4.3. Analysis of the Crack-Arresting Mechanism of Prestressed Rockbolts

In the absence of control measures, the propagation of cracks in rock masses follows a dynamic process of initiation, rapid expansion, self-arresting, re-initiation, and subsequent rapid expansion [35]. Relevant studies have found that macroscopic and microscopic parameters such as peak stress, elastic modulus, and total number of cracks of the anchored crack body are highly sensitive to crack-arresting measures [36]. Therefore, analyzing the mechanical and damage characteristics of the anchored crack body can effectively characterize the crack-arresting effect of rockbolts.

4.3.1. Mechanical Characteristic Analysis

The stress–strain curves of specimens under different pre-tension are shown in Figure 13. Using the specimen without anchoring as a reference, it is evident that the mechanical properties of specimens reinforced with different pre-tensioned rockbolts are improved. Specifically, high pre-tensions applied to the rockbolt demonstrate a more pronounced enhancement effect. The peak strength of the specimen increases from 10.2 MPa to 12.5 MPa, marking a 22.5% improvement, while the elastic modulus increases from 1.38 GPa to 1.82 GPa, indicating a 31.9% enhancement. In contrast, the use of low pre-tensions results in increases of 5.9% and 7.2% in peak strength and elastic modulus, respectively. Statistical data suggests that high pre-tensions applied by rockbolts achieve better anchoring effects in rock masses, effectively strengthening rock mass integrity and mitigating the adverse effects of cracks on rock mechanical properties.

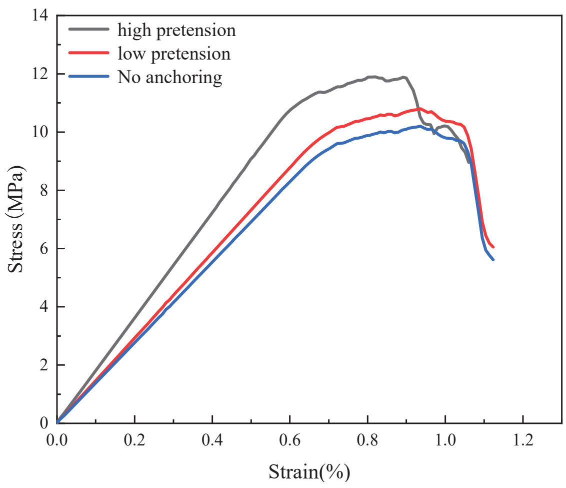

Figure 13. Stress–strain curves of specimens under different pre-tension.

4.3.2. Damage Characteristic Analysis

According to fracture mechanics theory, when the stress intensity factor at the crack tip exceeds its fracture toughness, crack initiation occurs. In UDEC simulations, when the contact surface exceeds its ultimate strength, cracks are generated and continue to propagate. The criteria for determining cracking between the two have certain similarities. Therefore, analyzing the number of cracks and damage characteristics of anchored crack rock specimens under different pre-tension is illustrated in Figure 14. Red lines represent tensile cracks, while green lines represent shear cracks.

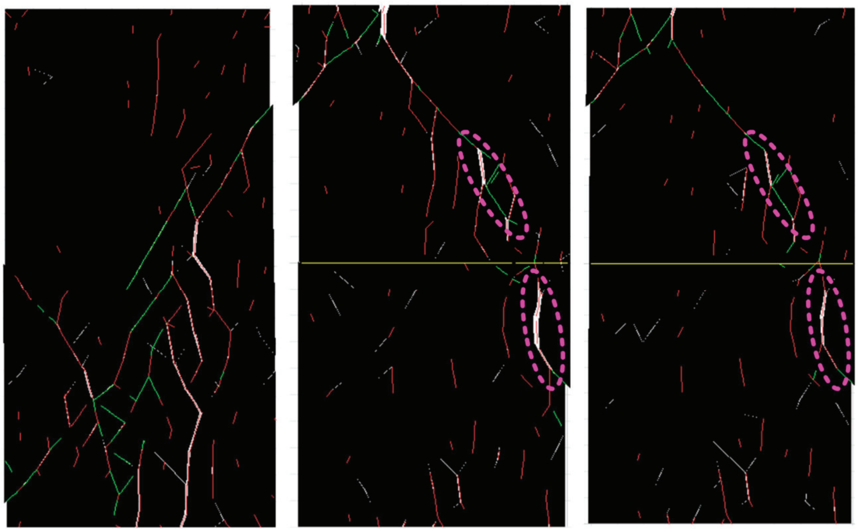

Figure 14. Damage characteristics of specimens under different pre-tension (**a**) without anchoring; (**b**) low pre-tension; (**c**) high pre-tension.

In Figure 14a, without support, the specimen's failure primarily progresses along the pre-existing crack direction. Under external load, the pre-existing crack extends towards the upper right corner and the middle-lower position of the specimen, forming a tilted-through main crack within the specimen with multiple wing cracks around the main crack. Eventually, the specimen fails due to shear fracture.

Figure 14b,c shows the damage after low-pre-tensioned and high-pre-tensioned support, respectively. It is observed that the rockbolt support alters the crack propagation pattern and failure mode of the specimen. Since the rockbolt passes through the pre-existing crack in the specimen, no expansion occurs at this position; instead, the main crack forms from the upper 1/3 boundary to the right boundary of the specimen, exhibiting a splitting failure pattern. Comparing circled cracks, it is evident that under high pre-tension, the extent of crack opening is significantly reduced.

In general, without support, numerous tensile cracks are distributed inside the specimen. Upon installing a low-pre-tensioned rockbolt, tensile cracks mainly appear around the macroscopic crack and its vicinity. With further increase in pre-tension, tensile cracks only appear at the macroscopic crack, while other areas mainly exhibit shear cracks.

Figure 15 shows the evolution curves of crack numbers and damage degree for specimens anchored with different pre-tension. Table 5 provides the detailed statistics of the data presented in this Figure, with the change rates calculated in comparison to the unanchored group.

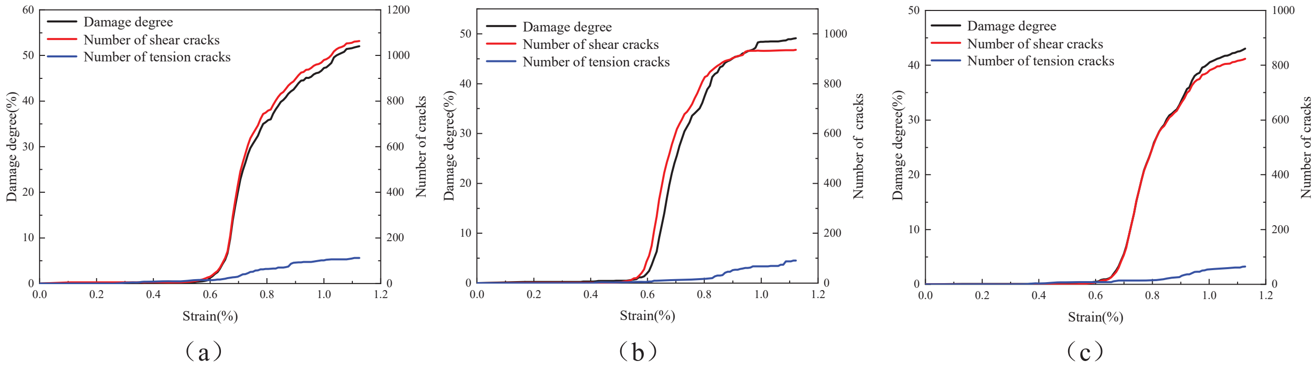

Figure 15. The evolution curves of crack number and damage degree of cracked specimens with different pre-tension (**a**) without anchoring; (**b**) low pre-tension; (**c**) high pre-tension.

Table 5. Comparison of damage data of specimens.

	Without Anchoring	Low Pre-Tension	High Pre-Tension	Change Rate/%
Damage degree/%	52.1	49.1	43	−5.7 −17.4
Number of shear cracks/count	1063	936	823	−11.9 −22.6
Number of tensile cracks/count	112	91	64	−18.8 −42.9

Analyzing the graph and Table data reveals that as damage degree significantly increases, the number of tensile and shear cracks also increases. Prior to peak strength, damage is mainly caused by shear cracks. In the post-peak stage, shear crack growth slows down and the number of tensile cracks begins to rise. Hence, although tensile cracks constitute a smaller proportion, they are the primary cause of macroscopic failure of the specimen. Prestressed rockbolts can effectively reduce the damage degree of crack specimens. Using rockbolts with different pre-tension results in a reduction of 5.7% and 17.4% in damage degree, 11.9% and 22.6% in shear crack numbers, and 18.8% and 42.9% in tensile crack numbers, respectively. The significant reduction in tensile crack numbers indicates the inhibitory effect of prestressed rockbolts on the initiation and propagation of tensile cracks. The inflection point of damage is observed at a strain value of 0.59% without anchoring, while for specimens anchored with low pre-tension, the inflection point occurs at a strain value of 0.57%. This slight advancement of the inflection point may be attributed to the initial ineffective active support of low-pre-tensioned rockbolts, requiring a certain amount of deformation damage before exerting active crack-arresting effects.

In conclusion, prestressed rockbolts enhance the mechanical performance of crack specimens, increase load-bearing capacity, and alter the failure mode of crack specimens. They reduce the number of internal cracks, suppress the initiation and propagation of tensile cracks, and decrease the damage degree of the specimens. Therefore, it is proposed to use high-pre-tensioned rockbolts to control the deformation of roadway surrounding rock in Ji-15-23090 headgate of Pingdingshan No. 4 Coal Mine.

5. Industrial Testing

5.1. Surrounding Rock Control Plan

The widening of the Ji-15-23090 headgate ranges from 600 mm to 800 mm. During the widening and repair period, experiments are conducted at the sides of the roadway to verify the effectiveness of tensioned rockbolts for surrounding rock control. In non-experimental sections, after widening, three additional Φ22 × 2400 mm left-handed high-strength resin rockbolts are installed in the sides, torqued to 300 N·m. In the experimental section, residual rockbolts after widening are directly tensioned to 60 kN for pre-tensioning. One day after installation, monitoring rockbolt axial forces showed that tensioned rockbolts generally exceeded 60 kN (Figure 16), whereas conventional rockbolts only reached 20–30 kN.

Figure 16. Axial force of tensioned rockbolt.

5.2. Analysis of Control Effectiveness

The cross-point method was used to observe the deformation of the two sides of the roadway in the experimental section and the non-experimental section, and the monitoring data were sorted into evolution curves. The borehole imager was used to peep at the side of the roadway in the test section, and the crack-arrest effect of the high-pre-tightening bolt was observed. The observation results are organized as shown in Figure 17.

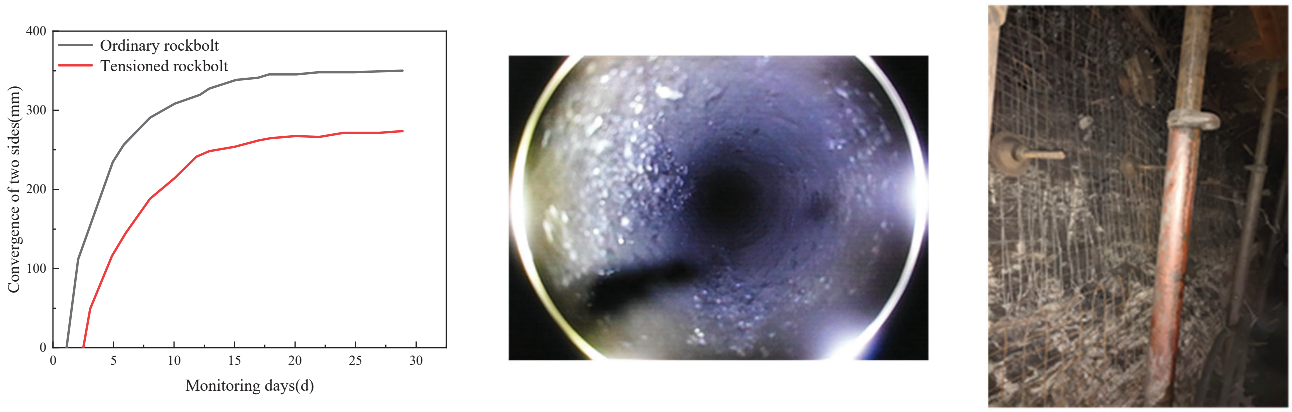

(**a**) (**b**) (**c**)

Figure 17. Field observation results. (**a**) Convergence of two sides. (**b**) Borehole inspection of the sidewalls in the experimental section. (**c**) Support effectiveness.

In the non-experimental section, the deformation of two sides of the roadway is 350 mm. In contrast, in the section supported by tensioned rockbolts, the deformation is reduced to 273 mm, achieving a reduction of 22%. Borehole inspection results in the experimental section show good coal seam integrity with no longitudinal or circumferential crack distributions, and the borehole walls are smooth with good adherence of the rockbolts. The overall support effectiveness has significantly improved, with notable enhancement in the active load-bearing performance of the rockbolts. This confirms that the optimized support scheme provides excellent ground control.

6. Conclusions

(1) Based on fracture mechanics theory, an influence model of rockbolt axial force is established to analyze the expression of the stress intensity factor difference in cracks within the anchoring range. The difference in stress intensity factor of cracks is related to parameters such as pre-tension, anchor point of the rockbolt, anchoring angle, and crack position. As the pre-tension increases and the anchor point moves towards the center of the crack, the stress intensity factor of the crack continuously decreases and moves away from the fracture toughness, thereby inhibiting the initiation and propagation of cracks.

(2) Based on the modified parameters of the rockbolt and rock, a numerical analysis model is established. Simulation results show that high-pre-tensioned rockbolts significantly enhance the mechanical characteristics of the specimen: the peak strength of the specimen increases from 10.2 MPa to 12.5 MPa, a 22.5% improvement; the elastic modulus increases from 1.38 GPa to 1.82 GPa, a 31.9% improvement. Prestressed rockbolts not only suppress shear slip failure along pre-existing cracks, but also alter the expansion pattern of cracks and the failure mode of the specimen. After anchoring with high-pre-tensioned rockbolts, the damage degree of the crack specimen decreases by 17.4%, the number of shear cracks decreases by 22.6%, and the number of tensile cracks decreases by 42.9%.

(3) By applying high-pre-tension to rockbolts after widening the roadway, the axial forces of rockbolts have been increased from 20 to 30 kN to over 60 kN. A comparison of mining pressure observation data between the experimental and non-experimental sections reveals that the deformation of the two sides of the roadway is reduced by 22%, from 350 mm in the non-experimental section to 273 mm in the experimental section. Borehole inspection results in the experimental section show good integrity of the coal seam in the sidewall. Increasing the pre-tension of rockbolts has achieved effective control of the surrounding rock.

Author Contributions: Conceptualization, B.W.; methodology, B.W. and X.W.; software, B.W. and D.C.; data curation, J.C., W.S. and C.L.; writing—original draft preparation, B.W. and D.C.; writing—review and editing, X.W. and J.C.; funding acquisition, B.W. and J.C. All authors have read and agreed to the published version of the manuscript.

Funding: This research was funded by National Natural Science Foundation of China, grant number 52204079, National Natural Science Foundation of China, grant number 52104117, Scientific Research Foundation for High-level Talents of Anhui University of Science and Technology, grant number 2024yjrc48 and Anhui Province Excellent Research and Innovation Team, grant number 2023AH010023.

Data Availability Statement: The data used to support the findings of this study are included within the article.

Conflicts of Interest: The authors declare no conflicts of interest.

References

1. Kang, H. Development and prospects of support and reinforcement materials for coal mine roadways. *Coal Sci. Technol.* **2021**, *49*, 1–11.
2. Chen, D.; Wang, X.; Zhang, F.; Bai, J.; Zhao, X.; Li, M.; Yu, Y.; Wang, X. Study on the mechanism of progressive instability of special-shaped coal pillar and the stability control of roadway under the influence of mining. *Rock Mech. Rock Eng.* **2024**, *57*, 6461–6483. [CrossRef]
3. Kang, H.; Yuan, G.; Si, L.; Gao, F.; Lou, J.; Yang, J.; Dong, S. Mechanical behavior and failure mechanisms of rock bolts subjected to static-dynamic loads. *Int. J. Min. Sci. Technol.* **2024**, *34*, 281–288. [CrossRef]
4. Kang, H. Seventy years development and prospects of strata control technologies for coal mine roadways in China. *Chin. J. Rock Mech. Eng.* **2021**, *40*, 1–30.

5. Chen, W.; Wang, L.; Tan, X.; Yang, D.; Yuan, J.; Yang, J. State-of-the-art and development tendency of the underground engineering stability of fractured rock mass. *Chin. J. Rock Mech. Eng.* **2021**, *40*, 1945–1961.
6. Wang, W.J.; Dong, E.Y.; Zhao, Z.W.; Wu, H.; Yuan, C. Experimental study on mechanical properties of anchorage body and on anchorage mechanism. *J. China Coal Soc.* **2020**, *45*, 82–89.
7. Wei, S.; Li, X.; Huang, Y. Present situation and prospect of damage mechanism and surrounding rock control of anchored fractured rock. *Coal Eng.* **2023**, *55*, 88–95.
8. Vandermaat, D.; Saydam, S.; Hagan, P.C.; Crosky, A.G. Examination of rockbolt stress corrosion cracking utilising full size rockbolts in a controlled mine environment. *Int. J. Rock Mech. Min. Sci.* **2016**, *81*, 86–95. [CrossRef]
9. Liu, A.Q.; Ju, W.J.; Hu, H.T.; Wang, X. Experiment study on the effect of bolt prestress on the shear behavior of jointed rock mass. *J. China Coal Soc.* **2013**, *38*, 391–396.
10. Liu, Q.S.; Lei, G.F.; Peng, X.X.; Wei, L.; Luo, C.Y. Study on shear mechanical properties of sandstone, marble and granite after anchoring. *Chin. J. Rock Mech. Eng.* **2018**, *37*, 4007–4015.
11. Liu, Q.; Lei, G.; Peng, X.; Wei, L.; Liu, J.; Pan, Y. Experimental study and mechanism analysis of influence of bolt anchoring on shear properties of jointed rock mass. *Rock Soil Mech.* **2017**, *38*, 27–35.
12. Zhou, S.; Ji, X.; Li, L.; Liu, H.; Zhu, C.; Fan, H.; Zhang, Q.; Shi, C. The mechanism of rockbolts in jointed rock under uniaxial tension. *KSCE J. Civ. Eng.* **2023**, *27*, 4938–4947. [CrossRef]
13. Wang, G.; Wang, X.; Yang, J.; Zhu, X. Mechanism analysis of pre-stressed bonded rockbolt controlling the deformation in joint surround rocks. *J. China Univ. Min. Technol.* **2021**, *50*, 60–68.
14. Shi, H.; Zhang, H.; Chen, W.; Song, L.; Li, M. Pull-out debonding characteristics of rockbolt with prefabricated cracks in rock: A numerical study based on particle flow code. *Comput. Part. Mech.* **2024**, *11*, 29–53. [CrossRef]
15. Teng, J.; Tang, J.; Zhang, Y.; Li, X. CT experimental study on the damage characteristics of anchored layered rocks. *KSCE J. Civ. Eng.* **2018**, *22*, 3653–3662. [CrossRef]
16. Zhao, T.; Zou, J.; Fu, Z.; Yu, F. Experimental study on anchoring mechanism of double persistent jointed rock. *J. China Coal Soc.* **2020**, *45*, 3065–3072.
17. Wang, T.; Wang, W.; Du, Y. Research on pre-tensioned bolts reinforcing roadway roof in joint rock mass. *J. China Univ. Min. Technol.* **2007**, *36*, 618–621.
18. Wu, Q.; Chen, L.; Shen, B.; Dlamini, B.; Li, S.; Zhu, Y. Experimental investigation on rockbolt performance under the tension load. *Rock Mech. Rock Eng.* **2019**, *52*, 4605–4618. [CrossRef]
19. Zu, G.; Wang, J.; Ning, J.; Pu, Z.; Yan, L.; Ren, Z.; Hu, H. Experimental study on anchoring crack-resistance effects of prestressed anchor under impact loads. *Chin. J. Geol. Eng.* **2023**, *45*, 1743–1753.
20. Zhang, J.P.; Liu, L.M.; Liu, C.X.; Sun, D.L.; Shao, J.; Li, Y. Research on mechanism of bolt-grouting reinforcement for deep fractured rock mass based on prestressed anchor and self-stress grouting. *Rock Soil Mech.* **2020**, *41*, 3651–3662.
21. Li, S.; Chen, W.; Zhu, W.; Wang, S. Catastrophe model of crack propagating in bolt-supported jointed rockmass. *Chin. J. Rock Mech. Eng.* **2003**, *22*, 1661–1666.
22. Ge, R.; Liu, J. Study on shear performance of anchored joint surface. *Chin. J. GeoEng.* **1988**, *1*, 8–19.
23. Wang, P.; Feng, T.; Zhu, Y.; Yu, W. Experimental study and numerical simulation of anchoring mechanism of anchored rocklike material with prefabricated fracture. *Rock Soil Mech.* **2016**, *37*, 793–801.
24. Yuan, K.; Jiang, Y.; Chu, Z.; Wang, G.; Gong, B. Microscopic research on anchorage mechanism of bolted rock joint based on DEM. *J. Shangdong Univ. Sci. Technol. Nat. Sci.* **2014**, *33*, 76–84.
25. Zhou, H.; Xu, R.; Zhang, C.; Shen, Z.; Meng, F.; Liu, H. Experimental study of crack prevention effect of pre-stressed bolt anchoring. *Chin. J. Rock Mech. Eng.* **2015**, *34*, 2027–2037.
26. Chen, Y.; Yang, Y.; Yan, S.; Hao, S.; Cao, Q. Study on reinforcement mechanism of filling body in gob-side entry retaining. *J. Min. Saf. Eng.* **2018**, *35*, 1129–1134.
27. Wu, B.; Wang, X.; Bai, J.; Wu, W.; Zhu, X.; Li, G. Study on crack evolution mechanism of roadside backfill body in gob-side entry retaining based on UDEC trigon model. *Rock Mech. Rock Eng.* **2019**, *52*, 3385–3399. [CrossRef]
28. Wu, Y. Study on Tunnel Stability and Reinforcing Mechanism of Bolts and Shotcrete Based on Rock Fracture Mechanics. Ph.D. Thesis, Huazhong University of Science and Technology, Wuhan, China, 2004.
29. Sheng, K. *Fracture Mechanics*; Tongji University Press: Shanghai, China, 1996; pp. 1–3.
30. You, C. Theory and Application Study on Stress-Transfer Mechanism of Anchoring System. Ph.D. Thesis, Shandong University of Science and Technology, Qingdao, China, 2004.
31. Zheng, Y. Explaining Bolt—Shotcrete support mechanism by fracture mechanics. *Coal Sci. Technol.* **1980**, *7*, 11–14+64.
32. Yi, S.; Zhu, Z. *Introduction to Fracture Rock Mass Damage Mechanics*; Science Press: Beijing, China, 2005; pp. 25–26.
33. Wu, D.; Yu, L.; Su, H.; Wu, J.; Liu, R.; Zhou, J. Experimental study and PFC3D simulation on crack propagation of fractured rock-like specimens with bolts under uniaxial compression. *Rock Soil Mech.* **2021**, *42*, 1681–1692.
34. Hu, X.; He, C.; Walton, G.; Chen, Z. A combined support system associated with the segmental lining in a jointed rock mass: The case of the inclined shaft tunnel at the bulianta coal mine. *Rock Mech. Rock Eng.* **2020**, *53*, 2653–2669. [CrossRef]

35. Zhou, L.; Jiang, Y.; Zhu, Z.; Dong, Y.; Niu, C.; Wang, M. Mechanism study of preventing crack propagation of fractured rock under dynamic loads. *Explor. Shock Waves* **2021**, *41*, 34–44.
36. Liu, S.; Xiao, F.; Li, T.; Zhang, B. Analysis of impact tendency and sensitivity of fractured rock with different crack arrest measures. *Sustainability* **2022**, *14*, 13833. [CrossRef]

buildings

MDPI

Article

Study on the Propagation Law and Waveform Characteristics of a Blasting Shock Wave in a Highway Tunnel with the Bench Method

Tao Yu [1], Junfeng Sun [1], Jianfeng Wang [1,*], Jianping Feng [2], Liangjun Chen [2], Guofeng Su [3,*], Jun Man [4] and Zhen Wu [5]

[1] State Key Laboratory of Intelligent Geotechnics and Tunnelling, Southwest Jiaotong University, Chengdu 610031, China; ytao1015@my.swjtu.edu.cn (T.Y.); junfengsun@my.swjtu.edu.cn (J.S.)
[2] China Railway City Development Investment Group Co., Ltd., Sichuan Southwest Branch, Chengdu 610213, China; 17713563039@163.com (J.F.); chen20081601@163.com (L.C.)
[3] Southwest Jiaotong University Research Institute (Chengdu) Co., Ltd., Chengdu 610036, China
[4] China Railway Erju 6TH Engineering Co., Ltd., Chengdu 610031, China; 15520477740@163.com
[5] Sichuan Railway Construction Co., Ltd., Chengdu 610041, China; wuzhen1632024@163.com
* Correspondence: wjf2019210118@my.swjtu.edu.cn (J.W.); suguofeng1006@my.swjtu.edu.cn (G.S.)

Abstract: In the bench method of tunnel excavation, the blasting impact from upper bench blasting poses significant risks to personnel and equipment. This study employed dynamic analysis software, ANSYS/LS-DYNA, and field testing to examine the propagation characteristics and attenuation behavior of tunnel shock waves. The findings revealed that, near the central axis of the tunnel, shock wave overpressure was lower compared to areas near the tunnel wall due to reflections from the wall. As the shock wave traveled a distance six times the tunnel diameter, it transitioned from a spherical wave to a plane wave. The attenuation coefficient for the plane wave ranged from 1.03 to 1.17. A fitting formula for shock wave overpressure attenuation, based on field test results, was proposed, and it showed good agreement with the numerical simulation results. This provided valuable theoretical insights for predicting shock wave overpressure during bench method tunnel excavation.

Keywords: highway tunnel; bench method; blasting shock wave; numerical simulation; modified formula

1. Introduction and Background

Blasting is a cost-effective and efficient method widely utilized in tunnel construction, hydraulic engineering, mining, and various other civil engineering projects [1–4]. Approximately 70% to 80% of the energy released during a blast is dissipated in the form of vibration and air blasts, with only a small amount of the energy utilized for rock breakage [5]. Simultaneously, while crushing rock, the blast strongly compresses the air near the tunnel face, leading to an instantaneous rise in temperature and air pressure and forming a blasting shock wave. When this shock wave propagates in a high-pressure and high-speed state along the tunnel, it can cause serious harm to both field equipment and personnel. Hence, studying the laws of shock wave propagation from tunnel blasting is crucial.

Numerous research projects have focused on analyzing air blast waves (or shock waves) induced by the explosive charges. Via experimental methods, Brode [6] and Henrych [7] determined that the primary factors affecting the peak overpressure of an air shock wave are the quantity of explosive material used and the distance from the point of detonation. The overpressure formula of a free field explosion was proposed by Brode and Henrych. Baker et al. [8] provided an investigation table of shock wave parameters, including the overpressure peak, propagation distance, and propagation time. In addition, numerical simulation methods to study fluid motion have great advantages [9,10]. For example, Chapman et al. [11] used numerical methods to simulate the transmission of a shock wave through an air medium. Zukas et al. [12] and Luccioni et al. [13] investigated the effect of the grid size on blasting results in computational fluid dynamics (CFD) and concluded that a grid size of 100 mm is appropriate for accurately simulating shock wave propagation.

The blasting shock wave is constrained in narrow spaces, such as tunnels, resulting in slower attenuation and farther blasting in open spaces [14–16]. Smith et al. [17] designed several equally scaled tunnel models with different section shapes, and tested the overpressure values inside the tunnels through a series of blasting experiments. Rodriguez et al. [18] proposed a semi-empirical approach to predict the air pressure at the tunnel exit during propagation of the blast shock wave. Benselama et al. [19] classified the propagation of shock waves in tunnels into two distinct modes: a three-dimensional overpressure attenuation mode near the explosion point and a one-dimensional overpressure attenuation mode at greater distances from the explosion. Uystepruyst et al. [20] observed that when an explosion occurs in a rectangular tunnel, the shock wave propagation follows a two-dimensional pattern. By means of numerical simulation and model tests, Pennetier et al. [21] proved that shock waves in subway stations can propagate multiple times through reflection and refraction in connecting channels. Wu et al. [22] investigated wave propagation characteristics in a confined environment, providing a comprehensive description of wave dynamics during the blasting process and valuable insights into wave propagation. Figuli et al. [23] examined the attenuation behavior of shock waves across different explosion modes. Fang et al. [24] conducted field tests to study the propagation behavior of shock waves in a highway tunnel and discovered that the attenuation patterns varied across different regions. Many researchers have explored the propagation characteristics of shock waves resulting from explosions in air, military tunnels, and coal mine roadways, and have identified the attenuation laws for these shock waves. However, there is a lack of research specifically on the propagation characteristics of shock waves following blasting in highway tunnels. Due to the larger excavation section of highway tunnels compared to military and coal mine tunnels, a greater quantity of explosives is required for blasting operations, leading to a more pronounced dynamic impact from shock waves [25–27]. In particular, despite the widespread use of the bench method for tunnel excavation in complex geological conditions, research on blasting shock waves associated with this technique is limited.

In this study, the numerical simulation method is utilized to perform a dynamic analysis of the tunnel's blasting scheme, simulating the propagation process of a shock wave generated by upper bench blasting. The study investigates the fundamental characteristics of shock wave propagation on the tunnel's upper bench, focusing on changes in the shock wave flow field, cross-sectional overpressure distribution, and longitudinal overpressure attenuation. Based on field tests, the empirical formula of a blasting shock wave in a single tunnel is modified to make it more suitable for similar engineering environments.

2. Engineering Background

Dual-lane highways predominate in China, and there is widespread use of the bench blasting method for excavating tunnels in Grade IV and V rock masses. The Shengli tunnel serves as a crucial component of the Jinshajiang expressway in Southwest China, connecting Ningnan City to Panzhihua City. The tunnel has a semicircular arch cross-section of 12 m $\times$ 8 m (width $\times$ height), with a tunnel length of 1.7 km and a maximum buried depth of 178 m. The surrounding rock has low strength and fractures are developed, and 78.4% of the total length of the tunnel has been classified as Grade IV.

The tunnel was excavated with the bench blasting excavation scheme. The upper bench had an excavation height of 6.5 m and a length ranging from 130 to 150 m. The lower bench had an excavation height of 2.5 m and a length of 20 m. The excavation area of the upper bench was 2.2 times greater than that of the lower bench, and the charge quantity for the upper bench was significantly larger. Consequently, this paper primarily focused on the propagation process and overpressure attenuation law of shock waves generated by blasting in the upper bench.

Figure 1 displays the blasting schemes utilized for bench excavation in the tunnel. In order to ensure the blasting effect, an emulsion explosive and a segmented electronic millisecond detonator were adopted in the blasting. The diameter of the contour holes was 42 mm, the length of the cartridge was 200 mm, and the single-quantity explosive was 200 g. The diameter of the remaining blasting holes was 42 mm, the length of the cartridge was 300 mm, and the single-quantity explosive was 300 g. The blasting parameters are shown in Table 1.

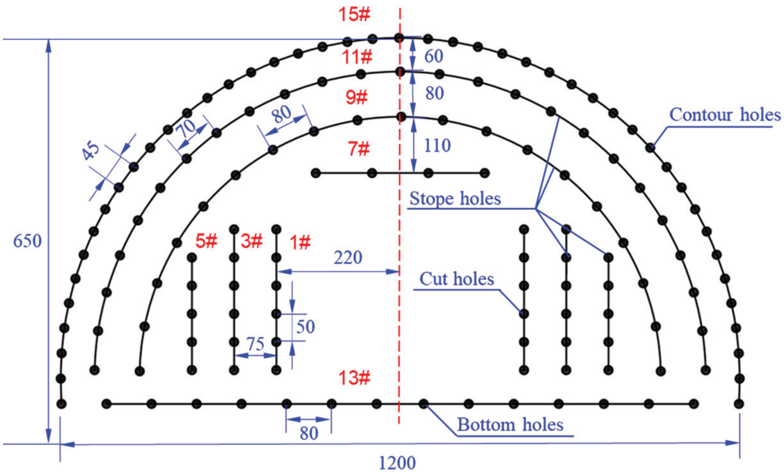

(**a**)

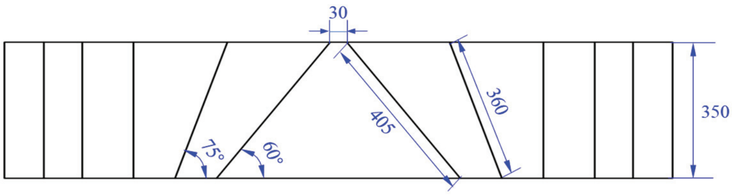

(**b**)

Figure 1. Layout of tunnel blasting holes for the upper bench (unit: cm). (**a**) Cross-section and (**b**) vertical section, 1#~15# represents the blasthole segment, and the design of odd-numbered segments avoids simultaneous explosions caused by overlapping delay times.

Table 1. Blasting parameters.

Hole Classification	Segment/#	Hole Number	Hole Depth/m	Single-Hole Cartridge Number	Single-Hole Charge/kg	Delay Time/(ms)	Segment Charge/kg
Cut hole	1	12	4.05	8	2.4	0	28.8
Stope hole	3	12	3.6	7	2.1	50	25.2
Stope hole	5	10	3.5	6/7	1.8/2.1	110	19.8
Stope hole	7	4	3.5	5	1.5	200	6
Stope hole	9	19	3.5	4	1.2	310	22.8
Stope hole	11	25	3.5	3/4	0.9/1.2	460	26.1
Bottom hole	13	14	3.7	5	1.5	650	21
Contour hole	15	45	3.5	3/4	0.6/0.8	880	31.4
Total		141					181.1

3. Establishment of Numerical Calculation Model

Numerical simulations are highly effective for analyzing changes in airflow patterns and shock wave propagation. The explicit dynamic analysis finite element software, ANSYS/LS-DYNA, provides high precision and reliability in simulating the explosion process. Establishing a three-dimensional model enhances the ability to observe variations in the waveform and propagation characteristics of the shock wave. The ALE algorithm can effectively solve the deformation problem of the large mesh and is widely used in the study of fluid–solid coupling problems. The explosion involves two materials, namely, explosives and air, and the shock wave causes the mesh elements to undergo huge deformation. Therefore, using the multi-material ALE algorithm for simulation is suitable for explosives and air [28,29].

Assuming a constant curvature along the tunnel axis, a long, straight tunnel model was established due to the tunnel's axisymmetric shape. To simplify the calculations, a 1/2 tunnel model was created along the tunnel's centerline. Fixed boundary conditions were applied at the tunnel face and at the contact boundary between the air and the tunnel wall. The tunnel's end was assigned a transmission boundary condition to permit the passage of shock wave energy. Therefore, only the explosive and air were considered in the model, where the explosive was simulated by the 3DSOLID164 solid element and air was simulated by Eulerian meshes. The model utilized hexahedral solid elements for meshing, with a maximum grid size of 0.45 m and a minimum grid element size of 0.1 m. The entire calculation model operates using the cm-g-μs unit system. As shown in Figure 2, the geometric model and mesh of the tunnel were mirrored. The tunnel model had a width of 12 m, a height of 6.5 m, and a length of 150 m. The cross-sectional area was 62.54 m^2, and the equivalent diameter was 7.87 m.

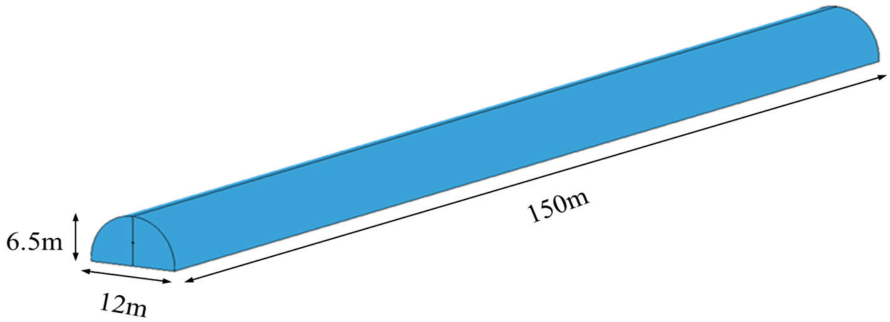

Figure 2. Geometric model of the tunnel.

The maximum overpressure peak of the shock wave was influenced by the TNT equivalent of the explosive used in the cut hole [30]. Therefore, the parameters of the emulsion explosive need to be reduced by the TNT equivalent coefficient and the shock wave energy conversion coefficient. When the peak overpressure of the shock wave generated by the explosive and TNT was the same, the ratio of the explosive charge mass to TNT mass was referred to as the equivalent coefficient, which had a value of 0.582. The shock wave energy conversion coefficient was 0.4 [18,21]. The 28.8 kg of emulsion explosive used in the upper bench cutting section of the tunnel was equivalent in energy to the blasting of 6.5 kg of TNT explosive in the open air of the tunnel.

The TNT explosive was set at 3 m above the bottom of the upper bench as the detonation point. Blasting holes were symmetrically arranged according to the tunnel centerline, so a semi-tunnel model was established, as shown in Figure 3. The explosive size was 20 cm × 10 cm × 10 cm (length × width × height), which formed a rectangular charge shape. The size of the TNT explosive was very small for the tunnel, which can be regarded as an ideal point explosion source, and the detonation was completed instantly to reach the detonation pressure.

The material parameters for the explosive were defined using the *MAT_HIGGINS_EX PLOSIVE_BURN keyword in LS-DYNA. As detailed in Table 2, ρ represents the density of the explosive, D denotes the detonation velocity, and PCJ indicates the detonation pressure of the explosive.

Table 2. Explosive material parameters.

Parameters	ρ/(kg/m^3)	D/(m/s)	PCJ/(MPa)
Value	1.63×10^3	6.93×10^3	2.55×10^4

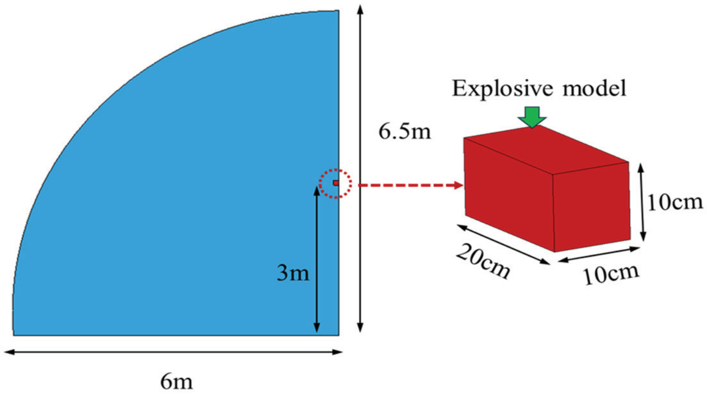

Figure 3. Detonation point's position and explosive detail size.

The equation of state for the explosive is given by *EOS_JWL, as shown in Equation (1). The state equation parameters of the explosive are listed in Table 3. Here, A, B, R_1, and R_2 are the parameters to be determined, E represents the internal energy per unit volume of the explosive, and V denotes the relative volume at the initial moment of the explosion:

$$P = A\left(1 - \frac{\omega}{R_1 V}\right)e^{-R_1 V} + B\left(1 - \frac{\omega}{R_2 V}\right)e^{-R_2 V} + \frac{\omega E}{V} \tag{1}$$

Table 3. State equation parameters of the explosive.

Parameters	ρ_0/(kg/m^3)	C_0	C_1	C_2	C_3	C_4	C_5	C_6	E/(J/m^3)
Value	1.29	0	0	0	0	0.4	0.4	0	2.5×10^5

The material parameters for air were defined using the LS-DYNA keyword *MAT_NULL, and the state equation was specified by *EOS_LINEAR_POLYNOMIAL. The state equation followed a linear polynomial form, given as:

$$P = C_0 + C_1\mu + C_2\mu^2 + C_3\mu^3 + \left(C_4 + C_5\mu + C_6\mu^2\right)E \tag{2}$$

where $\mu = \frac{\rho}{\rho_0} - 1$, ρ is the current density of air, ρ_0 is the initial density of air, C_0, C_1, C_2, C_3, C_4, C_5, and C_6 are constants, and E is the internal energy per unit volume of air. The selection of parameters is shown in Table 4.

Table 4. State equation parameters of air.

Parameters	ρ_0/(kg/m^3)	C_0	C_1	C_2	C_3	C_4	C_5	C_6	E/(J/m^3)
Value	1.29	0	0	0	0	0.4	0.4	0	2.5×10^5

4. Calculation Results Analysis

4.1. Measuring Point Arrangement

In the calculation model, 15 measuring points were positioned along the longitudinal direction of the upper bench tunnel model to analyze the attenuation of overpressure from the blasting shock wave along the tunnel's axis. Additionally, three measuring points were placed radially at four cross-sections located 30 m, 40 m, 50 m, and 60 m from the explosion center to observe the formation of the plane wave. In total, 27 measuring points were arranged, as illustrated in Figure 4.

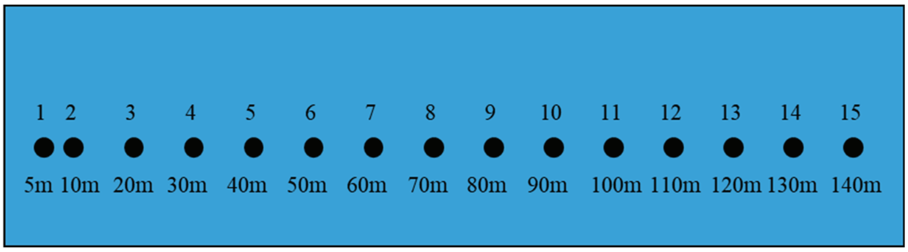

(**a**)

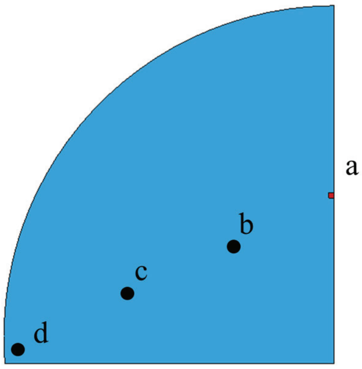

(**b**)

Figure 4. Tunnel measuring point layout. (**a**) Longitudinal section and (**b**) cross-section (30 m, 40 m, 50 m, and 60 m).

4.2. Shock Wave Flow Field Changes

The shock wave pressure cloud diagram following the explosion of the upper bench explosive is depicted in Figure 5. As illustrated in Figure 5a, the shock wave initially propagated as a spherical wave after the explosion. As the shock wave encountered the tunnel wall, it was constrained by the tunnel's enclosed structure, and multiple reflections occurred with the wall, leading to a reflected overpressure significantly greater than the incident overpressure, as shown in Figure 5b. Figure 5c demonstrates that the collision of the shock wave with the tunnel wall created a reflected wave and compressive wave superimposition, resulting in the Mach effect. Subsequently, a stable plane wave formed at the front of the shock wave and continued to propagate forward, while regular oblique and Mach reflections persisted at the tail of the shock wave.

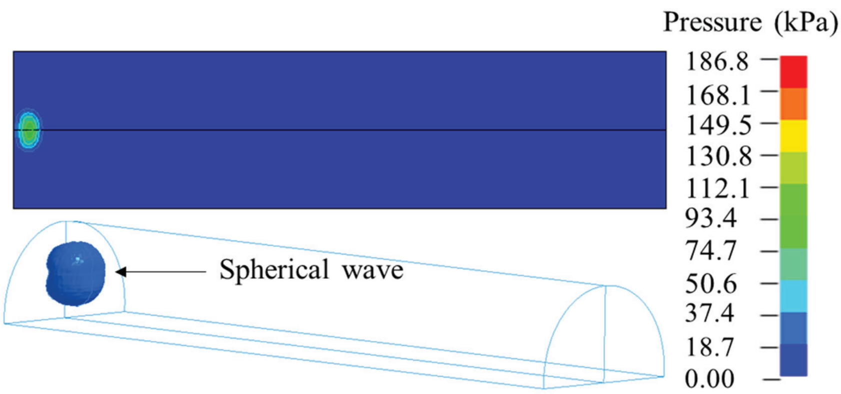

(**a**)

Figure 5. *Cont.*

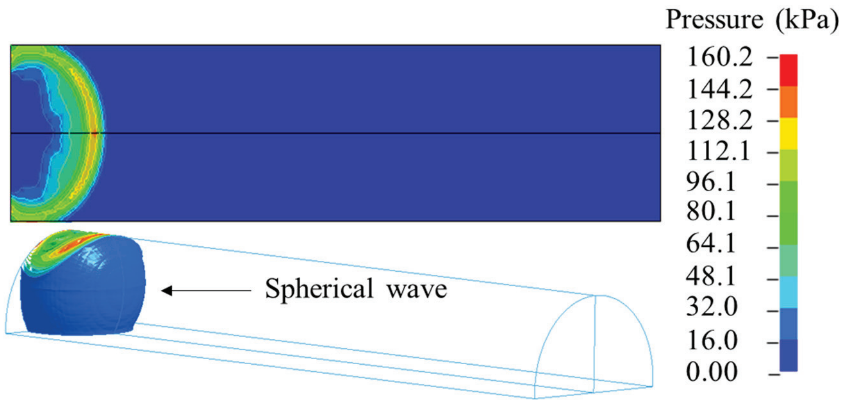

(**b**)

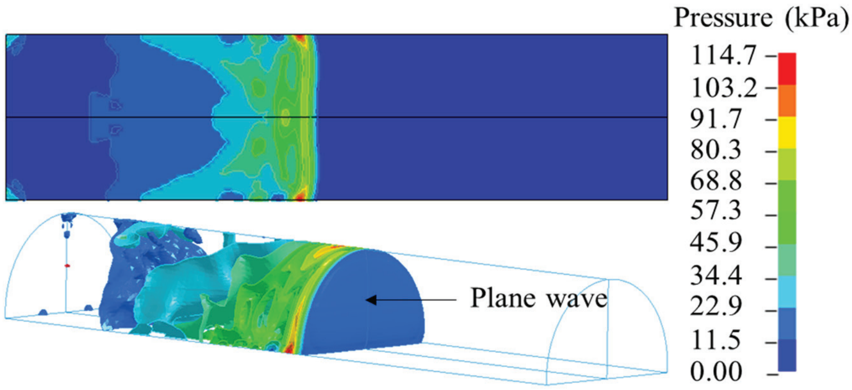

(**c**)

Figure 5. Blasting shock wave pressure nephogram: (**a**) 4 ms, (**b**) 14 ms, and (**c**) 60 ms.

4.3. Cross-Section Overpressure Analysis

The equivalent diameter of the upper bench in the tunnel was 7.87 m. The blasting shock wave developed into a plane shock wave at a distance of approximately 4 to 8 times the equivalent diameter from the explosion center, as illustrated in Figure 5. To pinpoint the exact location where the plane shock wave formed, four sections spaced 10 m apart were selected, starting from 30 m away from the explosion center. The following formula was applied:

$$\begin{cases} P_{\max}/P_{\min} \leq \vartheta_P \\ I_{\max}/I_{\min} \leq \vartheta_I \end{cases} \tag{3}$$

where $P_{\max}$ and $P_{\min}$ are the maximum and minimum overpressure values of a section, respectively. $I_{\max}$ and $I_{\min}$ are the maximum and minimum impulses of a section. When $\vartheta_P = 1.5$, the spherical wave was restored to a plane wave, and when $\vartheta_I = 1.05$, a plane wave was completely formed.

The overpressure and impulse values at various measuring points on the cross-section, located at different distances from the explosion center, are presented in Tables 5 and 6. These tables allowed for the determination of overpressure and impulse ratios at various distances from the explosive, as shown in Figure 6. Further analysis revealed that the ratio of maximum to minimum overpressure of the shock wave was less than 1.5 at a distance of 40 m from the tunnel face. Similarly, the ratio of maximum to minimum impulse was less than 1.05 at distances ranging from 40 m to 50 m from the tunnel face. Beyond 48.5 m from the explosion center, the ratio of maximum to minimum impulse was also less than 1.05, as determined by linear interpolation. Thus, the plane wave formed by the blasting shock wave on the upper bench of the tunnel occurred at a distance of 48.5 m, approximately 6 times the equivalent diameter of the tunnel.

Table 5. Overpressure ratio of the radial measuring point in the cross-section.

Distance/(m)	Point a/(kPa)	Point b/(kPa)	Point c/(kPa)	Point d/(kPa)	P_{max}/P_{min}
30	49.26	49.24	55.97	76.96	1.563
40	44.32	44.79	51.02	63.31	1.428
50	37.73	37.79	40.05	52.48	1.391
60	35.71	35.68	36.53	49.70	1.393

Table 6. Impulse ratio of the radial measuring point in the cross-section.

Distance/(m)	Point a/(kg·m/s)	Point b/(kg·m/s)	Point c/(kg·m/s)	Point d/(kg·m/s)	I_{max}/I_{min}
30	4080.70	4075.15	4072.64	5510.93	1.353
40	4054.98	4036.54	4041.83	4643.83	1.150
50	4008.58	4005.20	4006.37	4137.37	1.033
60	3955.87	3954.16	3953.47	4008.819	1.014

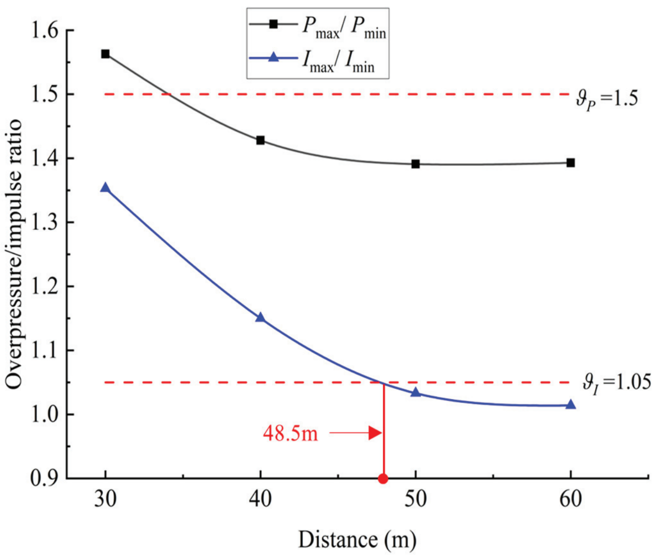

Figure 6. Overpressure/impulse ratio at different distances from the center of the explosion.

4.4. Analysis of Shock Wave Overpressure Attenuation

As shown in Figure 7, the shock wave exhibited multiple peaks during its propagation, followed by pronounced serrated attenuation and noticeable oscillations before eventually returning to atmospheric pressure. The peak overpressure was higher near the explosion center, resulting in more rapid attenuation. As the shock wave propagated further, the rate of attenuation decreased, the time required for reduction increased, and the duration of the overpressure also increased.

Following the explosion, the overpressure peak at 5 m rapidly reached 90.3 kPa, before quickly attenuating. Due to shock wave reflections, a smaller overpressure peak of 9.3 kPa was observed at 55 ms. At 10 m, two closely spaced overpressure peaks of 75.9 kPa and 76.5 kPa were recorded. The first peak represented the initial shock wave front pressure immediately after the explosion, while the second peak resulted from the superposition of air compression waves generated by multiple reflections of the shock wave from the tunnel wall. At 20 m, the peak overpressure was slightly higher than the maximum overpressure observed at 10 m. This increase was attributed to the higher pressure and propagation speed of the reflected wave compared to the incident shock wave. Both regular oblique and Mach reflections occurred, intensifying the shock wave at this distance.

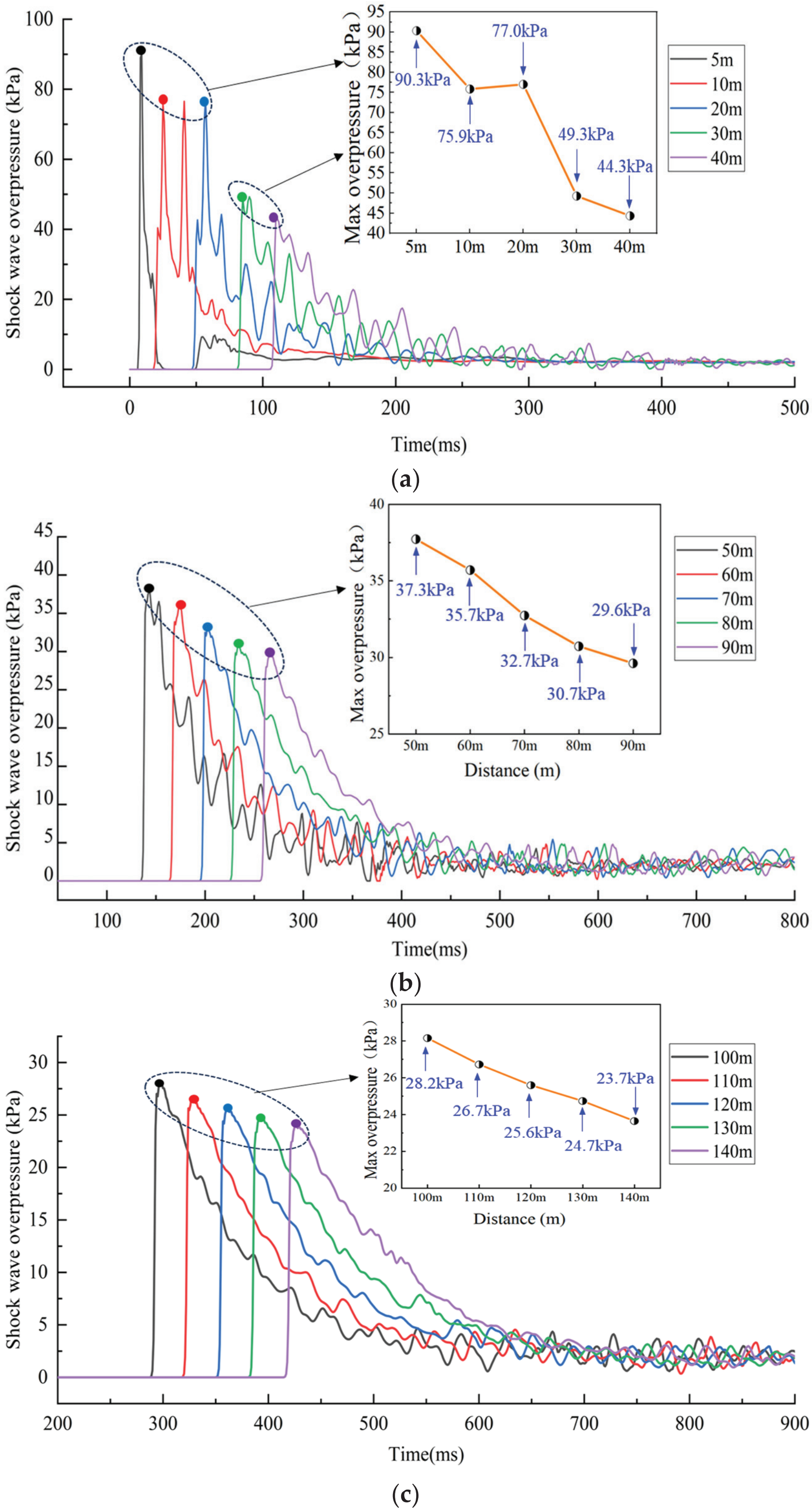

Figure 7. Time–history curves of shock wave overpressure at different positions: (**a**) 5~40 m, (**b**) 50~90 m, and (**c**) 100~140 m.

The shock wave overpressure generated at the tunnel face decreased rapidly near the explosion center. As the shock wave propagated farther, the rate of attenuation of the overpressure peak changed. To quantify this attenuation rate, the attenuation coefficient of the shock wave overpressure is defined by Equation (4):

$$\delta = \frac{\Delta P}{\Delta P_1} \tag{4}$$

where ΔP is the shock wave overpressure peak at the previous position, and ΔP_1 is the shock wave overpressure peak at the latter position.

As shown in Figure 8, the shock wave initially underwent rapid attenuation. Within 0 m to 20 m from the explosion center, the reflected shock wave compressed the air again and quickly caught up with the wave front of the initial shock wave. This superposition, which was due to multiple reflections of the shock wave off the tunnel walls and floor, resulted in an increase in the shock wave overpressure peak. After this phase, at 30 m from the detonation center, the shock wave overpressure decreased dramatically, and the attenuation coefficient rose sharply to 1.56. Beyond 30 m, the attenuation of the shock wave overpressure peak stabilized, with the attenuation coefficient ranging from 1.17 to 1.03.

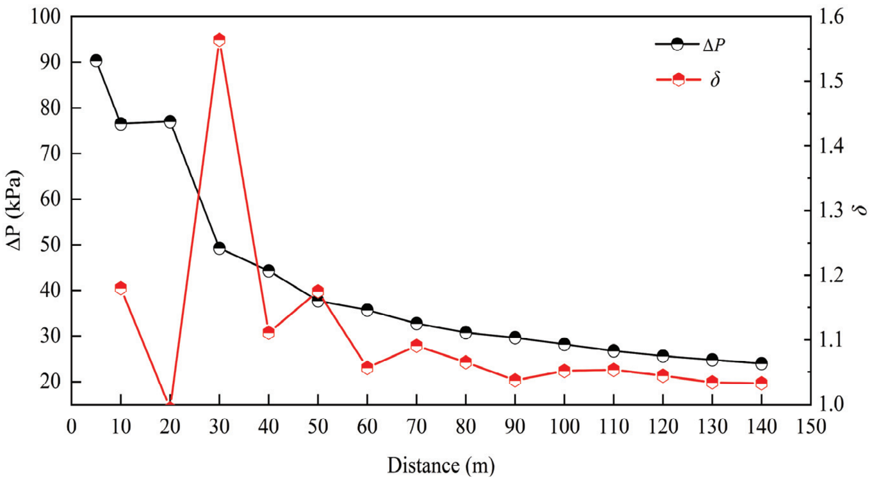

Figure 8. Shock wave overpressure attenuation and attenuation coefficient curves.

5. Blasting Shock Wave Field Test and Overpressure Prediction

5.1. Test Instruments

The setup for the field test of shock waves in the upper bench of the Shengli highway tunnel is shown in Figure 9. A shock wave overpressure sensor (PCB 113B28 SN, produced by PCB Piezotronics Inc., New York, NY, USA) and a shock wave acquisition instrument (Blast-PRO, produced by Chengdu Taice Technology Co., LTD, Chengdu, China) were used to test the blasting shock wave. Table 7 shows the parameters of the test instruments.

Table 7. Test instrument parameters.

Test instrument	Parameter	Technical Index
Shock wave overpressure sensor	Sensitivity	14.5 mV/kPa
	Resolution	0.07 kPa
	Measuring range	344.7 kPa output in ±5 V
		689.4 kPa output in ±10 V
Shock wave test instrument	Channel number	2
	Sampling rates	500 k~4 MHz
	A/D precision	24-bit
	Bandwidth	>700 Hz

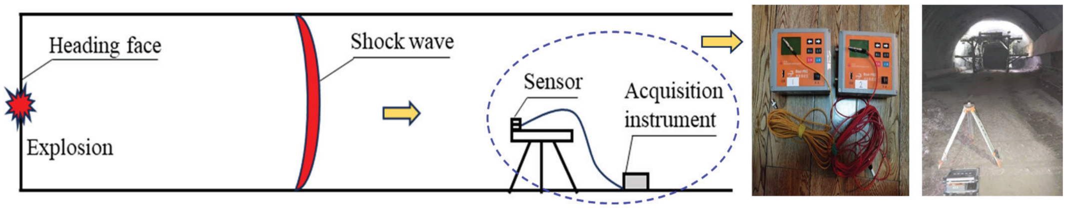

Figure 9. Test equipment and field photos.

5.2. Analysis Results

We conducted 21 tests on the upper bench and obtained 15 sets of valid data. Before the blast, a tripod was setup at the measurement point, and a sensor was fixed above the tripod, parallel to the ground. The measurement system was checked to ensure it was in normal working condition. When the test system was started, the shock wave data collection began, with measurement data recorded during the tunnel face blasting.

The test results are shown in Table 8: Q is the total explosive charge of the tunnel face blasting, R is the distance from the shock wave measuring point to the tunnel face, S is the tunnel section area, V is the volume of the shock wave propagation area, d is the equivalent diameter of the tunnel section, and ΔP is the peak value of the blasting shock wave overpressure at the measuring point.

Table 8. Blasting shock wave test results.

Number	Q (kg)	R (m)	S (m^2)	V (m^3)	d (m)	ΔP (kPa)
1	174	74	62.8	4647.2	7.87	
2	180	74.5	62.8	4678.6	7.87	39.17
3	174	76	62.8	4772.8	7.87	36.49
4	180	80	62.8	5024	7.87	31.56
5	168	83	62.8	5024	7.87	26.57
6	168	87.6	62.8	5501.3	7.87	24.72
7	174	90	62.8	5652	7.87	23.80
8	168	96	62.8	6028.8	7.87	23.16
9	186	99	62.8	6217.2	7.87	21.77
10	168	100	62.8	6280	7.87	20.60
11	186	104.5	62.8	6374.2	7.87	19.28
12	180	110	62.8	6908	7.87	18.03
13	174	124	62.8	7787.2	7.87	17.46
14	180	130	62.8	8164	7.87	16.33
15	180	142.5	62.8	8949	7.87	14.82

Since the tunnel was a single-ended excavation tunnel, the empirical formula for the peak value of shock wave overpressure in roadways with one-end openings, proposed by Pokrovsky, could be applied for fitting. Then, field-measured data were combined with the Pokrovsky formula. Finally, a prediction formula for blasting shock wave overpressure suitable for the tunnel was proposed.

(1) Attenuation formula fitting

The formula proposed by Pokrovsky is provided in Equation (5). The overpressure data at the measuring point were considered valid only when the propagation distance was equal to or greater than 6 times the equivalent diameter of the tunnel. Since the distance from the measuring point to the tunnel face exceeded 47.22 m (where 6d = 6 × 7.87 = 47.22 m), the overpressure data for these measuring points were deemed valid.

$$\Delta P = \left[\frac{8Q}{SR} + 14.6\sqrt[3]{\left(\frac{Q}{SR}\right)^2} + 1.81\sqrt[3]{\frac{Q}{SR}}\right]10Q, (R \geq 6d) \tag{5}$$

The model test usually uses a TNT explosive to detonate directly in the air or tunnel. The tunnel is blasted by an emulsion explosive, and Q in Equation (5) is the mass of the TNT explosive. Therefore, it is necessary to convert the explosive mass used in tunnel blasting into the equivalent TNT explosive and increase the TNT equivalent conversion coefficient, γ. In addition, most of the energy of the blasting explosives in tunnel excavation is used to crush rock mass, and the remaining part is converted into shock wave energy, so a shock wave energy conversion coefficient, η, is added. Combined with the above analysis, the parameters in Equation (5) were modified and expressed by parameters a_0, b_0 and c_0 to establish a new empirical formula for shock wave overpressure:

$$\Delta P = \left[\frac{a_0 Q\gamma\eta}{SR} + b_0 \sqrt[3]{\left(\frac{Q\gamma\eta}{SR}\right)^2} + c_0 \sqrt[3]{\frac{Q\gamma\eta}{SR}} \right] Q \quad (6)$$

In Equation (6), SR is the volume of the shock wave propagation area, which can be replaced by V, which can be written as Equation (7):

$$\frac{\Delta P}{Q} = a_0\gamma\eta\frac{Q}{V} + b_0(\gamma\eta)^{\frac{2}{3}}\left(\frac{Q}{V}\right)^{\frac{2}{3}} + c_0(\gamma\eta)^{\frac{1}{3}}\left(\frac{Q}{V}\right)^{\frac{1}{3}} \quad (7)$$

Let $y = \frac{\Delta P}{Q}$, $x = \left(\frac{Q}{V}\right)^{\frac{1}{3}}$, and Equation (7) can be written as:

$$y = a_0\gamma\eta x^3 + b_0(\gamma\eta)^{\frac{2}{3}}x^2 + c_0(\gamma\eta)^{\frac{1}{3}}x \quad (8)$$

Since a_0, b_0, c_0, γ, and η are constants, we can use new parameters to replace the parameters in Equation (9), as follows:

$$y = a_1x^3 + b_1x^2 + c_1x \quad (9)$$

Through the least-squares method, the field shock wave test data were fitted to obtain $a_1 = 99.2$, $b_1 = -55.37$, and $c_1 = 8.05$, and finally, to fit the tunnel shock wave empirical formula:

$$\frac{\Delta P}{Q} = 99.2\frac{Q}{V} - 55.37\left(\frac{Q}{V}\right)^{\frac{2}{3}} + 8.05\left(\frac{Q}{V}\right)^{\frac{1}{3}} \quad (10)$$

Comparing the fitted shock wave overpressure prediction formula with the field-measured data, taking $\left(\frac{Q}{V}\right)^{\frac{1}{3}}$ as the X-axis and $\frac{\Delta P}{Q}$ as the Y-axis, the relationship curve was drawn, as shown in Figure 10. The fitting degree, R^2 = 0.99, shows that the curve fitting was good. Equation (10) can be used as the empirical formula for predicting the attenuation of shock wave overpressure in the tunnel.

(2) Applicability analysis

By substituting various total charge quantities into Equation (10), the attenuation curves of shock wave overpressure for different charges could be derived. As shown in Figure 11, the closer the blasting distance was to the tunnel working face, the higher the shock wave overpressure. With the increasing propagation distance, the shock wave overpressure gradually decreased. The attenuation law of shock wave overpressure predicted by the empirical formula aligned well with the results of the numerical simulations. The empirical formula indicated a faster attenuation rate of overpressure in the 70 m to 100 m range, with a slower attenuation after 100 m, while the numerical simulation showed a more gradual attenuation curve. The discrepancies between the empirical formula and numerical simulation results may have arisen because the empirical formula was based on field test data, which accounted for a more complex tunnel environment (e.g., trolleys, vehicles, and other obstacles), whereas the numerical simulation assumed a simpler tunnel environment.

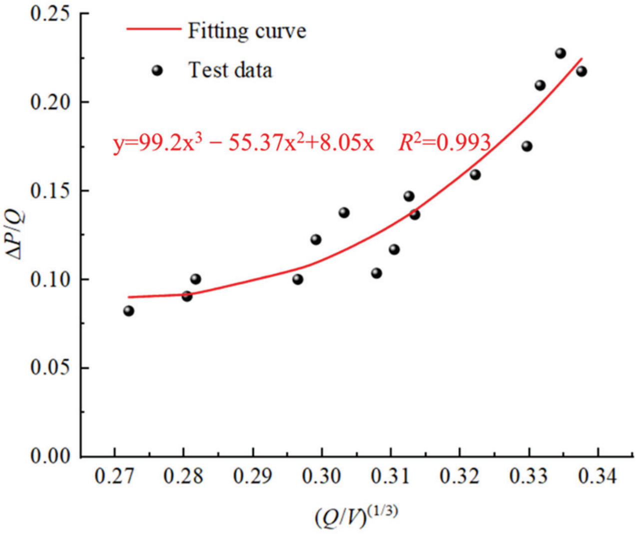

Figure 10. Relationship between the fitting formula and test data.

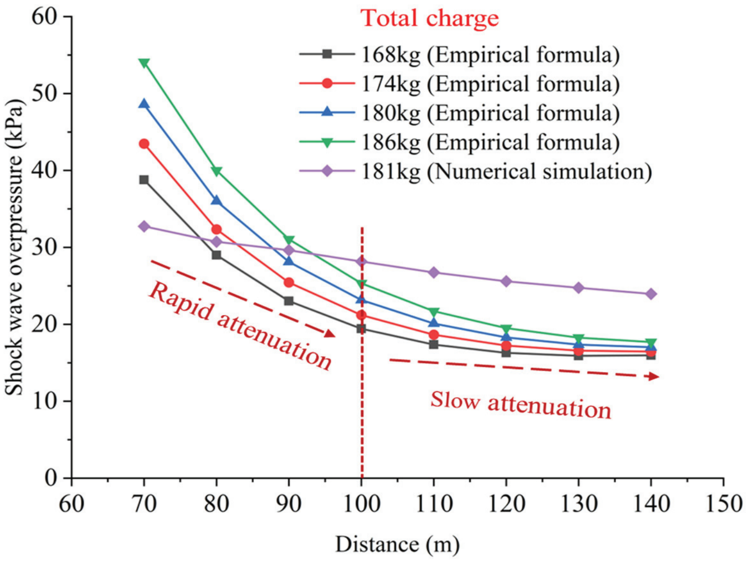

Figure 11. Shock wave overpressure attenuation with different explosive quantities.

6. Discussion

In accordance with 'Blasting Safety Regulations', the overpressure peak of a shock wave is categorized into five grades based on its impact on the human body, as illustrated in Table 9.

Table 9. Damage level of shock wave overpressure peaks to the human body.

Level	Overpressure Peak Value (kPa)	Extent of Damage to the Body
I	<2	None
II	20~30	Minor bruises
III	30~50	Hearing and organ damage; fractures
IV	50~100	Internal organs have suffered severe damage; possibly death
V	>100	Most individuals die

As shown in Table 9, the overpressure peak value should be less than 2 kPa to ensure personnel safety. Considering the law of pressure wave overpressure attenuation and the attenuation coefficient, we obtained the minimum safe distance for personnel from the blast source in the tunnel as 236.8 m.

Blasting Safety Regulations provide Equation (11) for determining the air shock wave overpressure during tunnel blasting:

$$\Delta p = \left(3270\frac{qm_y}{RS} + 780\sqrt{\frac{qm_y}{RS}}\right)e^{\frac{\beta R}{d}} \tag{11}$$

where ΔP is the shock wave overpressure value (kPa), R denotes the distance from the measuring point to the explosion point (m), S is the tunnel cross-sectional area (m^2), q is the mass of the explosive charge (kg), m_y is the shock wave conversion factor, taken as 0.007, β is the roughness factor of the tunnel wall, taken as 0.014, and d is the equivalent diameter of the tunnel section.

Figure 12 illustrates the attenuation law of shock waves, based on field test data, numerical simulation results, the overpressure empirical formula proposed in this study, and the empirical formula specified in the Blasting Safety Regulations. Our analysis showed that the empirical formula proposed in this study closely aligned with both the field test results and the numerical simulation outcomes. In contrast, the overpressure values obtained from the empirical formula in the 'Blasting Safety Regulations' were significantly smaller.

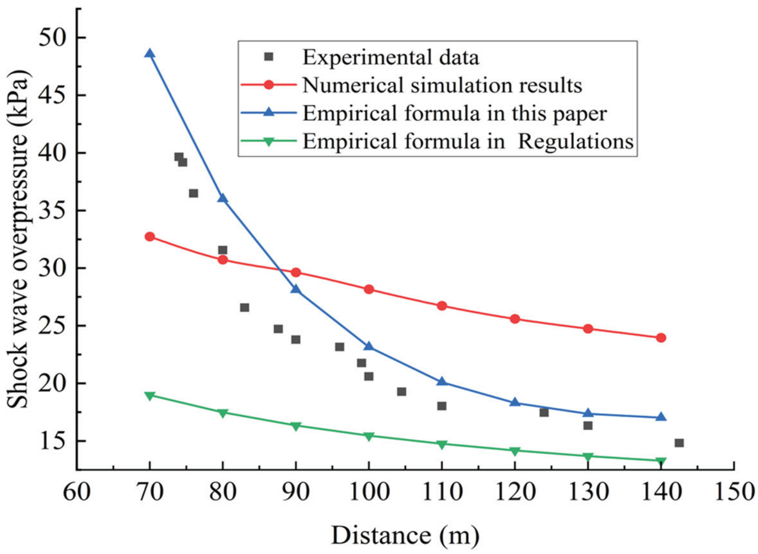

Figure 12. Shock wave overpressure attenuation curve.

7. Conclusions

In this paper, the explicit dynamic analysis finite element software, ANSYS/LS-DYNA, was utilized to simulate the propagation process of a blasting shock wave within a tunnel. The study analyzed the changes in the shock wave flow field and the attenuation behavior of overpressure across the tunnel's cross-section. Based on these simulations and field test data, a predictive formula for blasting shock wave overpressure suitable for tunnels was proposed. The main conclusions were as follow:

(1) Initially, the shock wave propagated spherically, but it was subsequently affected by the enclosed structure of the tunnel. This interaction caused multiple reflections of the shock wave with the tunnel walls, resulting in a significant increase in overpressure values at the vault, side wall, and arch foot positions. At a distance of 6 times the equivalent diameter from the explosion center (48.5 m from the tunnel

face), the spherical shock wave transitioned into a plane wave and continued to propagate forward.

(2) As the shock wave reached a specific position, its overpressure instantaneously peaked before undergoing multiple-peak oscillation, zigzag attenuation, and gradual restoration to initial atmospheric pressure. Within 0~20 m from the tunnel face, repeated reflection between the shock wave and tunnel wall caused an increase in the overpressure value at 20 m, while exhibiting significant fluctuations in the attenuation coefficient. Beyond 50 m, propagation occurred as a stable plane wave, with an overpressure attenuation coefficient ranging from 1.17 to 1.03. The minimum safe distance between personnel and the explosion source in the tunnel was 236.8 m.

(3) Through on-site testing of shock wave overpressure values, Pokrovsky's empirical formula for shock wave overpressure has been refined based on parameters derived using the least-squares method. This paper proposed an empirical attenuation formula for shock wave overpressure with a good fitting degree (R^2 = 0.993). When excavating tunnels using drilling and blasting methods, this formula can be utilized to predict plane shock wave overpressures in the upper bench of the tunnel.

Author Contributions: Conceptualization, T.Y., J.S., J.W. and J.F.; methodology, T.Y.; software, T.Y.; validation, J.S., J.W. and G.S.; formal analysis, T.Y.; investigation, J.F. and L.C.; resources, J.F., L.C. and J.M.; data curation, J.M. and Z.W.; writing—original draft preparation, T.Y.; writing—review and editing, J.S., J.W. and G.S.; visualization, T.Y. and J.S.; supervision, J.W., J.M. and Z.W.; project administration, J.W., J.M. and Z.W.; funding acquisition, T.Y. and J.W. All authors have read and agreed to the published version of the manuscript.

Funding: This work was financially supported by the Sichuan Youth Science and Technology Innovation Research Team Project (Grant No. 2024NSFTD0013).

Data Availability Statement: The data can be made available upon request.

Conflicts of Interest: Liangjun Chen was employed by the company China Railway City Development Investment Group Co., Ltd. Sichuan southwest branch, Chengdu 610213, China. Jun Man was employed by the company China Railway Erju 6TH Engineering Co., Ltd., Chengdu 610031, China. Zhen Wu was employed by the company Sichuan Railway Construction Co., Ltd., Chengdu 610041, China. The remaining authors declare that the research was conducted in the absence of any commercial or financial relationships that could be construed as a potential conflict of interest.

References

1. Sun, Z.; Zhang, D.; Fang, Q. Technologies for Large Cross-Section Subsea Tunnel Construction Using Drilling and Blasting Method. *Tunn. Undergr. Space Technol.* **2023**, *141*, 105161. [CrossRef]
2. Guo, Y.; Wang, Y.; Geng, F.; Zhang, Z. Study on Dust Distribution in a Highway Tunnel during the Full-Face Excavation with Drilling-Blasting Method. *Tunn. Undergr. Space Technol.* **2023**, *139*, 105229. [CrossRef]
3. Wang, M.; Zhao, S.; Tong, J.; Wang, Z.; Yao, M.; Li, J.; Yi, W. Intelligent Classification Model of Surrounding Rock of Tunnel Using Drilling and Blasting Method. *Undergr. Space* **2021**, *6*, 539–550. [CrossRef]
4. Zhang, G.-H.; Chen, W.; Jiao, Y.-Y.; Wang, H.; Wang, C.-T. A Failure Probability Evaluation Method for Collapse of Drill-and-Blast Tunnels Based on Multistate Fuzzy Bayesian Network. *Eng. Geol.* **2020**, *276*, 105752. [CrossRef]
5. Trivedi, R.; Singh, T.N.; Raina, A.K. Prediction of Blast-Induced Flyrock in Indian Limestone Mines Using Neural Networks. *J. Rock Mech. Geotech. Eng.* **2014**, *6*, 447–454. [CrossRef]
6. Brode, H.L. Blast Wave from a Spherical Charge. *Phys. Fluids* **1959**, *2*, 217–229. [CrossRef]
7. Henrych, J.; Abrahamson, G.R. The Dynamics of Explosion and Its Use. *J. Appl. Mech.* **1980**, *47*, 218. [CrossRef]
8. Baker, W.E.; Cox, P.A.; Kulesz, J.J.; Strehlow, R.A.; Westine, P.S. *Explosion Hazards and Evaluation*; Elsevier: Amsterdam, The Netherlands, 2012; ISBN 978-0-444-59988-9.
9. Fang, Y.; Yao, Z.; Lei, S. Air Flow and Gas Dispersion in the Forced Ventilation of a Road Tunnel during Construction. *Undergr. Space* **2019**, *4*, 168–179. [CrossRef]
10. Fang, Y.; Fan, J.; Kenneally, B.; Mooney, M. Air Flow Behavior and Gas Dispersion in the Recirculation Ventilation System of a Twin-Tunnel Construction. *Tunn. Undergr. Space Technol.* **2016**, *58*, 30–39. [CrossRef]
11. Chapman, T.C.; Rose, T.A.; Smith, P.D. Blast Wave Simulation Using AUTODYN2D: A Parametric Study. *Int. J. Impact Eng.* **1995**, *16*, 777–787. [CrossRef]
12. Zukas, J.A.; Scheffler, D.R. Practical Aspects of Numerical Simulations of Dynamic Events: Effects of Meshing. *Int. J. Impact Eng.* **2000**, *24*, 925–945. [CrossRef]

13. Luccioni, B.; Ambrosini, D.; Danesi, R. Blast Load Assessment Using Hydrocodes. *Eng. Struct.* **2006**, *28*, 1736–1744. [CrossRef]
14. Genova, B.; Silvestrini, M.; Leon Trujillo, F.J. Evaluation of the Blast-Wave Overpressure and Fragments Initial Velocity for a BLEVE Event via Empirical Correlations Derived by a Simplified Model of Released Energy. *J. Loss Prev. Process Ind.* **2008**, *21*, 110–117. [CrossRef]
15. Wu, C.; Hao, H. Numerical Simulation of Structural Response and Damage to Simultaneous Ground Shock and Airblast Loads. *Int. J. Impact Eng.* **2007**, *34*, 556–572. [CrossRef]
16. Ishikawa, N.; Beppu, M. Lessons from Past Explosive Tests on Protective Structures in Japan. *Int. J. Impact Eng.* **2007**, *34*, 1535–1545. [CrossRef]
17. Smith, P.D.; Vismeg, P.; Teo, L.C.; Tingey, L. Blast Wave Transmission along Rough-Walled Tunnels. *Int. J. Impact Eng.* **1998**, *21*, 419–432. [CrossRef]
18. Rodríguez, R.; Toraño, J.; Menéndez, M. Prediction of the Airblast Wave Effects near a Tunnel Advanced by Drilling and Blasting. *Tunn. Undergr. Space Technol.* **2007**, *22*, 241–251. [CrossRef]
19. Benselama, A.M.; William-Louis, M.J.-P.; Monnoyer, F.; Proust, C. A Numerical Study of the Evolution of the Blast Wave Shape in Tunnels. *J. Hazard. Mater.* **2010**, *181*, 609–616. [CrossRef]
20. Uystepruyst, D.; Monnoyer, F. A Numerical Study of the Evolution of the Blast Wave Shape in Rectangular Tunnels. *J. Loss Prev. Process Ind.* **2015**, *34*, 225–231. [CrossRef]
21. Pennetier, O.; William-Louis, M.; Langlet, A. Numerical and Reduced-Scale Experimental Investigation of Blast Wave Shape in Underground Transportation Infrastructure. *Process Saf. Environ. Prot.* **2015**, *94*, 96–104. [CrossRef]
22. Wu, M.; Wang, B.; Ba, Z.; Dai, K.; Liang, J. Propagation Attenuation of Elastic Waves in Multi-Row Infinitely Periodic Pile Barriers: A Closed-Form Analytical Solution. *Eng. Struct.* **2024**, *315*, 118480. [CrossRef]
23. Figuli, L.; Cekerevac, D.; Bedon, C.; Leitner, B. Numerical Analysis of the Blast Wave Propagation Due to Various Explosive Charges. *Adv. Civ. Eng.* **2020**, *2020*, 8871412. [CrossRef]
24. Fang, Y.; Zou, Y.-L.; Zhou, J.; Yao, Z.; Lei, S.; Yang, W. Field Tests on the Attenuation Characteristics of the Blast Air Waves in a Long Road Tunnel: A Case Study. *Shock Vib.* **2019**, *2019*, 9693524. [CrossRef]
25. Deng, X.F.; Zhu, J.B.; Chen, S.G.; Zhao, Z.Y.; Zhou, Y.X.; Zhao, J. Numerical Study on Tunnel Damage Subject to Blast-Induced Shock Wave in Jointed Rock Masses. *Tunn. Undergr. Space Technol.* **2014**, *43*, 88–100. [CrossRef]
26. Kumar, R.; Choudhury, D.; Bhargava, K. Prediction of Blast-Induced Vibration Parameters for Soil Sites. *Int. J. Geomech.* **2014**, *14*, 04014007. [CrossRef]
27. Yao, Z.; Tian, Q.; Fang, Y.; Ye, L.; Pu, S.; Fang, X. Propagation and Attenuation of Blast Vibration Waves in Closely Spaced Tunnels: A Case Study. *Arab. J. Sci. Eng.* **2022**, *47*, 4239–4252. [CrossRef]
28. Li, H.; Wu, H.; Wang, Z.; Zhang, G.; Li, J.; Zhou, H.; Wang, M.; He, Y. Experimental and Numerical Simulation of the Propagation Law of Shock Waves in Corrugated Steel-Lined Tunnels. *Process Saf. Environ. Prot.* **2022**, *168*, 1019–1030. [CrossRef]
29. Yi, C.P.; Nordlund, E.; Zhang, P.; Warema, S.; Shirzadegan, S. Numerical Modeling for a Simulated Rockburst Experiment Using LS-DYNA. *Undergr. Space* **2021**, *6*, 153–162. [CrossRef]
30. Xiao, W.; Andrae, M.; Gebbeken, N. Air Blast TNT Equivalence Factors of High Explosive Material PETN for Bare Charges. *J. Hazard. Mater.* **2019**, *377*, 152–162. [CrossRef]

buildings

MDPI

Article

Research on Axial Stress and Strain Characteristics of Reinforced-Concrete Curved Pipe Jacking in Power Tunnels

Yongjun He [1], Jian Cheng [2], Zengli Shi [3], Bin Zhang [1], Li Chen [1], Xi Li [2], Xiaoli Wang [1] and Peng Zhang [4,*]

1 State Grid ShanDong Electric Power Company of Construction Company, Jinan 250001, China; heyongjunsd@126.com
2 State Grid ShanDong Electric Power Company, Jinan 250001, China
3 China Electric Power Research Institute, Beijing 100192, China
4 Faculty of Engineering, China University of Geosciences (Wuhan), Wuhan 430074, China
* Correspondence: cugpengzhang@cug.edu.cn

Abstract: Joint deflection during curved pipe jacking in power tunnels poses a significant risk of structural failure due to the resulting eccentric and diagonal loading on the pipes. This study investigated the axial stress and strain characteristics of reinforced-concrete pipes under varying joint deflection angles and jacking forces, using a combined approach of experimental model testing and finite element method (FEM) numerical simulations. The experimental setup replicated curved pipe jacking conditions, allowing for the measurement of strains and deformation under controlled loading. Numerical simulations, validated against experimental data, provided detailed insights into the stress distribution patterns. The results revealed distinct stress states in different pipe sections. The pipe closest to the jacking force (3# pipe) experienced eccentric loading, leading to localized stress concentrations and inelastic strain on the inner wall at the point of eccentricity, indicating vulnerability to compressive failure. The middle pipe section (2# pipe) underwent complex diagonal loading, resulting in the development of inelastic strain on both the inner and outer walls at specific orientations, highlighting a risk of both compressive and shear failure modes. The study also demonstrated that the magnitude of the axial jacking force and the degree of joint deflection significantly influence the stress distribution and the extent of inelastic strain. These findings provide important information for optimizing the design and construction of curved pipe jacking projects in power tunnels. The identified failure mechanisms and the influence of key parameters on pipe behavior can inform strategies to mitigate the risk of structural failure, improve the resilience of pipe systems, and enhance the overall safety and reliability of underground power tunnel infrastructure.

Keywords: curved pipe jacking; joint deflection; finite element method; pipe stress and strain

1. Introduction

Large-diameter, reinforced-concrete pipe jacking is a primary technology for constructing urban power tunnels. This method offers several benefits: rapid construction, minimal impact on the surrounding environment, cost effectiveness, and adherence to environmentally friendly practices. These advantages contribute to the advancement of underground power tunnel construction in urban areas.

The pipe jacking process involves pushing a series of connected pipe sections into a tunnel created by a tunnel boring machine. This is achieved through the application of a jacking force. Each pipe section is subjected to a complex and dynamic spatial force system. These forces include the axial jacking force, head-on resistance, surrounding soil and water pressure, lubricating grouting pressure, pipe–soil friction, the weight of the pipe itself, and potential surface traffic loads. Additionally, the jacking force is cyclic, meaning that the pipe sections undergo repeated loading and unloading throughout the process.

In curved pipe jacking, the joints between adjacent pipes have eccentric angles. This results in the axial jacking force acting as an eccentric load on the pipes. In many cases, pipe failures during curved pipe jacking construction are attributed to the concentration of axial stress caused by this eccentricity. Consequently, understanding the pipe force characteristics under varying axial jacking forces and joint eccentricities is essential for the successful execution of curved pipe jacking projects.

Current research on the stress characteristics of pipe jacking joints primarily focuses on two approaches, as follows:

(1) Theoretical analysis: Researchers have employed various theoretical frameworks to investigate the internal forces and deformations of pipe joints under different conditions. These frameworks include the cross-section kernel theory of material mechanics [1,2], thin-walled cylinder stability theory of elastodynamics [3], thick-walled cylinder models of elastodynamics [4], and shell theory [5]. Studies have examined both straightline jacking and curvilinear deflection scenarios for thick-walled steel-reinforced concrete, glass fiber-reinforced plastic, and thin-walled steel pipe joints. These analyses have led to the development of calculation models for the internal forces and wall thickness of pipe joints;

(2) Internal force monitoring tests: Researchers have also conducted field tests to monitor the internal forces within pipe joints during construction. Milligan and Norris [6] performed on-site monitoring to gather data on pipe–soil contact pressure and reinforcement stress in reinforced-concrete pipe jacking. Pan [7] conducted an experimental study on stress, contact pressure, and soil deformation, during the construction of large-caliber, sharply curved, reinforced-concrete pipe jacking. Wei et al. [8] used similar methods to monitor the contact pressure and reinforcement stress on linear reinforced-concrete pipe jacking joints, establishing stress patterns for both curved and straightline jacking. Yang [9] monitored and analyzed the stress in terms of large-diameter, linear, steel pipe jacking using a pipe curtain preconstruction method, revealing that the pipe section was predominantly under pressure;

(3) Numerical simulation: Numerical methods, particularly finite element analysis, have been employed to investigate the stress behavior of pipe joints. Huang et al. [10] used finite element simulation to study the dynamic jacking process of large-diameter FRP-sandwiched pipes, highlighting the tendency for stress concentration at pipe joints. Chen [1] employed the ABAQUS 6.14 software to analyze the stresses in glass fiber-reinforced plastic pipe joints under deflection conditions, demonstrating a rapid increase in the stresses with increasing deflection angles, beyond the free deflection angle.

In a recent study of the construction and operation of curved pipe jacking, Pan et al. [11] introduced an automatic guidance system for long-distance curved pipe jacking based on single-prism technology, with further advancements in multivariate data fusion that enabled 3D orientations of the tunnel boring machine (TBM) to be obtained. Choo et al. [12] assessed the non-linear rock strength parameters to estimate the pipe-jacking forces through numerical modeling, emphasizing the importance of an equivalent tangential cohesion and friction angle in the finite element analysis. Zhou et al. [13] explored the static equilibrium configuration and non-linear dynamics of slightly curved, cantilevered pipes, conveying fluid, highlighting the unique behavior of nonconservative systems in fluid–structure interactions. Zhong et al. [14] addressed the frictional characteristics and contact properties of pipe strings to understand and verify solutions for pipe sticking issues encountered during rock pipe-jacking projects. Zhang et al. [15] discuss field monitoring and analysis of soil deformation during curved steel pipe jacking in the Gongbei Tunnel, emphasizing the importance of monitoring and analyzing soil behavior during construction. Zhou et al. [16] and Zu et al. [17] focused on predicting jacking forces in curved pipe roofs using different algorithms and de-noising methods, highlighting the significance of accurate force estimation in ensuring the success of pipe-jacking projects.

While substantial research has been conducted on the forces in linear jacking pipes using theoretical analysis, field monitoring, and numerical simulation, the investigation of forces in regard to curved jacking pipes has primarily relied on theoretical analysis and a limited number of field tests. Consequently, the relationship between pipe stress, joint deflection, and the axial jacking force remains unclear. To address this gap, this study utilizes a test system and a three-dimensional finite element model, comprising three sections of reinforced-concrete pipes. This setup simulates joint deflection in curved pipe jacking under various axial jacking forces. By analyzing the resulting axial stress changes under different deflection angles and axial forces, this research aims to elucidate the underlying relationships.

2. Methodology

2.1. Curved Pipe Jacking Test

(1) Test pipes

The test utilized C50 reinforced-concrete jacking pipes, with an inner diameter of 600 mm, an outer diameter of 740 mm, and F-type socket joints. Each pipe section had a length of 2000 mm. A single layer of steel cage reinforcement was embedded within the pipe wall. The rebar had a diameter of 5 mm and was arranged longitudinally at 45° intervals, totaling eight bars. The ring bar pitch was 60 mm. At the pipe joints, a 10 mm thick pad plate was bonded to the socket end. The inner and outer diameters of the pad plate were 610 mm and 730 mm, respectively.

(2) Test setup

Figures 1 and 2 show the schematic diagram and actual picture of the test setup. Three test pipes were connected in a straightline. One end of the assembly was fixed to a reaction wall, while the other end was connected to loading jacks. The jacks applied force parallel to the axial direction of the pipe, with the combined force centered on the pipe.

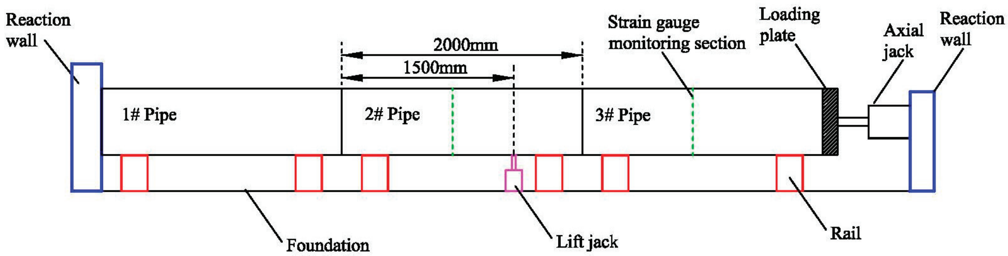

Figure 1. Schematic diagram of the test.

Figure 2. The actual test picture.

Moreover, 1# pipe was restrained by the reaction wall, limiting its vertical displacement. In addition to this, 3# pipe was connected to an axial jack. Joint deflection was achieved by raising a jack positioned beneath 2# pipe. During testing, 2# pipe was deflected relative to pipes 1# and 3#, by the jack beneath it. Subsequently, the axial jack at the end of 3# pipe applied the jacking force, simulating the axial force conditions during curved pipe jacking construction.

The pipe joint deflection test setup is shown in Figure 3. The distance between the centerline of the jacking jack and 1# pipe joint was maintained at 1500 mm throughout the test. When the jacking jack extended by Δh, the pipe 2# was deflected upwards by an angle of θ/2. Due to the constraint imposed by the joint between pipes 2# and 3#, alongside the proximity of the jacking jack to the pipe 3# joint, pipe 2# lifted upwards as pipe 3# was deflected upwards by θ/2. Consequently, the relative deflection angle between pipes 2# and 3# was θ.

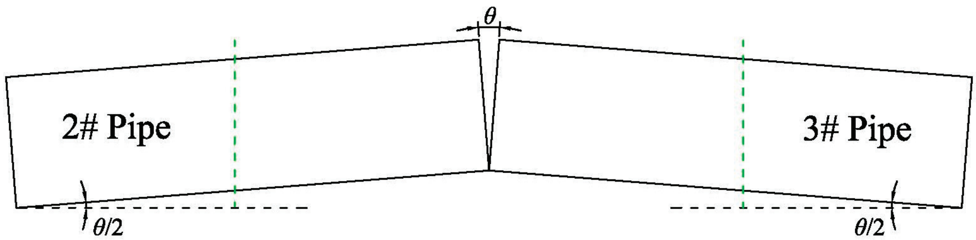

Figure 3. Pipe joint deflection in the test.

To monitor axial force changes in the pipe sections at different stages, strain gauges were affixed to the middle of the inner wall of pipes 2# and 3#. The gauges were positioned to ensure that the direction of the tensile stress was parallel to the axial direction of the pipe sections. Each monitoring section had eight strain gauges, evenly distributed along the circumference and numbered 1–8, as depicted in Figure 4. The static stress–strain test and analysis system acquired and stored real-time strain data from the gauges.

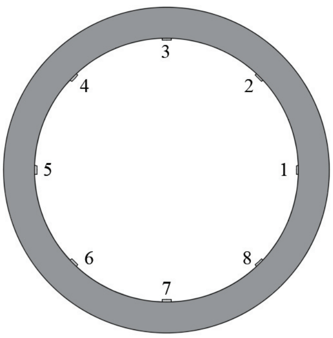

Figure 4. Schematic diagram of pipe strain measurement point locations.

Figure 1 presents a schematic diagram of the test setup. Three test pipes were connected in a straightline. One end was fixed to a reaction wall, while the other end was connected to loading jacks. The jacks applied force parallel to the pipe's axial direction, with the combined force centered on the pipe. During testing, 1# pipe was restrained by the reaction wall, restricting its vertical movement. Additionally, 3# pipe was connected to an axial jack, and joint deflection was achieved by raising a jack positioned beneath 2# pipe. This configuration simulated the axial force state during curved pipe-jacking construction.

The pipe joint deflection test setup is detailed in Figure 2. The distance between the jacking jack's centerline and the pipe 1# joint was maintained at 1500 mm throughout the test. When the jacking jack extended by Δh, 2# pipe was deflected upwards by an angle of θ/2. Due to the joint constraint between pipes 2# and 3# and the proximity of the jacking jack to the pipe 3# joint, 2# pipe lifted upwards as 3# pipe was deflected by θ/2. This resulted in a relative deflection angle of θ between pipes 2# and 3#.

During testing, the jacking jack lifted 2# pipe by 26 mm, resulting in a deflection angle θ/2 of 1.0°. Subsequently, the main jack applied axial loads of 50 kN, 100 kN, 150 kN, 200 kN, and 250 kN to the socket end of the pipe 3# section in sequence.

(3) Test steps

The test procedure followed these steps:

(i) With the axial jack unloaded, the jacking jack was activated, and the jacking displacement was set. Once the set value was reached, 2# pipe was lifted 26 mm upwards, and the jacking jack extension was maintained;
(ii) The axial jack was activated, extending and gradually making contact with the end of 3# pipe. The jacking force was increased to 50 kN and held for 60 s, while strain data were collected;
(iii) The axial jack load was controlled and then incrementally increased to 100 kN, 150 kN, 200 kN, and 250 kN, with a 60 s hold at each load level for strain data collection;
(iv) The axial jack and jacking jack were fully unloaded, restoring the pipe joint deflection angle to 0°.

2.2. FEM Numerical Simulation

(1) Pipe model

To further investigate the influence of varying joint deflection angles on pipe stress, a three-dimensional pipe model was constructed using the ABAQUS simulation software, with 14,544 continuum 3D 8-node reduced integration (C3D8R) elements and 4776 2-node 3D truss (T3D2) elements, as shown in Figure 5. The dimensions of the pipes and the wooden cushion plate in the model matched those used in the physical test.

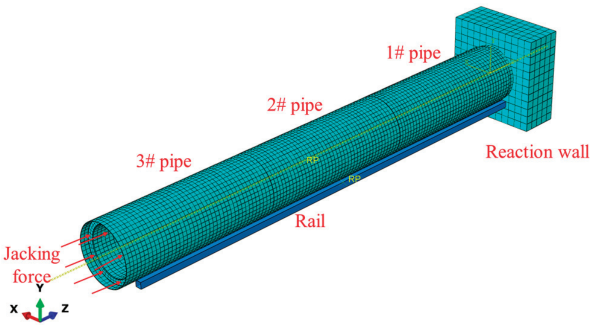

Figure 5. A 3D finite element model of the pipes.

In the model, the reaction wall and rail restrained the movement in three directions. The end of pipe #1 was constrained to simulate its connection to the reaction wall. The contact pairs between the rail and the outer surface of the pipe was established. Deflection was achieved by applying an upward displacement at pipe joint #2, incrementally deflecting it upwards by 0.5°, 1.0°, 1.5°, 2.0°, 2.5°, and 3.0° around the socket end. At each deflection angle, axial loads equivalent to 50 kN, 100 kN, 150 kN, 200 kN, and 250 kN, were sequentially applied to the end of pipe joint #3.

(2) Material parameters

The concrete used to make the pipe was modeled with a modulus of elasticity of 34,500 MPa, a density of 2400 kg/m^3, and a Poisson's ratio of 0.2. The concrete damage plasticity (CDP) model was employed within the ABAQUS software and the parameters were the same as applied by Younis et al. [18].

The steel reinforcement and steel collar were modeled using an elastic model, with a modulus of elasticity of 200,000 MPa, a density of 7850 kg/m^3, and a Poisson's ratio of 0.3. The wooden mat boards were also modeled using an elastic model, with a modulus of elasticity of 100 MPa, a density of 600 kg/m^3, and a Poisson's ratio of 0.2.

(3) Validation of simulation results

To ensure the accuracy of the numerical simulation results, the simulated pipe strain under a joint deflection of 1.0° was compared with the experimental results, as shown in Figure 5. The figure demonstrates that the distribution of the strain in the simulation closely matches that of the test across the range of applied axial loads, indicating that the numerical simulation accurately reflects the changes in pipe joint forces observed in the physical test.

As shown in Figure 6a, when the axial load on pipe #2 is less than 150 kN, the compressive strain at the top and bottom are greater in the simulation results, while the compressive strain at points 6 and 8 are relatively smaller. In contrast, the compressive strain at each point in the test is more uniform. Once the axial load reaches 200 kN, the compressive strain at points 1, 2, 4, and 5 in the simulation results increases rapidly, with the compressive strain at the bottom approaching zero. During the test, the changes in compressive strain at these points is generally smaller than in the simulation, and the compressive strain at the bottom remains around 20 με.

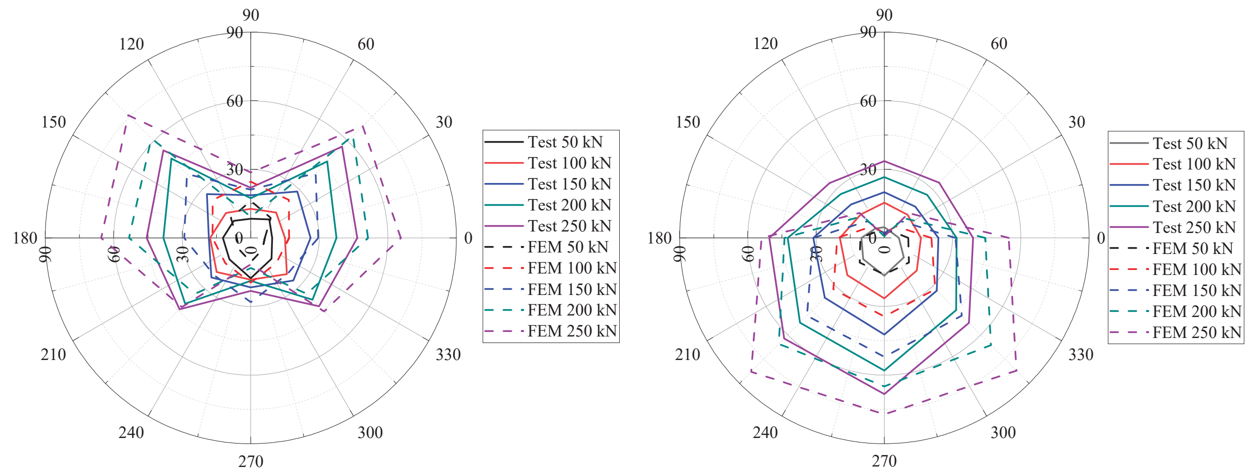

(**a**) Pipe 2# deflection at 1.0°. (**b**) Pipe 3# deflection at 1.0°.

Figure 6. Experimental and numerical simulation of pipe strain distribution (unit: με).

Figure 6b reveals a more pronounced eccentric strain phenomenon in the simulation results for pipe #3. The compressive strain at the top approaches zero and the compressive strain at the bottom is generally larger than the experimental values.

3. Analysis of the Numerical Simulation Results

3.1. Effect of Jacking Force on Axial Stress Distribution in Pipes

To illustrate the effect of the jacking force on the axial stress distribution, the numerical simulation results with a pipe deflection angle of 1.5° and axial jacking force of 50 kN and 250 kN were analyzed. Figure 7 presents cloud diagrams illustrating the distribution of axial stress in pipe #3 and pipe #2 under the different axial loads.

Figure 7a,c shows that as the axial jacking force increases, the area of compressive stress concentration at the end of pipe #3 expands significantly, and the maximum compressive stress increases substantially from 5.1 MPa to 15.1 MPa. In Figure 7b,d, the diagonal compressive area in the pipe #2 section also enlarges with increasing axial stress, accompanied by a significant increase in the maximum compressive stress. These findings indicate that, under a constant deflection angle, increasing axial loads enlarge the contact area between the pipe joints, thereby mitigating compressive stress concentration.

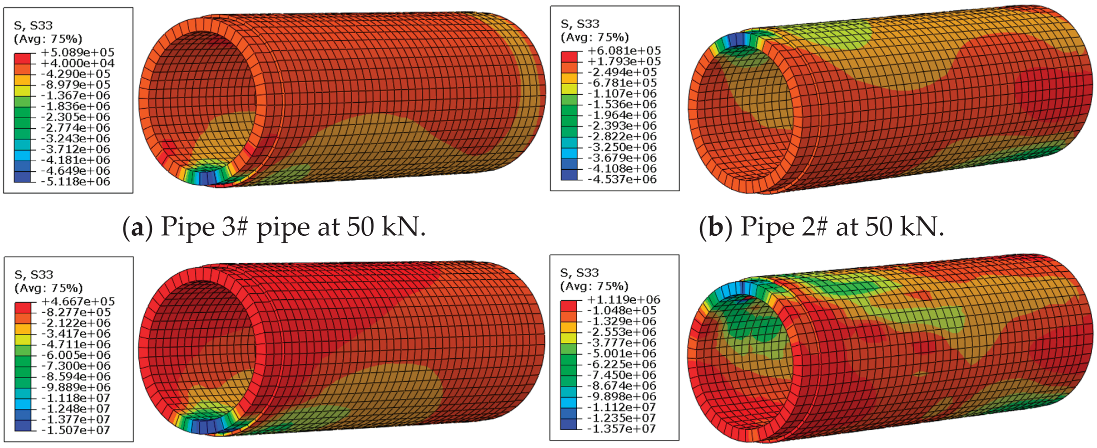

(**a**) Pipe 3# pipe at 50 kN. (**b**) Pipe 2# at 50 kN.

(**c**) Pipe 3# pipe at 250 kN. (**d**) Pipe 2# at 250 kN.

Figure 7. Axial stress distribution in pipe joints under different axial loads (unit: Pa).

3.2. Effect of Deflection Angle on Axial Stress Distribution in Pipes

To examine the effect of the deflection angle on the axial stress distribution, the axial stresses in pipe #2 and pipe #3 were analyzed under varying deflection angles at an axial jacking force of 150 kN, as shown in Figure 8.

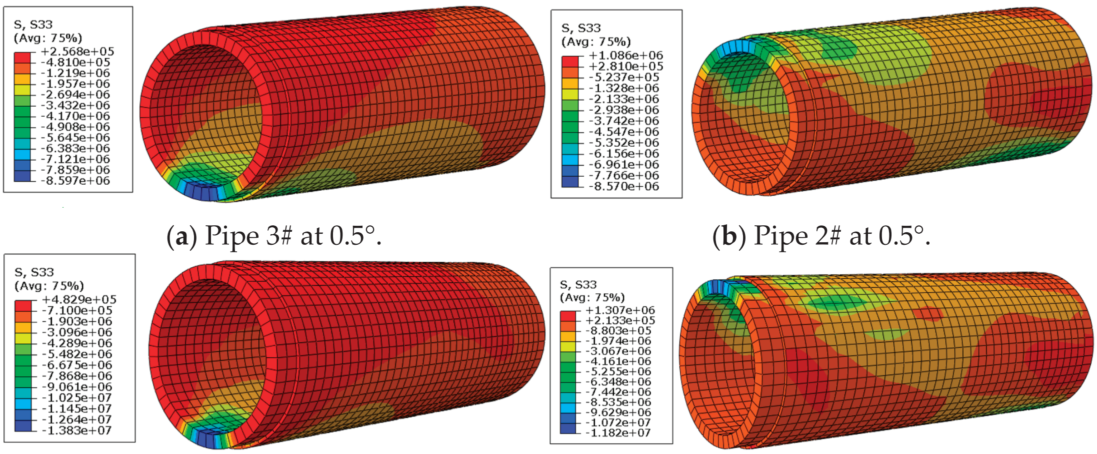

(**a**) Pipe 3# at 0.5°. (**b**) Pipe 2# at 0.5°.

(**c**) Pipe 3# at 2.5°. (**d**) Pipe 2# at 2.5°.

Figure 8. Axial stress distribution at the pipe joints under different deflection angles (unit: Pa).

In Figure 8a,c, after the relative deflection in terms of pipes 3# and 2#, the pipe 3# section experiences eccentric compression, with a significant concentration of compressive stress in the bottom area of the joint. This stress concentration extends backwards, along the pipe body. In contrast, the compressive stress in the upper part of the pipe is significantly reduced, and tensile stress may even occur. As the deflection angle increases, the area of compressive stress concentration at the joint decreases, but the maximum compressive stress increases notably, from 8.6 MPa at 0.5° to 13.8 MPa at 2.5°. Simultaneously, the tensile area above the pipe expands backwards, along the pipe body, and the maximum tensile stress also increases, from 0.26 MPa at 0.5° to 0.48 MPa at 2.5°.

Figure 8b,d reveals that, due to the constraint on the vertical displacement of the pipe 1# section, the pipe 2# section experiences diagonal compression after deflection. Compressive stress concentration areas emerge at the top and bottom of both ends of the pipe. The stress distribution in the pipe 2# section is complex, with multiple tensile stress zones appearing. The maximum tensile stress reaches 1.3 MPa when the deflection angle is 2.5°.

3.3. Plastic Strain Analysis of the Pipes

The concrete material in the numerical simulation model was assigned a plastic damage constitutive model to assess the degree of pipe damage due to loading. Figure 9 illustrates the distribution of inelastic strain in pipe joints under various deflection angles, when subjected to an axial jacking force of 250 kN. For reference, the direction facing the right side of the loading direction is designated as 0° azimuth, with the counterclockwise azimuth angle increasing (as depicted in Figure 9a). The strain cloud exhibits approximate symmetry at about 90° and 270° of the pipe circumference.

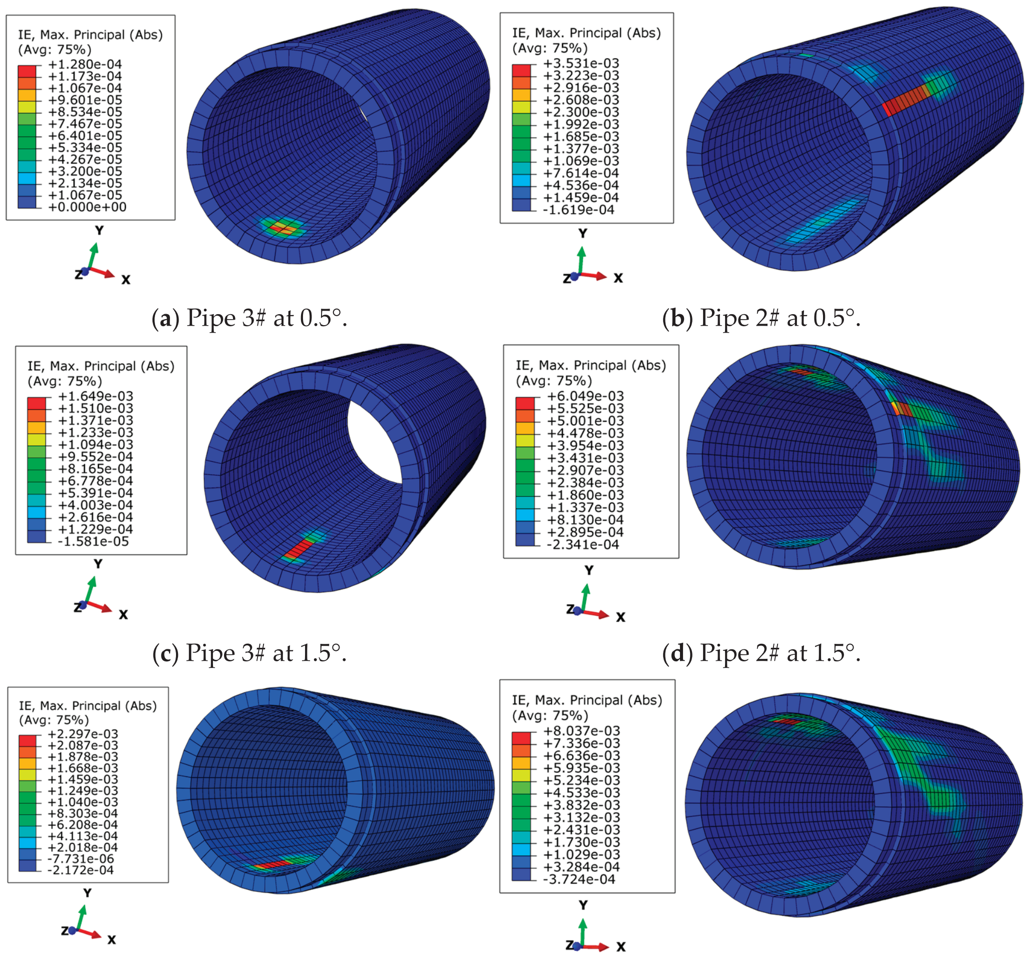

(**a**) Pipe 3# at 0.5°. (**b**) Pipe 2# at 0.5°.

(**c**) Pipe 3# at 1.5°. (**d**) Pipe 2# at 1.5°.

(**e**) Pipe 3# at 2.5°. (**f**) Pipe 2# at 2.5°.

Figure 9. Plastic strain distribution at the pipe joints under different deflection angles.

At a deflection angle of 0.5°, inelastic strain areas emerge on the inner wall of the joint at 90° and 270° in pipe section #2. Long strip-shaped inelastic strain concentration areas develop on the outer wall of the joint at approximately 30° and 150°, with a maximum inelastic strain of about 3531 με. When the deflection angle increases to 1.5°, the inelastic strain areas at 90° and 270° expand, while the long strip-shaped strain concentration areas on the outer wall do not extend along the pipe body but spread towards the lower area. The maximum inelastic strain at this stage is approximately 6049 με. Upon reaching a deflection angle of 2.5°, the extent of the previous inelastic strain areas expands considerably, showing a tendency to connect and rapidly extend along the pipe body. The maximum inelastic strain at this point reaches 8037 με.

The inelastic strain in pipe #3 initially emerged near the inner wall of the socket end at 270°, forming a peach-shaped strain concentration area, with a maximum inelastic strain of approximately 128 με. When the deflection angle increased to 1.5°, this area developed into a long strip, extending along the inner wall of the pipe section. Concurrently, inelastic strain areas appeared near the outer wall of the socket end at 225° and 315°, with a maximum strain of about 1649 με. With a further increase in the deflection angle to 2.5°, the elongated strain concentration area at the 270° inner-wall position continued to extend and new inelastic strain zones emerged on both sides, reaching a maximum inelastic strain of approximately 2297 με.

As indicated in the CDP model, the peak compressive strength of the concrete is reached at an inelastic strain of 676 με. This implies that yielding has already occurred in the pipe joints under most of the aforementioned conditions. For the pipe 2# section, the stress state is notably inferior to that of the pipe 3# section, resulting in a larger yield region. The inelastic strain in the inner wall at 90° and 270°, as well as the outer wall at 30° and 150°, exceeds the yield strain. For the pipe 3# section, yielding first appears on the inner wall on the side experiencing eccentric strain, making it susceptible to compressive damage in that location.

4. Conclusions

In this study, a combined approach involving model tests and numerical simulations was employed to comprehensively analyze the strain distribution in pipes subjected to varying deflection angles and axial jacking forces during curved pipe jacking. The experimental observations revealed distinct stress states in different pipe sections. In the pipe 3# section, a state of eccentric strain was observed, characterized by higher compressive strain in the lower part, compared to the corresponding upper part. Furthermore, as the deflection angle increased, the closing circle representing the strain values shifted downwards. This shift suggests a redistribution of stresses within the pipe section, highlighting the dynamic nature of stress distribution in curved pipe-jacking scenarios.

The pipe 2# section exhibited a more complex stress state, identified as diagonal compression. This was evidenced by the occurrence of extreme compressive strain values at specific orientations, namely 45° and 135°. The complex nature of diagonal compression underscores the importance of considering multiple stress components when assessing the structural integrity of pipes in curved configurations.

The numerical simulations provided further insights into the inelastic strain behavior of the pipes. The pipe 2# section, subjected to diagonal compression, displayed inelastic strain on both the inner and outer walls at specific orientations. Specifically, inelastic strain emerged on the inner wall at 90° and 270° and on the outer wall at 30° and 150°. This distribution of inelastic strain suggests that the pipe section is susceptible to damage at multiple locations under diagonal compression.

Conversely, the pipe 3# section, experiencing eccentric compression, showed inelastic strain predominantly on the inner wall, particularly on the side exposed to eccentric strain. This observation indicates a higher vulnerability to localized damage in this region due to the concentration of stress.

The study also revealed a clear relationship between the magnitude of the axial load and the potential for damage. With increasing axial loads, the risk of localized stress damage on the inner wall of the pipe 3# section intensified, especially on the side subjected to eccentric stress. Additionally, the pipe 2# section faced a dual threat of both localized stress damage and diagonal shear damage, underscoring the importance of considering combined loading effects in curved pipe-jacking design and analysis.

Author Contributions: Methodology, Y.H.; Software, Z.S. and B.Z.; Validation, Z.S.; Formal analysis, X.W.; Investigation, J.C. and X.L.; Resources, X.L.; Data curation, J.C., B.Z., L.C. and X.W.; Writing—original draft, Y.H.; Writing—review & editing, P.Z.; Visualization, L.C.; Supervision, P.Z. All authors have read and agreed to the published version of the manuscript.

Funding: This research was funded by the Science and Technology project of State Grid ShanDong Electric Power Company: Optimization Design Research on Large Diameter Curved Electric Power Pipe Jacking and Standardization of Pipe Structure (No. 520632230007).

Data Availability Statement: All data that support the findings of this study are available from the corresponding author upon reasonable request.

Conflicts of Interest: Authors Yongjun He, Bin Zhang, Li Chen and Xiaoli Wang were employed by the State Grid ShanDong Electric Power Company of Construction Company. Authors Jian Cheng and Xi Li were employed by the State Grid ShanDong Electric Power Company. The remaining authors declare that the research was conducted in the absence of any commercial or financial relationships that could be construed as a potential conflict of interest.

References

1. Chen, J.Z. Analysis the Force of Glass Fiber Reinforced Plastics Jacking Pipe Joints. Ph.D. Thesis, Wuhan University of Technology, Wuhan, China, 2010.
2. Jin, W.H. Analysis and Research on Long Distance Curve Pipe Jacking Technology. Ph.D. Thesis, Zhejiang University, Hangzhou, China, 2005.
3. Zhao, Z.F.; Shao, G.H. Stability analysis of wall stability of steel pipe in pipe-jacking and optimization of proper wall thickness. *Eng. J. Wuhan Univ.* **2011**, *44*, 481–486.
4. Chen, Z. Precise Solution to the Elastic Stresses in a Round Pipe Jacked into Soft Soils and Its Applications. *Spec. Struct.* **2005**, *22*, 66–69.
5. Zhu, H.H.; Wu, J.B.; Pan, T.Y. Theoretical analysis of three-dimensional mechanical model of curved pipe jacking and its application. *Chin. J. Geotech. Eng.* **2003**, *25*, 492–495.
6. Milligan, G.W.E.; Norris, P. Site-based research in pipe jacking-objectives, procedures and a case history. *Tunn. Undergr. Space Technol.* **1996**, *11*, 3–24. [CrossRef]
7. Pan, T.Y. Research on Mechanical Analysis and Monitoring Technology of Large Diameter Sharp Curve Jacking Pipe Construction. Ph.D. Thesis, Tongji University, Shanghai, China, 2000.
8. Wei, G.; Xu, R.Q.; Yu, J.Y. Site-based experimental study on pipe behavior during pipe jacking. *Rock Soil Mech.* **2005**, *26*, 1273–1277.
9. Yang, X. Research of Large Diameter Jacking-Pipes with Small Space in Pipe-Roof Pre-Construction Method. Ph.D. Thesis, Central South University, Changsha, China, 2012.
10. Huang, J.L.; Chen, J.J.; Wang, J.H.; Fang, W. Numerical Analysis of Large Diameter Pipe-Jacking. *Chin. J. Undergr. Space Eng.* **2008**, *4*, 489–493.
11. Pan, G.R.; Wei, F. Automatic guidance system for long-distance curved pipe-jacking. *KSCE J. Civ. Eng.* **2020**, *24*, 2505–2518. [CrossRef]
12. Choo, C.S.; Ong, D.E.L. Assessment of non-linear rock strength parameters for the estimation of pipe-jacking forces. Part 2. Numerical modeling. *Eng. Geol.* **2020**, *265*, 105405. [CrossRef]
13. Zhou, K.; Ni, Q.; Chen, W.; Dai, H.; Hagedorn, P.; Wang, L. Static equilibrium configuration and nonlinear dynamics of slightly curved cantilevered pipe conveying fluid. *J. Sound Vib.* **2021**, *490*, 115711. [CrossRef]
14. Zhong, Z.; Li, C.; Liu, X.R.; Xiong, Y.; Fan, Y.; Liang, N. Assessment of experimental friction parameters and contact property of pipe string for the estimation and verification of a solution for pipe stuck in the China's first rock pipe jacking. *Tunn. Undergr. Space Technol.* **2021**, *107*, 103671. [CrossRef]
15. Zhang, P.; Zhang, Y.; Ariaratnam, S.T.; Ma, B.; Zeng, C.; Liu, K. Field monitoring and analysis of soil deformation of curved steel pipe jacking in Gongbei tunnel. *Tunn. Undergr. Space Technol.* **2023**, *138*, 105153. [CrossRef]
16. Zhou, H.; Huang, S.; Zhang, P.; Ma, B.; Ma, P.; Feng, X. Prediction of Jacking Force Using PSO-BPNN and PSO-SVR Algorithm in Curved Pipe Roof. *Tunn. Undergr. Space Technol.* **2023**, *138*, 105159. [CrossRef]
17. Zu, Y.; Wang, L.; Hu, Y.; Yang, G. CEEMDAN-LWT De-Noising Method for Pipe-Jacking Inertial Guidance System Based on Fiber Optic Gyroscope. *Sensors* **2024**, *24*, 1097. [CrossRef] [PubMed]
18. Younis, A.A.; Shehata, A.; Ramadan, A.; Wong, L.S.; Nehdi, M.L. Modeling structural behavior of reinforced-concrete pipe with single, double and triple cage reinforcement. *Eng. Struct.* **2021**, *240*, 112374. [CrossRef]

buildings

Article

Soil Displacement of Slurry Shield Tunnelling in Sandy Pebble Soil Based on Field Monitoring and Numerical Simulation

Jian Cui [1,2], Zhigang Yao [3,*], Tao Yu [3], Jianfeng Wang [3], Kaichen Ying [3], Bo Liu [1,2], Shu Zhu [4] and Xiaonan Yan [5]

1 Railway Engineering Research Institute, China Academy of Railway Sciences Co., Ltd., Beijing 100081, China; cj1333@my.swjtu.edu.cn (J.C.); liubo@rails.cn (B.L.)
2 National Key Laboratory of High Speed Railway Track System, Beijing 100081, China
3 School of Civil Engineering, Southwest Jiaotong University, Chengdu 610031, China; ytao1015@my.swjtu.edu.cn (T.Y.); wjf2019210118@my.swjtu.edu.cn (J.W.); kaichenying@my.swjtu.edu.cn (K.Y.)
4 State Grid Economic and Technological Research Institute Co., Ltd., Beijing 102209, China; zhushu@chinasperi.sgcc.com.cn
5 School of Civil Engineering, Chongqing Jiaotong University, Chongqing 400074, China; xiaonan2022@cqjtu.edu.cn
* Correspondence: bk20110739@my.swjtu.edu.cn; Tel.: +86-182-0028-3326

Abstract: Due to its inherent advantages, shield tunnelling has become the primary construction method for urban tunnels, such as high-speed railway and metro tunnels. However, there are numerous technical challenges to shield tunnelling in complex geological conditions. Under the disturbance induced by shield tunnelling, sandy pebble soil is highly susceptible to ground loss and disturbance, which may subsequently lead to the risk of surface collapse. In this paper, large-diameter slurry shield tunnelling in sandy pebble soil is the engineering background. A combination of field monitoring and numerical simulation is employed to analyze tunnelling parameters, surface settlement, and deep soil horizontal displacement. The patterns of ground disturbance induced by shield tunnelling in sandy pebble soil are explored. The findings reveal that slurry pressure, shield thrust, and cutterhead torque exhibit a strong correlation during shield tunnelling. In silty clay sections, surface settlement values fluctuate significantly, while in sandy pebble soil, the settlement remains relatively stable. The longitudinal horizontal displacement of deep soil is significantly greater than the transverse horizontal displacement. In order to improve the surface settlement troughs obtained by numerical simulation, a cross-anisotropic constitutive model is used to account for the anisotropy of the soil. A sensitivity analysis of the cross-anisotropy parameter α was performed, revealing that as α increases, the maximum vertical displacement of the ground surface gradually decreases, but the rate of decrease slows down and tends to level off. Conversely, as the cross-anisotropy parameter α decreases, the width of the settlement trough narrows, improving the settlement trough profile.

Keywords: shield tunnelling; field monitoring; numerical simulation; surface settlement; horizontal displacement of deep soil; cross-anisotropy

1. Introduction

When constructing subways and high-speed railways, tunnels are typically used to traverse urban areas. Due to its construction advantages, shield tunnelling is commonly selected as the preferred method for building these urban tunnels [1]. However, as more cities join the wave of subway and high-speed railway construction, the engineering geological conditions the tunnels must navigate through are becoming increasingly complex, presenting numerous engineering challenges that urgently need to be addressed [2,3]. In China, these challenges include the collapsible loess layer encountered during the construction of the Xi'an Metro [4–6]; the composite strata with varying hardness faced in the metro and high-speed rail projects in cities like Guangzhou, Shenzhen, and Qingdao [7–9]; the peat soils in Kunming; the highly abrasive cobble layers in the river-crossing metro projects in Wuhan and Nanjing; and the sandy pebble soils encountered in the metro and high-speed rail constructions in Beijing and Chengdu [10,11]. Sandy pebble soil can be considered an extremely heterogeneous and loose geotechnical system consisting of a mixture of coarse and fine particles [12]. When tunnelling through this type of soil with a shield machine, the disturbances induced can lead to rock mass deformation and ground settlement, making it difficult to control the settlement magnitude and rate. Sandy pebble soil layers are widespread in Southwest China and the North China Plain [13], characterized by large voids between particles, a lack of cohesion, and high sensitivity. In the Beijing area, the spaces between the sandy pebbles are filled with fine sand, clay, and other small particles, resulting in a dense structure with localized cementation. This gives the soil high overall strength, making cutting tools more prone to wear, complicating shield tunnelling, and increasing the likelihood of disturbances to the surrounding strata.

In shield tunnelling-induced ground disturbances, the magnitude and distribution patterns of ground deformation have consistently been a focus of interest among tunnel research scholars. Engineering practice indicates that even with the most advanced shield tunnelling techniques, ground disturbances during excavation are unavoidable. These disturbances lead to stress redistribution, which in turn induces ground settlement and can impact the normal functioning of surrounding buildings and structures. Accurately predicting ground settlement patterns and assessing their impacts is of significant engineering importance for the planning, design, and construction of shield tunnels.

Numerous scholars have conducted a series of studies related to shield tunnelling in sandy pebble soil. Taking the launching section of a tunnel in the Chengdu Metro as the engineering background, Yang [14] conducted a preliminary exploration of slurry shield construction techniques in sandy pebble soil and analyzed the adaptability of the cutterhead and the reasons for excessive ground settlement. Zhang and Chen [15] focused on the water-rich sandy pebble soil in Beijing, analyzing the structural characteristics of various types of shield machines. They investigated the relationships between shield types and soil permeability, clay content, and particle size distribution. Zhao et al. [16] conducted a study on the surface settlement patterns during large-diameter slurry shield tunnelling in sandy pebble soil, but they primarily focused on the impact of tunnelling parameters on slurry shield construction, without providing a systematic analysis of ground deformation. Xu et al. [17] conducted a study on micro-disturbances induced by shield tunnelling and the corresponding control methods in sandy pebble soil. Compared with silty clay layers, they found that shield tunnelling in sandy pebble soil causes greater settlement and more significant disturbances to the ground. Moeinossadat et al. [18] demonstrated that surface settlement in sandy pebble soil is closely related to various shield tunnelling parameters, with grouting filling rate and grouting pressure identified as the most influential factors. Liang and Bai [19] focused on ground deformation control during shield tunnelling in sandy pebble soil, in their study of the new Line 17 of the Beijing Metro, the tunnel of which crosses above a water conveyance tunnel. Through field monitoring and numerical simulation, they investigated the optimal tunnelling parameters, deformation patterns, and control methods for shield tunnelling in this complex geological condition. Li et al. [11] studied the water ingress mechanisms and impacts during shield tunnelling in sandy pebble soil. Du et al. [20] proposed a composite analysis method to simulate tunnel excavation in sandy pebble soil. Their multi-scale analytical approach offers high efficiency in simulating tunnel excavation in sandy pebble layers without compromising accuracy in loose material representation.

Research on the movement and deformation patterns induced by shield tunnelling is quite advanced, but most studies focus on earth pressure balance shields and soft clay layers. There is relatively limited research on the deformation patterns and control methods for slurry shield tunnelling in sandy pebble soils, and field measurement data for shield excavation in such conditions are particularly scarce. This study uses the Tsinghuayuan

Tunnel of the Beijing–Zhangjiakou High-Speed Railway as a case background to explore and analyze the ground disturbance induced by large-diameter slurry shield tunnelling in sandy pebble soil through field tests and numerical simulations. A correlation analysis was conducted on the main tunnelling parameters during the excavation process of the shield in both silty clay and sandy pebble soil. Sensors were installed on-site to monitor surface settlement and deep soil horizontal displacement, providing a substantial amount of valuable field data, particularly for deep soil horizontal displacement. Three-dimensional numerical simulations were conducted to analyze the ground disturbance caused by shield tunnelling. Optimized simulations of the transverse settlement trough were performed, yielding more accurate inversion results.

This paper is organized as follows. The background of the research is introduced in Section 1, including the discussions of the engineering background and shield tunnelling in sandy pebble soil. A brief introduction of the settlement principle induced by tunnelling is presented in Section 2. The research project is described in Section 3, including project overview and geological conditions, which provides basic data for this research. Field monitoring including tunnelling parameters, surface settlement, and horizontal displacement of deep soil, is described in Section 4 to contextualize the soil displacement induced by shield tunnelling. A numerical simulation of shield tunneling-induced soil displacement, especially for the optimized simulations of the transverse settlement trough, is presented in Section 5. Finally, some concluding remarks are offered in Section 6. The results of this study are useful in analyzing shield tunnelling-induced ground disturbance in sandy pebble soil in China and globally and represent an original contribution to the field measurement and numerical simulation analysis of large-diameter slurry shield tunnelling in sandy pebble soil.

2. Brief Introduction of Settlement Induced by Tunnelling

Tunnel construction will cause the relaxation of in situ stress and lead to the movement of soil to the formed hole, leading to deformation of the surrounding strata and generating pressure on the lining. The typical green field surface settlement trough related to tunnel excavation is depicted in Figure 1. It should be noted here that the green field condition refers to the surface deformation caused by tunnel excavation only, without other factors. According to Mair and Taylor [21], the components of ground movements can be listed as follows:

(a) Deformations of the ground towards the face caused by stress relief.
(b) Radial ground movements caused by over-cutting and ploughing.
(c) Tail void, i.e., the gap between the tail skin of the TBM (tunnel-boring machines) and the installed lining.
(d) Deflection of the lining with the development of ground loading. Consolidation settlement due to the changes in water pressure in the ground to their long-term equilibrium values.

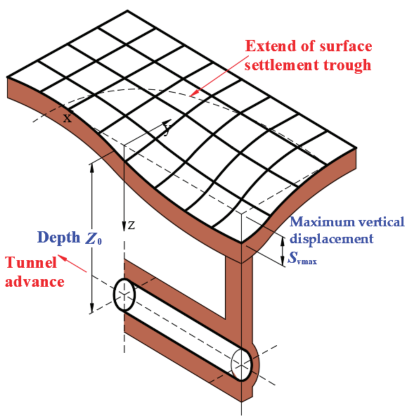

Figure 1. Ground movements induced by tunnelling.

It is obvious from Figure 1 that tunnelling is a three-dimensional problem. It is therefore necessary to consider a three-dimensional effect for both analytical and numerical convenience.

There have been many studies on the disturbance and movements of surrounding strata induced by tunnel excavation. Peck [22] first proposed an empirical Gaussian distribution curve to describe this transverse settlement trough. It is described by the following error function (geometrical details of the parameters are shown in Figure 2):

$$S_v(x) = S_{v\max} \cdot \exp\left(-\frac{x^2}{2i^2}\right) \tag{1}$$

where S_v is the vertical displacement; $S_{v\max}$ is the maximum vertical soil settlement at the centerline of the tunnel; x is the horizontal offset from the tunnel centerline; and i is the horizontal distance from the centerline to the location of the inflexion point.

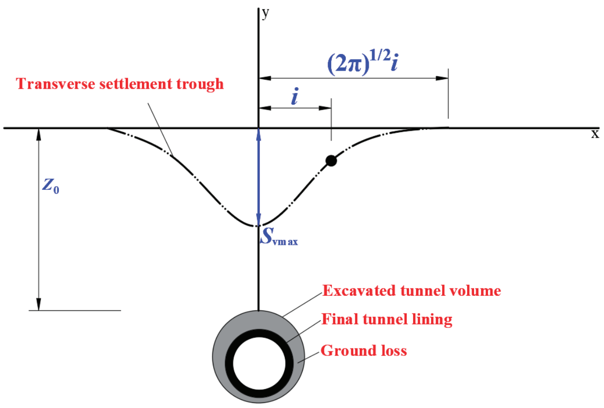

Figure 2. Settlement troughs defined by Gaussian distribution curve after Peck [22].

In the process of tunnel excavation, in addition to the horizontal distribution of surface settlement, the longitudinal distribution of surface settlement is also particularly important. Attewell and Woodam [23] and Attewell et al. [24] proposed an empirical formula based on the Peck formula, which uses the error accumulation function to characterize the longitudinal distribution of surface settlement above the tunnel centerline, as shown in Equation (2):

$$\delta_z = \frac{V_s}{\sqrt{2\pi}i} \exp\frac{-x^2}{2i^2}\left[\Phi\left(\frac{y-y_i}{i}\right) - \Phi\left(\frac{y-y_f}{i}\right)\right] \tag{2}$$

where V_s is the volume of the transverse settlement trough per unit distance during tunnel excavation; y_i is the starting point of tunnel excavation; y_f is the location of the tunnel excavation face; and Φ is the standard normal function. Based on this, the empirical formula for surface settlement has been extended to three-dimensional situations.

3. Project Description

3.1. Project Overview

The Tsinghuayuan Tunnel of the Beijing–Zhangjiakou High-Speed Railway extends for a total length of 6020 m. Construction was carried out simultaneously using two slurry shield TBMs, each with an outer diameter of 12.64 m. The tunnel excavation is divided into two segments: 2#~1# Shield Section and 3#~2# Shield Section. It is located in the bustling urban area of Haidian District, Beijing, where buildings and structures are densely concentrated and highly complex. The construction also involved crossing multiple subway lines, municipal roads, and utility pipelines. The tunnel lining was assembled using a 6 + 2 + 1 segment arrangement, with an inner diameter of 11.1 m and an outer diameter of 12.2 m. The thickness of the segments is 0.55 m. The TBM is designed with a maximum excavation speed of 60 mm/min. The maximum thrust and torque are 160,850 kN and 26,118 kN·m, respectively.

3.2. Geological Conditions

The 3#~2# Shield Section was selected as the subject of this study, as shown in Figure 3. The geological conditions in this section are complex and variable: the launching shaft at 3# is relatively shallow, with the excavation cross-section consisting entirely of silty clay. As the depth of the overburden increases, the excavation cross-section gradually transitions to a sandy pebble soil composed of sand, silty clay, and pebble soil. The pebbly soil content is approximately 60%, characteristic of a typical soft upper layer and hard lower layer stratum. As observed in the geological profile in Figure 3, the launch section from DK18+200 to DK18+100 is primarily composed of silty clay. Beyond this segment, the excavation is predominantly in the sandy pebble soil. Within this section, the pebble-bearing stratum extends for 3700 m, with the tunnel-boring machine excavating entirely through the pebble stratum for a distance of 2400 m. The pebble stratum covers a significant proportion of the excavation, with pebbles measuring 2 cm to 6 cm in diameter accounting for over 60% of the material. The largest pebbles exceed 15 cm in diameter. A core sample from the pebble stratum is shown in Figure 4. Due to severe over-extraction of groundwater in the suburban areas of Beijing, the water table is in a state of negative balance, leading to a significant supply–demand conflict. Consequently, there is little to no groundwater in the soil layers being tunneled through. Therefore, the impact of groundwater is not considered in this study.

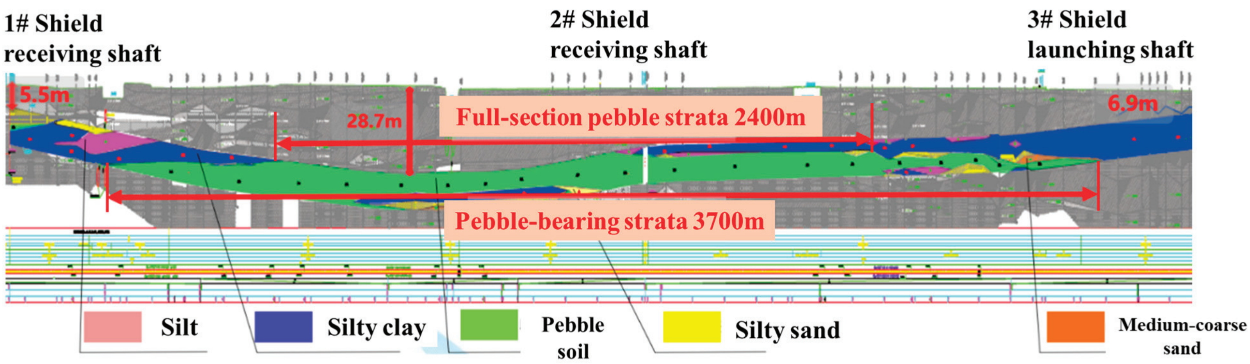

Figure 3. Geological profile of Tsinghuayuan shield tunnel.

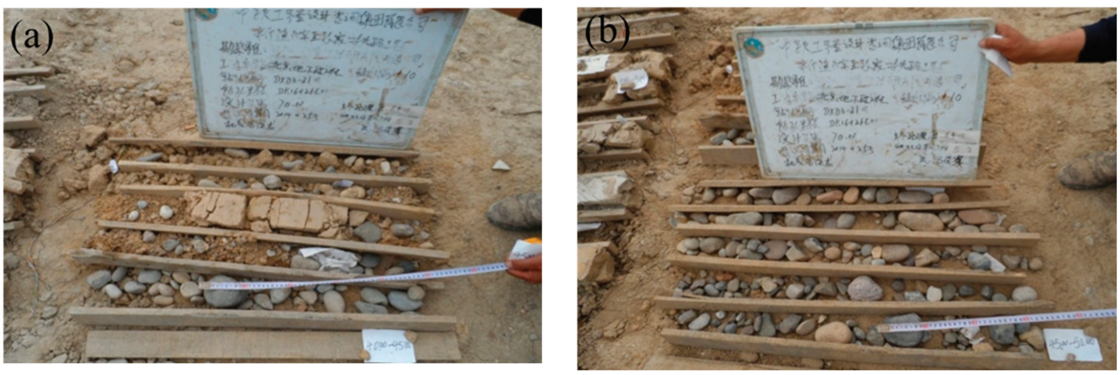

Figure 4. Core photos: (**a**) depth of 40–45 m; (**b**) depth of 45–50 m.

4. Field Monitoring

This section reports the ground disturbance caused by large-diameter slurry shield tunnelling based on field monitoring considering tunnelling parameters, surface settlement, and the horizontal displacement of the deep soil.

4.1. Monitoring Scheme

Referring to the plan and longitudinal section diagrams of the Tsinghuayuan Tunnel shield section, as well as the feasibility of field testing, an open area within the shield section was selected for the installation of field monitoring equipment. A series of typical monitoring cross-sections of the stratum were selected, as shown in Figure 5. The monitoring range extends from DK17+600 to DK17+700, with the arrangement of the monitoring cross-sections shown in Figure 6. Surface settlement monitoring points were placed every 10 m along the surface above the tunnel axis. Monitoring cross-sections of the transverse surface settlement trough were installed every 50 m, with 5 m spacing between the transverse monitoring points. Horizontal displacement monitoring points for the deep soil were arranged from DK17+680 to DK17+692, as shown in Figure 6c. The deep soil horizontal displacement monitoring equipment after installation is shown in Figure 7. The physical and mechanical indexes of each soil layer at the monitoring section DK17+650 are shown in Table 1.

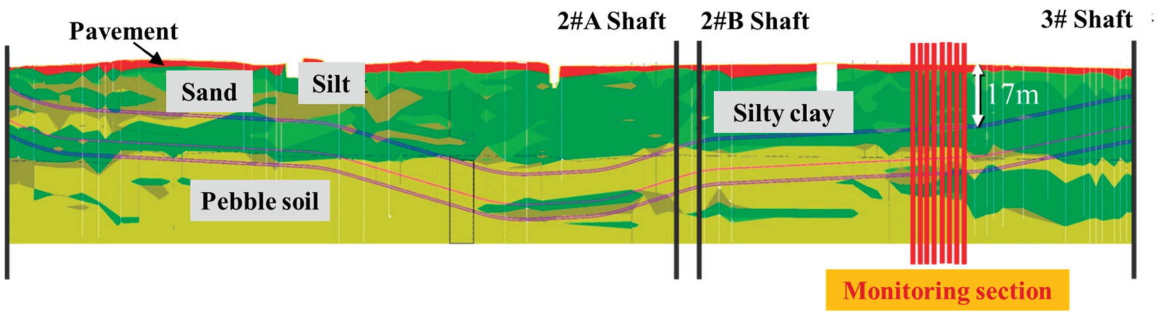

Figure 5. Typical strata monitoring section layout diagram.

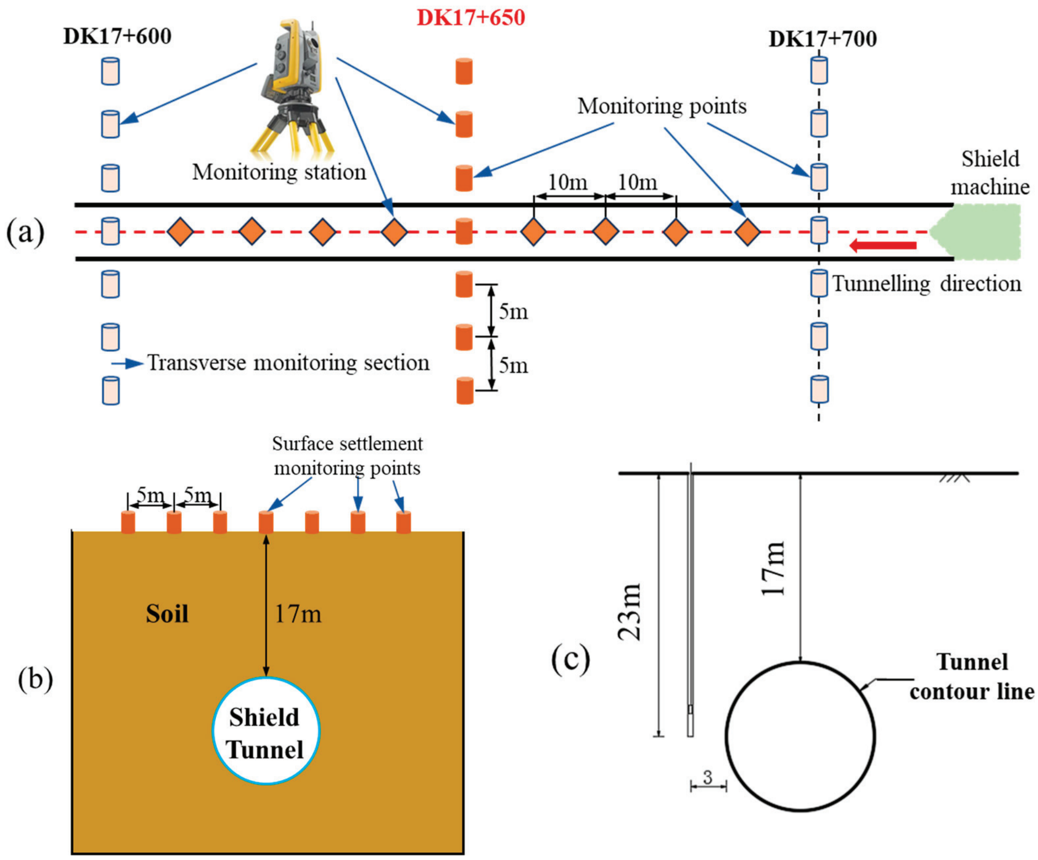

Figure 6. Distribution and arrangement of measuring points: (**a**) monitoring system of transverse surface settlement; (**b**) layout of surface settlement monitoring points; (**c**) layout of horizontal displacement.

Figure 7. Field test inclinometer.

Table 1. Physico-mechanical parameters of soil layers for the monitoring section.

Strata Layer	Bulk Density (kN/m^3)	Young's Modulus (Mpa)	Poisson's Ratio	Friction Angle (°)	Cohesion (kPa)
Pavement	25.0	1366.00	0.30		
Silt	20.1	41.25	0.30	25.2	14.3
Silty clay 1	19.9	37.00	0.30	18.4	33.8
Pebble soil	20.2	226.00	0.28	45.0	
Silty clay 2	20.0	38.00	0.30	19.6	36.0

4.2. Shield Tunnelling Parameters

The reasonable selection and control of tunnelling parameters are crucial for tunnelling efficiency, cutter wear management, cutterhead protection, and surface settlement control. To evaluate the tunnelling performance of the shield machine in the sandy pebble soil, the monitoring interval from ring 1 to ring 447 of the 3#~2# Shield Section was selected for statistical analysis. The main tunnelling parameters in the sandy pebble soil and silty clay strata—specifically, shield thrust, cutterhead torque, tunnelling speed, and slurry pressure—were analyzed. The time history of the variation in the key tunnelling parameters within the monitoring interval is shown in Figure 8.

Figure 8a shows the time history of the total thrust of the shield machine as it progresses during tunnelling. During the initial launching stage, the shield thrust fluctuated significantly within the first 70 rings, and then the fluctuation amplitude decreased. Under different geological conditions, the average total thrust of the shield increased from 33,632 kN in the silty clay section to 48,586 kN in the sandy pebble soil, representing a 44.46% increase. Since the shield operation remained generally stable, the significant change in total thrust can be primarily attributed to the variation in geological strata. In the sandy pebble soil, maintaining a stable shield tunnelling speed requires a higher thrust to overcome the resistance encountered during the excavation process.

Figure 8b shows the variation of the cutterhead torque with the progress of tunnelling under different geological conditions. The average cutterhead torque increased from 5.75 MN·m in the silty clay section to 8.42 MN·m in the sandy pebble soil, an increase of 46.43%. This increase is primarily due to changes in geological conditions rather than variations in the tunnelling process caused by operator actions. In the sandy pebble soil, the physical and mechanical properties of the strata become more complex, and the significant increase in pebble content raises the resistance that the tunnelling tools must overcome to break the surrounding rock. This results in a substantial increase in the torque required by the cutterhead during excavation.

The tunnelling speed and slurry pressure directly reflect the tunnelling efficiency of the shield. Figure 8c,d show the statistical time series of slurry pressure and tunnelling speed, respectively. The setting of slurry pressure is crucial for maintaining stable excavation at the tunnel face. As shown in Figure 8c, the slurry pressure typically ranges from 0.1 bar to 2.0 bar, which is approximately 12.5% to 23.6% of the peak slurry pressure. The slurry pressure in the silty clay is more stable compared to that in the sandy pebble soil. In the sandy pebble soil, the slurry pressure continuously increases. The trend of slurry pressure is steadily rising, which is closely related to the depth of cover and the variations in the soil layers at the tunnel face. Unlike slurry pressure, the average tunnelling speed decreases from 20.49 mm/min in the silty clay to 18.23 mm/min in the sandy pebble soil, representing a reduction of 11.03%. Reducing the tunnelling speed appropriately allows the cutter tools to fully break up the harder pebbles at the bottom, thereby effectively reducing the wear on the tools caused by large-sized pebbles.

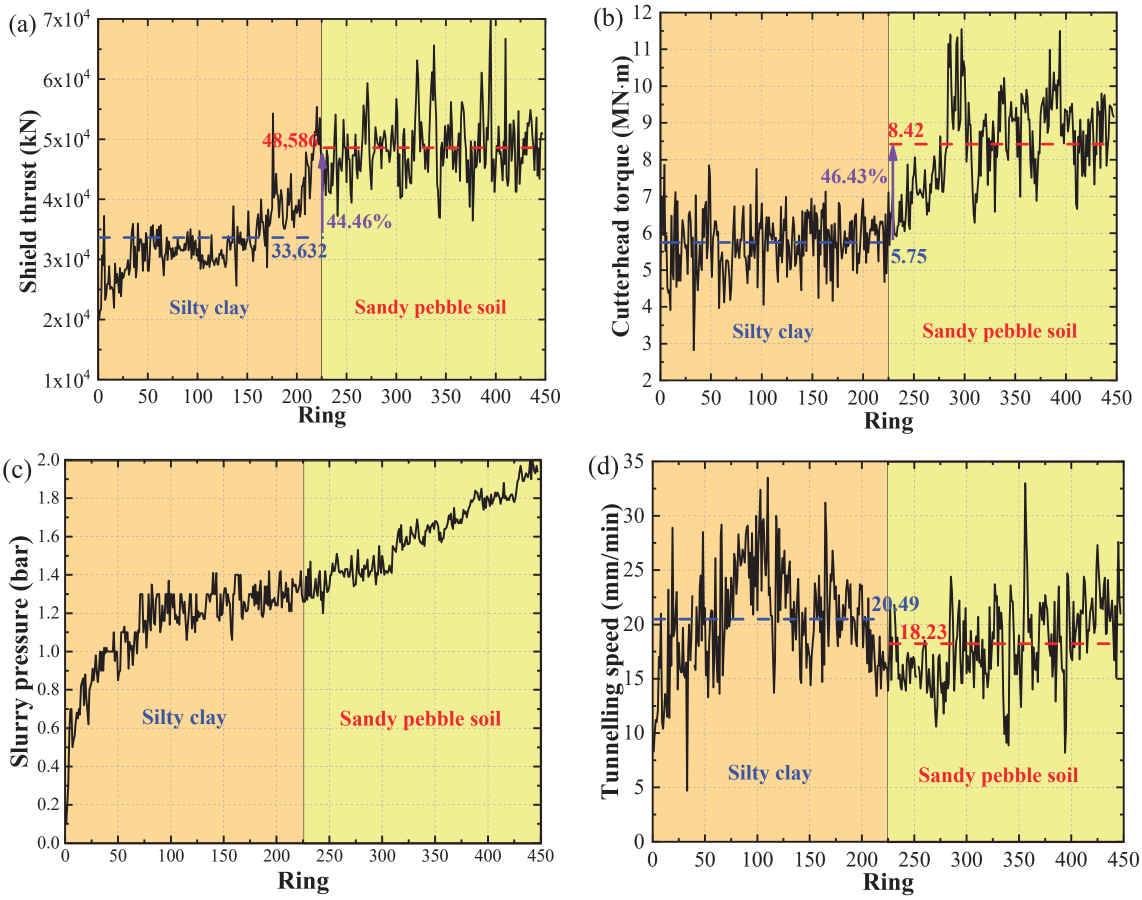

Figure 8. Main tunnelling parameters: (**a**) shield thrust; (**b**) cutterhead torque; (**c**) slurry pressure; (**d**) tunnelling speed.

A preliminary analysis of the shield tunnelling parameters was conducted using the correlation coefficient. Correlation is used to measure the degree to which two variables deviate from being independent of each other. The correlation coefficients among the four parameters of the slurry balance shield—slurry pressure, shield thrust, cutterhead torque, and tunnelling speed—are presented in Table 2.

Table 2. Correlation coefficients between tunnelling parameters.

Parameters	Slurry Pressure	Shield Thrust	Cutterhead Torque	Tunnelling Speed
Slurry pressure	1.0000	0.7726	0.7057	0.1459
Shield thrust	0.7726	1.0000	0.7019	−0.2377
Cutterhead torque	0.7057	0.7019	1.0000	−0.0558
Tunnelling speed	0.1459	−0.2377	−0.0558	1.0000

4.3. Surface Settlement Monitoring

The surface settlement trough induced by tunnel excavation typically resembles a Gaussian curve [22], meaning that the maximum surface settlement generally occurs directly above the tunnel axis. Figure 9 presents the surface settlement monitoring data collected from the Tsinghuayuan Tunnel's 3#~2# Shield Section. The transverse surface settlement trough follows a Gaussian normal curve, with the maximum settlement at the tunnel centerline and gradually diminishing on both sides. Due to ground reinforcement in the shield launching section, the settlement values are relatively small. In the normal tunnelling section, the maximum surface settlement values mostly range from 10 mm to 13 mm. Surface settlement is effectively controlled, with the maximum surface settlement value being approximately 24 mm.

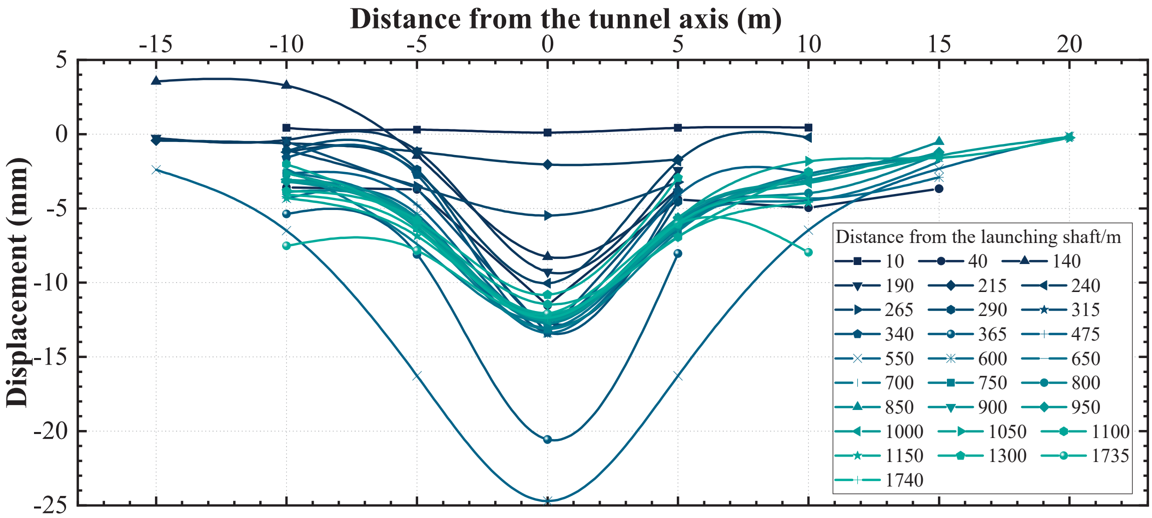

Figure 9. Transverse surface settlement troughs obtained from field measurements of the 3#~2# Shield Section of the Tsinghuayuan Tunnel.

4.4. Horizontal Displacement Monitoring of Deep Soil

Horizontal displacements at different depths in the soil surrounding the tunnel can be obtained by measuring the variation in the angle between the inclinometer axis and the vertical plumb line. When monitoring deep soil horizontal displacement, the bottom of the inclinometer casing is used as a fixed point, and the horizontal displacement of the soil is measured at 1 m vertical intervals using an inclinometer. To offset measurement errors, each inclinometer casing is measured twice in both the horizontal and vertical directions. The measurement frequency is determined based on the shield tunnelling and ring assembly progress. When the cutterhead of the shield machine is within 20 m of the monitoring section, data are recorded after the completion of each ring, continuing day and night without interruption. Once the shield cutterhead moves more than 20 m away from the monitoring section, the data measurement frequency is reduced.

As shown in Figure 10, the sign conventions for horizontal displacements are as follows: for the tunnel cross-section, displacements towards the axis of the tunnel are considered positive; for the longitudinal section, displacements in the direction of the shield tunnelling are considered positive. The horizontal relative displacements measured at the monitoring section relative to the inclinometer bottom are shown in Figure 11. The time history of the horizontal displacements in the deep soil during tunnelling is illustrated in Figure 12.

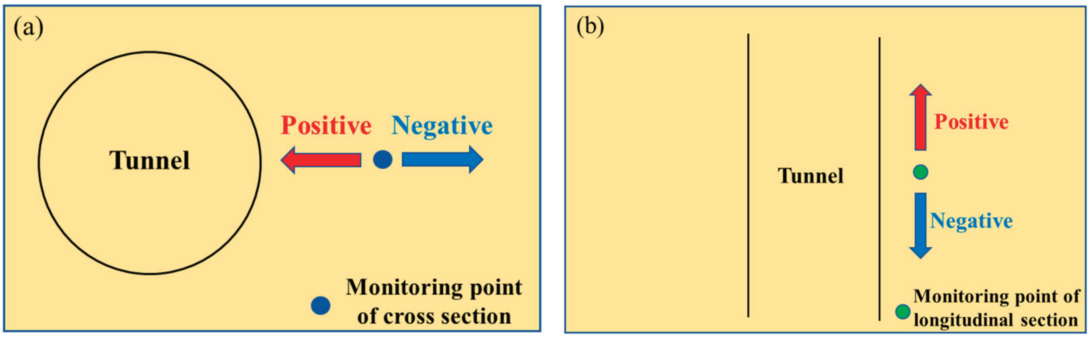

Figure 10. Horizontal displacement direction diagram of deep soil: (**a**) cross-section; (**b**) longitudinal section.

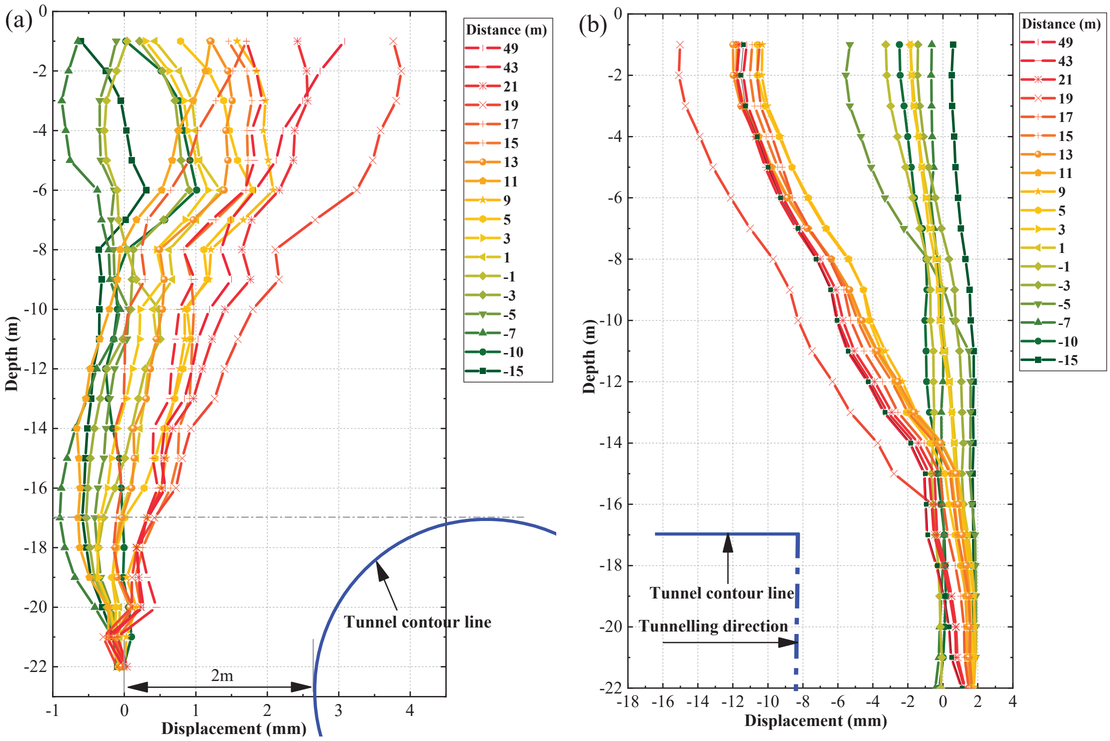

Figure 11. Horizontal displacement of deep soil at different depths: (**a**) transverse direction; (**b**) longitudinal direction.

As shown in Figures 11a and 12a, before the shield machine reaches the monitoring section, the displacement values fluctuate within a range of −1~1 mm. This suggests that the tunnelling process causes minimal transverse disturbance to the soil before the shield machine reaches the monitoring section. As the shield machine passes through the monitoring section, the transverse displacement gradually shifts to positive values, indicating that the soil tends to move towards the tunnel axis. Before and after the shield machine's tail passes through the ring, the ground displacement increases significantly. This is due to the fact that the backfill grouting has not yet hardened during the passage of the shield tail through the monitoring section, leading to substantial ground loss. As the shield continues to advance, the transverse movement of the soil tends to stabilize. At this point, the impact of shield tunnelling on the ground diminishes, and subsequent displacements are primarily due to soil consolidation and deformation. The maximum transverse horizontal displacement of the deep soil occurs after the shield tail passes, with a value of approximately 3.8 mm.

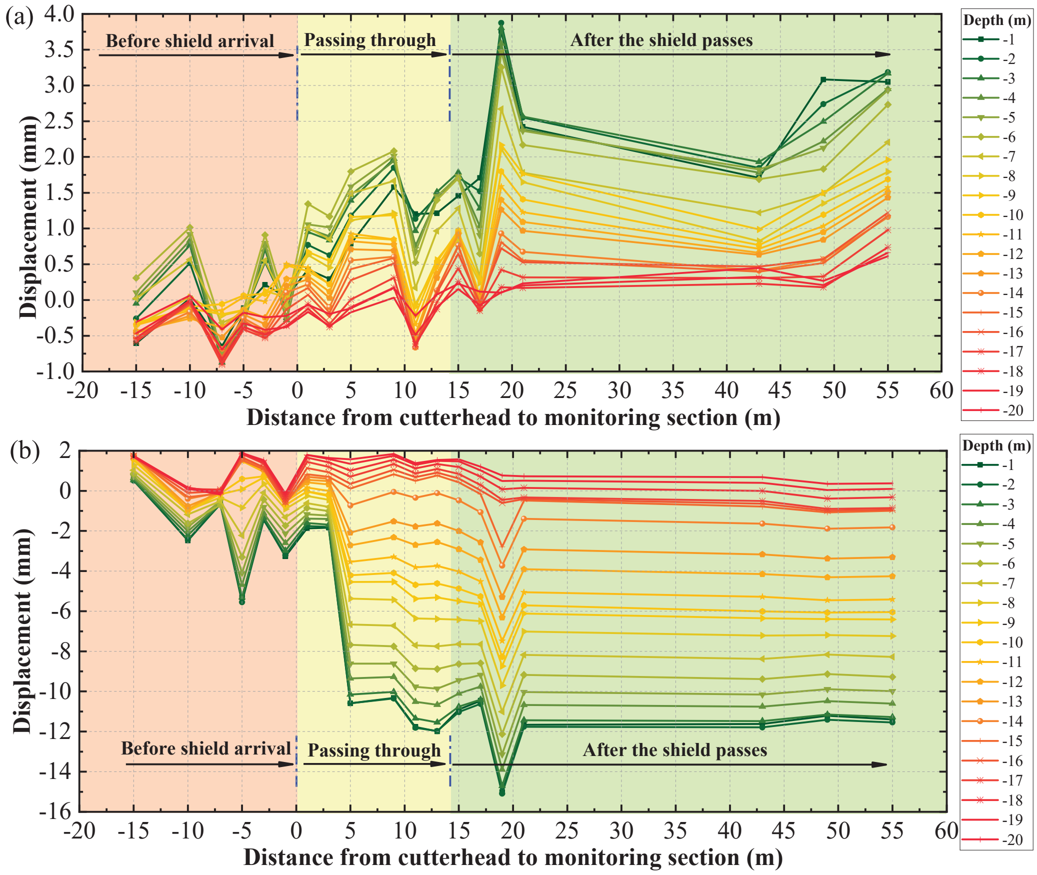

Figure 12. Time history of horizontal displacement of deep soil in shield tunnelling: (**a**) transverse direction; (**b**) longitudinal direction.

As shown in Figures 11b and 12b, there is a noticeable difference between the longitudinal and transverse displacements of the deep soil. Approximately 10 m before the shield reaches the monitoring section, the longitudinal displacement is negative, meaning that the displacement direction is opposite to the shield tunnelling direction. As the shield machine reaches the monitoring section, the longitudinal displacement values show a significant increasing trend, indicating that the soil is moving in the direction of the shield tail. The displacement peak, which is approximately 15 mm, occurs 3~5 m after the shield tail passes through the monitoring section.

The law of horizontal displacement of deep soil in the transverse direction is as follows: Before the shield arrives, the horizontal displacement of the deep soil is not obvious. When the shield passes through, the soil on both sides of the shield machine moves toward the tunnel. During the passage of the shield tail, the displacement of the soil will fluctuate greatly and reach the maximum value. As the shield continues tunnelling, the soil displacement gradually stabilizes.

The law of horizontal displacement of deep soil in the longitudinal direction is as follows: Before the shield arrives, the longitudinal displacement of the soil is not obvious. When the shield passes through, the soil will move opposite to the driving direction because of the extrusion effect of the shield tunnelling machine. When the shield body passes through, the soil accelerates its displacement opposite to the tunnelling direction. The longitudinal displacement of the soil reaches the maximum value after the shield passes. As the shield continues tunnelling, the longitudinal displacement of the soil falls back to a stable value.

In summary, the horizontal displacement of deep soil primarily occurs during the passage of the shield machine through the monitoring section and after the shield tail has passed. Factors such as shield attitude adjustments, cutterhead over-excavation, uneven slurry pressure, and irregular backfill grouting pressure can all lead to variations and discrepancies in deep soil deformation.

5. Numerical Simulation

5.1. Numerical Modeling

A three-dimensional numerical model of shield tunnel excavation was established based on the actual engineering conditions and excavation environment of the Tsinghuayuan Tunnel. The tunnelling section corresponds to the Tsinghuayuan Tunnel from DK17+600 to DK17+700, as illustrated in Figure 13. Due to the symmetry of the model, only half of the structure is shown in the figure. The X-axis represents the tunnel width direction (transverse), the Y-axis represents the direction opposite to the tunnel axis (longitudinal), and the Z-axis represents the tunnel depth direction. Considering Saint-Venant's principle and the influence range of tunnel excavation, the model extends 140 m in the X direction, 155 m in the Y direction (with 100 m from y = 0 m to y = 100 m representing the tunnel excavation section, and 55 m from y = 100 m to y = 155 m representing the extended influence zone), and 80 m in the Z direction. A transverse monitoring section is set at the surface along y = 50 m, and a longitudinal monitoring section is set at the surface along x = 0 m. The shield tunnel axis is buried at a depth of 23.32 m, and the tunnel crown is buried at a depth of 17.0 m. The shield has an outer diameter of 12.64 m, with each tunnel segment ring having a width of 2.0 m. The segment's inner diameter is 11.1 m, and the segment thickness is 0.55 m. The shield machine body is 14 m long, equivalent to the width of seven segment rings.

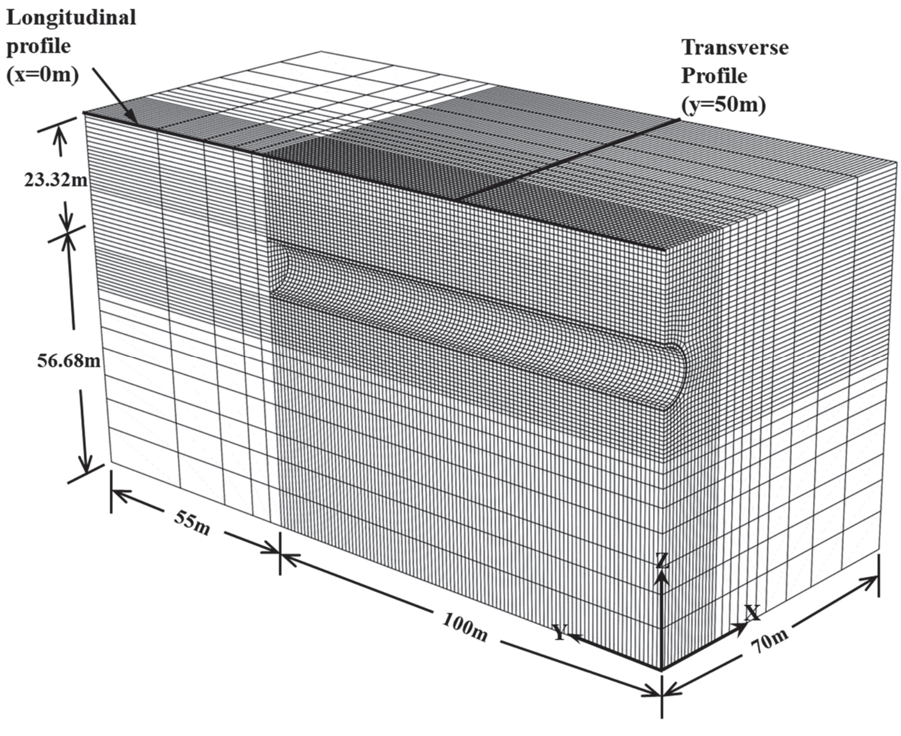

Figure 13. Three-dimensional numerical model.

The Tsinghuayuan Tunnel project of the Beijing–Zhangjiakou High-Speed Railway falls under the category of high-speed railway tunnels. China has stringent requirements for the longitudinal gradient of these tunnels. The maximum longitudinal gradient of the Tsinghuayuan Tunnel is 30‰, which meets the requirements of the Railway Tunnel Design Code (TB10003-2016). For the shield section studied in this paper, the depth variation of the tunnel from DK17+600 to DK17+700 is only 1.2 m, resulting in a longitudinal gradient of 12‰. At the monitoring section DK17+650, compared to DK17+600 or DK17+700, the tunnel depth variation is only 0.6 m, which constitutes just 3.5% of the depth at the monitoring section (17 m). Such a depth variation has a minimal impact on surface settlement. Therefore, this study does not consider the effects of depth variation and longitudinal gradient on surface settlement caused by shield tunnelling.

The boundary conditions in the numerical model are set as follows: In the X-axis direction of the model, horizontal constraints in the x direction are applied at the boundary surfaces of $x = -70$ m and $x = 70$ m. In the Y-axis direction, horizontal constraints in the y direction are applied at the boundary surfaces of $y = 0$ m and $y = 155$ m. These horizontal constraints in both the X and Y directions are intended to account for the surrounding soil's restraining effects. A vertical constraint in the Z direction is applied to the bottom boundary surface of the model ($z = 0$ m), while the top boundary surface of the model ($z = 0$ m) is set as a free boundary.

In the numerical model, all soil materials are discretized with eight-node linear brick integration elements (C3D8), as well as the shield, lining elements, and grouting layer. It should be noted that the focus of this study is on ground deformation induced by shield tunnelling. Therefore, detailed simulation of the segmental lining is not conducted and the interactions between segment blocks, as well as between rings, are not analyzed. The interactions between the soil and the shield, the soil and the grouting layer, and the grouting layer and the lining are all simulated using contact surfaces. The contact behavior is modeled using a tied constraint (Tie contact). In the elastic stage, the stress–strain relationship of the soil is modeled using a cross-anisotropic elastic model. For comparative analysis, an isotropic linear elastic model is used in the comparison model. In the plastic stage, the modified Mohr–Coulomb yield criterion is applied. In order to implement the 3D cross-anisotropic elastic model, the modified Mohr–Coulomb yield criterion for the plastic stage had to be custom programmed and developed through secondary development. Therefore, both the stress–strain relationships in the elastic and plastic stages were obtained through custom programming via UMAT secondary development. These were then utilized in ABAQUS 6.14 by invoking the UMAT subroutine for the calculations. The shield structure, concrete lining structure, and concrete grouting layer structure are all modeled using a linear elastic model.

The physical and mechanical parameters of the soil are provided in Table 1, while the physical and mechanical parameters of the lining segments, grouting layer, and shield are detailed in Table 3. It is worth noting that the properties of cement, such as the Young's modulus and Poisson's ratio, change as the grouting material hardens. The strength of cement increases from 0.6 MPa to 1.2 MPa after initial setting, indicating that the Young's modulus undergoes significant changes as the grout hardens, while the Poisson's ratio remains relatively stable. Therefore, following the simulation methods referenced in the works of Thomas and Gunther [25], Lambrughi et al. [26], and Michael et al. [27], the Young's modulus is divided into three stages to account for the hardening process of the grouting layer over time, as shown in Table 3. The meshing of the 3D numerical finite element model was conducted manually. Since the soil elements surrounding the tunnel are of primary interest, the mesh around the tunnel was refined, while the mesh elements for the soil further away from the tunnel were gradually coarsened. Ultimately, the entire 3D model consists of 303,030 nodes and 277,760 elements.

Table 3. Physico-mechanical parameters of shield tunnel.

Specification	Reinforced Concrete Lining	Backfill Grouting		Shield Machine
Bulk density (kN/m^3)	25	22		76
Young's modulus (MPa)	35,500	I-level	36	210,000
		II-level	50	
		III-level	60	
Poisson's ratio	0.25	0.25		0.2
Thickness (m)	0.55	0.22		0.22

5.2. Model Verification

To verify the validity of the numerical simulation, a comparative analysis was first conducted between the field measurements and the numerical simulation results of the transverse and longitudinal surface settlement troughs, as shown in Figures 14 and 15. Since the settlement troughs are symmetrical along the vertical plane of the tunnel axis, only half of the surface lateral settlement troughs are displayed in this paper. As shown in Figure 14, the shape of the surface lateral settlement troughs is generally consistent, resembling a Gaussian curve. The transverse settlement trough obtained from the field measurements is noticeably narrower and deeper compared to that predicted by the numerical simulation; this discrepancy can be unfavorable for tunnel design and construction. As shown in Figure 15, the shape of the surface longitudinal settlement trough is also generally consistent, matching the cumulative distribution function curve proposed by Attewell and Woodman [23]. This indicates that the numerical simulation conducted in this study is effective.

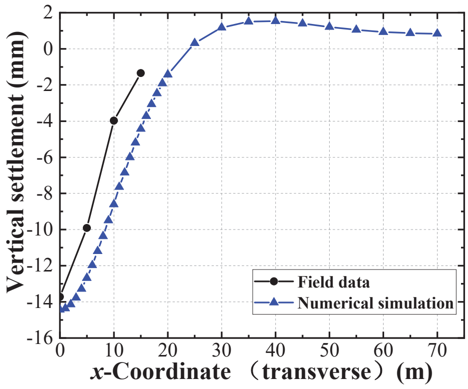

Figure 14. Comparison of horizontal settlement troughs.

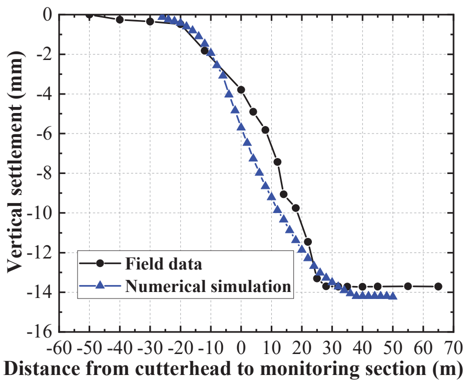

Figure 15. Comparison of surface monitoring point displacements over the tunnel axis during shield tunnelling.

A comparative analysis was conducted between the field measurements and numerical simulations of the deep soil horizontal displacement, as shown in Figure 16. The shape of the deep soil horizontal displacement from both the numerical simulation and the field measurements is generally consistent, though the field measurements show greater variability. This greater fluctuation is related to other disturbance factors present during the monitoring process. The longitudinal horizontal displacements induced by tunnel excavation are significantly larger than the transverse horizontal displacements. This indicates that, after excavation, the soil moves more noticeably towards the newly created excavation face, and longitudinal unloading of the soil more readily triggers displacement and movement. Therefore, during tunnel excavation, it is crucial to enhance monitoring of longitudinal deep soil horizontal displacement. If necessary, reinforcement measures should be implemented to prevent accidents caused by excessive displacement.

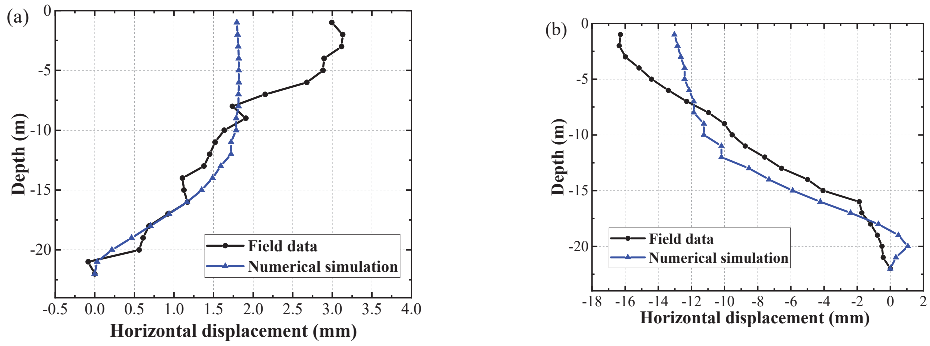

Figure 16. Horizontal displacement obtained from numerical simulation and field measurements: (**a**) transverse horizontal displacement; (**b**) longitudinal horizontal displacement.

Overall, the results obtained from the numerical model of tunnel excavation in this study align well with the field measurements and are consistent with the patterns of ground disturbance caused by tunnel excavation. Therefore, it can be concluded that the numerical simulation used in this study is reasonable and effective.

5.3. Analysis of Surface Settlement Trough Considering 3D Cross-Anisotropy

The longitudinal settlement trough above the tunnel axis, obtained from three-dimensional simulations based on the traditional isotropic Mohr–Coulomb yield criterion, shows the development trend as the shield tunnel excavation progresses, as illustrated by the curves in Figure 17. As the shield tunnel advances from y = 10 m to y = 100 m, the longitudinal settlement curves at different excavation stages are provided at 10 m excavation intervals. In the initial stages of excavation, the shape of the longitudinal settlement trough resembles a cumulative error curve, which is commonly used to estimate the longitudinal settlement caused by tunnel excavation [23,28]. As the shield tunnel excavation progresses to y = 70 m, this trend becomes less apparent. When the excavation reaches y = 80 m, the longitudinal settlement curve exhibits a reverse curvature. Due to the boundary effect of the model, the settlement at y = 0 m first increases and then decreases. The maximum settlement occurs when the shield excavation reaches y = 80 m. The overall trend of the longitudinal surface settlement trough is consistent with the results obtained by Franzius et al. [28], with the exception of slight differences in the soil heave value in front of the shield cutterhead. This further confirms the feasibility and reliability of the three-dimensional numerical model used in this study.

The surface settlement trough calculated using the traditional isotropic Mohr–Coulomb model differs from the field measurements, with the field-measured surface settlement trough being relatively narrower and deeper. To address this issue, an anisotropic constitutive model is used for the numerical simulations, specifically the three-dimensional cross-anisotropic elastoplastic constitutive model (CAM model). Considering that the cross-anisotropy of the soil in the elastic stage can also reflect soil anisotropy, this approach can partially address the issues with the results obtained from three-dimensional simulations using the traditional isotropic Mohr–Coulomb yield criterion.

Figure 18 presents the transverse surface settlement trough considering the cross-anisotropy of the soil in the elastic stage, along with a parametric analysis conducted for different values of the corresponding parameters. For the case of $\alpha = 1.0$ in Figure 18, the cross-anisotropic elastic stiffness matrix degenerates into the traditional isotropic elastic stiffness matrix defined by Hooke's law. The results obtained from the CAM model under this condition are consistent with those calculated using the traditional isotropic Mohr–Coulomb model. The maximum vertical settlement along the tunnel axis increases as the degree of cross-anisotropy increases, meaning it becomes larger as the α value decreases. Furthermore, the shape of the surface transverse settlement trough becomes narrower and deeper as the α value decreases. When $\alpha < 0.63$, the surface transverse settlement trough exhibits a pronounced narrow and deep characteristic. When $\alpha > 0.63$, the normalized settlement trough becomes even wider than the one calculated using the isotropic Mohr–Coulomb model. This indicates that using the CAM model, which accounts for cross-anisotropy in the elastic phase, to simulate shield tunnel excavation can significantly impact the maximum vertical displacement of the surface transverse settlement trough and the normalized trough width caused by the tunnel excavation.

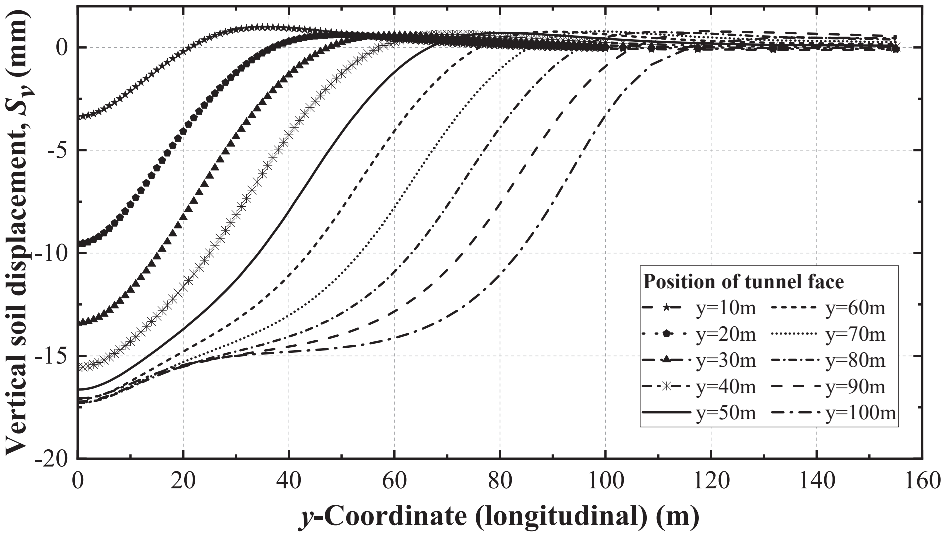

Figure 17. Longitudinal surface settlement based on the traditional isotropic Mohr–Coulomb model.

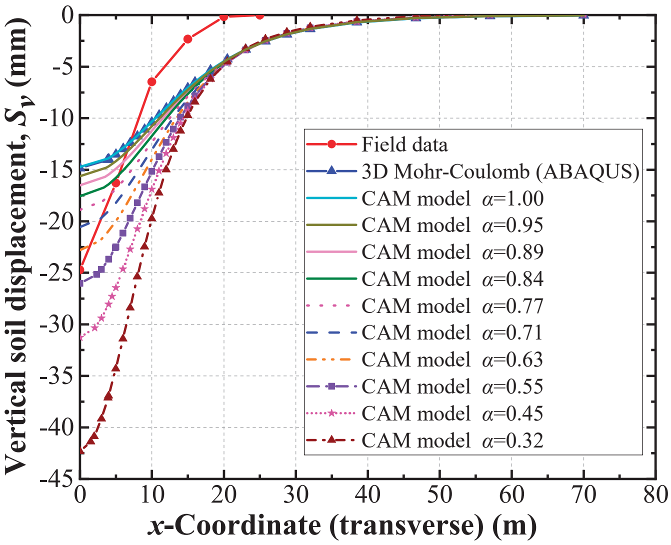

Figure 18. Transverse surface settlement based on the cross-anisotropic model.

The relationships between the cross-anisotropic parameter α and the maximum vertical displacement and between the cross-anisotropic parameter α and the settlement trough width, are illustrated in Figures 19 and 20, respectively. The relevant data for the settlement trough width are presented in Table 4. As the parameter α increases, the maximum vertical displacement of the ground surface gradually decreases, but the rate of decrease diminishes, becoming more gradual. The width of the settlement trough calculated from the transverse settlement trough data obtained through three-dimensional simulations using the Mohr–Coulomb yield criterion embedded in ABAQUS is 10.44 m, with a linear fit evaluation metric R^2 of 0.99. The settlement trough width values obtained from the three-dimensional numerical simulations using cross-anisotropy are consistently larger than those measured on-site.

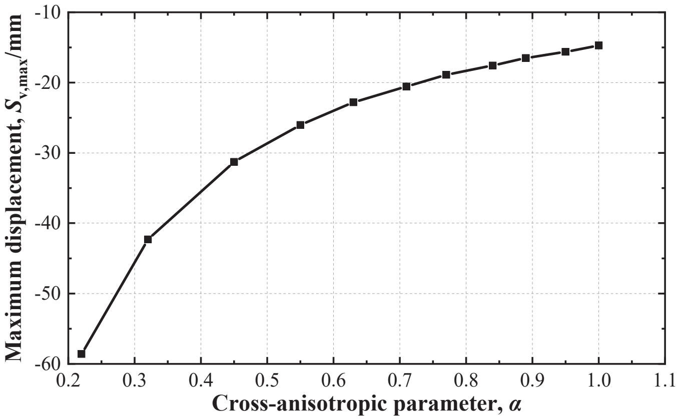

Figure 19. Relationship between cross-anisotropic parameter α and maximum vertical displacement.

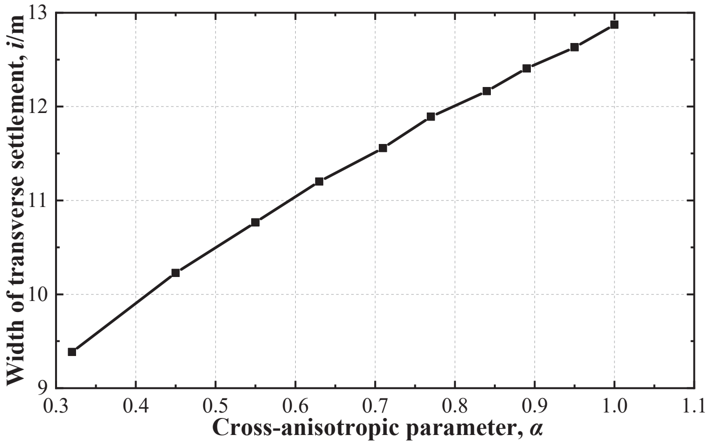

Figure 20. Relationship between cross-anisotropic parameter α and transverse settlement trough width.

Table 4. Settlement trough width *i* obtained from the cross-anisotropic numerical simulation.

Cross-Anisotropic Parameter, α	Width of Transverse Settlement, *i*	R^2	Deviation of Maximum Vertical Displacement Obtained from Simulation from the Field Data (%)
1	12.87	0.99	1.03
0.95	12.63	0.99	0.99
0.89	12.41	0.99	0.96
0.84	12.16	0.99	0.92
0.77	11.89	0.99	0.88
0.71	11.56	0.99	0.82
0.63	11.2	0.99	0.77
0.55	10.77	0.99	0.7
0.45	10.23	0.99	0.61
0.32	9.38	0.99	0.48

Also shown in Figure 20 and Table 4, as the transverse isotropy parameter α decreases, the width of the settlement trough gradually decreases, thus improving the accuracy of the settlement trough predictions. Furthermore, as the parameter α decreases, the maximum vertical displacement increases, leading to a greater deviation from the field data. This discrepancy may be attributed to the fact that the cross-anisotropic stress–strain relationship proposed in this study is based on improvements in the elastic phase. In the elastic phase, the deformation of the soil influenced by anisotropy tends to be more pronounced. It can be seen from Table 4 that when the cross-anisotropic parameter α changes from 1 to 0.32, the width of the transverse settlement changes from 12.87 to 9.38 (a decrease of 27%), and the maximum vertical settlement variation changes from 1.03 to 0.48 (a decrease of 53.4%). There is a significant difference in the magnitude of changes between the two, with the maximum vertical settlement being greater than the width of the settlement trough, indicating that the maximum vertical settlement is more sensitive to changes in the cross-anisotropy.

By optimizing the constitutive model and numerical model, the deformation law obtained from numerical simulation is basically consistent with the on-site monitoring results, but there are still deviations. This is because numerical simulation cannot fully simulate the actual situation on-site, and there are certain simplifications and assumptions. It only considers and analyzes the important influencing factors, which inevitably leads to certain discrepancies.

In order to reduce the soil displacement caused by the excavation of shield tunnels, many possible measures have been proposed. Appropriate tunnelling parameters can be adopted and adjusted in real-time to avoid surface settlement and uplift caused by uneven pressure [29]. The posture of the shield tunneling machine can be controlled to avoid unnecessary correction operations, thereby reducing the risk of soil settlement [30]. Timely grouting behind the wall will prevent soil displacement caused by the gap at the tail of the shield [31]. Stronger monitoring and feedback of soil displacement and taking effective measures in a timely manner will achieve the goal of controlling settlement [32]. For shield tunneling under special geological conditions, it is necessary to reinforce the strata to ensure the smooth excavation of the shield machine and to control surface settlement.

6. Conclusions

In this paper, field measurements and 3D FE modeling were carried out to evaluate the strata disturbance induced by shield tunnelling. Tunnelling parameters, surface settlement, and horizontal displacement of deep soil were analyzed and the following conclusions were drawn:

(1) The tunnelling parameters obtained from the shield machine were analyzed during tunnelling from silty clay to sandy cobble soil. The cutterhead rotational speed remained at a relatively stable level, while the tunnelling speed decreased slightly. However, due to the change in geological conditions, the thrust increased by a notable amount. In sandy pebble soils, the thrust increased by 44.46%. The force required for the shield machine to propel forward was larger than the thrust in silty clay, resulting in increased torque. When the shield excavation encounters adverse geological conditions, it simultaneously leads to significant changes in slurry pressure, shield thrust, and cutterhead torque. Moreover, these three parameters exhibit a strong correlation in their variations.

(2) By installing monitoring equipment on-site to measure surface settlement and deep soil horizontal displacement, data were collected on surface settlement and deep soil horizontal displacement at typical monitoring sections during shield tunnelling. The field measurements indicate that surface settlement values fluctuate significantly in silty clay sections but remain relatively stable in sandy pebble soil. The horizontal displacement of deep soil primarily occurs during the passage of the shield machine through the monitoring section and after the tail void. The longitudinal horizontal displacement of deep soil is significantly greater than the transverse horizontal displacement. Attention should be primarily focused on longitudinal horizontal displacement, and protective measures should be implemented when necessary.

(3) A three-dimensional finite element numerical simulation was conducted to analyze the surface settlement and horizontal displacement of the deep soil induced by shield tunnelling. The use of a cross-anisotropic constitutive model effectively accounts for the anisotropy of the soil, thereby providing corrections and improvements to the numerical simulation results for surface transverse settlement troughs caused by

shield tunnel excavation. A sensitivity analysis of the cross-anisotropic parameter α revealed that as α increases, the maximum vertical displacement of the ground surface gradually decreases, but the rate of decrease slows down and tends to level off. Conversely, as the cross-anisotropic parameter α decreases, the width of the settlement trough narrows, improving the settlement trough profile.

Author Contributions: Conceptualization, J.C. and Z.Y.; methodology, T.Y. and J.W.; software, K.Y.; validation and data curation, B.L., S.Z. and X.Y.; formal analysis, Z.Y.; investigation, J.C. and T.Y.; resources, J.W.; writing—original draft preparation, J.C. and Z.Y.; writing—review and editing, K.Y. and B.L.; supervision, S.Z.; funding acquisition, J.C., Z.Y. and X.Y. All authors have read and agreed to the published version of the manuscript.

Funding: This work was supported by the Fund Project of the China Academy of Railway Sciences Group Co., Ltd. (2023YJ190), the National Natural Science Foundation of China (52425807), the Science and Technology Research and Development Plan of the China National Railway Group Co., Ltd. (K2023S004), the Science and Technology Department of Qinghai Province (2022-SF-158), Chongqing Postdoctoral Research Project Special Funding (2023CQBSHTB3052), and China Postdoctoral Science Foundation (2024M753629).

Data Availability Statement: All data used during the study are available from the corresponding author by request.

Conflicts of Interest: Authors Jian Cui and Bo Liu were employed by the company Railway Engineering Research Institute, China Academy of Railway Sciences Co., Ltd. Author Shu Zhu was employed by the company State Grid Economic and Technological Research Institute Co., Ltd. The remaining authors declare that the research was conducted in the absence of any commercial or financial relationships that could be construed as a potential conflict of interest.

References

1. He, C.; Feng, K.; Fang, Y. Review and prospects on constructing technologies of metro tunnels using shield tunnelling method. *J. Southwest Jiaotong Univ.* **2015**, *50*, 97–109. (In Chinese)
2. Zhou, W.I.; Bobet, A. Predictions of ground deformations in shallow tunnels in clay. *Tunn. Undergr. Space Technol.* **2002**, *17*, 3–9.
3. Lin, C.G.; Zhang, Z.M.; Wu, S.M.; Yu, F. Key techniques and important issues for slurry shield under-passing embankments: A case study of Hangzhou Qiantang River Tunnel. *Tunn. Undergr. Space Technol.* **2013**, *38*, 306–325. [CrossRef]
4. Wang, J. Study on the Mechanical Characteristics of the Large Thickness Subway Tunnel on Remnant Collapse of Loess after Immersion. Ph.D. Thesis, Chang'an University, Xi'an, China, 2017. (In Chinese)
5. Li, J.; Shao, S.J.; Shuai, S. Collapsible characteristics of loess tunnel site and their effects on tunnel structure. *Tunn. Undergr. Space Technol.* **2019**, *83*, 509–519. [CrossRef]
6. Weng, X.L.; Sun, Y.F.; Zhang, Y.W.; Niu, H.S.; Liu, X.; Dong, Y.L. Physical modeling of wetting-induced collapse of shield tunneling in loess strata. *Tunn. Undergr. Space Technol.* **2019**, *90*, 208–219. [CrossRef]
7. Tan, Z.S.; Hong, K.R.; Wan, J.L.; Wang, M.S. Study on composite shield and construction technique in complex uneven strata. *Chin. J. Rock Mech. Eng.* **2006**, *z2*, 3945–3952. (In Chinese)
8. Yang, S.Q.; Chen, M.; Fang, G.; Wang, Y.C.; Meng, B.; Li, Y.H.; Jing, H.W. Physical experiment and numerical modelling of tunnel excavation in slanted upper-soft and lower-hard strata. *Tunn. Undergr. Space Technol.* **2018**, *82*, 248–264. [CrossRef]
9. Liu, C.; Zhang, S.L.; Zhang, D.L.; Zhang, K.P.; Wang, Z.Z. Model tests on progressive collapse mechanism of a shallow subway tunnel in soft upper and hard lower composite strata. *Tunn. Undergr. Space Technol.* **2023**, *131*, 104824. [CrossRef]
10. Di, Q.G.; Li, P.F.; Zhang, M.J.; Cui, X.P. Experimental study of face stability for shield tunnels in sandy cobble strata of different densities. *Tunn. Undergr. Space Technol.* **2023**, *135*, 105029. [CrossRef]
11. Li, P.; Wang, Q.S.; Li, J.H.; Pei, Y.; He, P. Mechanism and impact of water seepage during shield tunnelling in sandy cobble strata: A case study. *Tunn. Undergr. Space Technol.* **2024**, *149*, 105784. [CrossRef]
12. Wei, Y.J. Study on Tool Wear Mechanism and Evaluation Method of Shield Machine in Beijing Anhydrous Sandy Pebble Stratum. Ph.D. Thesis, China University of Geosciences, Beijing, China, 2019. (In Chinese)
13. Teng, L.; Zhang, H. Meso-macro analysis of surface settlement characteristics during shield tunneling in sandy cobble ground. *Rock Soil Mech.* **2012**, *33*, 1141–11150. (In Chinese)
14. Yang, S.J. Slurry shield construction technology for launching section of south railway station-provincial stadium running tunnel of Chengdu Metro. *Tunn. Constr.* **2007**, *6*, 43–46. (In Chinese)
15. Zhang, S.Y.; Chen, K. Shield type selection for Beijing Underground Transit line. *J. Railw. Eng. Soc.* **2007**, *3*, 70–73. (In Chinese)
16. Zhao, B.H.; Hu, X.B.; Zhang, B.; Li, W.J. Study on ground settlement of large diameter slurry shield construction in water-rich sandy gravel stratum. *Eng. Sci.* **2010**, *12*, 94–102. (In Chinese)

17. Xu, Q.W.; He, X.; Gong, Z.Y.; Xing, H.T.; Ma, S.K.; Huang, S. Study on micro-disturbance construction and tunneling control of shield in sandy pebble stratum. *J. Railw. Eng.* **2020**, *9*, 72–77. (In Chinese)
18. Moeinossadat, S.R.; Ahangari, K.; Shahriarm, K. Calculation shield tunnelling and introducing most effective parameter. *J. Cent. South Univ. Sci. Technol.* **2016**, *12*, 3273–3283. [CrossRef]
19. Liang, M.C.; Bai, X.F. Study on deformation control technology of shield tunneling through water conveyance tunnel in sandy pebble stratum. *Tunn. Constr.* **2022**, *S2*, 458–465. (In Chinese)
20. Du, X.L.; Zhang, P.; Jin, L.; Lu, D. A multi-scale analysis method for the simulation of tunnel excavation in sandy cobble stratum. *Tunn. Undergr. Space Technol.* **2019**, *83*, 220–230. [CrossRef]
21. Mair, R.J.; Taylor, R.N. Theme lecture: Bored tunnelling in the urban environment. In Proceedings of the 14th International Conference on Soil Mechanics and Foundation Engineering, Hamburg, Germany, 6–12 September 1997; pp. 2353–2385.
22. Peck, R.B. Deep excavations and tunnelling in soft ground. In Proceedings of the 7th International Conference on Soil Mechanics and Foundation Engineering, Mexico City, Mexico, 25–29 August 1969; pp. 225–290.
23. Attewell, P.B.; Woodman, J.P. Predicting the dynamics of ground settlement and its derivatives caused by tunnelling in soil. *Ground Eng.* **1982**, *15*, 13–20.
24. Attewell, P.B.; Yeates, J.; Selby, A.R. *Soil Movements Induced by Tunnelling and Their Effects on Pipelines and Structures*; Blackie and Son: London, UK, 1986.
25. Thomas, K.; Gunther, M. A 3D finite element simulation model for TBM tunnelling in soft ground. *Int. J. Numer. Anal. Methods Geomech.* **2004**, *28*, 1441–1460.
26. Lambrughi, A.; Medina Rodriguez, L.; Castellanza, R. Development and validation of a 3D numerical model for TBM-EPB mechanized excavations. *Comput. Geotech.* **2012**, *40*, 97–113. [CrossRef]
27. Michael, K.; Dimitris, L.; Ioannis, V.; Petros, F. Development of a 3D finite element model for shield EPB tunnelling. *Tunn. Undergr. Space Technol.* **2017**, *65*, 22–34.
28. Franzius, J.N.; Potts, D.M.; Burland, J.B. The influence of soil anisotropy and K_0 on ground surface movements resulting from tunnel excavation. *Geotechnique* **2005**, *55*, 189–199. [CrossRef]
29. Zhang, K.J.; Zhao, X.; Zhang, Z.Q. Influences of tunnelling parameters in tunnel boring machine on stress and displacement characteristics of surrounding rocks. *Tunn. Undergr. Space Technol.* **2023**, *137*, 105129. [CrossRef]
30. Jin, H.; Yuan, D.J.; Jin, D.L.; Wu, J.; Wang, X.Y.; Han, B.Y.; Mao, J.H. Ground deformation induced by shield tunneling posture in soft soil. *Tunn. Undergr. Space Technol.* **2023**, *139*, 105227. [CrossRef]
31. Wang, S.M.; He, C.; Nie, L.; Zhang, G.C. Study on the long-term performance of cement-sodium silicate grout and its impact on segment lining structure in synchronous backfill grouting of shield tunnels. *Tunn. Undergr. Space Technol.* **2019**, *92*, 103015. [CrossRef]
32. Mu, B.G.; Xie, X.K.; Li, X.; Li, J.C.; Shao, C.M.; Zhao, J. Monitoring, modelling and prediction of segmental lining deformation and ground settlement of an EPB tunnel in different soils. *Tunn. Undergr. Space Technol.* **2021**, *113*, 103870. [CrossRef]

buildings

MDPI

Article

Effect of Sandstone Pore Morphology on Mechanics, Acoustic Emission, and Energy Evolution

Gang Liu [1,2], Dongwei Wang [1,*], Shengxuan Wang [1], Yonglong Zan [1], Qiqi Zhang [1], Zhitao Yang [2,*], Jiazhen Li [2,3] and Zhen Wei [4]

[1] Heilongjiang Ground Pressure and Gas Control in Deep Mining Key Laboratory, Heilongjiang University of Science and Technology, Harbin 150022, China; liugang@usth.edu.cn (G.L.); w13140438798@163.com (S.W.); 17353693207@163.com (Y.Z.); zqq1162170954@163.com (Q.Z.)
[2] Baotailong New Material Co., Ltd., Postdoctoral Research Station, Beijing 100000, China; lijiazhen@usth.edu.cn
[3] Postdoctoral Research Station of Safety Science and Engineering, Heilongjiang University of Science and Technology, Harbin 150022, China
[4] School of Civil Engineering, Lanzhou Institute of Technology, Lanzhou 730050, China; sdweizhen0302@163.com
* Correspondence: 18297919986@163.com (D.W.); w120559779@163.com (Z.Y.)

Abstract: Roadway section form is an important part of the underground engineering structure, and it directly affects the overall stability of the roadway and the occurrence of underground disasters in coal mines. Based on this, this paper adopts a TYJ-500 electro-hydraulic servo rock shear rheology testing machine to conduct a uniaxial compression test on sandstone containing different prefabricated hole section morphology and analyzes the damage characteristics seen during the damage evolution process, with the help of a high-speed camera and acoustic emission monitoring equipment. The test results show that the pore morphology is the main factor affecting the mechanical parameters of sandstone, and the peak stress and elastic modulus of sandstone with pore sections have the characteristics of increasing and decreasing at the same time, except for the intact rock samples. The pore morphology exhibits central symmetry (circular holes and rectangular holes) damage, more pressure-shear cracks and shear cracks, and the acoustic emission characteristics of high-energy–low-amplitude–low-count of the "two low-trend and one high-trend characteristic curves" attributes; moreover, due to the special existence of its pore morphology, it leads to the rock samples having less energy accumulation and release. The axisymmetric hole types (trapezoidal holes and straight-wall domed holes) are damaged by tensile cracks and shear cracks, and their acoustic emission characteristics show the characteristic properties of "three high-trend characteristic curves" of high-energy–high-amplitude–high-count, and there is a strong elastic energy accumulation and output. The conclusions of this article can provide a certain theoretical basis for the design of coal mine roadway sections in underground structures, failure analysis, and stability evaluation of roadway structures.

Keywords: roadway section form; porous sandstone; fracture morphology; acoustic emission characteristics; energy evolution

1. Introduction

In the field of coal mining, the roadway is the main channel of coal resource mining and transportation, and the design of its cross-section pattern is not only related to mining efficiency, but also closely related to the safety of underground coal production. As an important part of the underground engineering structure, the roadway section pattern directly affects the stress distribution of the surrounding rock, the deformation characteristics, and the overall stability of the roadway, which is closely related to the occurrence of underground coal mine disasters [1–4]. Underground coal disasters, such as roof fall, coal and gas protrusion, impact pressure, etc., are the main safety threats in the process of coal mining, and the occurrence of these disasters is often closely related to the irrational design of the roadway section pattern. For example, when the roadway section pattern cannot effectively disperse the surrounding rock stress, it can easily lead to the stress concentration phenomenon, increasing the risk of roof fall; in addition, some specific section patterns may also exacerbate the conditions of coal and gas protrusion, increasing the possibility of disasters. Therefore, an in-depth study of the relationship between roadway section morphology and the occurrence of underground coal disasters is of great significance for optimizing roadway design and improving the safety of coal mining.

Many scholars in China have produced a lot of research on the morphology of the roadway section. In the research of sandstone with a single-hole section, Yang Shengqi [5–7] and other scholars have studied the characteristics of crack initiation, expansion, evolution, and penetration of marble with a single hole under uniaxial compression, combined with a numerical simulation to analyze the effect of non-homogeneity on crack expansion, and found that the crack expansion pattern is significantly affected by the grain and its size. The experimental and simulation results are highly consistent with each other, and a more systematic description of the crack gradual evolution and microanalysis was carried out. Liu Zhaowei et al. [8] conducted an experimental study on the deformation and rupture process of a rock specimen containing a single circular hole under uniaxial compression and clarified that the localized deformation started at 80% of the axial displacement before the peak point and the deformation was the most intense near the peak point. They also found that the variation curve of the average maximum shear strain on the surface of the rock with the axial displacement reflected the evolution of the deformation and rupture of the rock. Zhou Junhua et al. [9] used a particle flow simulation program to conduct uniaxial compression tests on rock samples containing circular holes with different fracture morphologies and found that the fracture has a significant effect on the damage pattern of the hole-containing rock samples. They also found that fractures with different locations and characteristics change the formation of the main rupture zone, and that the damage modification coefficient ranges from 0.77 to 0.90. In the comparative experimental study of several holes, Li Guichen et al. [10] investigated the perimeter rock response of six roadway section shapes after rock excavation through numerical simulation and put forward the concepts of “equivalent excavation” and “ineffective reinforcement zone,” which emphasize the importance of section shapes on the distribution of the perimeter rock plasticity zone. The research of Du Mingrui et al. [11] goes deeper into the level of internal defects in rocks, especially the influence of hole geometry on the mechanical properties of sandstone. Through uniaxial compression tests and numerical simulations, the significant deterioration phenomena of bearing capacity and the elastic modulus of sandstone specimens containing holes were revealed, as well as the complex role of hole shapes on damage modes and crack extension characteristics. The study of Xu Lei et al. [12] explored the zonal rupture patterns and surrounding rock stability structure of different section shapes under equivalent excavation conditions through a combination of theoretical analysis, on-site measurements, and simulation analysis, and proposed a roadway stabilization principle that promotes the interdependence of multilayered load-bearing structures and joint load bearing. Gao Fuqiang et al. [13], on the other hand, used numerical calculations to directly compare the stability of the perimeter rock of the circular arch with that of the rectangular roadway, and emphasized the advantages of the circular-arch roadway in enhancing the stability of the perimeter rock. The study of Liu Gang et al. [14] focused on the local deformation and overall damage law of defective coal rock under bias loading, introduced the dynamic response analysis under bias loading conditions, and revealed the significant influence of the spatial arrangement morphology of the holes on the mechanical properties of sandstone through the bias loading test and acoustic emission monitoring of sandstone with the different morphology of three holes. Zhao Guoyan and Li Diyuan, on the other hand, carried out a detailed study on a variety of pore morphologies in order to further refine the effect of pore morphology on the mechanical properties of the rock. Zhao Guoyan et al. [15] systematically investigated the effects of circular, trapezoidal, horseshoe, and square pores on the mechanical properties and fracture damage evolution law of red sandstone through uniaxial compression tests and digital image correlation techniques and deeply discussed the interaction mechanism between tensile cracks and shear cracks. Li Diyuan et al. [16] systematically analyzed the effects of circular, rectangular, trapezoidal, elliptical, and three-centered arch-shaped holes on the mechanical properties, damage modes, and crack extension characteristics of marble, revealing the relationship between the hole shape and the energy drop coefficient of brittle damage and the ejection intensity of the rock mass. They also further verified the experimental observations with numerical simulations to make clear the distribution of the stress and concentration characteristics of different hole shapes, which provides scientific information for an in-depth understanding of the damage mechanism of rocks. Lu Shasha et al. [17] analyzed the stress distribution range of three types of tunnels surrounding rock on the basis of theoretical research and carried out on-site verification.

Many scholars have focused on the mechanical properties of rock and their impact on the stability of underground engineering structures. Through experimental research, they have unveiled the mechanism of the stick–slip behavior in jointed rock masses as a source of rockbursts [18], investigated the load-bearing effect of prestressed anchor bolt structures and the mechanical properties of the surrounding rock [19], conducted a systematic analysis of the stress and deformation of the surrounding rock and support structures in ultra-large cross-section tunnels [20], explored in-depth the influence of natural discontinuities in hard rock on the deformation and failure mechanisms of deep rock [21], and studied the dynamic mechanical mechanisms and optimization methods for water injection into the roadway surrounding rock to prevent dynamic disasters [22]. Collectively, they have provided theoretical support for the design of underground engineering supports and offered new insights for the prevention of dynamic disasters in underground engineering.

In summary, the research on the roadway section in underground coal mines has been quite abundant, but further in-depth analysis of and discussion on the stability of the surrounding rock, the deformation characteristics, and energy evolution analysis for different section patterns are still needed. The previous research is not based on a certain coal mine roadway foundation, and the choice of hole morphology is also detached from the actual situation of the roadway cross-section morphology, while this paper is more skillfully derived from mechanical experiments regarding the underground structure of the roadway structural analysis and stability evaluation. Based on this, the author will carry out an in-depth study on the four common roadway section types, namely, circular, rectangular, trapezoidal, and straight-wall domed. By using a TAW-2000 electro-hydraulic servo rock shear rheology testing machine, combined with acoustic emission equipment, to conduct uniaxial compression tests on rock samples of the four types of prefabricated holes, the differences in the force characteristics, stress distribution characteristics, damage characteristics, and energy evolution laws of the different section types in underground engineering are analyzed. The research results are of great significance for improving the stability of the tunnel structure and preventing geological roof disasters.

2. Uniaxial Compression Damage Test of Different Holes

2.1. Test Equipment and Roadway Section Morphology Preparation

The test object adopted sandstone, conducted a non-metallic ultrasonic wave velocity test, and selected rock samples with relatively similar wave velocities. The raw rock samples were selected according to the requirements of the International Society of Rock Mechanics test specifications and procedures, with a size of 100 mm × 100 mm × 25 mm for the rectangular rock samples, using the center drilling method to prefabricate the type of roadway section. A complete specimen was used for the control of the test study. Three specimens were used in each group for the test, totaling 15 groups of tests. The effect of the four section types of fabrication and the arrangement are shown schematically in Figure 1. In order to ensure that there is only one single variable in the experimental study, it is required that the holes are located in the center of the rock samples, as much as possible. In addition, in order to avoid the influence of the section area on the experimental results, and to only consider the different results due to the different morphology of the holes, it is required that the area of the prefabricated holes is kept consistent as much as possible (the area of holes was maintained at around 310 mm^2). We extended the coal mine roadway section form area consistency, thereby ensuring the consistency of the mine in transportation, ventilation, and other functions. The inner diameter of the circular section was 20 mm, the length of the rectangular section was 20 mm, the width was 15 mm, the semi-circular diameter of the straight-wall arched section was 15 mm, the length of the bottom was 15 mm, the width was 15 mm, and the trapezoidal section had an upper bottom of 10 mm, a lower bottom of 20 mm, and a height of 20 mm. The specific specimens and the dimensions of the holes preformed are shown in Table 1 below.

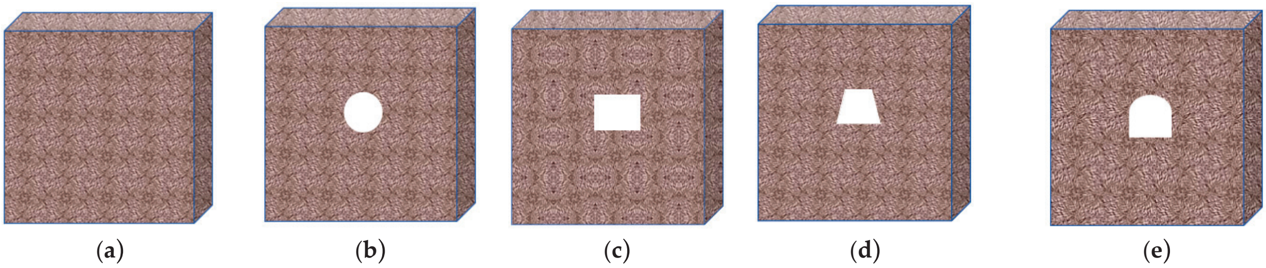

Figure 1. Prefabricated roadway cross-section morphology sandstone specimen. (**a**) Complete rock sample; (**b**) orbicular; (**c**) rectangular; (**d**) trapezoidal; (**e**) straight-wall domed form.

Table 1. Specimen form and dimensions.

Specimen Number	Hole Patterns	Hole Pattern and Its Size/mm	Hole Area/mm^2
WZ-YY-01	Complete rock sample	/	0
WZ-YY-02	Complete rock sample	/	0
WZ-YY-03	Complete rock sample	/	0
YX-DM-01	Orbicular	Calibre: 19.86	309.78
YX-DM-02	Orbicular	Calibre: 20.01	314.47
YX-DM-03	Orbicular	Calibre: 19.92	311.65
JX-DM-01	Rectangular	Length: 20.21, Width: 15.28	308.81
JX-DM-02	Rectangular	Length: 20.25, Width: 15.22	308.21
JX-DM-03	Rectangular	Length: 20.16, Width: 15.24	307.24
GX-DM-01	Straight-wall domed form	Semicircular diameter: 15.12, Underneath: 15.10, Width: 15.12	318.19
GX-DM-02	Straight-wall domed form	Semicircular diameter: 15.02, Underneath: 15.06, Width: 15.04	315.10
GX-DM-03	Straight-wall domed form	Semicircular diameter: 15.04, Underneath: 15.01, Width: 15.03	314.43
TX-DM-01	Trapezoidal	Upper bottom: 10.23, Underneath: 20.21, Height: 20.05	305.71
TX-DM-02	Trapezoidal	Upper bottom: 10.13, Underneath: 20.26, Height: 20.17	305.90
TX-DM-03	Trapezoidal	Upper bottom: 10.08, Underneath: 20.17, Height: 20.18	305.58

2.2. Test Method

The test was conducted using the loading device for the TAW-2000 microcomputer control electro-hydraulic servo universal testing machine. The test system can perform a real-time recording of the specimen loading process of force and displacement data, through the supporting analysis software, which can be obtained from the stress–strain data test loading end and the control system, as shown in Figure 2. The test adopted a displacement-controlled loading mode, where the loading rate was 0.02 mm/s. A high-speed camera was used to collect the whole process information of the sandstone specimen from contact to compression density until the final destabilization and destruction of crack germination and development to the final penetration. We can also conduct real-time monitoring of the whole process of sandstone stress–strain data with the stress–strain acquisition device. With the help of the acoustic emission instrumentation, used to detect acoustic signals during the whole process of the test, we can show their time–space and time–strain data during the rupture gestation process and their spatial and temporal distribution during the rupture brewing process. The threshold was set to 100 dB to eliminate the high signal-to-noise ratio. The acoustic emission probe was fixed to the middle part of both sides of the specimen with a rubber strap, while a petroleum jelly reagent was used to couple the acoustic emission probe to the specimen.

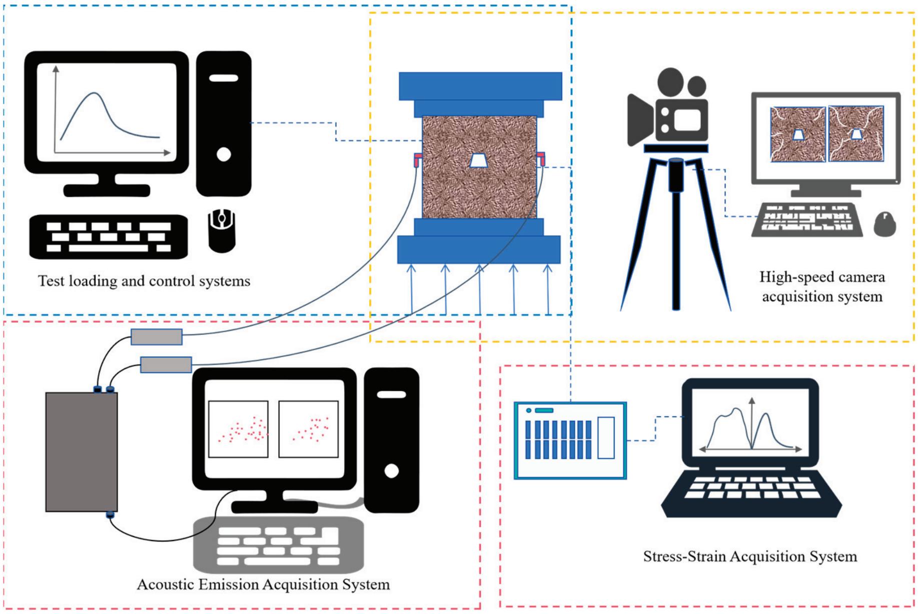

Figure 2. Experimental test system.

By analyzing the stress–strain curves of the four section morphologies and the intact sandstone specimens, as shown in Figure 3 below, the data of the ultimate compressive strength, peak displacement, and modulus of elasticity of the prefabricated sandstones with different section morphologies under uniaxial compression were obtained, as shown in Table 2.

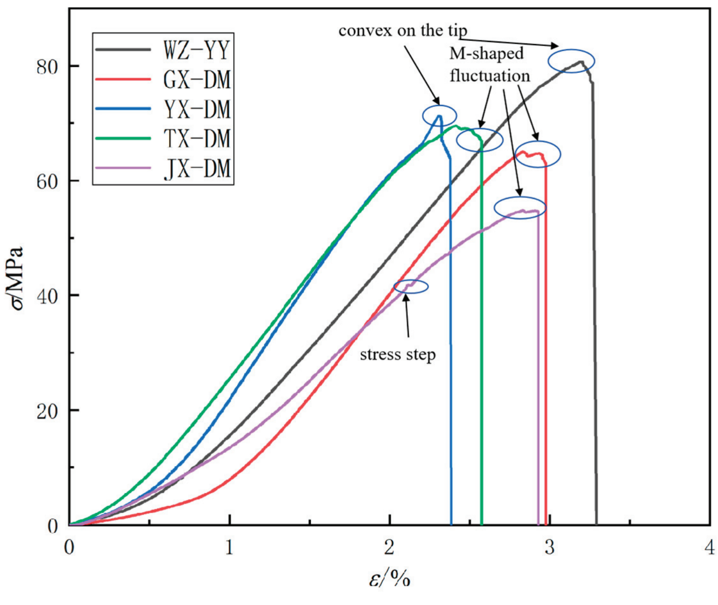

Figure 3. Full stress–strain curves for sandstones with different pore morphologies.

Table 2. Mechanical parameters of sandstone specimens with different pore sections.

Specimen Number	σ_{max}/MPa	ε_{max}/%	E/GPa
WZ-YY	81.48	0.38	41.22
YX-DM	72.03	0.23	38.95
JX-DM	54.89	0.28	27.42
GX-DM	66.60	0.29	36.99
TX-DM	70.10	0.24	36.27

The stress–strain curves of the rock samples with different cross-sectional morphologies are shown in Figure 3. Upon observing the curves, it is evident that, regardless of the preformed hole cross-sectional morphology in the samples, there exists a noticeable crack compaction stage. However, when considering the duration of the compaction stage, the straight-wall circular-arch cross-section and the circular-hole cross-section both experience significantly longer compaction stages compared to the other three types of hole-containing rock samples. This can be attributed to their unique hole shapes, which cause the stress to be transmitted downward along the curved upper surface in "raindrop-like" dispersion, requiring more time for stress transmission and facilitating energy concentration and storage. The shape of the holes also influences the energy evolution of the rock during compression. In the early stages of compression, the rock primarily absorbs energy and undergoes elastic deformation. As the uniaxial compression test progresses, the rock surrounding the holes exhibits different energy absorption rates and release characteristics, due to the varying shapes. The circular holes, with their relatively uniform shape, transmit stress to the lower part in a circular-arch pattern, resulting in a relatively stable energy absorption and release process. In contrast, the straight-wall circular-arch, trapezoidal, and rectangular holes, due to their linear structures in the lower part, may experience sudden changes in energy release caused by local stress concentrations and secondary damage, leading to noticeable fluctuations in the stress–strain curve. This results in a more significant "M"-shaped wave pattern at the peak failure point for the rectangular-, arch-shaped, and trapezoidal-hole cross-sectional sandstone samples. Conversely, the intact rock samples and the circular-hole cross-sectional samples accumulate energy and then exhibit a large tip protrusion at peak failure, causing a substantial one-time energy release. From the curves, it can be observed that, during the initial compaction stage, the rectangular cross-section curve rises rapidly in an upward parabola, while the intact rock, arch cross-section, circular-hole cross-section, and trapezoidal-hole cross-section curves rise in a downward parabola, with a slower ascent. At the same time, the different cross-sectional morphologies have varying degrees of impact on the curve's drop and the shift of the peak yield point.

Overall, all of the types of hole-containing sandstone samples exhibited a typical deformation pattern, transitioning from plasticity to elasticity, and then back to plasticity during the stress process. In the initial stage of deformation, the sandstone samples with different hole morphologies showed distinct crack closure stages. The samples with linear boundary holes (rectangular, arch-shaped, and trapezoidal cross-sections) had more microcracks (more fluctuations), while those with curved-hole cross-sections (circular and straight-wall circular-arch cross-sections) had fewer curve fluctuations, instead showing instantaneous brittle failure with tip protrusion. The reason for this lies in the special curved structural cross-section, which allows the vertical load to be distributed uniformly, thereby slowing down the damage process. When the peak stress is subsequently reached, significant brittle failure occurs immediately. In addition, when transitioning from the crack compaction stage to the elastic stage on the rectangular cross-section curve, a noticeable stress step phenomenon appears, indicating that the rectangular-hole cross-section samples will experience more intense failure. Furthermore, in the post-peak stage, they mostly exhibit strain-softening plastic failure characteristics.

A comparison of the peak failure strength and the elastic modulus for the different cross-sectional shapes is shown in Figure 4. As can be seen from the figure, the relative errors of the elastic modulus among each group of samples with circular, trapezoidal, straight-wall circular-arch, and rectangular shapes are all relatively small, indicating that the selected samples are mostly homogeneous in texture and similar in internal pore structure and distribution. Compared with the intact samples, the average peak compressive strengths of the circular, trapezoidal, straight-wall circular-arch, and rectangular cross-sectional hole samples were 88.40%, 86.03%, 81.74%, and 67.37% of the average peak compressive strength of the intact rock, respectively. The experimental data show that the circular cross-sectional hole had the lowest weakening effect on the compressive strength of the sandstone samples in terms of structure, with only an 11.6% reduction compared to the ultimate compressive strength of the intact rock samples, while the rectangular cross-sectional hole led to the most significant strength reduction, with a decrease of 32.63%. This is because, when the circular hole is subjected to force, the stress distribution is relatively more uniform, due to the symmetry of its shape. This uniform stress distribution helps to reduce local damage to the sample during compression, thereby delaying the overall failure process. The circular hole has no sharp edges, so it is less prone to stress concentration. Stress concentration is one of the important factors leading to material failure, and the design of circular holes effectively reduces this risk. Square holes are more prone to stress concentration at their sharp edges. Stress concentration can cause local stress to exceed the material's strength limit, leading to crack propagation and sample failure. This failure often occurs at lower stress levels, so square holes have a more severe weakening effect on the compressive strength of the samples. A square hole creates a relatively larger material discontinuity in the sample. This discontinuity can lead to uneven stress distribution around the hole, further exacerbating the stress concentration phenomenon. At the same time, this discontinuity also provides a path for crack propagation, reducing the overall strength of the sample.

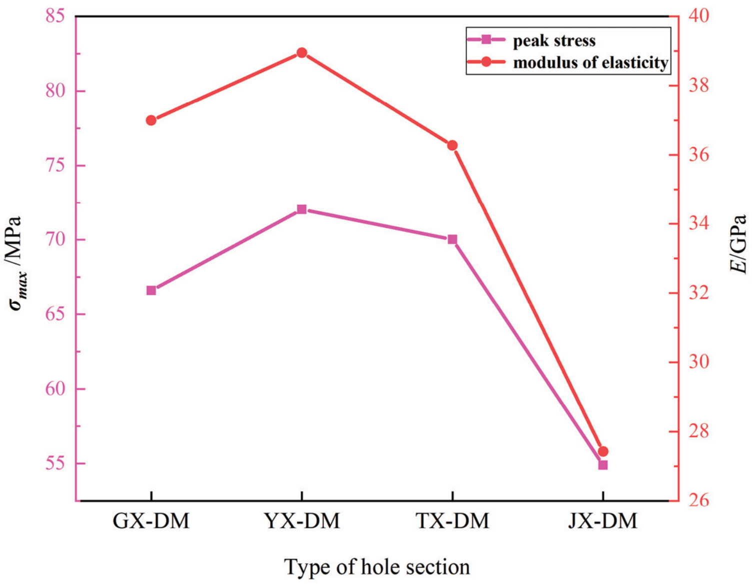

Figure 4. Peak stress versus modulus of elasticity data for the different hole specimens.

Further analysis of the peak strengths of the sandstone samples revealed the following pattern: the circular-hole samples exhibited a relatively high peak strength of 72.03 MPa; followed by the trapezoidal and straight-wall circular-arch samples with peak strengths of 70.10 MPa and 66.60 MPa, respectively; while the rectangular hole samples had the lowest peak strength of only 54.89 MPa. Similarly, a comparable trend was observed in the comparison of the elastic moduli, where the circular-hole samples had the highest elastic modulus of 38.95 GPa, followed by the trapezoidal and straight-wall circular-arch samples, with the rectangular hole samples having the lowest elastic modulus of just 27.42 GPa. This demonstrates that the prefabricated hole defects significantly weaken the compressive strength and deformation characteristics of the rock samples. The different types of samples showed similar trends in peak strength and elastic modulus, and it is evident that the elastic modulus and the peak stress of the samples with different hole cross-sections exhibited concurrent increases or decreases.

On the other hand, it is clear that the arc-shaped holes (such as the circular holes) performed superiorly in terms of their load-bearing capacity and material stiffness, while the mixed arc and straight-line holes (such as the straight-wall circular-arch holes) fell in the middle range. In contrast, the fully straight-line holes (such as the rectangular and trapezoidal holes) exhibited poorer mechanical properties. Given that all of the samples in the experiment were highly consistent in size, hole position, and cross-sectional area, with only the hole shape being set as an independent variable, it is evident that hole shape is a crucial factor influencing the mechanical properties of sandstone samples. In the design of roadway cross-sections in underground coal mines, selecting trapezoidal or straight-wall circular-arch cross-sections is more conducive to the stability of the roadway and can, to a certain extent, delay the occurrence of disasters.

3. Analysis of Crack Progressive Damage Process Under Uniaxial Compression

Grasping the rupture characteristics of rock samples with different section patterns is of great significance for the control of the surrounding rock stability and disaster prevention, so the derivation and rupture characteristics of cracks and crack types of prefabricated pore patterns under uniaxial action are discussed and analyzed here. In order to quantitatively analyze and identify the secondary crack extension process and its fracture type (e.g., tensile, shear, or compressive shear modes) in the porous sandstone specimens under uniaxial compression conditions, we have illustrated (in Figure 5) the typical macroscopic damage pattern of sandstone with porous fractures during uniaxial compression. The letter markers in this illustration are intended to distinguish the different types of crack extension, while the corner numbers represent only the chronological order of the crack appearance.

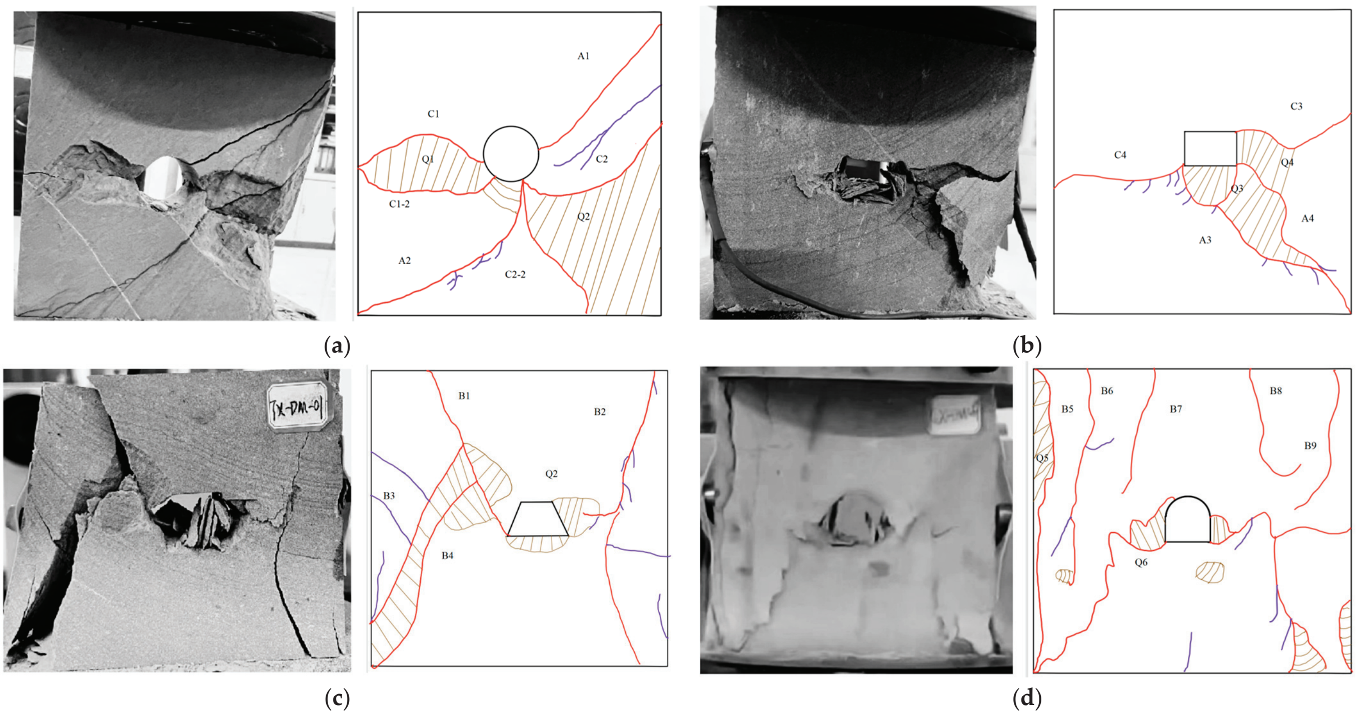

Figure 5. Schematic diagram of progressive damage in sandstone with different pore patterns. (**a**) Orbicular form; (**b**) Rectangular pattern; (**c**) Trapezoidal pattern; (**d**) Straight-wall domed form.

The different mechanisms of crack formation can be categorized into the following three types: tensile cracks, shear cracks, and compressive-shear cracks. Tensile cracks can be divided into two kinds, as follows: one kind of tensile crack is distributed at the top and the bottom of the hole section, which are the two regions with more concentrated tensile stresses; and the other kind of tensile crack is distributed along the vertical laminations, which is the tensile damage of the laminations. The shear cracks started in the compressive stress concentration area on both sides of the hole and gradually developed to the far side under continuous loading, and the failure modes of the specimens mainly covered the following three types: the collapse of the inner wall of the hole, the initial formation and expansion of the cracks, and the peeling and fragmentation of the surface material. These failure modes are closely related to the specific morphology of the hole cross-section in the specimen, and the different morphologies of the holes lead to significant differences in the degree of inner wall collapse.

Figure 5 presents the failure modes of the sandstone samples with different hole sections under uniaxial compression. The macroscopic failure characteristics of the samples mainly include hole-wall collapse, crack propagation and extension, and surface spalling damage. According to Zhu Tantan et al. [23], based on the generation mechanism of secondary cracks, shear-dominated cracks occur when the shear strength of the rock is overcome during crack propagation, causing the crack to propagate along a shear plane. During crack propagation, acoustic emission phenomena may accompany this process, due to the sudden decrease in the internal energy of the rock caused by the release of shear stress. The failure mode of the rock may manifest as shear failure, such as splitting failure or sliding failure along a certain plane. Tensile-dominated cracks occur when the tensile strength of the rock is overcome during crack propagation, leading to crack propagation occurring along the tensile direction. Crack propagation typically exhibits sudden brittle fractures, because tensile stress can quickly reach the strength limit of the rock. The failure mode of the rock may manifest as tensile failure, such as a tensile fracture or tearing along a certain direction. Compressive-shear cracks, which are jointly dominated by both shear and tensile stresses during crack propagation, result in complex and varied crack paths. The failure mode of the rock may manifest as composite failure, incorporating characteristics of both shear and tensile failure. The acoustic emission phenomena may be more complex because the combined action of shear and tensile stresses leads to multiple releases and the redistribution of internal energy within the rock. Drawing on the research experience of previous scholars and combining the specific samples in this experiment, the crack types can be specifically subdivided into three categories, A, B, and C, each with unique characteristics and evolution laws, as follows:

Category A cracks (shear-dominated cracks): These cracks originate from the areas formed by hole wall collapse on the left and right sides of the prefabricated holes. Their propagation paths trend diagonally upward or downward, typically manifesting as inclined main cracks with two wings penetrating the sample surface. The surrounding hole walls gradually collapse, ultimately leading to the formation of fracture surfaces, indicating the concentration and release of shear stresses within the rock samples containing holes.

Category B cracks (tensile-dominated cracks): These cracks originate from the destruction of the upper and lower hole walls within the central range of the sample under tensile stress. The initial propagation direction is mostly along the axial loading path. However, due to the heterogeneity of the rock material and the stress concentration effect at the ends of the sample, the Category B cracks may deviate from the original axial direction during the later stages of propagation, exhibiting more complex path changes. On the surface of the rock sample, macroscopic cracks parallel to the stress application direction are formed, causing certain tensile and tearing effects in the vertical direction.

Category C cracks (compressive-shear composite cracks): The formation of these cracks is closely related to the overall instability of the sample, manifesting as the structural transverse fracture of the rock sample containing holes. Their appearance is generally delayed compared to Category A and B cracks. They are the ultimate manifestation of the loss of structural integrity of the sample under complex stress conditions, especially with the combined action of compressive and shear stresses. The direction of the compressive-shear composite cracks on the sample surface usually has a certain angle with the stress direction of the sample. This is because, under composite compressive-shear stress conditions, the crack propagation direction is jointly influenced by normal stress and shear stress. Macroscopically, compressive-shear composite cracks may manifest as obvious crack lines or crack zones, which may penetrate the entire sample or only appear locally on the sample surface. Microscopically, crack propagation paths may exhibit features such as tortuosity, bifurcation, or propagation along the grain boundaries.

There is a significant difference between the fracture mode and the fracture characteristics of the pore-bearing sandstone rock samples. As shown in Figure 5a, during the axial loading of the sandstone samples with circular holes, two macroscopic shear cracks (A1 and A2) are generated around the holes that are close to the diagonal angles along the left and right sides of the holes, under the action of the holes. The reason for analyzing this factor is that, when the loads are transmitted downward, the circular holes cause stress concentration, which results in greater stresses on the material around the holes, and the loads select the weakest point. When "attacking" the lower rock sample, the end position was chosen first, which led to a cracking stress of 25.2 MPa at the right end of the circular-hole specimen. The stress then continues to conduct downward in the process due to the specificity of the circular specimen morphology. In the specimen on the left and right sides of the formation of more symmetrical compression, as well as in shear cracks C1 and C2, a starting stress of 35.7 MPa is observed, which gradually moves to the specimen on the lower end face of the development of the main cracks to generate secondary cracks C1-2 and C2-2 before shear crack A2 cracking and expansion. When they continue to load, the cracks expand rapidly to the end face expansion, the main crack formation of through stress falls violently, the material begins to show fatigue damage and spalling regions Q1 and Q2.

Comparing the final damage pattern and the damage sequence of the sandstone samples with different pore morphologies, it was found that the damage characteristics of the two types of pore samples, circular and rectangular, are the same as those of the two types of pore samples that are symmetrically distributed up and down in morphology, as shown in Figure 5b. It can be observed that, in the rectangular pore samples, the initial shear zones C3 and C4, which were formed on the left and right sides of the holes with an angle of 45 degrees from the loading direction, were formed in the vicinity of the main cracks and secondary cracks A3 and A4 gradually when the load continued to be transmitted downward. As the load continues to be transmitted downward, secondary cracks A3 and A4 are formed in the vicinity of the main cracks, and large-scale debris spalling zones Q3 and Q4 are formed around the hole due to the through stress damage of the main cracks and the secondary cracks. When analyzing the morphology of the sample with the symmetry between the circular and rectangular shapes in the horizontal direction, compressive-shear cracks appear symmetrically on the left and right sides of the hole when the sample is subjected to the uniaxial compression test. The reason for this may lie in the special nature of the mathematical shape of the holes, where the main stresses on the rock samples are applied along the vertical direction, but additional shear stresses may be generated around the holes. These shear stresses are the main cause of the formation of cracks, especially if there are defects or weaknesses in the surface of the specimen, when the number of compressive-shear cracks becomes more evident.

It can be observed that the crack derivation patterns of the trapezoidal-hole and straight-wall domed hole specimens are well characterized by symmetrical damage along both sides of the main axis. As shown in Figure 5c, firstly, the stress on both sides of the trapezoidal-hole specimen is transmitted downward, which then produces two larger tensile cracks (B1 and B2), and, at the same time, due to the specificity of the two bottom corners of the trapezoidal shape, it has a certain rupture-inducing effect on tensile crack B2, and then reaches the crack-initiating stress of 27 MPa on the left side, which produces two more obvious tensile cracks (B2 and B3) on the left side of the rock sample. Thereafter, the local stress of the specimen reaches 27 MPa. Here, the local stress of the specimen reaches its stress limit, and microcrack penetration damage produces a crushed spalling zone in the right middle region of the specimen. Similar to the trapezoidal shape, the straight-wall domed specimen produces multiple more uniform tensile cracks (B5, B6, B7, B8, and B9) in the upper part of the specimen at the early stage of compression, and, at the same time, the initial cracks on the left side of the hole cross-section also extend approximately along the direction of the expansion of the original cracks in a tensile damage pattern toward the loaded end face to form crack-breaking surface Q5.

Compared with the first three holes, the damage process of the straight-wall domed hole is gentler, as shown in Figure 5d, only in the compression process at the end of the surface, where a small amount of fragmentation occurs. In addition, the stress in the search for the optimal unloading path along the edge of the hole form unloads, due to the stress relief brought about by the significant crack rupture surface Q6, as well as in the macroscopic crack extension. At the same time, there are varying degrees of rock debris fall with crisp sound along the macrocrack expansion path. As in the case of the trapezoidal holes, due to the special position of the two bottom corners of the dome shape, the optimal unloading path after stress transfer to the periphery of the holes is also determined to be in the diagonal transfer of the two bottom corners to the bottom of the rock samples.

The comparative analysis of the rupture morphology of the rock samples containing different pore morphologies is mainly manifested in the different types of cracks appearing, with the centrosymmetric pore types (circular pore and rectangular pore) showing more compressive-shear cracks and shear cracks, while the axisymmetric pore types (trapezoidal pore and straight-wall domed pore) show more tensile cracks and shear cracks.

In the uniaxial compression failure mechanism of brittle rocks, the variability mainly originates from two aspects, as follows: one is the difference in the pore morphology and its geometric characteristics, and the other is the inherent inhomogeneity of the rock materials. From a macroscopic perspective, the final damage of the rock is the result of the gradual accumulation and evolution of the micro-damage in the early stage, in which the main manifestation of the early damage is the local microcracks induced by the stress concentration at the edge of the prefabricated holes.

When comparing the macroscopic fracture patterns of the different specimens, it can be clearly observed that the course of crack initiation is expansion until penetration is highly consistent with the dynamic evolution of the principal strain field on the fine-scale. Specifically, crack development is a dynamic process, accompanied by the continuous expansion of the high-strain region, during which microscopic ruptures continue to sprout, develop, and eventually converge into a nucleus to form a macroscopically visible crack system. This process reveals the close connection between the micro-mechanism of rock damage and the macro-expression, i.e., the macro-damage is the final manifestation of the accumulation and evolution of the micro-damage.

4. Characterization of Acoustic Emission Under Uniaxial Compression

From the schematic diagrams combining acoustic emission (AE) characteristic parameters with stress–strain curves for four different cross-sectional shapes provided in Figure 6, it is evident that, during the initial contact between the circular and trapezoidal specimens with the press ram, there was no significant acoustic signal in the AE event count during the compaction stage of the curve, resulting in a notable blank window period. As the rock samples entered the nonlinear deformation stage, the axial stress–strain curve gradually deviated from a straight line and rose slowly and uniformly. A substantial number of AE events occurred in the single-hole sandstone samples with different cross-sectional shapes, and the number of AE activities increased significantly. The peak energy of the circular-hole specimen reached 762,000 aj, the peak amplitude reached 87 db, and the limit ring-down count even reached 12,218. For the trapezoidal-hole specimen, the peak energy reached 743,695 aj, the peak amplitude reached 86 db, and the limit ring-down count reached 32,128. This phenomenon indicates that the brittle sandstone is about to undergo instability and failure. Both the circular- and the rectangular-hole cross-sectional sandstone specimens generated a small number of AE signals during the initial compaction stage. The reason for this is that real rock masses have some degree of initial primary rock damage, which results in the production of certain AE events. Observing the four images clearly shows that many AE events are concentrated around potential tensile damage zones. Therefore, the pores and fractures within the rock are the causes of cracks in the sandstone specimens. The tensile fracture zone ultimately reaches the vertical upper and lower boundaries. In contrast, the rectangular-hole cross-section exhibits a relatively obvious characteristic failure point during the initial compaction stage. Subsequently, the AE signals showed a relatively prolonged period of inactivity. According to the analysis by scholars [24], the reason for this is that, during the initial stage, the press ram causes some acoustic signals due to the internal particle compression and collision resulting from the accumulation of relatively hollow material within the rock sample. Then, the specimen enters the elastic yield stage. Due to the uniqueness of the rectangular hole shape, there are not many AE signals in the early stage, leading to the emergence of the inactive period.

The locations of acoustic emission (AE) events for the specimens with straight-wall circular-arch-shaped hole cross-sections during uniaxial compression are shown in Figure 6a. It is clearly visible that, when the vertical stress reaches around the critical stress value, the AE events are predominantly concentrated around the perimeter of the cylindrical cavity. The AE events are mainly focused on the upper and lower surfaces of the circular hole in the upper half, gradually forming clusters, which initiate tensile and shear fractures. Although many AE events are recorded outside of the rock mass region surrounding the cavity, these AE events do not represent active microcracks. In the initial stage, it is difficult to predict the initiation location of macroscopic cracks during loading, because the AE events are discrete within the specimen. The AE active zones connect to form a large AE active area, with the quantity levels of AE characteristic parameters having a limit energy of 572,933 aj, a limit amplitude of 79 db, and a peak ring-down count of 19,501, which correspond to the locations of the macroscopic cracks. In contrast, during the entire loading process, local AE events rarely occur in the region near the cavity wall.

Under the influence of strong interactions between isolated microcracks, these isolated microcracks gradually expand in an unstable manner, resulting in a U-shaped fluctuating growth tendency, which eventually merges to form split macrocrack damage. Tensile cracks begin to appear in the top bottom plate of the domed cavity. With the increase in axial load, the tensile cracks gradually expand, nucleate, and agglomerate, and, thus, the rock sample is destabilized, and the tensile cracks sprout and develop from the top and bottom plates. With the increase in compressive stress, cracks begin to appear near the termination point of tensile fracture and at a certain distance from the cylindrical cavities of the top and bottom plates, and the cracks expand parallel to the direction of the axial stress, appearing in the period of extremely rapid activity of the AE, and eventually causing damage to the specimen. On the contrary, the circular-hole section with the same curved upper edge, in the elastic yielding stage, is not as "enthusiastic" as the signal of the circular-arch section, due to the fact that it is not easy to form stress concentration at the top. In addition, the stress is uniformly dispersed to the top of the various parts, resulting in the amplitude of the absolute energy and ringing counts being in the way of the stress–strain curve characteristics of the upward throwing shape, which slowly rises until the sample is broken. The stress–strain curve is characterized by a slow upward throw until the rock sample is broken. Turning to the trapezoidal pore samples, the number of acoustic emission events is limited, and the trend is smooth at the initial stage of press loading when the load is at a low level. However, a significant increase in the acoustic emission signals was observed at a time point of about 50 s. This phenomenon can likely be attributed to the sudden destabilization of the localized areas (e.g., at pores or micro-defects), due to the uneven distribution of stress within the sample, which is manifested as localized collapses or micro-fractures on the surface. This phase is still defined as a compaction phase, characterized by the fact that the microcracks within the sample have not yet expanded significantly, and, therefore, the overall level of acoustic emission activity remains relatively low.

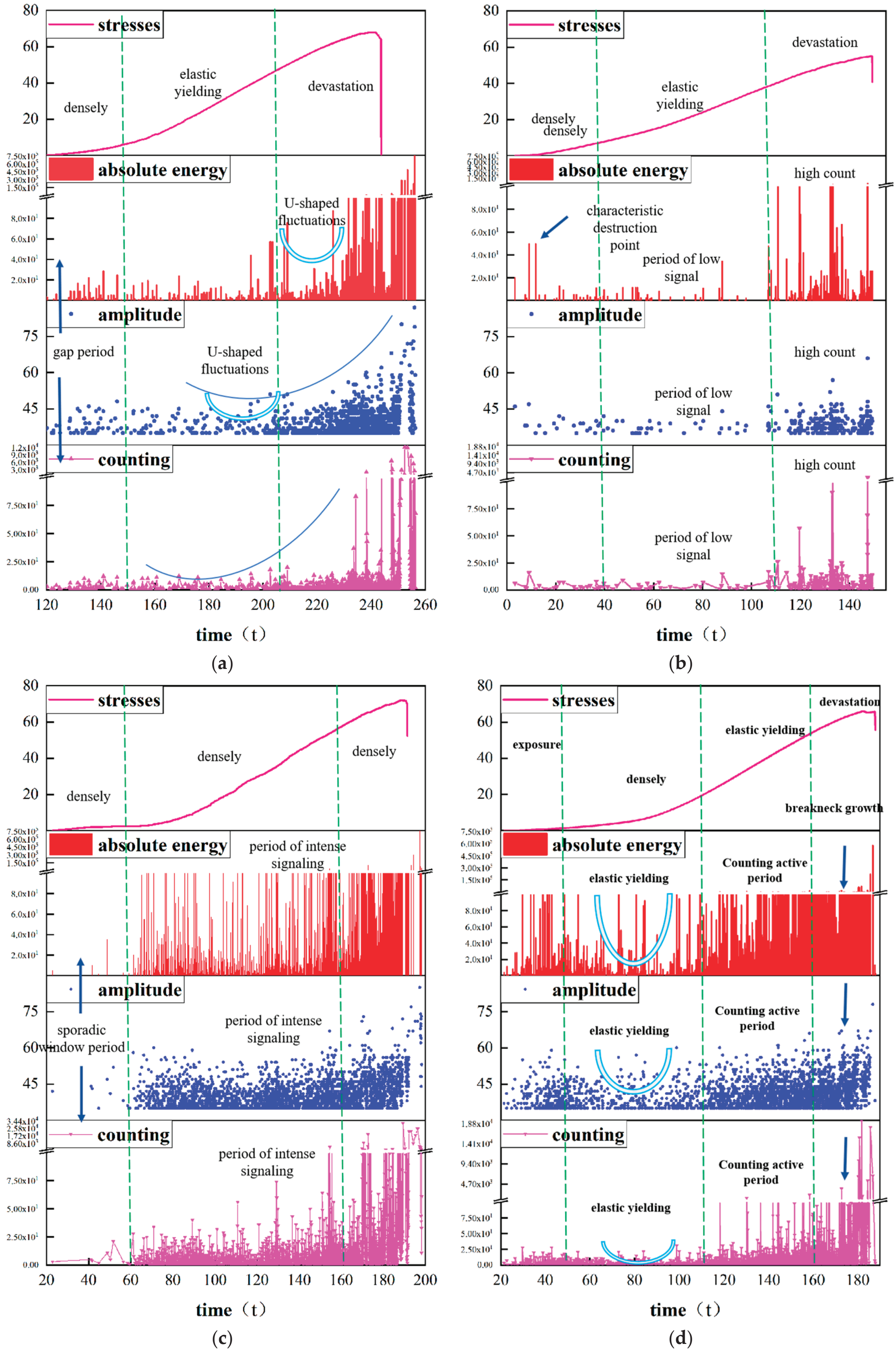

Figure 6. Schematic characterization of acoustic emission events of the rock samples from different hole sections. (**a**) Orbicular form; (**b**) Rectangular pattern; (**c**) Trapezoidal pattern; (**d**) Straight-wall domed form.

To comprehensively analyze the AE events (stress-absolute energy-amplitude-ringer counts), diagrams of sandstone with four different pore section morphologies were created, according to the law analyzed in Section III, which show the acoustic emission characteristics of the axisymmetric-shaped pore (straight-wall domed and trapezoidal). They show the characteristic attributes of high energy, high amplitude, and high counts, referred to as the "three highs." The acoustic emission characteristics of holes (circular and rectangular) in a centrosymmetric shape show the characteristic attributes of high energy, low amplitude, and low counts, referred to as high-energy–low-amplitude–low-count, which are "two lows and one high." In terms of a local comparison, from the specimen-loaded stress curve and acoustic emission ringer counts, the acoustic emission energy curve correspondence can be seen, the stress occur suddenly, and the drop acoustic emission ringer counts and acoustic emission energy appear as a surge phenomenon, but ringer counts surge and acoustic emission energy show a surge phenomenon, and the stress curve does not necessarily show sudden drop changes, and, at the same time, we observed the sandstone specimen before the peak stress. At the same time, observing the "silent period" before the peak stress and the "silent period" of acoustic emission parameter changes, it can be clearly found that the "silent period" of acoustic emission parameter changes does not mean that the destructive deformation field of the rock is in a stable stage, however, in the peak stress of the specimen, the stress curve does not necessarily undergo a sudden drop. On the contrary, in the "quiet period" before and after the peak stress of the specimen, the acoustic emission parameters have more obvious violent fluctuations, according to the research of Song Yimin et al. [25], due to the localization of the deformation during this period brought about by the size of the specimen and the value of the obvious increase.

5. Analysis of Energy Evolution Laws

Many scholars have jointly focused on wave propagation in media, energy evolution during rock failure processes, and the dynamic properties of materials. Xu et al. [26] investigated the influence of nonlinear barriers on the wave propagation in saturated soil systems, providing a new perspective for understanding wave propagation characteristics. Feng et al. [27] delved into the delayed failure process of granite, along with its energy evolution and acoustic emission characteristics, offering significant data support for the study of rock failure mechanisms. These studies have not only enhanced our understanding of wave propagation, failure mechanisms, and material properties in rocks and soils, but have also provided theoretical support for disaster prevention and mitigation in related engineering fields. The deformation and breakage of rocks is essentially an energy dynamic conversion process, which involves both the accumulation of elastic strain energy and the gradual dissipation of energy. In particular, the common interlayer structures in rocks show obvious directional differences in energy storage and release, due to the different directions of force application, resulting in their deformation and damage behaviors. This anisotropic property of energy release plays a crucial role in assessing the stability of engineering structures during deformation.

Based on the theoretical framework of energy dissipation and release proposed by scholars, as well as the energy-driven damage and rupture mechanism [28–32], we can see that rocks undergo a complex energy flow process when they are subjected to compression and deformation until destruction, as follows: from external energy input, to the gradual accumulation of releasable elastic strain energy, to the continuous dissipation and release of such energy through different forms. If we envision an independent system with closed energy, the rock unit undergoes deformation and damage under the action of external force, and, according to the basic principle of energy conservation and conversion, there exists a dynamic equilibrium and conversion relationship between the different forms of deformation energy [33–35], as shown in Figure 7. In addition, because there is no peripheral pressure, the whole test involves only the unidirectional energy input of axial load; moreover, through the integral operation of the stress–strain curve, the change in strain energy in each stage can be directly calculated, and the integral schematic is shown in Figure 8. The mathematical relationship between the energies is as follows:

$$U = U^{\mathrm{e}} + U^{\mathrm{d}} \tag{1}$$

Among them,

$$U = \int_0^{\varepsilon_1} \sigma_1 d\varepsilon_1 \tag{2}$$

$$U^{\mathrm{e}} = \frac{1}{2}\sigma_1 \varepsilon_1^{\mathrm{e}} = \frac{1}{2E_{\mathrm{u}}}\sigma_1^2 \tag{3}$$

The rock samples were put under uniaxial compression without an unloading process, but due to the elastic response of the rock, its elastic modulus in the loading and unloading process to maintain a relatively stable consistency of the slope of the curve is approximately the same. Therefore, Equation (3) can be changed to the following:

$$U^{\mathrm{e}} = \frac{1}{2E}\sigma_1^2 \tag{4}$$

$$U^{\mathrm{d}} = U - U^{\mathrm{e}} \tag{5}$$

In the formula, the following applies:

U is the total strain energy, kJ/m^3; U^{e} is the elastic strain energy, kJ/m^3, U^{d} is the dissipated energy, kJ/m^3; σ_1 is the axial stress, MPa; $\varepsilon_1^{\mathrm{e}}$ is the elastic strain; E is the loaded elastic modulus, MPa; and E_u is the unloaded elastic modulus, MPa.

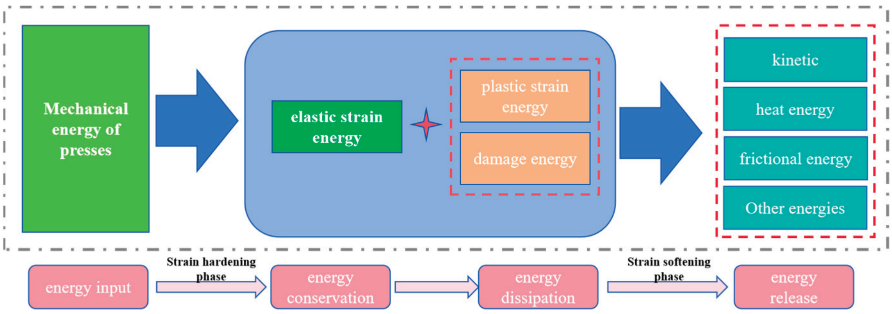

Figure 7. Schematic diagram of energy transfer in the internal system of the loaded coal rock mass.

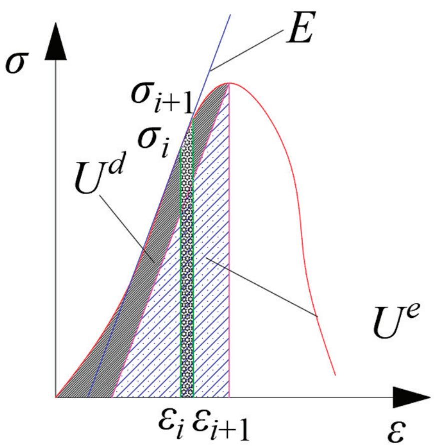

Figure 8. Calculation method of energy conversion of the stress–strain curve.

In uniaxial compression tests, the mechanical energy input to the press is mainly converted into the elastic strain energy, plastic deformation energy, and thermal energy of the specimen [36,37]. Specifically, as the stress increases, the specimen first undergoes an elastic deformation stage, at which time the input energy is mainly converted into elastic strain energy within the specimen, which is stored in the form of potential energy in the microstructure of the material. When the stress exceeds the elastic limit of the material, the specimen enters the plastic deformation stage, at which time the input energy continues to be converted into elastic strain energy, but is also significantly converted into plastic deformation energy, which involves the irreversible energy dissipation of the material's internal dislocations, slip, and other microscopic mechanisms. At the same time, due to friction, microstructural rearrangement, and possible phase transitions during deformation, some of the input energy is also converted into thermal energy, resulting in a localized or overall increase in specimen temperature. These energy conversion processes together determine the stress–strain relationship, damage mode, and energy dissipation characteristics of the specimen during the test. In this paper, we will analyze the energy evolution characteristics under uniaxial compression with different pore morphologies in conjunction with the stage of stress–strain curves observed during the loading process. The evolution trend of energy under uniaxial action with the strain growth for the sandstone specimens with different pore section morphologies is shown in Figure 9.

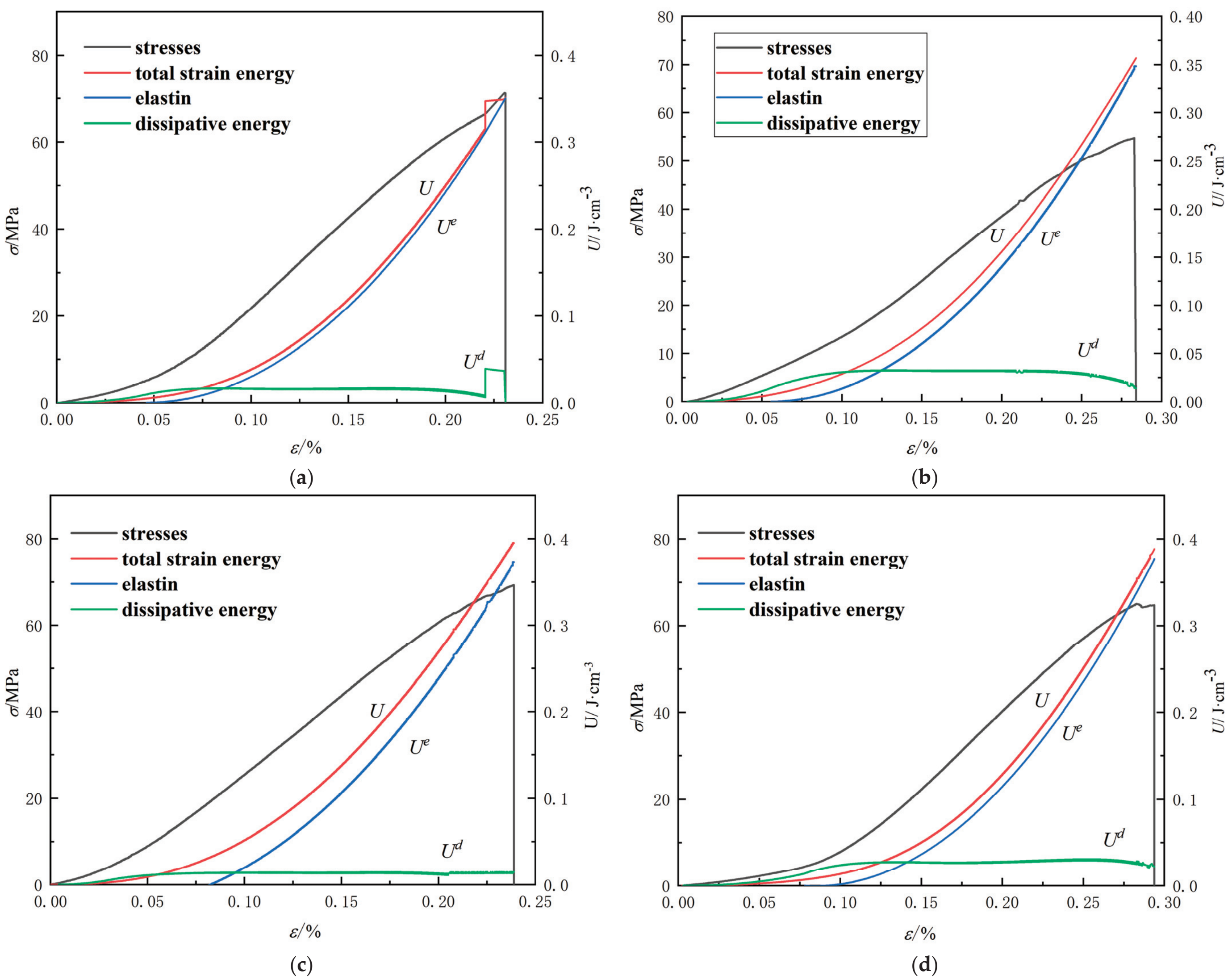

Figure 9. Trend of energy evolution of sandstone with different pore section forms. (**a**) Orbicular form; (**b**) Rectangular pattern; (**c**) Trapezoidal pattern; (**d**) Straight-wall domed form.

It is not difficult to see from the figure that the energy variation curves of sandstone with different pore section morphologies all exhibit a common characteristic, that is, the total strain energy and elastic energy increase in a concave curve, while the dissipated energy increases in a convex curve. This is because, in rock mechanics, when rock is subjected to external forces, it undergoes two stages, as follows: elastic deformation and plastic deformation, which correspond to different energy storage and dissipation modes. The manifestation of total strain energy, elastic energy, and dissipated energy during rock deformation is as follows: In the initial stage of external force application, the rock mainly undergoes elastic deformation, at which point the elastic energy increases rapidly, while the dissipated energy increases slowly. During this stage, the growth trends of the total strain energy and the elastic energy are similar, with both showing a rapid upward trend. The elastic deformation of rock is reversible, meaning that, when the external force is removed, the rock can return to its original state. As the external force continues to increase, the rock begins to transition from an elastic state to a plastic state. During this stage, the rate of increase in elastic energy gradually slows and reaches a peak before beginning to decrease. This signifies that the rock's elastic deformation capacity has reached its limit, and plastic deformation begins to occur. At the same time, the dissipated energy begins to increase significantly, indicating an intensification of energy dissipation caused by external forces. When the external force exceeds the rock's elastic limit, the rock enters the plastic deformation stage. During this stage, the elastic energy remains relatively constant or slightly decreases, while the dissipated energy continues to increase rapidly. The plastic deformation of rock is irreversible, meaning that, when the external force is removed, the rock cannot return to its original state. In summary, the increase in the elastic energy is fast at first, and then slows down, while the increase in dissipated energy gradually accelerates, leading to the concave curve of total strain energy and elastic energy and the convex curve of dissipated energy. This characteristic of the energy variation curve reflects the process of rock transitioning from an elastic response to a plastic response when subjected to external forces. The concave curve of total strain energy and elastic energy reflects a slowdown in the rate of increase in elastic energy during the transition from elastic deformation to plastic deformation, while the convex curve of dissipated energy reflects the accelerated accumulation of dissipated energy during plastic deformation. These curve morphologies are an intuitive representation of energy distribution and conversion characteristics that occur during axial compressive deformation of rock samples with pores.

It can be observed that the section specimens with straight-wall domed and trapezoidal holes accumulate more energy than the other two, both in terms of total strain energy and elastic energy, which is due to the special properties of the hole morphology. The presence of straight-wall domed and trapezoidal holes increases the perimeter of the rock specimens, and the complex morphology of the holes results in more stress concentration points and irregular stress distributions, relative to that of the circular and rectangular holes. Under uniaxial compressive loading, these morphologies of holes lead to more complex strain distributions and stress transfer paths, which increase the deformability and elastic deformation capacity of the rock specimens. As a result, the rock specimens are able to absorb and release more elastic energy when subjected to pressure, resulting in a significant increase in the value of the elastic energy curve. On the contrary, circular and rectangular holes, due to their more regular morphology and simpler stress distribution, have lower values of elastic and total energy curves compared to holes with complex morphology. This is because these hole patterns do not induce the same degree of stress concentration effect, and, therefore, they generally exhibit less elastic energy in compression tests.

Furthermore, their irregular morphology and boundary conditions often lead to more complex and tortuous crack extension paths within the specimen. These irregularly shaped holes guide crack expansion in different directions inside of the specimen, which results in more efficient and adequate energy dissipation during the loading process. In contrast, the crack extension paths of circular- and rectangular-hole specimens are relatively direct and simple, and the cracks are more likely to extend along the neutral axis or the principal stress direction of the specimen, which may lead to less efficient energy absorption during uniaxial compression. In this case, the values of the total elastic energy curves of the specimens are relatively low, because the crack extension paths are relatively direct and the energy dissipation is not as adequate as that of the straight-wall domed and trapezoidal-hole specimens.

Therefore, the morphology and complexity of the holes directly affect the numerical performance of the elastic energy curves of the rock specimens in uniaxial compression tests, and the presence of straight-wall domed and trapezoidal holes leads to higher elastic energy output, which is macroscopically shown by the extremely active acoustic emission signals, and produces the occurrence of violent spalling, ejection, and fragmentation of the rock specimens.

6. Discussion

In this paper, the mechanical properties, damage modes, acoustic emission characteristics, and energy evolution laws of sandstones with different pore morphologies (circular, rectangular, trapezoidal, and straight-wall domed) under uniaxial compression are discussed. It was found that the pore morphology significantly affects the mechanical parameters of sandstone, and the damage modes and acoustic emission characteristics of sandstone with different pore morphologies are different. These research results can help to guide the optimization of coal mine roadway structures, improve the stability of the roadway, and prevent geologic roof disasters, which is of great significance to the safe production of coal. The limitation is that this thesis is established in the state of stress under uniform load, and, due to the complex spatial layout of shaft mining, this will also lead to uneven stress distribution at a certain period and to a certain extent, and the phenomenon of eccentric load occurs above the coal mine roadway, which induces different degrees of damage to the roadway section, etc. Therefore, the research can be continued for the development of this field.

7. Conclusions

Through uniaxial compression tests conducted on sandstone samples with various hole sections, along with an analysis of the stress–strain characteristic curves, fracture patterns, and acoustic emission event counts of different rock samples, an investigation was carried out to explore the characteristics, similarities, and differences in the microstructure of the fracture surfaces of sandstone samples with different hole sections. The brittle failure characteristics of sandstone under the experimental conditions were studied, and a preliminary analysis of the brittle failure mechanisms of sandstone with different hole sections was performed. Overall, the trapezoidal sections and the straight-wall circular-arch sections demonstrate superior stability and can withstand greater energy, making them the preferred choices for the design of underground roadway sections in coal mines. Their acoustic emission characteristic parameters and the gradual evolution of cracks can provide certain analytical tools for disaster early warning and forecasting. The specific conclusions are as follows:

1 The type of pore morphology is an important factor affecting the mechanical parameters of sandstone specimens. The generation of microfractures in the linear boundary pore specimen is greater, while the curved pore section morphology is the emergence of the tip raised transient brittle damage phenomenon, and its modulus of elasticity and peak stress have the same rise and fall of the characteristics of change.
2 The hole morphology shows that, in centrosymmetric hole types (circular holes and rectangular holes), more pressure-shear cracks and shear cracks appear, while, in axisymmetric hole types (trapezoidal holes and straight-wall arched holes), more tensile cracks and shear cracks appear.
3 The acoustic emission characteristics of holes with an axisymmetric shape (straight-wall domed and trapezoidal) show the characteristic properties of high-energy–high-amplitude–high-count of the "three highs." On the other hand, the acoustic emission

characteristics of centrosymmetric holes (circular and rectangular) show the characteristic attribute of "two lows and one high" of "high-energy–low-amplitude–low-count," and the stress change curve has good correspondence with the evolution trend of the acoustic emission ringing counts, and has nothing to do with the change in amplitude. The stress change curve has good correspondence with the evolution trend of the acoustic emission ring counts, but not with the amplitude change.

4 In the uniaxial compression test, the accumulation and dissipation of energy in the rock system are closely related to the morphology of the holes, and the trapezoidal and straight-wall domed holes are more conducive to the accumulation and release of energy, while the rectangular and circular holes have weaker energy accumulation and dissipation.

Author Contributions: G.L. and D.W. wrote the main text of the manuscript and the experimental data processing and summaries, while S.W., Y.Z., Q.Z., Z.Y., J.L. and Z.W. were the co-authors responsible for collecting the relevant information to organize the structure of the paper. All authors have read and agreed to the published version of the manuscript.

Funding: This research was funded by the Natural Science Foundation of Heilongjiang Province, grant number YQ2023E039; Basic Scientific Research Operating Expenses of Heilongjiang Provincial Universities and Colleges of China, grant number 2022-KYYWF-0554; the Scientific and Technological Key Project of "Revealing the List and Taking Command" in Heilongjiang Province, grant number 2021ZXJ02A03, 2021ZXJ02A04; Heilongjiang University of Science and Technology Introduces High-level Talents Scientific Research Start-up Fund Project, grant number HKD202304; Heilongjiang Provincial Undergraduate Colleges and Universities Basic Research Operating Expenses for Scientific Research Projects Young Talent Program Projects, grant number 2023-KYYWF-0513; the Gansu Provincial Youth Doctoral Support Program, grant number 2024QB-103; and the Gansu Youth Science and Technology Foundation, grant number 24JRRA1012.

Data Availability Statement: The datasets used and analyzed in this study can be provided by the authors Gang Liu and Dongwei Wang, according to reasonable requirements.

Acknowledgments: This research was supported by the Heilongjiang Ground Pressure and Gas Control in Deep Mining Key Laboratory, Heilongjiang University of Science and Technology.

Conflicts of Interest: The authors declare no conflicts of interest.

References

1. Meng, Q.; Han, L.; Qiao, W.; Lin, D.; Wei, L. Numerical simulation study on optimized design of section shape of deep high-stress soft rock roadway. *J. Min. Saf. Eng.* **2012**, *29*, 650–656.
2. Sun, G.; Chen, G.; Yu, P. Optimization design and application of deep mining roadway section. *Coal Eng.* **2008**, *9*, 57–60.
3. Dai, Y.; Chen, W.; Liu, Q.; Yi, X. Optimization of roadway section in deep high geostress. *J. Rock Mech. Eng.* **2004**, *S2*, 4960–4965.
4. Lv, A. Selection method of underground chamber section shape in high stress areas. *J. Coal Sci.* **1997**, *5*, 49–52.
5. Yang, S.; Xu, W.; Wei, L.; Su, C. Statistical ontological modeling and experimental study of rock damage under uniaxial compression. *J. Hohai Univ. (Nat. Sci. Ed.)* **2004**, *02*, 200–203.
6. Yang, S.; Lu, Z.; Qu, T. Fine-scale test and simulation of crack extension in marble with single pore. *J. China Univ. Min. Technol.* **2009**, *38*, 774–781.
7. Yang, S.; Liu, X.; Li, Y. Experimental analysis of mechanical properties of sandstone with pore-containing fractures under uniaxial compression. *J. Rock Mech. Eng.* **2012**, *31*, 3539–3546.
8. Liu, Z.; Li, Y. Experimental study on the deformation and rupture law of rocks with holes under uniaxial compression. *Eng. Mech.* **2010**, *27*, 133–139. [CrossRef]
9. Zhou, J.; Yang, K.; Fan, K.; Zhao, T.; Qiu, D. Influence of fracture on mechanical and damage evolution characteristics of pore-bearing sandstone. *J. Cent. South Univ. (Nat. Sci. Ed.)* **2019**, *50*, 968–975.
10. Li, G.; Zhang, N.; Wang, C.; Zhang, L.; Li, B. Numerical simulation study on optimization of section shape of high geostress roadway. *J. China Univ. Min. Technol.* **2010**, *39*, 652–658.
11. Du, M.; Jing, H.; Su, H.; Zhu, T. Effect of pore shape on strength and damage characteristics of sandstone. *Eng. Mech.* **2016**, *33*, 190–196+219.
12. Xu, L.; Guo, S.; Davide, E.; Liu, H.; Hong, Z.; Xiao, T. Zonal rupture pattern and control of surrounding rock structure in deep roadways with different sections. *J. Geotech. Eng.* **2023**, *45*, 720–729.

13. Gao, F. Numerical simulation analysis of the influence of section shape on the stability of roadway surrounding rock. *J. Shandong Univ. Sci. Technol. (Nat. Sci. Ed.)* **2007**, *02*, 43–46.
14. Liu, G.; Wang, D.; Yang, Z. Mechanical properties and acoustic emission characteristics of sandstone with three holes under bias load. *J. Heilongjiang Univ. Sci. Technol.* **2023**, *33*, 875–881.
15. Zhao, G.; Wang, E.; Wu, H.; Qiu, J.; Dai, Y. Fine-scale fracture evolution law of porous sandstone under uniaxial compression. *J. Cent. South Univ. (Nat. Sci. Ed.)* **2019**, *50*, 1891–1900.
16. Li, D.; Zhu, Q.; Li, X. Research on the effect of pore shape on the mechanical properties of marble progressive damage. *J. Undergr. Space Eng.* **2018**, *14*, 58–66.
17. Lu, S.; Ma, F.; Lu, Y. Numerical simulation analysis of the stability of roadway with different section shapes under impact load. *J. Saf. Environ.* **2017**, *17*, 76–80. [CrossRef]
18. Yao, Z.; Fang, Y.; Zhang, R.; Pu, S.; Zhao, G.; Yu, T.; Ma, C. The Mechanism of Stick–Slip as a Rockburst Source in Jointed Rockmass: An Experimental Study. *Rock Mech. Rock Eng.* **2023**, *56*, 3573–3593. [CrossRef]
19. Yu, T.; Fang, Y.; Yao, Z.; Pu, S.; Ye, L.; Zhao, G. Bearing effect of prestressed bolt-anchored structures and mechanical analysis of surrounding rock. *Chin. J. Geotech. Eng.* **2022**, *44*, 1069–1077.
20. Sun, Y.; Xu, S.; Xu, C.; Huang, W.; He, J.; Rong, Y.; Zheng, F.; Ding, L. Study on the Stress and Deformation of Surrounding Rock and Support Structure of Super Large Section Tunnels Based on Different Excavation Methods. *Appl. Sci.* **2024**, *14*, 7025. [CrossRef]
21. Xu, H.; Zhang, Z.; Zhang, Y.; Jiang, Q.; Qiu, S.; Zhou, Y.; Feng, G. Effects of natural stiff discontinuities on the deformation and failure mechanisms of deep hard rock under true triaxial conditions. *Eng. Fail. Anal.* **2024**, *158*, 108034. [CrossRef]
22. Gu, H.; Lai, X.; Tao, M.; Momeni, A.; Zhang, Q. Dynamic mechanical mechanism and optimization approach of roadway surrounding coal water infusion for dynamic disaster prevention. *Measurement* **2023**, *223*, 113639. [CrossRef]
23. Zhu, T.; Jing, H.; Su, H.; Su, H.; Yin, Q.; Du, M. Experimental study on uniaxial compressive mechanical properties of sandstone containing double circular holes. *J. Geotech. Eng.* **2015**, *37*, 1047–1056.
24. Liu, G.; Wang, D.; Zan, Y.; Wang, S.; Zhang, Q. Feasibility Study of Material Deformation and Similarity of Spatial Characteristics of Standard Coal Rocks. *Processes* **2024**, *12*, 454. [CrossRef]
25. Song, Y.; Xing, T.; Zhao, T.; Gao, P. Acoustic emission characterization of uniaxial compressive deformation field evolution in rocks. *J. Rock Mech. Eng.* **2017**, *36*, 534–542. [CrossRef]
26. Xu, S.; Tong, L.H.; Xu, C.; Ding, H. On wave transmission in saturated soil system separated by a nonlinear isolated layer. *Comput. Geotech.* **2021**, *136*, 104211. [CrossRef]
27. Feng, G.; Ma, Q.; He, Z.; Su, G.; Chen, B. Time-delayed failure process of granite and its energy evolution and acoustic emission characteristics. *Eng. Fail. Anal.* **2024**, *157*, 107854. [CrossRef]
28. Zhang, Z. Energy Evolution Mechanism During Rock Deformation and Destruction. Ph.D. Thesis, China University of Mining and Technology, Beijing, China, 2013.
29. Zhang, Z.; Gao, F. Experimental study on energy evolution of red sandstone under uniaxial compression. *J. Rock Mech. Eng.* **2012**, *31*, 953–962.
30. Xie, H.; Peng, R.; Ju, Y. Analysis of energy dissipation during rock deformation and damage. *J. Rock Mech. Eng.* **2004**, *21*, 3565–3570.
31. Xie, H.; Ju, Y.; Lai, L. Rock strength and overall damage criterion based on the principle of energy dissipation and release. *J. Rock Mech. Eng.* **2005**, *17*, 3003–3010.
32. Zhang, G.; Zhao, Y.; Sun, Y.; Gong, Z. Study on energy evolution and infrared radiation characteristics of different seam coals under uniaxial compression. *Coal Sci. Technol.* **2024**, *11*, 1–13.
33. You, M.; Hua, A. Energy analysis of the damage process of rock specimens. *J. Rock Mech. Eng.* **2002**, *06*, 778–781.
34. Liang, C.; Li, X.; Wang, S.; Li, S.; He, J.; Ma, C. Experimental study on rate correlation and energy mechanism of uniaxial compressive stress-strain characteristics of rocks. *J. Rock Mech. Eng.* **2012**, *31*, 1830–1838.
35. Hou, Z.; Wang, Y.; Liu, D.; Li, C. Study on mechanical properties and energy evolution anisotropy of laminated marble rupture process. *J. Min. Saf. Eng.* **2019**, *36*, 794–804. [CrossRef]
36. Liu, G. Mechanical Response Mechanism and Engineering Application of Sandstone Under Unloading Path. Ph.D. Thesis, Anhui University of Technology, Huainan, China, 2021. [CrossRef]
37. Liu, G.; Xiao, F.; Qin, T. Mechanical properties and acoustic emission law of rock under small size effect. *J. Rock Mech. Eng.* **2018**, *37*, 3905–3917. [CrossRef]

buildings

MDPI

Article

Technology for Treatment and Reinforcement of Soft Rock Tunnel Floor Using Sealing Material

Yongli Liu [1,2,*], Lei Tao [3], Shenglei Zhao [3,4], Weixin Chen [2] and Yaozu Ni [2]

1 Institute of Interdisciplinary Research on Intelligent Mines, Heilongjiang University of Science and Technology, Harbin 150022, China
2 School of Minging Engineering, Heilongjiang University of Science and Technology, Harbin 150022, China; cwxkygcxy@163.com (W.C.); m18013974763@163.com (Y.N.)
3 School of Safety Engineering, Heilongjiang University of Science and Technology, Harbin 150022, China; m19917562464@163.com (L.T.); 19026845300@163.com (S.Z.)
4 Heilongjiang Longmei Jixi Mining Group Co., Ltd., Jixi 158199, China
* Correspondence: yongliliu1968@126.com

Abstract: To maintain the stability of soft rock tunnels, the research team proposed a support scheme involving "floor grouting + floor anchors + sealing material". This scheme incorporates a new sealing material with excellent mechanical properties, airtightness, and cost-effectiveness. To develop the sealing material, a series of proportioning tests and optimization designs were conducted to investigate how various experimental factors influence material performance. Based on these experiments, a regression prediction model was established to reveal the characteristics of factor interactions and determine the optimal mix ratio. Practical engineering validation confirmed that this support scheme effectively controls floor heave in soft rock tunnels.

Keywords: sealing material; airtightness; support scheme; soft rock tunnels; floor heave; orthogonal experiments

1. Introduction

Floor heave is a phenomenon in which the floor of a tunnel rises due to the deformation of the roof, floor, and sidewalls caused by changes in the stress state of the surrounding rock, a result of mining activity [1]. With global coal resources increasingly being mined at greater depths, many regions have entered a phase of deep coal extraction. Under the combined effects of intense mining and high stress at these depths, extensive damage to the surrounding rock is common, with floor heave being one of the most frequent manifestations of mine pressure [2,3]. As coal mining in China progresses into deeper levels, high-stress and intensive mining activities further exacerbate the instability and damage to the surrounding rock, with floor heave being a typical occurrence [4,5].

Current methods for controlling floor heave include reinforcement control, pressure relief control, and combined reinforcement and pressure relief control [2]. However, it is challenging to control floor heave deformation in soft rock tunnel floors using single control methods [6]. Thus, a comprehensive approach combining pressure relief and reinforcement is typically used. Hou Zhaojiong proposed a method for controlling floor heave by reinforcing the floor and sidewalls of tunnels based on the "two points and three zones" deformation characteristics of deep tunnels with floor heave [7]. Wen Zhijie and colleagues employed a range of control methods such as inverted arches, anchor support, and grouting reinforcement to achieve favorable results in floor heave management [8–10]. Liu Quansheng and others employed a combination of methods, including inverted concrete flooring, shallow and deep grouting, and high pre-stress composite anchors, to comprehensively prevent floor heave in fractured soft rock tunnels in deep mines [11]. Xie Guangxiang proposed the use of over-excavation, anchoring, and backfill technology to control floor heave deformation [12].

Inspired by these studies, a support scheme consisting of “floor grouting + floor anchors + sealing material” was developed specifically to address floor heave in deep soft rock tunnels mainly composed of sandy mudstone, commonly found in Western coal mines. The experimental setup involves installing anchors into the fractured floor, followed by grouting both the floor and the grouting holes along the fractures to create a cohesive bond. Finally, a sealing material is applied to cover the floor, creating an integrated support structure for the tunnel floor, enhancing the three-dimensional stress state around the tunnel and significantly increasing the strength of the rock [13–15]. The sealing material plays a crucial role in this floor heave control method by consolidating the loose surrounding rock on the floor surface, effectively isolating air and water to prevent erosion and degradation and increasing lateral constraint on the floor [16–22].

In summary, this study addresses floor heave control in soft rock tunnels by developing a sealing material with excellent mechanical properties and high airtightness. A comprehensive support scheme of “floor grouting + floor anchors + sealing material” was implemented and tested in an on-site industrial experiment to validate the effectiveness of this floor heave control strategy and ensure the practical use of the tunnel.

2. Sealing Material Ratio Experiment

2.1. Specimen Preparation and Curing

Ordinary Portland cement, river sand, and gravel from the Songhua River in Jilin were chosen as the main raw materials. The KS-20 tea-based water reducer from Sichuan Keshui Additives Co., Ltd., Sichuang, China, and the JJ91 silicon densifier from Harbin Tianxing Waterproof Materials Factory, Harbin, China, were selected as additives. The preparation process is shown in Figure 1.

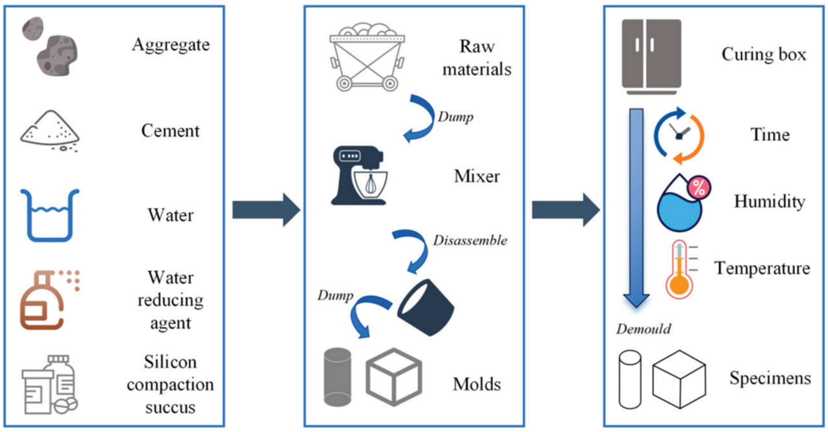

Figure 1. Preparation process of sealing material.

Two types of molds, φ 50 mm × 100 mm and 100 mm × 100 mm × 100 mm, were used to prepare the specimens. Following the order in Figure 1, aggregate, cement, water, water reducer, and silicon densifier were added to the mixer and stirred. The cement slurry was then poured into the molds, allowed to solidify, and cured in a curing chamber set to 21 °C and 98% humidity. After 28 days of curing, the specimens were demolded and labeled.

2.2. Experimental Scheme

2.2.1. Orthogonal Experimental Design

Generally, cement accounts for 15–20% of the mass in sealing materials. Based on extensive foundational experiments, the cement content was set at 28% of the total material mass to enhance material density. To determine the optimal ratio for the new airtight sealing material, an $L_9(3^4)$ orthogonal array was used to design the experimental plan, with the water–cement ratio, sand rate, water reducer dosage, and silicon densifier dosage as the four main factors. Each factor was tested at three levels, with compressive strength, tensile strength, and airtightness at 28 days as the evaluation indicators. The orthogonal test scheme is shown in Table 1.

Table 1. Orthogonal test program. X# denotes the number of trial groups and 1# denotes the 1st trial group. X = 1, 2, 3, 4, 5, 6, 7, 8, 9.

Groups	Factor Level (Code)			
	Water–Cement Ratio	Sand Rate	Water Reducing Agent Dosage	Silicon Compaction Succus Dosage
1#	1	1	1	1
2#	1	2	2	2
3#	1	3	3	3
4#	2	1	2	3
5#	2	2	3	1
6#	2	3	1	2
7#	3	1	3	2
8#	3	2	1	3
9#	3	3	2	1

2.2.2. Sieving Test

To ensure uniform aggregate gradation, the particle-size distribution of gravel and river sand was determined according to the DL/T5151-2001 standard [23] for sand and gravel aggregate testing in hydraulic concrete. An SXZ-100 top-striking standard vibrating sieve machine was used for the sieving experiment, with grading and classification in accordance with the GB/T14684-2001 standard [24] for construction sand. A sample of 3000 g of gravel and 500 g of river sand was randomly selected and baked at 105 ± 5 °C to a constant weight. After cooling to room temperature, particle size tests were conducted on both gravel and river sand. The gravel was sieved using meshes of 20 mm, 16 mm, 10 mm, 5 mm, 2 mm, 1.6 mm, and 1.25 mm, while dried river sand was sieved using 5 mm, 2.5 mm, 1.25 mm, 0.63 mm, 0.315 mm, and 0.16 mm meshes. The sieving test setup is shown in Figure 2.

(**a**) (**b**)

Figure 2. Sieving test: (**a**) sieving machine; (**b**) aggregate screening.

The sampling analysis of the sieved gravel and river sand showed that the gravel was primarily in the 2–10 mm range. The fineness modulus of the river sand was calculated to be 2.0, classifying it as medium sand. The analysis results are shown in Table 2, and the particle-size distribution is illustrated in Figure 3.

Table 2. Sampling analysis form.

Classification	Particle Size (mm)	Particle-Size Mass (g)	Particle-Size Mass Fraction (%)	Cumulative Mass (g)	Cumulative Mass Fraction (%)
Stone	16	7.00	0.234	2996.70	100.000
	10	12.00	0.400	2989.70	99.766
	5	2373.00	79.187	2977.70	99.366
	2	421.00	14.049	604.70	20.179
	1.6	35.80	1.195	183.70	6.130
	1.25	29.10	0.971	147.90	4.935
	0	118.80	3.964	118.80	3.964
River sand	5	15	3	15	3
	2.5	75	15	90	18
	1.25	95	19	185	37
	0.630	105	21	290	58
	0.315	115	23	405	81
	0.160	85	17	490	98
	0	10	2	500	100

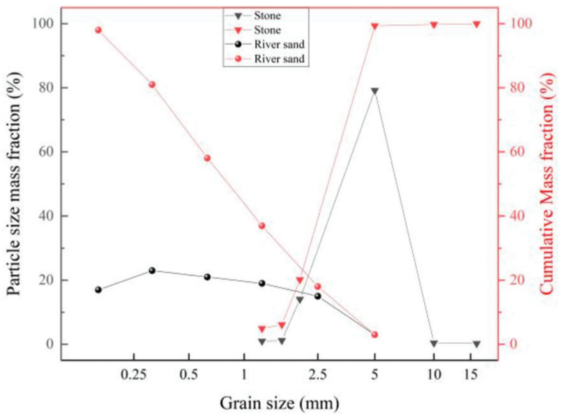

Figure 3. Graph of particle size analysis.

2.2.3. Compression Test

To evaluate the compressive properties of the material, uniaxial compression tests were performed on cubic specimens cured for 28 days, using a TAW-2000 kN computer-controlled electro-hydraulic servo triaxial testing machine. The setup is shown in Figure 4.

(**a**)

(**b**)

Figure 4. Compression test: (**a**) triaxial testing machine; (**b**) uniaxial compression.

2.2.4. Tensile Test

Using water-jet cutting technology, the φ 50 mm × 100 mm specimens cured for 28 days were cut. For each mix ratio, three φ 50 mm × 25 mm specimens were prepared and subjected to a Brazilian splitting test at a loading rate of 0.5 mm/min. The setup for the tensile test is shown in Figure 5.

(a)

(b)

Figure 5. Tensile test: (**a**) tension test specimen; (**b**) Brazilian splitting.

2.2.5. Airtightness Test

After 28 days of curing, φ 50 mm × 100 mm specimens of various mix ratios were sealed with paraffin and placed in an SHQ automatic concrete permeability tester. The air pressure was maintained at 0.6 MPa for 8 h, and data on air permeability were collected within the subsequent 30 min. The airtightness coefficient was calculated using Darcy's law. Airtightness Tes is shown in Figure 6.

(a)

(b)

Figure 6. Airtightness test: (**a**) airtightness testing instrument; (**b**) test specimen.

3. Experimental Results and Analysis

3.1. Results

According to the experimental design, nine groups of specimens with different mix ratios were tested for mechanical properties and airtightness. The test results are shown in Table 3.

Table 3. Orthogonal test results. X# denotes the number of trial groups and 1# denotes the 1st trial group. X = 1, 2, 3, 4, 5, 6, 7, 8, 9.

Matching Scheme	Water (%)	Cement (%)	Water Reducing Admixture (‰)	Silicon Compaction Succus (%)	River Sand (%)	Stone (%)	Compressive Strength (MPa)	Tensile Strength (MPa)	Airtightness (10^{-12} cm/h)
1#	11.20	28.00	0.03	0.84	17.98	41.95	42.8	1.8	82.3
2#	11.20	28.00	0.06	1.12	20.87	38.76	52.2	2.35	42.5
3#	11.20	28.00	0.08	1.40	23.73	35.59	45.8	2.8	62.9
4#	12.60	28.00	0.06	1.40	17.38	40.56	51	2.3	300.5
5#	12.60	28.00	0.08	0.84	20.47	38.01	35.8	2.5	370.9
6#	12.60	28.00	0.03	1.12	23.30	34.95	51	1.9	320.22
7#	14.00	28.00	0.08	1.12	17.04	39.76	42	2.4	600.5
8#	14.00	28.00	0.06	1.40	19.79	36.75	44.54	1.8	48.9
9#	11.20	28.00	0.03	0.84	17.98	41.95	46.18	1.9	645.9

3.2. Fitting Analysis

The experimental data were analyzed using SPSS to perform a multiple nonlinear regression and establish a predictive regression model for material performance as a function of the influencing factors. In the regression equations, Y_1, Y_2, and Y_3 represent compressive strength, tensile strength, and airtightness, respectively, while A, B, C, and D represent the water–cement ratio, sand rate, water reducer dosage, and silicon densifier dosage. This formula can be used to approximately regulate material performance.

$$Y_1 = 21.32 - 4.26B + 15.66C + 16.51D + 1.33B^2 - 5.57C^2 - 4.29D^2 + 2CD \quad (1)$$

$$Y_2 = 1.15 + 0.44C + 0.31D - 0.04A^2 - 0.03D^2 + 0.01BD - 0.04CD \quad (2)$$

$$Y_3 = (-176.5 + 356.9A + 167.94B^2 + 34.23D^2 - 153.67AB + 24.46AC - 14.25BC - 157.99BD) \times 10^{-12} \quad (3)$$

The fitting results are shown in Table 4.

Table 4. Fitting results.

	R^2	R^2_{adj}	F	P
Compressive strength	0.99	0.99	532.6515	0.0334
Tensile strength	0.99	0.99	3152.35	0.0068
Airtightness	0.99	0.99	1408.86	0.0001

R^2 is the coefficient of determination, R^2_{adj} is the corrected coefficient of determination, F denotes the significance of the fitted equation, and P denotes an indicator of the magnitude of the difference between the control and test groups.

$R^2 > 0.98$ and $R^2_{adj} > 0.98$ indicate that the regression model has a good fit. $F \gg P$, proving that the regression model is statistically significant. And $P < 0.05$ proves that the model fit is significant. In order to further verify the accuracy of the regression equation, the level value data from the nine groups of orthogonal test protocols were substituted into the above fitting equations, and after solving the calculated values of the equations, the differences between the calculated values and the experimental values were compared, and it was finally concluded that the relative error was within the range of −3%~+3%, which indicated that the calculated values of the regression model were close to the actual values, thus proving the accuracy of the model.

With $R^2 > 0.98$ and $R^2_{adj} > 0.98$, the regression model demonstrates a high degree of fit. The F value is much larger than P, indicating statistical significance, while $P < 0.05$ verifies the model's efficacy. To further validate the accuracy of the regression equation, the level values from the nine groups of the orthogonal test were substituted into the model, and the calculated values were compared with the experimental values, showing a relative error between −3% and +3%, thus proving the model's accuracy.

3.3. Analysis of the Effects of Single Factors

Range analysis, a statistical method used to evaluate the influence of various factors on a given outcome, assesses the significance of each factor by comparing the difference between the maximum and minimum response values across different levels of the factors under study. By comparing the maximum and minimum results across different levels (range analysis), the impact of each factor on the experiment outcomes was determined. This method, often used in quality control and industrial experiments, helps to quickly identify the most influential factors. Range analysis results for each factor′s influence on different material properties are shown in Table 5 and illustrated in Figure 7.

In order to show the significance of each influencing factor more intuitively, the degree of influence between each factor and each property of the material is plotted according to Table 5, as shown in Figure 7.

Table 5. Range analysis of each influencing factor on performance indicators.

	Factor	Same Level			Average at the Same Level			Extreme Difference
		K_1	K_2	K_3	$\overline{K_1}$	$\overline{K_2}$	$\overline{K_3}$	ΔK
Compressive strength	Water–cement ratio	140.80	137.80	132.72	46.93	45.93	44.24	2.69
	Sand rate	135.80	132.54	142.98	45.27	44.18	47.66	3.48
	Water reducer dosage	138.34	149.38	123.60	46.11	49.79	41.20	8.59
	Silicon densifier dosage	124.78	145.20	141.34	41.59	48.40	47.11	6.81
Tensile strength	Water–cement ratio	7.0	6.7	6.1	2.3	2.20	2.03	0.28
	Sand rate	6.5	6.7	6.6	2.2	2.22	2.20	0.05
	Water reducer dosage	5.5	6.6	7.7	1.8	2.18	2.57	0.73
	Silicon densifier dosage	6.2	6.7	6.9	2.1	2.22	2.30	0.23
Airtightness	Water–cement ratio	457.7	769.6	1275.3	152.57	256.54	425.10	272.53
	Sand rate	781.3	582.3	1139.0	260.43	194.10	379.67	185.57
	Water reducer dosage	491.4	886.9	1124.3	163.81	295.63	374.77	210.96
	Silicon densifier dosage	1139.1	1063.2	300.3	379.70	354.41	100.10	279.60

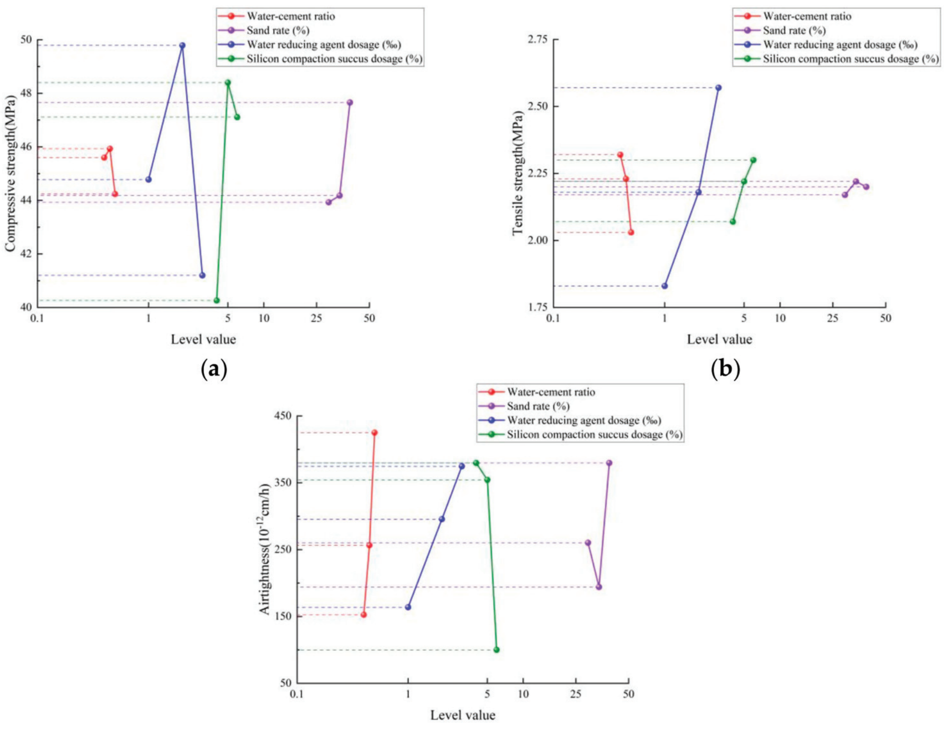

Figure 7. Degree of influence of single factors on various properties of materials: (**a**) patterns of influence on compressive strength; (**b**) patterns of influence on tensile strength; (**c**) patterns of influence on airtightness.

3.3.1. Analysis of the Influence Pattern of Each Factor on Compressive Strength

Using orthogonal tests, uniaxial compressive strength tests were conducted on sealing material specimens with different mix ratios. The stress–strain curves were obtained from initial loading to complete failure, allowing an analysis of the ultimate load-bearing capacity and compressive strength of the various formulations. Due to the large number of uniaxial test samples, each formulation's typical failure characteristics and stress–strain curves were selected, as shown in Figure 8. Most samples exhibited longitudinal splitting as the primary failure mode, with some localized shear failure. Even after complete failure, the stress–strain curves still displayed residual stress, attributed to the support structure of the sealing material.

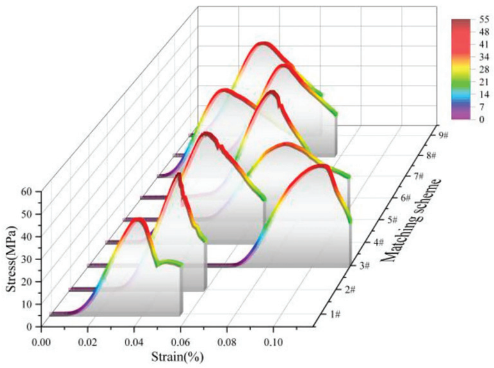

Figure 8. The stress–strain curves corresponding to different matching schemes. X# denotes the number of trial groups and 1# denotes the 1st trial group. X = 1, 2, 3, 4, 5, 6, 7, 8, 9.

As shown in Figure 8, among the factors affecting compressive strength, water reducer dosage has the largest differential effect, indicating it is the most significant factor influencing compressive strength. In contrast, the water–cement ratio showed only a minor effect on compressive strength. The primary-to-secondary sequence of factors affecting the 28-day compressive strength of this sealing material is as follows: water reducer dosage > silicon densifier dosage > sand rate > water–cement ratio.

Water reducers are concrete additives that, when added in appropriate amounts during mixing, effectively reduce water demand, thereby increasing the material's strength and durability, as well as improving its workability and mitigating shrinkage and cracking issues [25]. The experimental results indicate that adding a water reducer significantly enhances the compressive strength of the sealing material. However, an excessive water reducer may lead to over-fluidity, potentially causing phase separation. Considering the properties of the water reducer and the industrial background, reducing water demand while maintaining slump, enhancing material strength, and reducing costs is sufficient.

3.3.2. Analysis of the Influence Pattern of Each Factor on Tensile Strength

In practical engineering, soft and deformable tunnel surrounding rock is vulnerable to deformation and damage, especially under deep mining-induced stress, due to weak planes like stratifications and joints. Sandy mudstone tunnels have an average tensile strength of only 2.1 MPa, making tensile strength crucial for the sealing material.

In the tensile tests, the sealing material specimens fractured along the centerline of the disk under tensile stress, with the fracture initiation points aligned with the blade contact points, achieving effective tensile rupture. The stress–time curves for specimens with different formulations generally show a gradual increase, followed by a sudden drop, with a residual stress close to zero. Typical stress–time curves from initial loading to complete failure were selected for each formulation, as shown in Figure 9.

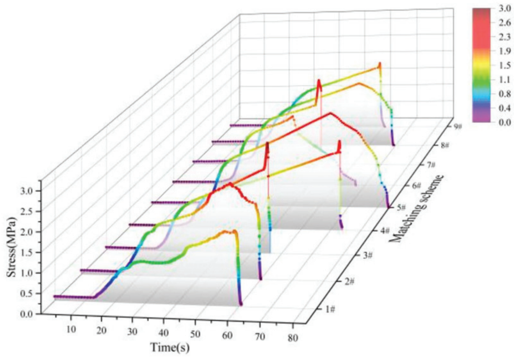

Figure 9. The stress–time curves corresponding to different matching schemes. X# denotes the number of trial groups and 1# denotes the 1st trial group. X = 1, 2, 3, 4, 5, 6, 7, 8, 9.

As shown in Figure 9, the hierarchy of factors affecting the 28-day tensile strength of the sealing material is as follows: water reducer dosage > water–cement ratio > silicon densifier dosage > sand rate.

3.3.3. Analysis of the Influence Law of Each Factor on Airtightness

As the water–cement ratio and water reducer dosage increase, the water content in the sealing material also increases, reducing its density and increasing its permeability, thereby weakening its airtightness. Airtightness is also related to the aggregate particle size. For the same weight, river sand has a higher specific surface area than stone. After mixing with cement slurry, the larger contact surface between river sand and cement creates air channels, reducing airtightness. When the river sand rate is low and stone content is high, the larger aggregate voids can also lower airtightness. A higher silicon densifier content improves material density, thereby enhancing airtightness. The primary-to-secondary sequence of factors affecting airtightness in the sealing material is as follows: silicon densifier dosage > water reducer dosage > water–cement ratio > sand rate.

3.4. Multi-Factor Analysis

The regression analysis of the test results shows that material properties are influenced not only by single factors but also by interactions between factors. Using the regression model, three-dimensional surface plots were created to visualize the interactions between paired factors, as shown in Figure 10.

In the 3D regression surface plots, a steeper slope and faster color changes indicate a stronger effect of factor interactions on material performance. Additionally, darker colors indicate better material performance, while lighter colors suggest poorer material performance.

Figure 10a–c show the interaction effects on compressive strength.

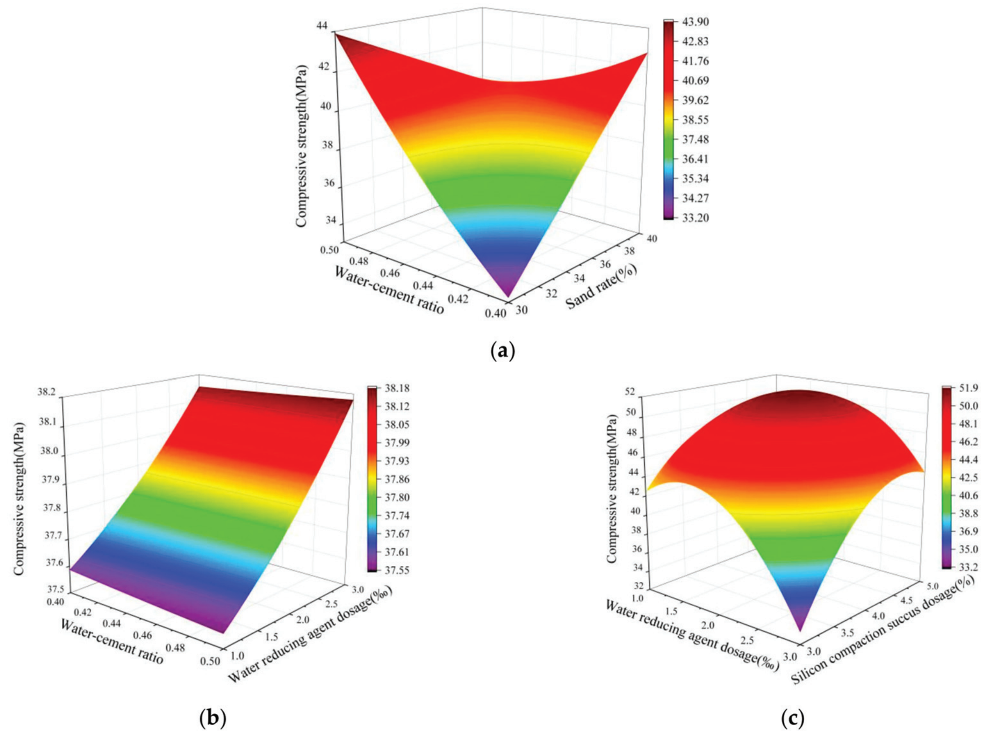

Figure 10. *Cont*.

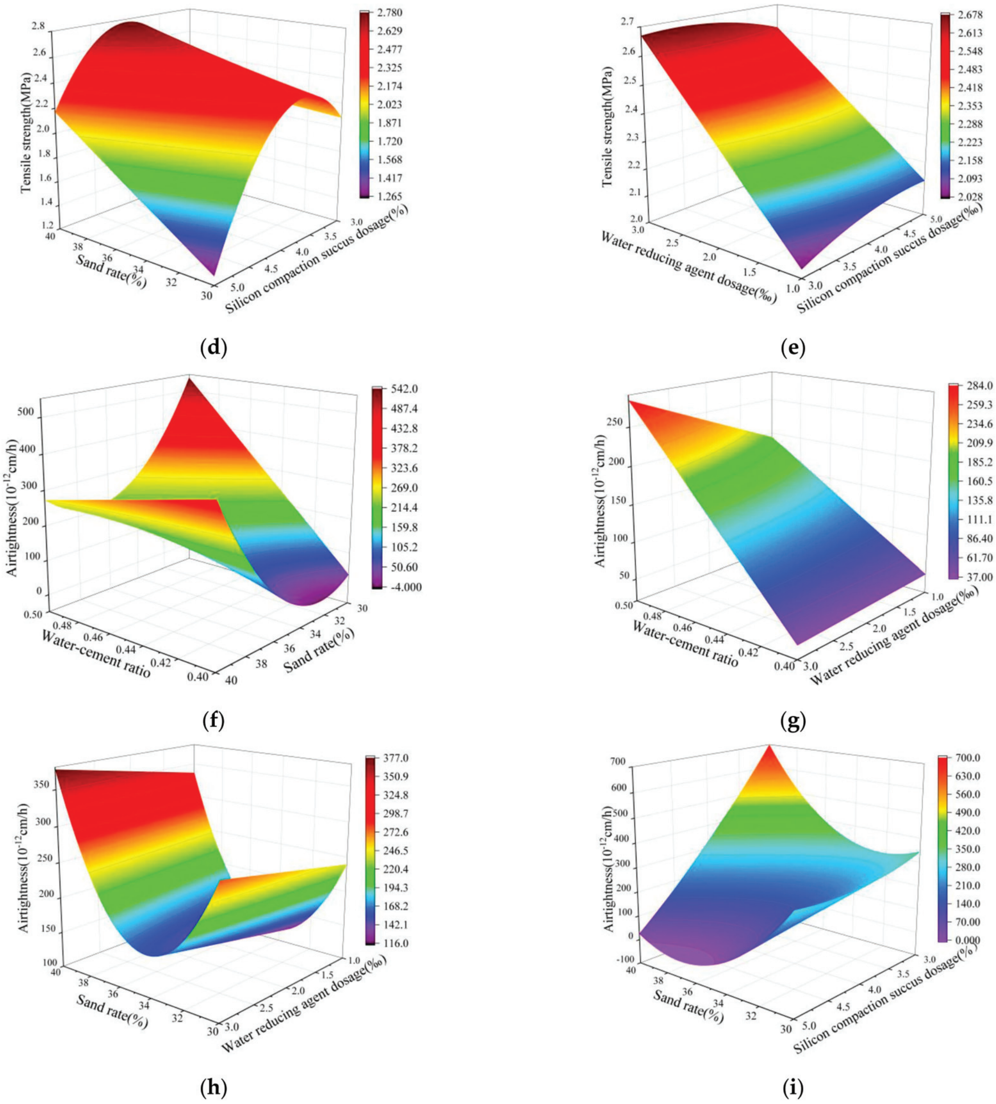

Figure 10. Three-dimensional regression analysis of surface plots: (**a**) effect of interaction of water–cement ratio and sand rate on compressive strength; (**b**) effect of interaction of water–cement ratio and water reducing agent dosage on compressive strength; (**c**) effect of interaction of water reducing agent dosage and silicon compaction succus dosage on compressive strength; (**d**) effect of interaction of sand rate and silicon compaction succus dosage on tensile strength; (**e**) effect of interaction of water reducing agent dosage and silicon compaction succus dosage on tensile strength; (**f**) effect of interaction of water–cement ratio and sand rate on airtightness; (**g**) effect of interaction of water–cement ratio and water reducing agent dosage on airtightness; (**h**) effect of interaction of sand rate and water reducing agent dosage on airtightness; and (**i**) effect of interaction of sand rate and silicon compaction succus dosage on airtightness.

Figure 10a reveals a V-shaped influence pattern for the interaction between water–cement ratio and sand rate. The peak strength of approximately 33.5 MPa occurs when the water–cement ratio is low and the sand rate is in the range of 30–34%, as indicated by the red region. As the water–cement ratio and sand rate increase or decrease from this range, the compressive strength gradually decreases, with the color shifting from red to green and blue, indicating a minimum compressive strength around 33 MPa. The optimal water–cement ratio is approximately 0.42, particularly when the sand rate is between 32 and 34%, suggesting that this combination minimizes porosity and enhances compressive strength. Increasing the water–cement ratio beyond 0.46 reduces the strength due to excessive dilution of the cement paste, weakening the hardened strength. Similarly, increasing the sand rate from 30% to 40% lowers the compressive strength, likely due to a reduced bond strength between aggregate and cement paste. Thus, a balanced water–cement ratio near 0.42 and a moderate sand rate are essential for maximizing the compressive strength, with the optimal sand rate range being 32 and 34%.

Figure 10b shows that as the water–cement ratio increases, the compressive strength decreases, while an increase in water reducer dosage slightly improves the compressive strength, albeit with a limited effect. The strength values range from 37.55 MPa to 38.18 MPa, with the narrow color gradient indicating a limited impact from water reducer. The optimal compressive strength occurs with a low water–cement ratio (around 0.42) and shows minor improvement with an increased water reducer dosage, especially when the water–cement ratio is already low. As the water–cement ratio increases, the compressive strength decreases, transitioning from red to blue, indicating excessive water in the concrete that compromises hardening and strength. A water reducer dosage between 0.5‰ and 3.0‰ has a minor effect on compressive strength, with a limited enhancement within this range, especially when the water–cement ratio is high.

Figure 10c illustrates the interaction between water reducer dosage and silicon densifier dosage on compressive strength, showing a parabolic curve that opens downward. The compressive strength initially increases and then decreases as the water reducer dosage increases, suggesting a significant interaction between the water reducer and silicon densifier when the water–cement ratio is 0.45 and sand rate is 35%.

Figure 10d,e depict the interaction effects on tensile strength.

In Figure 10d, the interaction between sand rate and silicon densifier dosage on tensile strength forms a parabolic ridge. Within the silicon densifier dosage threshold, the tensile strength increases with a higher sand rate, reaching a maximum at 40%, indicating that increasing the sand rate enhances gelation and thus tensile strength, regardless of silicon densifier dosage. Conversely, the tensile strength first increases and then decreases with a higher silicon densifier dosage, peaking at 4%, which suggests the silicon densifier dosage is critical to gelation. Both factors have significant interactive effects on tensile strength, with the silicon densifier dosage having slightly less impact than the sand rate.

Figure 10e shows the interaction between water reducer and silicon densifier dosage on tensile strength. As the silicon densifier dosage increases, the tensile strength decreases slightly with a higher water reducer dosage, suggesting excess water reducer can hinder gelation, reducing tensile strength.

Figure 10f–i show the interaction effects on airtightness. In these regression plots, steep slopes and dense contour lines indicate strong interaction effects on airtightness.

Figure 10f,g show that increasing the water–cement ratio reduces airtightness. A lower water reducer dosage always improves airtightness, consistent with the single-factor analysis results. In Figure 10h, at low water–cement ratios, the airtightness remains stable with an increased water reducer dosage, but the increase in water–cement ratio amplifies permeability. For instance, at a water–cement ratio of 0.5, the permeability increases from 193.78×10^{-12} cm/h to 283.54×10^{-12} cm/h as the water reducer dosage increases.

In each plot, the sand rate generally follows a downward parabolic curve in relation to airtightness, with an optimal sand rate for maximum airtightness. Figure 10i shows that increasing the sand rate initially decreases and then increases permeability, with the minimum permeability decreasing as the silicon densifier dosage increases. Additionally, at low sand rates, permeability initially decreases and then increases with a higher silicon densifier dosage, with minor changes. At high sand rates, permeability decreases, and the upward trend becomes more pronounced with an increasing sand rate.

In summary, the regression surface plots in Figure 10 align with the range analysis results in Table 5, confirming the feasibility of using regression models to optimize the mechanical properties of the sealing material.

3.5. Result Verification and Applicability Analysis

Considering the effectiveness of the regression model and range analysis, a multi-objective optimization was conducted using MATLAB R2020's genetic algorithm, with cost constraints factored into the boundary conditions. The optimal model parameters were found to be as follows: A = 0.4985, B = 37.45, C = 2.26, D = 4.6. This results in the following optimal material ratio: water 13.96%, cement 28%, river sand 21.23%, stone 35.46%, water reducer 0.06%, and silicon densifier 1.29%.

Verification experiments with the optimal mix were conducted, and Table 6 compares the measured and predicted values.

Table 6. Predicted values and actual values.

Material Function	Predicted Value	Actual Value	Error Rate (%)
Compressive strength (MPa)	41.24	40.56	1.68
Tensile strength (MPa)	2.22	2.12	4.72
Airtightness (10^{-12} cm/h)	80.06	78.99	1.35

Through the analysis of Table 6, the error rates for all performance indicators are below 5%, indicating a good fit between the measured and predicted values, which demonstrates the reliability of the regression model parameters for optimizing the sealing material ratio.

4. Engineering Practice

4.1. Support Scheme

To address the floor heave issue in the 11,303 roadway at Hongqingliang Coal Mine, a support scheme of "floor grouting + floor anchors + sealing material" was adopted, as shown in Figure 11. The roadway floor was first leveled, and grouting reinforcement was applied. Following grouting, high-strength anchors (φ 20 mm × 2500 mm) were installed with a spacing of 700 mm × 800 mm. A 50 mm sealing layer and a 200 mm concrete layer were then applied to complete the support system.

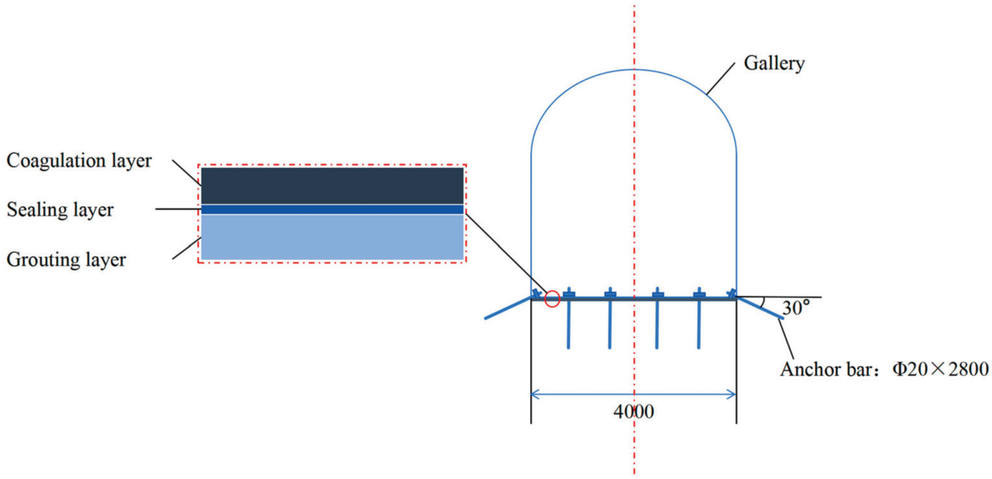

Figure 11. Support system.

4.2. Monitoring Floor Deformation

A section of the heave-prone roadway in the 11,303 working face of the Hongqingliang Coal Mine was selected as the research subject, and the deformation of the floor was monitored after the support was completed. An observation point was set 1 m away from the working face, and four measurement points were arranged using the cross-measurement method to observe the displacement of the roof, floor, and two sides. The observation point remained stationary as the working face advanced normally. The monitoring points and observation locations are shown in Figure 12.

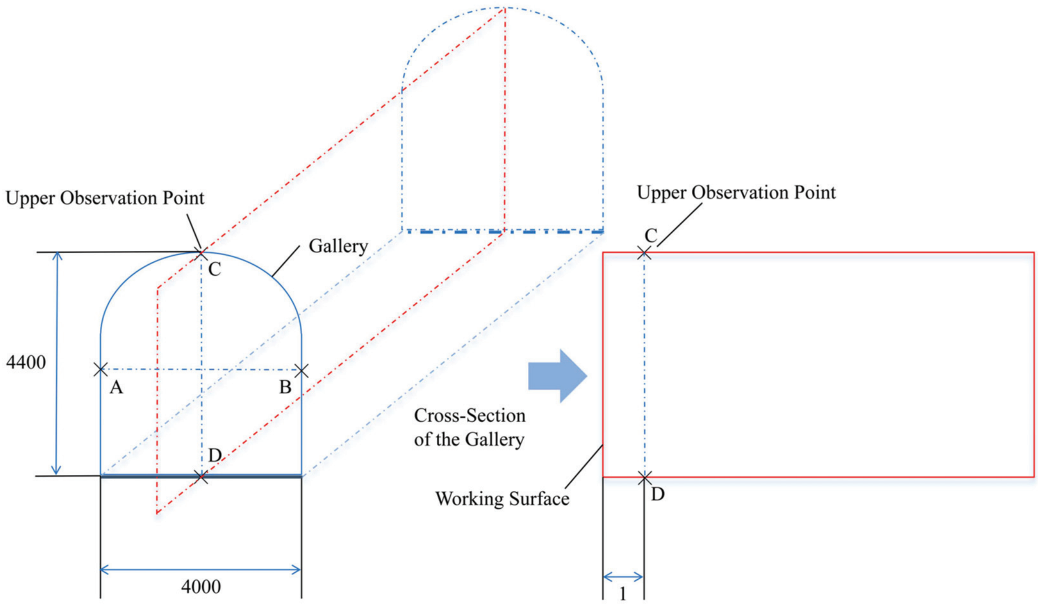

Figure 12. The observation points and location.

The deformation characteristics of the surrounding rock obtained from the monitoring are shown in Figure 13. As shown in Figure 13, the cumulative displacements of the roof, floor, left wall, and right wall were 124 mm, 150 mm, 110 mm, and 92 mm, respectively. Among these, the floor experienced the largest cumulative deformation, with a maximum of 150 mm, which is much lower than the floor deformation before the support measures (over 700 mm). This indicates that the support measures effectively suppressed the deformation of the surrounding rock and met the industry standard requirement that the floor heave in soft rock tunnels should be controlled within 200 mm.

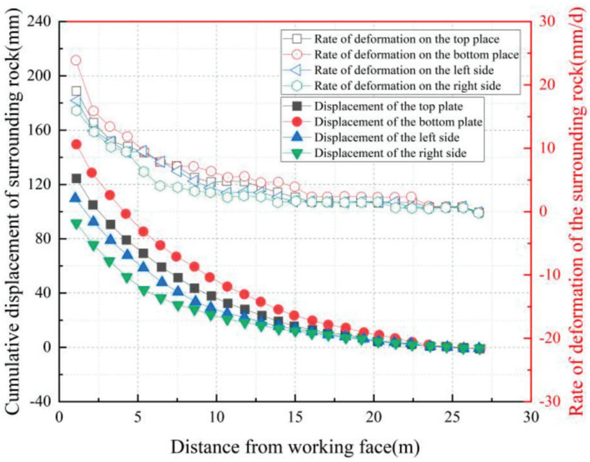

Figure 13. Deformation curve of roadway bottom plate.

Furthermore, the deformation rate analysis showed that the deformation rate of the surrounding rock increased as the distance to the working face decreased, with the highest deformation rate (24 mm/day) occurring in the region between 1 m and 2.5 m from the working face. This rate suggests that in areas strongly affected by mining, the floor support should be strengthened to prevent further deformation that could exceed safety thresholds (typically 30 mm/day).

The support measures enhanced the overall strength and stability of the surrounding rock, suppressed stress concentration and deformation development, and effectively controlled the plastic deformation and creep effect of the floor. Additionally, by grouting to seal cracks and anchoring the support, the influence of hydrological effects on the surrounding rock structure was reduced, significantly decreasing the floor heave. The deformation data from the tunnel monitoring points indicate that grouting the soft rock floor and covering it with an airtight and waterproof sealing material reduced the average floor heave from 700 mm to a maximum of 150 mm—a 4.7-fold reduction. This demonstrates that the technique can reinforce the soft rock floor, ensuring the roadway remains suitable for operational use.

5. Discussion

The support technology based on a combination of pressure relief and reinforcement proposed in this study effectively controls the bottom heave deformation of the Hongqingliang soft rock tunnel through the combination of "floor grouting + bottom side anchor bolts + sealing materials [2,4,5]". Compared to traditional support methods, this approach significantly reduces the likelihood of bottom heave by enhancing the strength of the surrounding rock, improving the stability of the support structure, and preventing groundwater infiltration [26,27]. This innovative support method provides a new solution for the design of soft rock tunnels.

In terms of research methods, this study used fitting methods to analyze the support effect and verified the feasibility of the design through regression analysis. Although this method improves the analytical precision, its applicability under complex geological conditions still needs further validation. In the future, machine learning techniques could be considered to enhance the accuracy of material performance research and support effect predictions [28]. Economically, although the initial investment is relatively high, this support method can effectively reduce maintenance costs and improve tunnel stability in the long term, thus offering a high cost-effectiveness. However, the complexity of the experiments is high, and machine learning could be used in the future to further optimize the support design, improving its efficiency and applicability.

Overall, the support scheme proposed in this study provides a new technical path for the safety and sustainable development of mining engineering.

6. Conclusions

1. Performance Characteristics and Influencing Factors

Experimental analysis revealed that the compressive and tensile strengths of the sealing material are significantly affected by water reducer dosage, with strength increasing as the dosage rises but decreasing when it is reduced. Key factors influencing airtightness include the water–cement ratio, sand rate, and water reducer and silicon densifier dosage. Lower water–cement ratios and an appropriate water reducer content enhance airtightness, while a higher silicon densifier content also contributes positively. Adjusting the sand rate to meet specific mixing requirements further optimizes the overall performance.

2. Optimal Mix Ratio and Predictive Accuracy

Using SPSS regression analysis and genetic algorithm optimization, the optimal mix ratio of the sealing material was determined to be water 13.96%, cement 28%, river sand 21.23%, stone 35.46%, water reducer 0.06%, and silicon densifier 1.29%. Experimental validation showed that the material's performance indicators deviate by less than 5% from the predicted values, confirming the accuracy and scientific reliability of the optimization method. These results provide a solid foundation for advancing the application of sealing materials in engineering practices.

3. Field Application and Future Outlook

The integrated support scheme of "floor grouting + floor anchors + sealing material" successfully mitigated floor heave in roadways, demonstrating the effectiveness, reliability, and economic benefits of this sealing material-based reinforcement technology for soft rock tunnel floors. Future research should focus on further enhancing the material's mechanical properties and exploring its adaptability under diverse geological and environmental conditions, contributing to more sustainable and efficient tunnel reinforcement solutions.

Author Contributions: Conceptualization, W.C.; methodology, Y.L.; data curation, L.T., Y.N., and S.Z.; software, S.Z. and Y.N.; validation, W.C.; formal analysis, L.T.; investigation, L.T.; resources, Y.L.; writing—original draft, L.T.; writing—review and editing, W.C. and Y.N.; visualization, S.Z.; supervision, Y.L.; project administration, Y.L. All authors have read and agreed to the published version of the manuscript.

Funding: This work was supported by the Scientific and Technological Key Project of "Revealing the List and Taking Command" in Heilongjiang Province (2021ZXJ02A03, 2021ZXJ02A04).

Data Availability Statement: The original contributions presented in the study are included in the article, further inquiries can be directed to the corresponding author.

Conflicts of Interest: Author Shenglei Zhao was employed by the company Heilongjiang Longmei Jixi Mining Group Co., Ltd. The remaining authors declare that the research was conducted in the absence of any commercial or financial relationships that could be construed as a potential conflict of interest.

References

1. Wang, C.; Wang, Y.; Lu, S. Deformational behaviour of roadways in soft rocks in underground coal mines and principles for stability control. *Int. J. Rock Mech. Min. Sci.* **2000**, *37*, 937–946. [CrossRef]
2. Xiao, T.Q.; Wang, Z.Y.; Liu, F.Y.; Dai, X.L.; Zhao, S.; Yu, Z.H. Study on the mechanism and technology of floor heave control of deep roadway with strong mining pressure. *Min. Saf. Eng.* **2023**, *41*, 666–676. [CrossRef]
3. Bai, J.B.; Li, W.F.; Wang, X.Y.; Xu, Y.; Huo, L.J. Mechanism of floor heave and control technology of roadway induced by mining. *J. Min. Saf. Eng.* **2011**, *28*, 1–5. Available online: https://kns.cnki.net/kcms2/article/abstract?v=rNedIcCUbLCYkAGH9pxZ54_EIZorcqerlBeENe7M0GsrqO8kCD1iLojOXZtUlOcWOVPWqDOeBR2V0hu_Tt3_D_XkS5gAt1pEy0FaZqt6QSBjdATTPucPcIMUx_OBCP-1z9_gJwbqCzE=&uniplatform=NZKPT&language=CHS (accessed on 9 November 2023).
4. Bai, J.B.; Hou, C.J. Control principle of surrounding rocks in deep roadway and its application. *J. China Univ. Min. Technol.* **2006**, *35*, 145–148. Available online: https://kns.cnki.net/kcms2/article/abstract?v=rNedIcCUbLAgZUQYLMKK7WTz4IO-Bouohp1UaY7r_FtXxpnfPLetZ0Zp0_kjfDPPY2IyLE8CPep2R7FHeC7wWbDyUCcYHXYyGT3yfBiltAO5p6ptQk4ulSXRT_Nhjh2IUjc42bwHS6U=&uniplatform=NZKPT&language=CHS (accessed on 9 November 2023).
5. Li, H.M.; Fu, K. Somemajor technical problems and countermeasures for deep mining. *J. Min. Saf. Eng. 2006, 468–471.* Available online: https://kns.cnki.net/kcms2/article/abstract?v=rNedIcCUbLC0RKqvlSFOr0rSyI9Ygy9psIGY5FNPahP0CmDfOepGNtniax9AwEquNXxJgG5nqutMmQiNVQyjEy62BtCLTfypcSJuWeKTGRIb40Xget0luFqXh7l4gXd9W3Zq9nGEv_U=&uniplatform=NZKPT&language=CHS (accessed on 9 November 2023).
6. Hou, C.J.; Wang, X.Y.; Bai, J.B.; Meng, N.K.; Wu, W.D. Basic theory and technology study of stability control for surrounding rock in deep roadway. *J. China Univ. Min. Technol.* **2021**, *50*, 1–12. [CrossRef]
7. Hou, C.J. Key technologyies for surrounding rock control in deep roadway. *China Univ. Min. Technol.* **2017**, *46*, 970–978. [CrossRef]
8. Wen, Z.J.; Lu, J.Y.; Xiao, Q.H.; Chen, G.Y.; Yang, T.; Jiang, Y.J.; Li, L.P.; Yang, S.L.; Zhao, R.L.; Chen, W.M. Failure mechanism of floor heave and supporting technology of soft rock roadway. *China Coal J.* **2019**, *44*, 1991–1999. [CrossRef]
9. Wang, J.; Hao, Y.X.; Guo, Z.B.; Zhu, G.L.; Han, Z. Floor heave mechanism and control technology for east rail roadway of Tingnan coal mine. *Min. Saf. Eng.* **2015**, *32*, 291–297. [CrossRef]
10. Zhang, B.; Bo, J.B.; Yan, S.; Wang, R.; Meng, N.K.; Wang, G.Y. Failure mechanism of surrounding rock and control of floor heave in heterogeneous composite rock roadway. *Chin. J. Geotech. Eng.* **2022**, *44*, 1699–1709. Available online: https://kns.cnki.net/kcms2/article/abstract?v=KaAwsYWd1tItBwqT5gnD49OaENbuHdIkkLO4CtYYLS9alXvfKJ2KpPNGhEvog26WcC898dowbXGhPyTnCiywrXGttGPcSHpVS7RyfkjOF6etzguFKhuevuf6s1QXJabCpgkfKjmBtN3beAgr72UGTg==&uniplatform=NZKPT&language=CHS (accessed on 9 November 2023).
11. Liu, Q.S.; Liu, X.W.; Huang, X.; Liu, B. Research on the floor heave reasons and supporting measures of deep soft-fractured rock roadway. *China Coal J.* **2013**, *38*, 566–571. [CrossRef]
12. Xie, G.X.; Chang, J.C. Study on overcutting-bolting & grouting-backfilling concete to control the floor heave of deep mine roadway. *China Coal J.* **2010**, *35*, 1242–1246. [CrossRef]
13. Kang, H.P. Stressdistribution characteristics and strata control technology for roadways in deep coal mines. *Coal Sci. Technol.* **2013**, *41*, 12–17. [CrossRef]
14. Li, G.C. Study on the Surrounding Rock Stability and Safety Control of Roadways Roof Embedded Weak Intercalated Weak Intercalated Seam. Ph.D. Thesis, China University of Mining and Technology: Xuzhou, China, 2008. Available online: https://kns.cnki.net/kcms2/article/abstract?v=KaAwsYWd1tJ9-l6kWw4uOZE0-EdJ6xo4Y-H7NkwSUbrgon3_yNaY7ldkgrSFdMncabxSAH0GHIhbxQ2zhbzPaK4WclfsM8VfJaKZk5i4_f_dnEiBBNR-IwLWcjT-zVa4cq-77me3zHt2B2Fcv4oUXw==&uniplatform=NZKPT&language=CHS (accessed on 9 November 2023).

15. Bai, J.B.; Wang, X.Y.; Yao, J.; Study of coupling support in soft rock roadway under high stress. China Univ. *Min. Technol. 2007*, *421–425.* Available online: https://kns.cnki.net/kcms2/article/abstract?v=KaAwsYWd1tIgZ0qycPhWe3-aF2O4JLrssQw88V90jFsUed2eXyQu7K2MfKnWxNGo1-qrAIw9km9hOecjJOOo10QwpfeeHey-KAAYNxpiMLGrE-Yfz9CnPqAKxDEU5s53W1tjNMcsjM4=&uniplatform=NZKPT&language=CHS (accessed on 9 November 2023).
16. Guan, X.M.; Li, X.F.; Zhang, H.B.; Yang, Z.P.; Li, H.P.; Li, H.Y.; DI, H.F.; Zhang, L. Research and application of inorganic and organic composite grouting reinforcement materials in deep soft rock. *Coal Sci. Technol.* **2023**, *51*, 1–11. [CrossRef]
17. Kang, H.P.; Wng, J.H.; Lin, J. Study and applications of roadway support techniques for coal mines. *J. China Coal Soc.* **2010**, *35*, 1809–1814. [CrossRef]
18. Kang, H.P.; Wang, J.H.; Lin, J. High pretensioned stress and intensive bolting system and its application in deep roadways. *J. China Coal Soc.* **2007**, *32*, 1233–1238. Available online: https://kns.cnki.net/kcms2/article/abstract?v=KaAwsYWd1tKrIm0vUtGiFSAxcetUNIuf6M77OlP5HcVgRzJP8hI7RmiRhCGJ9DrU7NBjtCJSchXXWbPnA-L8VVjX8hLe4bjI_9zCdrQa_PxBVHQBaBkd-2ChZViJB9KjW2_81RNqNc8=&uniplatform=NZKPT&language=CHS (accessed on 9 November 2023).
19. Kang, H.P. Development and prospects of support and reinforcement materials for coal mine roadways. *Coal Sci. Technol.* **2021**, *49*, 1–11. [CrossRef]
20. Kang, H.P.; Feng, Z.Q. Status and development tendency of roadway grouting reinforcement technology in coal mine. *Coal Min. Technol.* **2013**, *18*, 1–7. [CrossRef]
21. Kang, H.P.; Jiang, P.F.; Huang, B.X.; Guan, X.M.; Wang, Z.G.; Wu, Y.Z.; Gao, F.Q.; Yang, J.W.; Cheng, L.X.; Zheng, Y.F.; et al. Roadway strata control technology by means of bolting-modification-destressing in synergy in 1 000 m deep coal mines. *China Coal Soc.* **2020**, *45*, 845–864. [CrossRef]
22. Li, Z.F. Development and Application of Grouting Material and the Reinforcement Mechanism for Rich-Water Broken Rock Mass. Ph.D. Thesis, Shandong University: Jinan, China, 2016. Available online: https://kns.cnki.net/kcms2/article/abstract?v=KaAwsYWd1tI__JWaYzPDgEW1Lkzm6sEuNDbYx_O3tn6vA9vkXMdOThlJRcdbKcppje2DMwD01vNAHGvbOXQI38juZWxgvTwNGyUa2f8Vm3uLpwI5XTVQ1-x3Eun2CWCgiq5_wxt0Fwc8q8s0-BDN7w==&uniplatform=NZKPT&language=CHS (accessed on 9 November 2023).
23. *DL/T 5151-2001*; Test Code for Aggregates of Hydraulic Concrete. China Electric Power Press: Beijing, China, 2009.
24. *GB/T14684-2001*; Sand for Building. Standards Press of China: Beijing, China, 2001.
25. Collepardi, M. Admixtures used to enhance placing characteristics of concrete. *Cem. Concr. Compos.* **1998**, *20*, 103–112. [CrossRef]
26. Chung, J.W.; Rogers, J.D. Influence of assumed groundwater depth on mapping liquefaction potential. *Environ. Eng. Geosci.* **2013**, *19*, 377–389. [CrossRef]
27. Forcellini, D. The role of the water level in the assessment of seismic vulnerability for the 23 november 1980 Irpinia–Basilicata earthquake. *Geosciences* **2020**, *10*, 229. [CrossRef]
28. Savvides, A.A.; Antoniou, A.A.; Papadopoulos, L.; Monia, A.; Kofina, K. An estimation of clayey-oriented rock mass material properties, sited in Koropi, Athens, Greece, through feed-forward neural networks. *Geotechnics* **2023**, *3*, 975–988. [CrossRef]

buildings

MDPI

Article

Research on the Instability Mechanism and Control Technology of Gob-Side Entry in Deep Mines with Soft Rock

Lu Ma [1], Luyi Xing [2,*], Chang Liu [3], Tongyuan Cui [2], Xi Qiao [4], Wang Miao [5] and Peng Kong [3]

[1] China Coal Xinji Liuzhuang Mining Co., Ltd., Fuyang 236000, China; 15855402558@163.com
[2] School of Civil Engineering, Shandong Jianzhu University, Jinan 250101, China; 2023015117@stu.sdjzu.edu.cn
[3] School of Mining Engineering, Anhui University of Science and Technology, Huainan 232001, China; 2023201944@aust.edu.cn (C.L.); 2021001@aust.edu.cn (P.K.)
[4] Lanling Academy, Zaozhuang Vocational College, Zaozhuang 277100, China; josieqiao@126.com
[5] Natural Resources Bureau of Taierzhuang District, Zaozhuang 277100, China; qfmwstephen@163.com
* Correspondence: xingluyi20@sdjzu.edu.cn; Tel.: +86-17854257221

Abstract: The gob-side entry driving in deep mines with soft rock exhibits a complex deformation and instability mechanism. This complexity leads to challenges in roadway stability control which greatly affects the coal mine production succession and safe and efficient mining. This paper takes the gob-side entry in Liuzhuang Coal Mine as the background. By adopting the method of theoretical analysis, a dynamic model of the roof subsidence in the goaf is established. The calculation indicates that achieving the stable subsidence of the basic roof and the equilibrium of the lateral abutment stress within the goaf requires a minimum of 108.9 days, offering a theoretical foundation for selecting an optimal driving time for the gob-side entry. The control technologies and methods of gob-side entry through grouting modification and high-strength support are proposed. Enhancing the length of anchor ropes and the density of bolt (cable) support to improve the role of the roadway support components can be better utilized, so the role of the support components of the roadway can be better exerted. The method of grouting and the reinforcement of coal pillars can effectively improve the carrying capacity of coal pillars. The numerical simulation is used to analyze the deformation law of gob-side entry. The study reveals significant deformation in the coal pillar and substantial roof subsidence, highlighting that maintaining the stability of the coal pillar is crucial for ensuring roadway safety. Following the grouting process, the deformation of the coal pillar and roof subsidence decreased by 16.7% and 7.1%, respectively. This demonstrates that coal pillar grouting not only mitigates pillar deformation but also provides effective control over roof subsidence. This study offers a quantitative calculation method to ascertain the excavation time of gob-side entry, and suggests that the application of high-strength support and the practice of coal pillar grouting can effectively maintain the steadiness of gob-side entry in deep mines with soft rock.

Keywords: gob-side entry; roadway stability; microseismic events; numerical simulation

1. Introduction

Coal occupies a significant position in the international energy supply. Demand for coal has been constantly climbing. Under the precondition of ensuring safe production, maximizing the coal extraction rate as much as possible to reduce the squandering of the resources of coal has become an urgent demand in the field of coal mining [1–3]. When arranging the longwall panel of coal mining, gob-side entry driving is a widely adopted roadway protection method. Gob-side entry driving involves driving the mining roadway of the current section panel along the edge of the upper section panel's goaf with a pillar of narrow coal after the upper section panel's extraction is finished. In contrast to using a large coal pillar for roadway protection, the dimension of the coal pillar in gob-side entry driving is smaller, typically within 3 to 10 m, thus remarkably increasing the coal resources recovery rate [4–6].

Since the gob-side entry lies at the edge of the upper section panel's goaf, it is remarkably influenced by the lateral abutment stress of that panel [7,8]. During conducting the driving of the gob-side entry, selecting a rational driving time for the roadway serves as the foundation for ensuring its stability. Generally, the roadway driving should be initiated after the upper section of the working face roof and the lateral abutment stress have stabilized, thereby avoiding the impact of the dynamic pressure from the upper working area upon the gob-side entry roadway [9,10]. During actual production, on-site monitoring of the roof movement and the lateral abutment pressure distribution of the upper section workface is challenging, and accuracy is difficult to guarantee [11,12]; on the other hand, if the driving time lags too far behind the completion of the mining in the upper section panel, it is not advantageous for the succession continuation of the mine [13]. Hence, it is crucial to choose an appropriate tunneling time for driving. That is to say, when the roof and lateral support pressure of the upper section panel become stable, immediately starting to drive the tunnel is the best choice. This approach not only guarantees that the roadway will not be influenced by the upper section panel, but also mitigates the succession strain of the mine's working face.

The stability of the side entry roadway of gob is mainly associated with the coal pillar width, rock mass structure strength, surrounding rock stress distribution, and the interaction between support structures and the surrounding rock mass [14,15]. For deep mines with soft rock roadways, the rock mass is characterized by low strength and poor integrity, with a high stress level in the enclosing rock. If the support scheme is not rationally designed, the roadway is liable to experience severe distortion, and support elements like anchor bolts and cables might malfunction. Yin et al. [16] and Yang et al. [17] utilized numerical simulation and theoretical analysis methods. They investigated the evolution patterns of the roof overburden structure and lateral abutment stress. Also, they analyzed the reasonable coal pillar size to be retained for gob-side entry. In response to the challenges of surrounding rock control in gob-side entry, Kang et al. [18] proposed the asymmetric control principle and technology of high-strength and high-prestressed anchor fasteners and wire ropes to boost the support strength of the coal pillar beside the gob. Wang et al. [19] applied the roof cutting and pressure relief method to control the stress of the roadway's surrounding rock, attaining the goal of safeguarding the roadway by decreasing the stress concentration level of the surrounding rock. The studies by Bai et al. [20] and Pang et al. [21] indicated that the small coal pillar of the gob-side entry serves as the key point for support and reinforcement. When the small coal pillar experiences fracturing, ensuring that the anchor bolts and cables have sufficient anchoring force is a necessary prerequisite. The use of full-length anchoring and anchor grouting and other methods can increase the anchoring force.

At present, the selection of a reasonable timing for gob-side entry driving is mostly based on empirical judgments, lacking reliable quantitative design basis. Gob-side entry not only deforms sharply during driving, but also further deforms under the influence of advance abutment stress during mining. Therefore, the deformation law of the roadway is complicated. Moreover, as the depth of coal mining keeps increasing, the stability control of gob-side entry in deep mines under soft rock conditions remains an unresolved issue, and the related theories and technologies urgently require further research. In this study, with the gob-side entry of the 150806 working face in Liuzhuang Coal Mine as the engineering background, the theoretical analysis approach was utilized to construct a dynamic model of roof subsidence in the goaf and to acquire the minimum time needed for the main roof rock to reach a stable condition, thus furnishing a theoretical foundation for ascertaining a proper driving time for gob-side entry. Through the comprehensive utilization of numerical simulation and on-site monitoring methods, the control technologies and methods of gob-side entry, such as grouting modification and high-strength support, were proposed. Finally, microseismic and roadway deformations were monitored to verify the rationality of the gob-side entry excavation timing and roadway support method. The main methods and work of the research and the on-site project progress are shown in Table 1. The research findings offer a theoretical foundation for gob-side entry stability control in deep mines with soft rock.

Table 1. Schedule of main work progress.

Time	On-Site Project Progress	Methods and Work of Study
2023.07–2023.09	Mining of 150804 panel	Microseismic monitoring and data analysis
2023.10–2024.02	No mining and driving, the roof of 150804 goaf rotary sinking, lateral abutment stress adjustment	Microseismic monitoring and data analysis; Theoretical analysis
2024.03–2024.12	Gob-side entry driving of 150806 panel and working face mining	Numerical simulation; Roadway deformation monitoring

2. Engineering Background

Liuzhuang Coal Mine is positioned in the territory of Fuyang City, Anhui Province, China. The deposit is mined at a depth of the mine that varies from 600 to 800 m. Classified as deep mining, the primary coal seams extracted include Coal Seam 6, Coal Seam 8, and Coal Seam 11, all of which fall under the category of medium-thick coal seam mining. The longwall retreating mining method is adopted for coal extraction. The uniaxial compressive strength of the coal seams is less than 10 MPa, and it constitutes a mining of soft coal seam clusters, presenting significant difficulties in the support of mining roadways.

The 150806 panel lies in the West No. 1 mining area. The mined coal seam is Coal Seam 8, the thickness of the average coal seam is 3.5 m and the dip angle is about 14°. It commences from the West No. 1 centralized crosscut in the east and borders the F8 fault in the west. It is adjacent to the goaf of the 150804 panel in the north and the as-yet unmined area of Coal Seam 8 in the south. The designed advancing length of the 150806 panel is 1624.2 m, with a slope length of 320 m. The extraction roadways on both sides of the working face are excavated following the coal seam roof. The northern side of the tailgate roadway in the 150806 panel is the goaf of the 150804 panel. The 150804 panel completed its extraction on September, 2023. The coal pillar width between the two working faces is 10 m. Therefore, the tailgate roadway in the 150806 panel belongs to driving the entry along the gob. Its stability is significantly impacted by the lateral abutment pressure from the 150804 panel. The mining and excavation plan is presented in Figure 1.

The immediate roof of the 150806 panel is sandy mudstone, light gray to gray, dense, brittle, with a flat fracture, containing sand and fossil fragments of plants. The average thickness of this layer is approximately 4.6 m. The main roof consists of fine sandstone. It is gray, relatively dense and brittle, existing in a massive form with a relatively flat fracture. It contains a large number of fossilized plant leaves and has a slippery structure. From the east to the west of the panel, the thickness and sandy quality of the main roof sandstone gradually decrease, and the distance from Coal Seam 8 also gradually decreases. The main roof has an average thickness of 7.7 m. The direct floor comprises mudstone and the main floor consists of siltstone. The surrounding rocks in the tailgate roadway have a moderately stable condition. The comprehensive columnar section diagram of the strata in the tailgate roadway is shown in Figure 2. As per the results of the in situ stress test, for the 150806 panel, the max principal stress is vertical. Max horizontal principal stress makes a 72° angle with the roadway axial, and the min principal stress makes an 18° angle. Lateral pressure coefficients are 0.8 for the max horizontal and 0.65 for the min. A nearly perpendicular max horizontal stress direction to the roadway axial is unfavorable for roadway stability control.

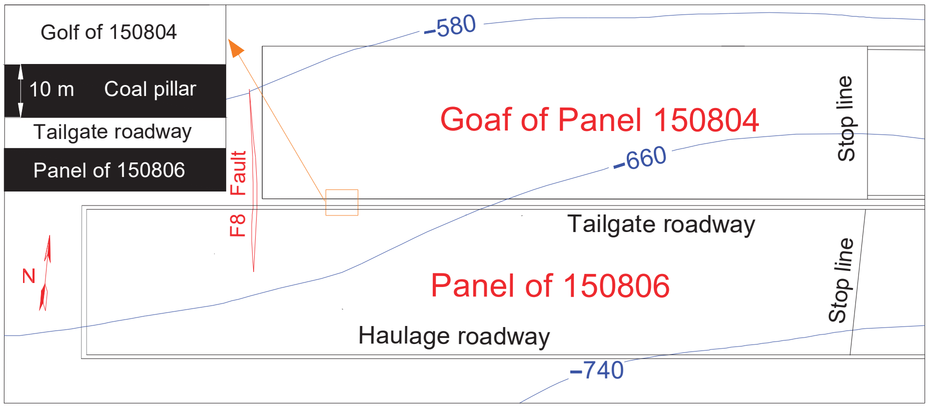

Figure 1. Mining engineering plan.

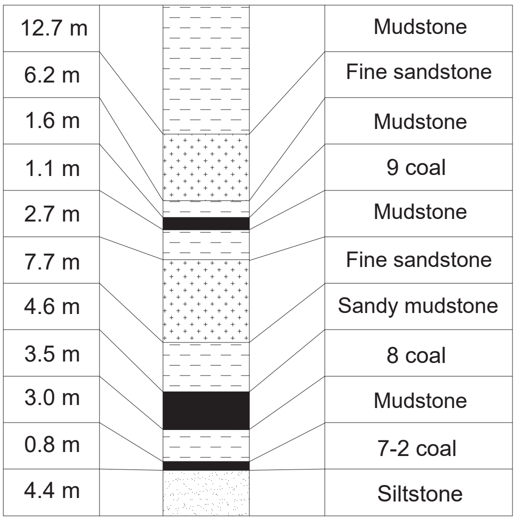

Figure 2. Comprehensive stratigraphic column diagram of the 150806 panel.

3. Determination of the Appropriate Driving Time for Gob-Side Entry

3.1. Temporal and Spatial Evolution Law of Lateral Abutment Pressure

Following the extraction of the 150804 panel, the roof of the goaf undergoes fracturing and subsidence, and the stress in the stope is redistributed. From the start of the extraction of the 150804 working face until the stress rebalances, the stress environment of the coal body along the goaf undergoes continuous changes. The peak side abutment stress keeps transferring to the deep part of the surrounding rock, and its variation process is illustrated in Figure 3. In the figure, Curve 1 indicates that immediately after the extraction of the panel is completed, the main roof of the stope has not fractured, the stress on the coal body at the edge of the goaf has not surpassed its elastic strength limit, and the coal body remains in an elastic state with no plastic zone development. Curve 2 is during the extraction of the panel, the overlying strata fracture and subside, and the stress on the coal near the goaf edge continuously increases. When the stress exceeds its elastic strength limit, plastic failure occurs in the coal near the goaf edge, and the peak side abutment stress continuously transfers to the interior of the surrounding rock. Curve 3 indicates that the overlying strata movement in the goaf becomes more gentle, and the stress of the coal body also becomes stable. The environment of the tailgate roadway in the 150806 panel during different periods shows a significant disparity. When driving the gob-side entry during the conditions of Curves 1 and 2, the influenced of the goaf dynamic pressure is inevitable. Therefore, choosing a reasonable timing for roadway driving has great significance for gob-side entry stability control.

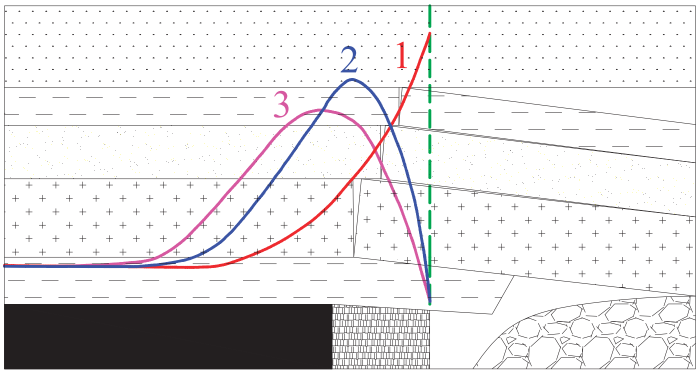

Figure 3. The evolution curve of the side abutment stress of a coal body with time.

3.2. Dynamic Model of Goaf Roof Subsidence

Prior to the fracture of the main roof rock beam in the extraction roadway, the maximum bending moment appears at the fixed end, supported by the coal body. Once the largest pull stress reaches the strength condition of the main roof, it fractures near the coal body. The movement pattern of the fractured main roof is rotational around the coal body's support end. This movement is not completed instantaneously but is a slow process related to time. We take the main roof as the object, and establish a dynamic model of roof subsidence. The model assumes that the roof strata are homogeneous and isotropic layered rock masses, and the roof fracture subsidence is not affected by geological bad bodies such as fault joints. Therefore, a stable hinged structure can be formed under certain conditions after the roof is broken.

Use an elastic simply supported beam to simplify the structural model of the broken main roof, with the coal body end as a fixed hinge support, and the support of the main roof by the fragmented and expanded gangue in the goaf is simplified as a spring support. The spring stiffness k is the compressive strength of the fragmented and expanded gangue, and the deformation $h(t)$ of the spring is a function of time, as shown in Figure 4.

To formulate the subsidence equation for the main roof within the extraction roadway, the main roof is considered a viscoelastic beam, with its material properties represented by the Maxwell model. The rheological property of this model features transience, creep, relaxation, viscous flow, and no elastic aftereffect. Its constitutive equation is:

$$\frac{\partial \varepsilon}{\partial t} = \left(\frac{1}{E_1} \frac{\partial \sigma}{\partial t} + \frac{\sigma}{\eta_1} \right) \tag{1}$$

The relationship between the linear strain ε when the main roof rock beam bends and the subsidence amount $W(x, t)$ is:

$$\varepsilon = y \frac{\partial W(x,t)}{\partial x^2} \tag{2}$$

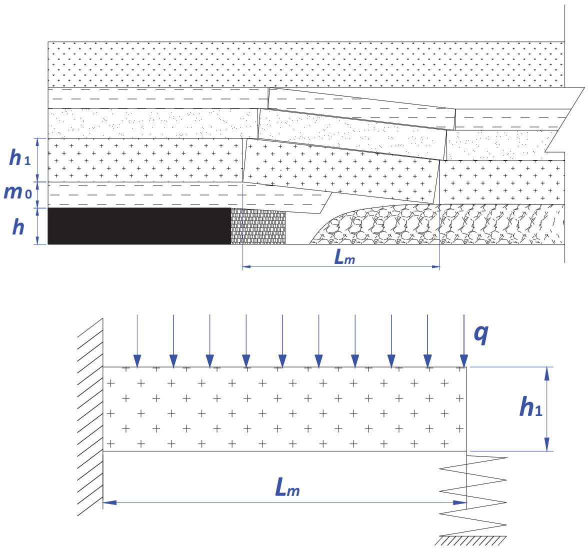

Figure 4. Mechanical structure model of the main roof after fracture.

By substituting ε into Equation (1), $W(x, t) = \partial w(x, t)/\partial t$, it is obtained that:

$$y\frac{W(x,t)}{\partial x^2} = \left(\frac{1}{E_1}\frac{\partial\sigma}{\partial t} + \frac{\sigma}{\eta_1}\right) \tag{3}$$

Multiply both sides of the foregoing equation by $y\mathrm{d}A$ and integrate over the cross-sectional area, and it is obtained that:

$$\frac{\partial W(x,t)}{\partial x^2}\int_A y^2\mathrm{d}A = \left[\frac{1}{E_1}\frac{\partial\sigma}{\partial t}\int_A \sigma_y\mathrm{d}A + \frac{1}{\eta_1}\int_A \sigma_y\mathrm{d}A\right] \tag{4}$$

The moment of inertia I_1 and the bending moment $M(x, t)$ of the rock beam of the main roof in the extraction roadway are, respectively:

$$I_1 = \int_A y^2\mathrm{d}A \tag{5}$$

$$M(x,t) = \int_A \sigma_y\mathrm{d}A \tag{6}$$

Substituting I_1 and $M(x, t)$ into Equation (4), it is obtained that:

$$I_1\frac{\partial W(x,t)}{\partial x^2} = \left[\frac{1}{E_1}\frac{\partial M(x,t)}{\partial t} + \frac{M(x,t)}{\eta_1}\right] \tag{7}$$

Derived from the structural model in Figure 4, the deflection equation of the main roof is as follows:

$$W(x,t) = \frac{1}{E_1 I_1}\left[\begin{array}{l} \frac{K\Delta h(t)xL_m^2}{3} - \frac{q_z L_m^3 x}{8} + \frac{k\Delta h(t)L_m^2(L_m-x)}{2} + \frac{q_z L_m^4}{8} \\ -\frac{K\Delta h(t)(L_m-x)^3}{6} - \frac{q_z L_m^3(L_m-x)}{6} + \frac{q_z(L_m-x)^4}{24} - \frac{K\Delta(t)L_m^3}{3} \end{array}\right] \tag{8}$$

When $t = 0$ and x is 0 and L_m, respectively, the subsidence amount $W(x, t)$ is equal to 0, satisfying the initial conditions. This indicates that the main roof rock beam of the extraction roadway has not subsided with time at the instant after the fracture. At this moment, the rock beam of the main roof is in an instantaneous relative static state. By taking the partial derivatives of Equation (8) with respect to t and x, respectively, it is obtained that:

$$\frac{\partial W(x,t)}{\partial x^2} = -\frac{k}{E_1 I_1}(L_m - x)\frac{\partial\Delta h(t)}{\partial t} \tag{9}$$

The bending moment equation of the rock beam of the main roof in the extraction roadway is:

$$M(x,t) = k\Delta h(t)(L_m - x) - q_z(L_m - x)^2/2 \tag{10}$$

Taking the derivative of $M(x, t)$ with respect to time t gives:

$$\frac{\partial M(x,t)}{\partial t} = k(L_m - x)\frac{\partial \Delta h(t)}{\partial t} \tag{11}$$

Substituting Equations (9)–(11) into Equation (8) and letting $x = 0$, a differential equation containing only $\Delta h(t)$ is established:

$$\frac{\partial \Delta h(t)}{\partial t} + \frac{E_1}{2\eta_1}\Delta h(t) = \frac{E_1 L_m q_z}{4k\eta_1} \tag{12}$$

The equation is a first-order linear differential equation, and its solution is:

$$\Delta h(t) = q_z L_m/2k + c_e^{-E_1^t/2\eta_1} \tag{13}$$

By utilizing the initial conditions to determine the integration constant, namely when $t = 0$, $\Delta h(t) = 0$, and this yields $C = -q_z L_m/2k$. Substituting this into Equation (13), the dynamic equation for the subsidence at the goaf end of the main roof rock beam of the extraction roadway is derived:

$$\Delta h(t) = \frac{q_z L_m}{2k}(1 - e^{-E_1^t/2\eta_1}) \tag{14}$$

By differentiating Equation (14) with respect to time t, the equation for the subsidence velocity is obtained as:

$$\frac{\partial \Delta h(t)}{\partial t} = \frac{E_1 q_z L_m}{4k\eta_1} e^{-\frac{E_1^t}{2\eta_1}} \tag{15}$$

Since $\Delta h(t)$ is an exponential function of time t, the following variation patterns exist.

When $t = 0$, $\Delta h(t) = 0$, $\partial\Delta h(t)/\partial t = E_1 q_z L_m/4k\eta_1$.

When $t \to \infty$, $\Delta h(t) \to q_z L_m/2k$, $\partial h(t)/\partial t \to 0$.

This variation trend suggests that under the action of the load, the subsidence of the main roof rock beam of the mining roadway tends to be a stable value and the subsidence velocity approaches zero over time.

When $t = T$, the subsidence amount of the main roof when it reaches a stable state is:

$$\Delta h(T) = h - (k_c - 1)m_z \tag{16}$$

In the formula,

h represents the mining thickness, m;

k_c represents residual coefficient of fragmentation dilation for caved gangue in goaf;

m_z represents the thickness of the immediate roof, m.

Substituting $\Delta h(T)$ into Equation (14) yields the calculation formula for the time needed for the main roof to reach a stable state:

$$T = \frac{2\eta_1}{E_1}\ln\frac{q_z L_m}{q_z L_m - 2k[M - (K_c - 1)h_z]} \tag{17}$$

In the formula,

E_1 represents the elastic modulus of the main roof, taken as 13.2 GPa;

η_1 represents the viscous modulus of the main roof, taken as 12 MPa·s;

q_z represents the upper load on the main roof, taken as 1.05 MPa;

L_m represents the periodic caving step spacing of the main roof, taken as 16 m;

M represents the coal seam height, taken as 3.5 m;

K_c represents the rock swelling coefficient, taken as 1.3;

h_z represents the thickness of the immediate roof, taken as 4.6 m;

k represents the compressive strength of the crushed rock, taken as 2 MPa.

The calculation yields T = 108.9 d, suggesting that approximately 108.9 d after the mining of the upper section working face is completed, the stress at the edge of the gob-side coal body tends to stabilize. Thus, to ensure the stability of the 150806 tailgate roadway, the driving time of the roadway should not be less than 108.9 d after the mining of the 150804 working face concludes.

4. Control Technology for Gob-Side Entry Stability

Determining the timing of the roadway driving can effectively evade the impact of the roof breakage and subsidence dynamic pressure in the goaf of the 150804 working face. Nevertheless, because of the existence of a small coal pillar with a width of 10 m between the 150804 workface and the 150806 track roadway, the small coal pillar remains influenced by the lateral abutment pressure from the 150804 working face goaf and the advance abutment pressure from the 150806 working face. Following the superposition of these stresses, the coal pillar becomes susceptible to damage, with significant deformations likely to occur. After the stress superposition, the coal pillar is prone to failure and large deformation. Hence, the key point to ensuring the stability of the gob-side roadway lies in effectively controlling the stabilization of the small coal pillar.

4.1. High-Strength Support of Roadways

In view of the characteristic that the highly stressed soft rock roadway in a kilometer-deep well has significant deformation, the combined support of anchor meshes and cables is adopted to enhance the support strength. Long anchor cables are employed to guarantee that the anchor cables can extend into the intact rock strata of the roof, maximizing the suspension function of the anchor cables. The support density of anchor bolts (cables) is appropriately increased to ensure that the roadway has adequate support strength. The torque of anchor bolts and the pretension force of anchor cables are enhanced to cut down the initial roadway deformation and effectively control the dilation of the roadway surrounding rock, such as the separation of strata, slippage, crack propagation, and the generation of new cracks, achieving the purpose of high prestress and timely active support.

Six anchor bolts are deployed on the roof of the roadway. The anchor bolts are of a threaded metal type without longitudinal ribs, with a diameter 22 mm and a length of 2500 mm. The spacing between rows and columns is 800 mm $\times$ 800 mm, and they are coordinated with M5 steel belts. Five anchor cables are installed on the roof. The anchor ropes' length at the shoulder socket on the entity coal side is 3200 mm, and the lengths of the remaining four anchor cables are 9200 mm. The anchor cables adopt prestressed steel strand anchor cables with a diameter of 21.8 mm, and the spacing between rows and columns is 1600 mm $\times$ 1200 mm. The torque of the anchor bolts in the coal seam is no less than 200 N·m, and the anchorage force is not inferior to 50 kN. The torque of the anchor bolts in the rock stratum is no less than 300 N·m, and the anchoring force is no lower than 100 kN.

Four anchor bolts are arranged on the solid coal side of the roadway, with a diameter of 22 mm and a length of 2500 mm. The spacing between rows and columns is 800 mm $\times$ 800 mm. Two anchor cables are deployed, with the length of the anchor cable at the roadway shoulder socket being 3200 mm, and the other being 9200 m. Four anchor bolts and three anchor cables are set on the side of the coal pillar. The lengths of the two anchor cables at the shoulder socket are 3200 mm, and the remaining one is 9200 mm. The shoulder socket and the side of the coal pillar are longitudinally reinforced with M5 steel belts. The anchor cable row pitch is 1200 mm, and the anchor bolt inter-row and inter-column pitch is 800 mm × 800 mm. The roadway support design drawing is presented in Figure 5.

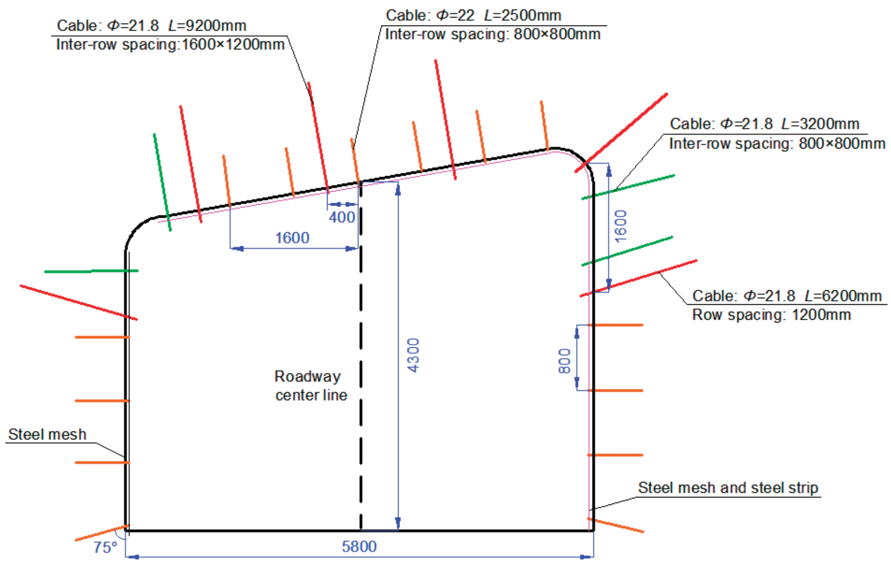

Figure 5. Support scheme of tailgate roadway in 150806 working face.

4.2. Reinforcement of Roadway Surrounding Rock Through Grouting

The coal pillar will produce fissures after it undergoes plastic failure under compression, fractures will occur, and a continuous large deformation will take place. In severe cases, it will cause instability in the roadway. Grouting to reinforce the surrounding rock uses grout to fill and rebind various weak surfaces in the surrounding rock, such as joints and fractures, so as to promote the overall stability of the surrounding rock and augmenting its bearing capacity. The combination of the grouting reinforcement of the surrounding rock and the anchor bolt support can not only enhance the mechanical properties and stress distribution of the surrounding rock, but can also boost the anchoring effect of the anchor bolts, substantially cut down the deformation of the roadway's surrounding rock, and significantly improve the roadway maintenance condition.

To boost the stability of the coal pillar and guarantee the grouting effect, grouting reinforcement is implemented during roadway excavation. The schematic diagram of the grouting holes' arrangement for the coal pillar of the tailgate roadway in the 150806 panel is presented in Figure 6. The grouting holes are set in a "three-patterned eye" pattern, at a position 1~1.5 m from the roadway roof and floor, with a hole spacing of 3 m, a hole diameter of φ 42 mm, and a hole depth of 6~8 m. Supplementary grouting reinforcement with deep and shallow holes is conducted in areas with severe roadway deformation based on the actual on-site conditions. The grouting of the roadway is generally less than 40 m behind the driving working face, especially for the surrounding rock of the roadway with developed cracks; grouting should be carried out in time. If the roadway's surrounding rock shows good integrity and stability, the spacing of grouting holes can be appropriately increased to reduce the amount of grouting. Shallow holes are grouted first, followed by deep holes. The holes are drilled using a sidewall anchor rig, and the holes are sealed and grouted using mining hole sealer in conjunction with a high-pressure rubber hose. The grouting material is a micro–nano inorganic–organic composite modified one, with a water—cement ratio of 0.8~1.0 and a grouting pressure of 6~8 MPa. The use of the inorganic–organic composite grouting materials can not only significantly improve the strength of the grouted rock mass, but can also reduce the cost of grouting compared to organic materials.

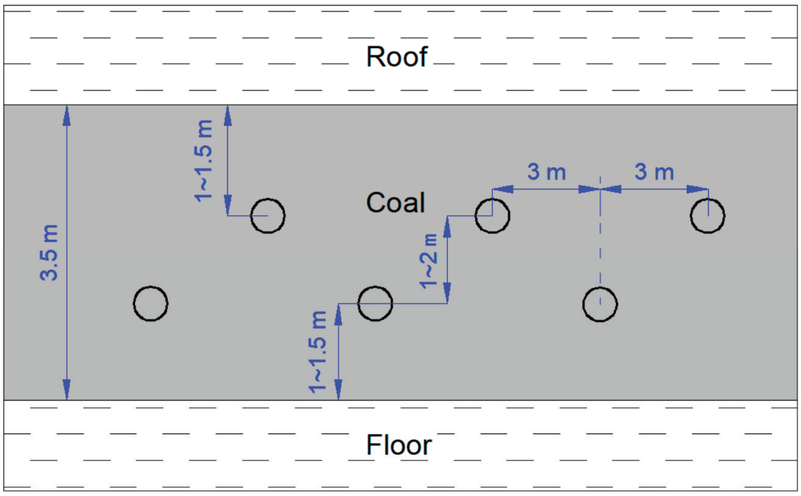

Figure 6. Schematic diagram of the arrangement of grouting holes in coal pillars.

5. Numerical Simulation Analysis on Stability Control of Gob-Side Entry

5.1. Methods and Models

The FLAC3D numerical simulation approach is used to simulate the tailgate roadway of the 150806 panel and analyze the support effect and deformation law of the tailgate roadway during mining influence. Firstly, the simulation of the mining of the 150804 panel is conducted; after the mining-induced stress redistribution becomes stable, the simulation of the driving of the tailgate roadway in the 150806 panel is carried out; finally, the mining of the 150806 panel is simulated to investigate the deformation behavior of the roadway.

The numerical calculation model measures 760 m × 520 m × 280 m (length × width × height). The coal bed inclination angle is 14°. The tailgate roadway in the simulation is buried 700 m deep. The unit weight of the rock strata above the model not being simulated is taken as 25 kN/m^3. The calculation of the corresponding load of the unmodeled rock strata is computed as 13.0 MPa and imposed on the upper border of the model. In order to negate the influence of the boundary effect during the numerical calculation process, the distance between the panel and the model boundary exceeds 100 m. The model of numerical calculation is shown in Figure 7. Based on the rock mechanics test and the integrity of the rock mass, and with the application of Rocklab 1.0 software, the rock mass mechanical parameters in the numerical calculation model are finally ascertained. The mechanical parameters of the coal and rock mass thus obtained are shown in Table 2 [22]. Based on the in situ stress test results, the side pressure coefficient in the x-direction of the model is set at 0.65, while in the y-direction, it is set at 0.8.

To comparatively analyze the effect of coal pillar grouting on the stability of the roadway, two sets of simulation experiments were carried out, respectively, to investigate the deformation laws of roadways under the conditions of grouting and non-grouting. The research indicates that grouting can effectively enhance the strength of coal. After grouting, the coal's uniaxial compressive strength increased from 70% to 200%, the internal friction angle increased by approximately 11%, and the cohesion increased by 200%. Therefore, when simulating the parameters of the grouted coal, the internal friction angle was raised from 30° to 33°, the cohesion was increased from 1.8 MPa to 3.6 MPa, and the tensile force was additionally increased from 1.2 MPa to 2.4 MPa.

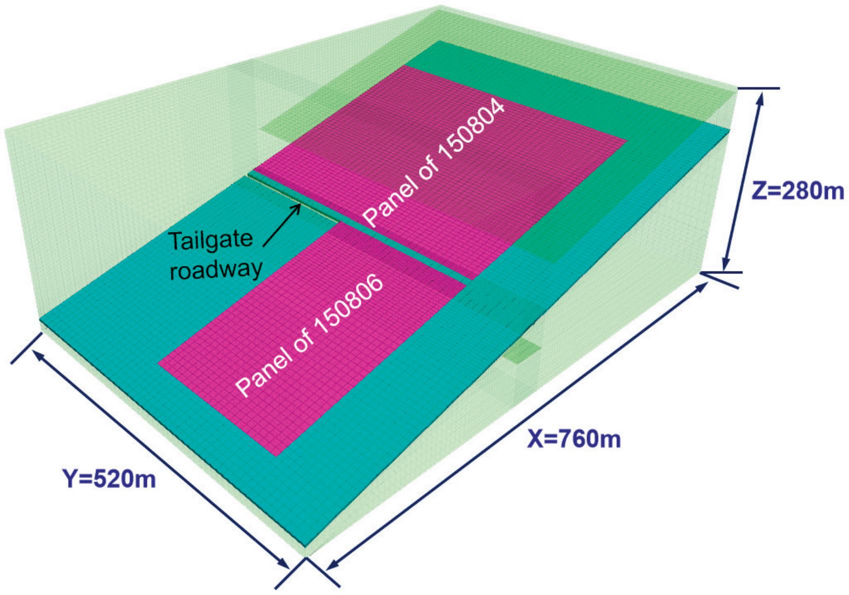

Figure 7. Numerical calculation model.

Table 2. Coal and rock mass properties.

Lithology	Elastic Modulus (GPa)	Poisson's Ratio	Cohesive (MPa)	Tensile Strength (MPa)	Friction Angle (°)	Residual Cohesive (MPa)
Fine sandstone	26.9	0.22	9.8	9.7	48	0.98
Mudstone	6.7	0.31	2.8	2.1	38	0.28
Sandy mudstone	8.1	0.30	3.2	2.7	40	0.32
Coal	1.2	0.34	1.8	1.2	30	0.18
Siltstone	14.7	0.26	5.3	4.9	44	0.54

5.2. The Laws of Stress and Plastic Zone Distribution During Gob-Side Entry Driving

Figure 8 displays the distribution laws of the plastic zone and stress in the stope after the roadway driving of the 150806 working face. Among them, Figure 8a and Figure 8b display the plastic region and stress distributed when the coal pillar has not been grouted, while Figure c and Figure d show the plastic zone and stress distributed in the surrounding rock of the roadway after grouting. It can be observed from the figure that after the mining of the 150804 panel is completed, the development height of the plastic zone in the roof is approximately 40 m. The tailgate roadway in the 150806 panel is excavated along the edge of the goaf, leaving a 10 m coal pillar. Although the coal pillar undergoes plastic failure, it still has a certain bearing capacity, and the peak stress in the middle of the coal pillar is 59.4 MPa. After grouting, the plastic zone's development range in the coal pillar is reduced to a certain extent, though the reduction is slight. The coal pillar still has plastic failure, yet its bearing capacity is strengthened, and the peak stress in the coal pillar's middle is 64.0 MPa. This shows that after grouting, the expansion range of the plastic zone can be inhibited as well as improving the load-bearing capacity of the coal pillar.

The development height of the roadway roof plastic zone is 4 m, while the development depth of the plastic zone on the solid coal side is 5.6 m. Thus, when conducting roadway support, it is quite difficult for short anchor cables to exert their suspension effect. Employing 9200 mm long anchor cables can effectively fix the anchoring end of the anchor cable within the range of stable coal and rock mass, which is more conducive to the stabilization of the surrounding rock.

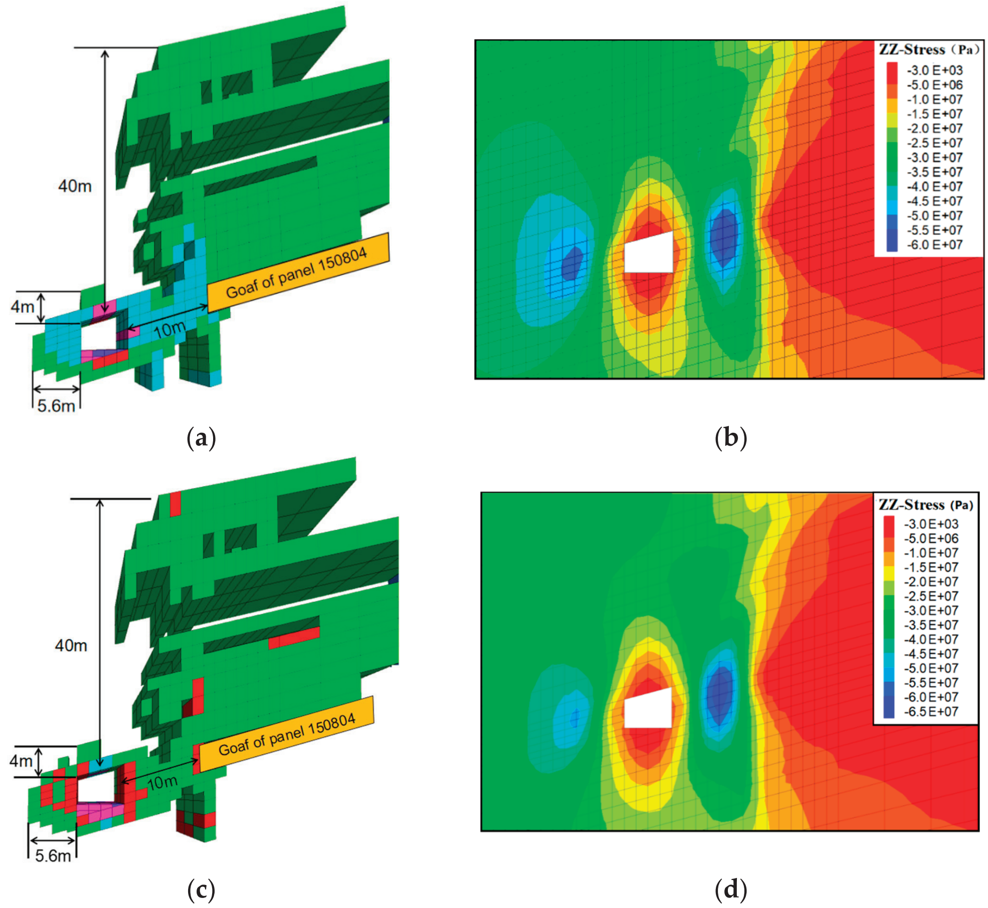

Figure 8. Distribution of plastic zone and vertical stress after roadway driving. (**a**) Distribution of plastic zone before grouting. (**b**) Vertical stress before grouting. (**c**) Distribution of plastic zone after grouting. (**d**) Vertical stress after grouting.

Figure 9 presents the deformation of the roadway after driving (before and after grouting). It can be observed that the right gang of the roadway adjacent to the coal pillar experiences the maximum amount of deformation, followed by the roof of the roadway. The left side and the floor of the roadway exhibit better stability. Before grouting, the maximum subsidence of the right side and the roof of the roadway are 17.6 mm and 14.7 mm, respectively. After grouting, the deformation of the roadway has been reduced to a certain extent, with the subsidence of the right side and the roof of the roadway decreasing to 16.1 mm and 14.6 mm, respectively. Grouting has exerted a certain inhibitory role on the deformation of the roadway during the driving process.

5.3. Analysis of Roadway Stability During the Mining Period of the 150806 Panel

Figure 10 illustrates the roadway's stress evolution during the 150806 panel mining process, both before and after grouting. The stress distribution in the roadway experiences significant fluctuations as the working face advances. When the working face is over 60 m away from the measurement point, stress changes are relatively minor. However, within a 60 m range, the stress variation becomes more pronounced, indicating that this zone exhibits intense mine pressure and the most severe roadway deformation. A comparison of the stress evolution before and after grouting reveals that grouting significantly enhances the coal pillar's load-bearing capacity. After grouting, the stress in the coal pillar rises notably from 85.5 MPa to 92.3 MPa, representing an increase of 6.8 MPa. Conversely, the stress on the roadway's left sidewall decreases after grouting. This reduction suggests that the improved load-bearing ability of the coal pillar reduces the stress concentration on the left sidewall, thereby enhancing overall roadway stability.

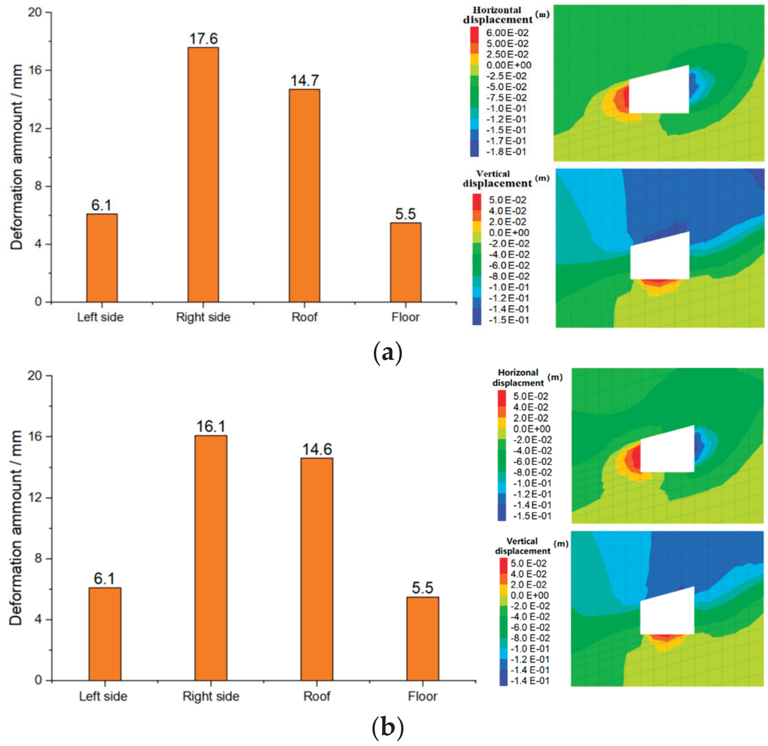

Figure 9. Deformation law of roadway after driving. (**a**) Before grouting; (**b**) After grouting.

Figure 11 shows the horizontal displacement pattern of the roadway during the extraction of the 150806 working face. The diagram indicates that as the working face approaches the deformation measurement points, roadway deformation gradually increases. Notably, within 60 m of the measurement points, deformation intensifies significantly. When the working face reaches the immediate vicinity of these points, the maximum displacement on the left side of the roadway is 15.1 mm, while on the coal pillar side, it reaches 29.3 mm, showing a much larger displacement on the coal pillar side. After grouting the coal pillar, the displacement on both sides of the roadway is reduced to varying degrees. Specifically, the displacement on the coal pillar side decreases significantly from 29.3 mm to 24.4 mm, a reduction of 16.7%. This clearly demonstrates that grouting enhances the coal pillar's stability, effectively limiting its deformation.

Figure 12 illustrates the vertical displacement behavior of the roadway during the 150806 panel mining process. The figure shows that the roadway roof is significantly impacted by the panel mining, whereas the floor displacement remains relatively minor. As the working face approaches the deformation measurement point, the roof displacement gradually increases. Upon reaching the vicinity of the measurement point, the roof subsidence peaks at 30.9 mm. After grouting the coal pillar, the roof subsidence is partially mitigated, with the maximum subsidence reduced to 28.7 mm—a decrease of 7.1%. This demonstrates that coal pillar grouting not only improves the coal pillar's load-bearing capacity and limits roadway side deformation but also effectively controls the surrounding rock and stabilizes the roof, thereby suppressing roof subsidence.

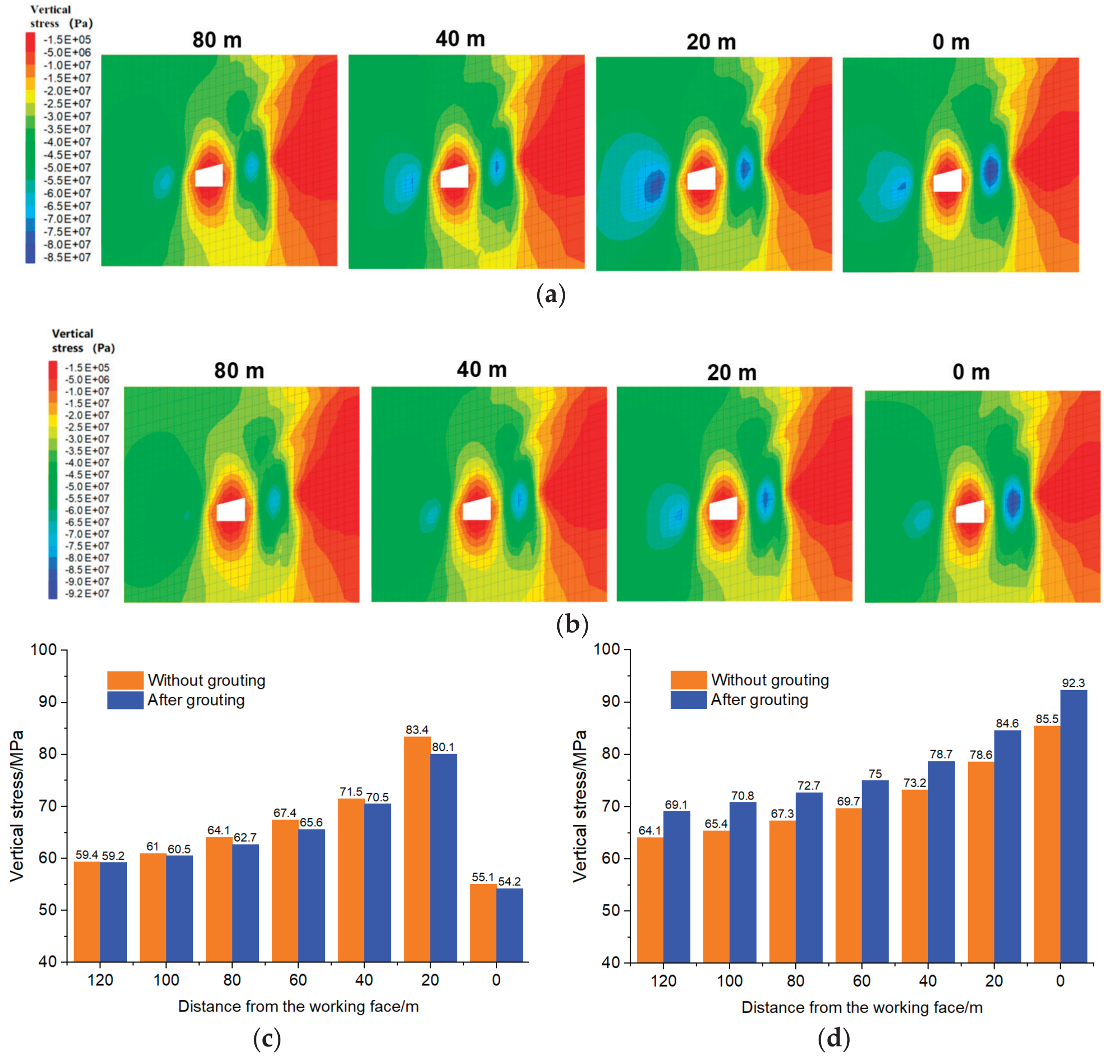

Figure 10. Stress evolution law of the roadway. (**a**) Stress cloud map before grouting; (**b**) stress cloud map after grouting; (**c**) peak vertical stress of the left roadway sidewall before and after grouting; (**d**) peak vertical stress of the right roadway sidewall before and after grouting.

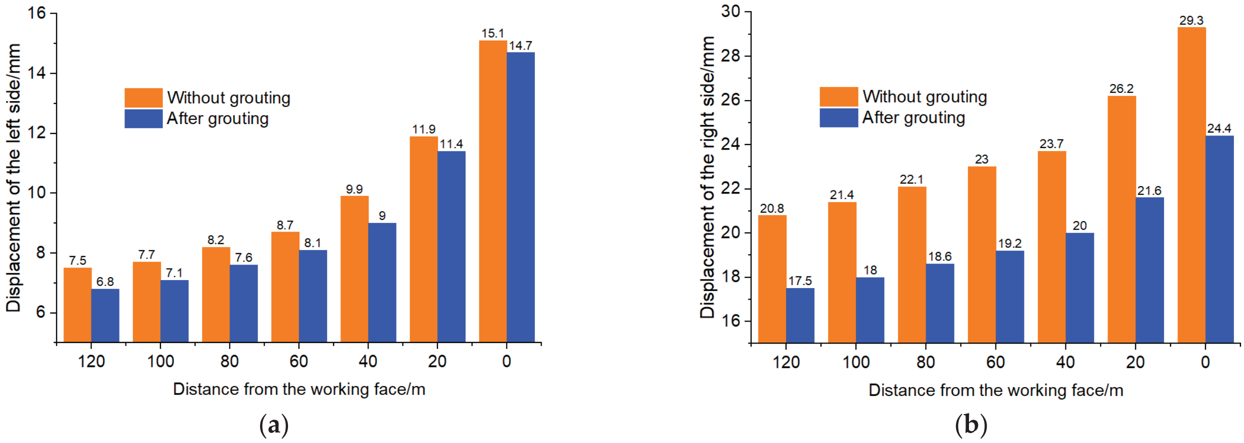

Figure 11. The law of horizontal deformation of the roadway. (**a**) The maximum displacement of the left sidewall of roadway before and after grouting; (**b**) the maximum displacement of the right sidewall of the roadway before and after grouting.

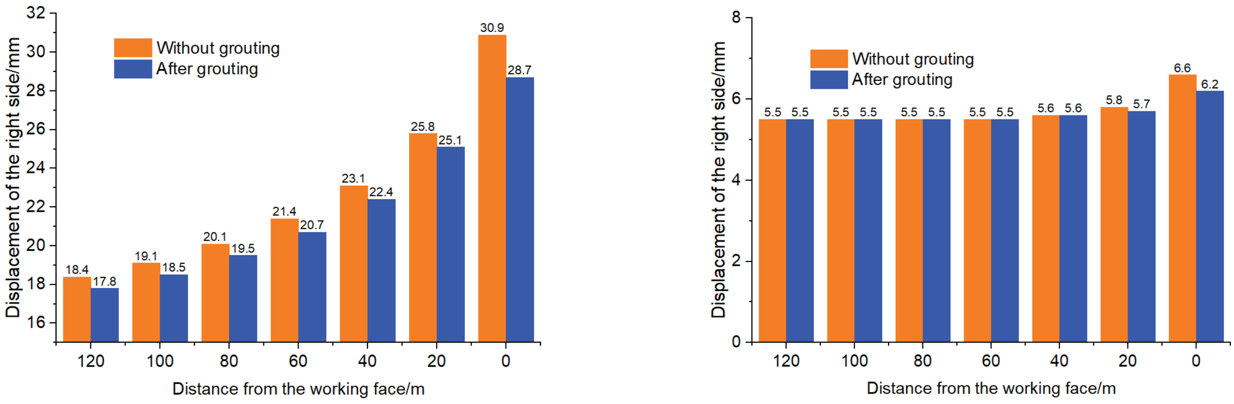

Figure 12. The law of the vertical deformation of the roadway. (**a**) The maximum value of roadway roof subsidence before and after grouting. (**b**) The maximum value of roadway floor heave before and after grouting.

6. Field Monitoring

The microseismic occurrences during a certain period before and after the end of the mining of the 150804 panel were measured on-site by adopting the microseismic monitoring method. The roof stability of the 150804 panel was analyzed to offer a reference for determining the driving time of the tailgate roadway of the 150806 panel. Additionally, measurement points were installed in the tailgate roadway of the 150806 working face to monitor roadway stability during mining and to analyze the deformation behavior caused by the mining activity.

6.1. Monitoring Results of Microseismic Events

The microseismic monitoring system adopts the Signal Hunter series products produced by the Nanjing Sessom Microseismic Technology Company. This system is a new type of passive source monitoring and analysis equipment specially developed for the damage and fracture of surrounding rock in the mine working face. The system adopts an advanced nonlinear absolute source location algorithm and analytical technology, combined with the optimal layout of monitoring scheme, with which the location error of surrounding rock damage can be controlled at a meter level. Ten uniaxial microseismic monitoring stations were set up in the West No.1 mining district of Liuzhuang Coal Mine, enabling the precise detection of surrounding rock damage and fractures during the mining of the 150804 working face.

Figure 13 shows the temporal and spatial distribution of microseismic events during and after the mining of the 150804 panel. Monitoring took place from 22 July to 14 November. On 22 July, the working face was 273 m from the end mining line. Mining was completed on 17 September, and 14 November marked the 88th day after the mining ended.

The figure indicates that microseismic events are mostly concentrated within 60 m above the coal seam. A higher concentration of events occurs near the tailgate roadway compared to the middle and lower sections of the panel, which can be attributed to the coal seam dip angle and the gob-side coal pillar. In terms of frequency and energy, both showed elevated levels between 28 August and 11 September. The main reason for this is that the working face excavation speed was faster during this period, causing more intense roof activities. The working face was stopped on 17 September. Within 21 days after the end of mining until 8 October, both the microseismic event frequency and energy maintained a comparatively high level. After 8 October, both the frequency and energy of microseismic events gradually decreased. Starting in November, there was a sharp decline in the energy levels and occurrence frequency of these activities. Also, no microseismic occurrence with an energy magnitude exceeding 1×10^2 J was identified after 9 November. Therefore, the roof activities were still relatively intense 21 days after the end of the working face, and gradually tended to stabilize 21 days later. Fifty-two days after mining ceased, no microseismic events with energy exceeding 1×10^2 J were recorded, suggesting that the roof was progressively stabilizing.

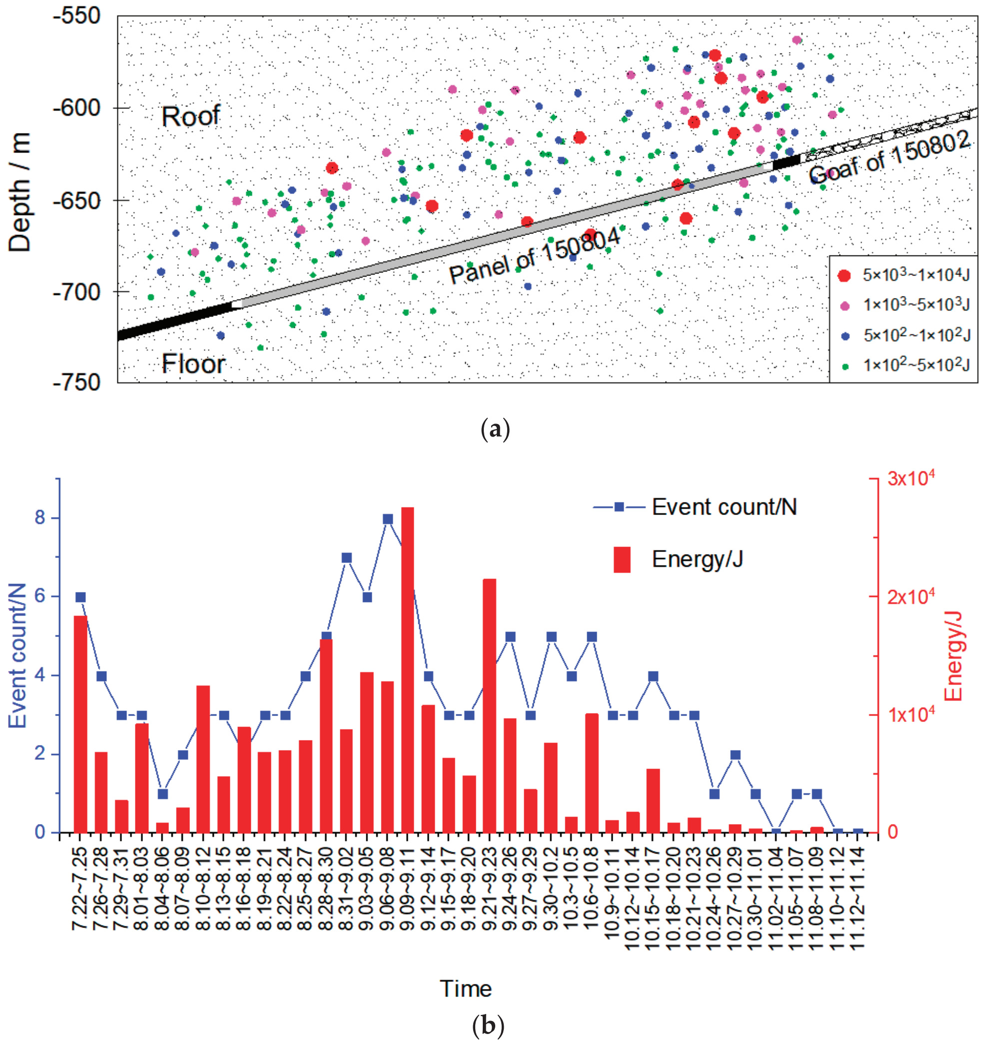

Figure 13. Microseismic events in the 150804 panel. (**a**) Microseismic spatial distribution. (**b**) Microseismic energy and frequency.

The theoretical analysis and calculation yielded that the minimum time required for roof stability is 108.9 days, which is slightly longer than the result of microseismic monitoring. This might be attributed to the fact that microseismic monitoring is more effective in detecting roof fractures and the fractures of coal and rock masses, but that it is unable to monitor the slow roof sinking and the gradual changes in the stress of the coal mass. Therefore, the results obtained from theoretical analysis are more favorable for keeping the roadway stable. To minimize the impact of dynamic pressure from the 150804 working face, the gob-side roadway excavation should commence no earlier than 108.9 days after mining concludes.

6.2. Monitoring Results of Gob-Side Entry Stability

To evaluate the effectiveness of roadway stability control, on-site monitoring of the gob-side roadway deformation was conducted during the mining of the 150806 working face. Measurement points were placed 200 m ahead of the open-off cut, monitoring the roof subsidence, floor heave, and displacement of both sides of the roadway. The results are shown in Figure 14. As seen in the figure, deformation began slowly when the working face reached 150 m from the roadway measurement point. When the distance decreased to about 60 m, deformation accelerated significantly. The largest deformation occurred on the coal pillar side of the roadway, followed by the roof, the left side, and the floor, which experienced the least deformation. The maximum deformations recorded were 420 mm at the coal pillar, 203 mm at the roof, 320 mm on the right side, and 153 mm at the floor. The specific values of the roadway deformation measured on-site exhibited certain differences from the numerical simulation results; however, the overall change patterns displayed a high degree of similarity, indicating that the simulation results were relatively reliable. On-site monitoring results indicated that the use of grouting and high-strength support measures to stabilize the gob-side entry in deep soft rock ensured the surrounding rock's stability throughout the mining process, thereby providing a reliable foundation for safe production at the working face.

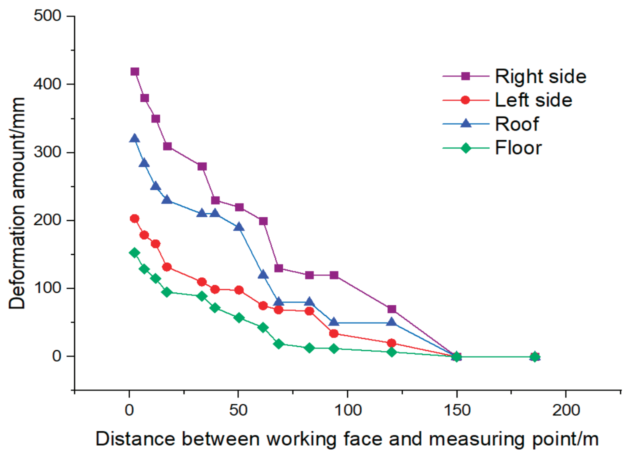

(**a**)

(**b**)

(**c**)

Figure 14. Roadway deformation laws during the mining period of the panel. (**a**) Monitoring values of roadway deformation; (**b**) deformation of roadway supported by low-strength and ungrouted supports; (**c**) deformation of roadway supported by high-strength and grouted supports.

7. Conclusions

Controlling the stability of the surrounding rock in roadways is challenging under deep mining conditions with soft rock. This study focuses on the gob-side entry of deep soft rock at Liuzhuang Coal Mine. Methods including theoretical analysis, numerical simulation, and on-site measurements are used to investigate roadway driving timing, deformation patterns, and control strategies. The findings provide valuable guidance for determining the optimal driving timing of the gob-side entry and managing roadway stability in deep soft rock environments.

(1) Through theoretical analysis, a dynamic model for the roof subsidence in the goaf is developed, and a calculation formula is provided to determine the minimum time required for the basic roof to stabilize and for the side abutment stress to balance. This offers a theoretical foundation for determining the optimal driving timing for the gob-side entry roadway. Based on the practical conditions at Liuzhuang Coal Mine, to ensure the stability of the gob-side entry in panel 150806, the roadway driving should be delayed by at least 108.9 days after the mining of panel 150804.

(2) The numerical simulation results demonstrate the significant deformation of the coal pillar and roof during both roadway driving and working face mining. The deformation is most severe when the working face is within 60 m of the roadway. Based on the observed deformation patterns, a roadway control method combining grouting modification and high-strength support is recommended. The long anchor cable and the high-density bolt (cable) support effectively increases the support strength and better plays the suspension role of the anchor cable. Following coal pillar grouting, the deformation of the coal pillar and roof subsidence were reduced by 16.7% and 7.1%, respectively. It is indicated that coal pillar grouting can not only reduce coal pillar deformation but also effectively control roof subsidence.

(3) Microseismic monitoring display that there still appeared to be microseismic events after the end of working face mining, which indicated that the roof of the goaf was still rotated and sunken and the side abutment stress was redistributed after the completion of panel mining. The microseismic monitoring results verify the reliability of the theoretical analysis. Moreover, the minimum time of roof stability and side abutment stress balance obtained by microseismic monitoring was less than that of theoretical analysis, which indicates that the driving time of gob-side entry calculated by theoretical analysis is safer. On-site measurements of roadway deformation showed satisfactory stability, suggesting that the roadway driving timing was appropriately chosen. Additionally, the use of high-strength support and grouting methods effectively ensures the stability of the gob-side entry.

Author Contributions: All authors were involved in the conception and design of the study. L.M. and L.X. contributed equally to this study. Conceptualization, L.M. and L.X.; methodology, C.L. and P.K.; investigation, T.C. and X.Q.; writing—original draft, L.M. and L.X.; writing—review and editing, W.M. and P.K.; software, W.M. All authors have read and agreed to the published version of the manuscript.

Funding: This study received funding from the National Natural Science Foundation of China Youth Program (52304074), the Doctoral Research Fund of Shandong Jianzhu University (XNBS20116), the Open Fund of Engineering Laboratory for Safe and Precise Coal Mining of Anhui Province (ESCMP202308), and the Start-up Fund for Introducing Talents and Scientific Research of Anhui University of Science and Technology (13210151).

Data Availability Statement: The original contributions of the study are contained in the article, and additional inquiries can be directed to the corresponding author.

Conflicts of Interest: Author Lu Ma was employed by the company China Coal Xinji Liuzhuang Mining Co., Ltd. The remaining authors declare that the research was conducted in the absence of any commercial or financial relationships that could be construed as a potential conflict of interest.

References

1. Wang, E.; Xie, S. Determination of coal pillar width for gob-side entry driving in isolated coal face and its control in deep soft broken coal seam: A case study. *Energy Sci. Eng.* **2022**, *10*, 2305–2316. [CrossRef]
2. Tian, Y.; Gong, P.; Zhao, T.; Yi, K.; Wen, G. Instability prediction model of remaining coal pillars under remining disturbance. *Energy Sci. Eng.* **2023**, *11*, 1842–1857. [CrossRef]
3. Yang, F.; Liu, W.; Zhu, X.; Xiang, C. The rock-breaking mechanism of thermal spalling-assisted rock cutting by PDC cutter. *Rock Mech. Rock Eng.* **2023**, *57*, 993–1012. [CrossRef]
4. Wu, H.; Li, Q.; Zhu, C.; He, L. Study on the failure law of surrounding rock in inclined coal seam with gob side entry. *Sci. Rep.* **2023**, *13*, 973. [CrossRef]
5. Shen, F.; Song, Y.; Zhao, W.; Zhao, S.; Yang, J.; Tian, Y.; Zheng, J.; Liu, C. Research on novel method of gob-side entry retaining under the synergistic effect of roof cutting and roadside filling in thick coal seams. *Rock Mech. Rock Eng.* **2023**, *56*, 7217–7236. [CrossRef]
6. Li, Z.; Zhang, Y.; Ma, Q.; Zheng, Y.; Song, G.; Yan, W.; Zhang, Y.; Hu, L. The floor heave mechanism and control technology of gob-side entry retaining of soft rock floor. *Sustainability* **2023**, *15*, 6074. [CrossRef]
7. Ma, Q.; Zhang, Y.; Li, Z.; Song, G.; Zheng, Y. The roadway layout and control technology of pillar-free mining of soft coal seams in high gassy mines. *Processes* **2022**, *10*, 1784. [CrossRef]
8. Wang, J.; Li, W.; Zhu, D.; Gong, W.; Su, Y. Novel application of the roof-cutting-type gob-side entry retaining in coal mine. *Math. Probl. Eng.* **2021**, *2021*, 1625282. [CrossRef]
9. Feng, S.; Chen, X.; Wang, L.; Li, L.; Li, X. Air flow movement law in working face and gob with roof-cutting and pressure-releasing mining: A numerical simulation and engineering verification. *ACS Omega* **2023**, *8*, 25960–25971. [CrossRef]
10. Li, C.; Liu, J.; Bai, Y.; Ge, Q. Study on stability of filling wall under lateral large-span composite hinge fracture of hard critical block. *Sci. Prog.* **2021**, *104*, 00368504211021694. [CrossRef]
11. Du, W.; Li, H.; Qi, Q.; Zheng, W.; Yang, S. Research on multifactor analysis and quantitative evaluation method of rockburst risk in coal mines. *Lithosphere* **2022**, *11*, 5005317. [CrossRef]
12. Wen, Y.; Cao, A.; Guo, W.; Xue, C.; Lv, G.; Yan, X. Strata movement and mining-induced stress identification for an isolated working face surrounded by two goafs. *Energies* **2023**, *16*, 2839. [CrossRef]
13. Zhao, Y.; Xiang, Z. Structural stability and surrounding rock integrity analysis for goaf-side entry with small coal pillars in longwall mining. *Appl. Sci.* **2023**, *13*, 6877. [CrossRef]
14. Li, L.; Qian, D.; Yang, X.; Jiao, H. Pressure relief and bolt grouting reinforcement and width optimization of narrow coal pillar for goaf-side entry driving in deep thick coal seam: A Case Study. *Mineral* **2022**, *2*, 1292. [CrossRef]
15. Zhang, Z.; Chen, X.; Yu, Z.; Sun, H.; Huang, D.; Wu, J.; Zhang, H. Mitigating coal spontaneous combustion risk within goaf of gob-side entry retaining by roof cutting: Investigation of air leakage characteristics and effective plugging techniques. *Fire* **2024**, *7*, 98. [CrossRef]
16. Yin, Z.; Liu, J.; Liu, Y.; Li, W. Analysis for overburden destruction on lateral boundary of stope based on viscoelastic-plastic finite element method. *Adv. Civ. Eng.* **2021**, *2021*, 8882481. [CrossRef]
17. Yang, Y.; Meng, L.; Yuan, L. Analysis of overburden movement and side abutment pressure distribution in deep stope with varying coal seam thickness. *Front. Earth Sci.* **2023**, *11*, 1323679. [CrossRef]
18. Kang, H.; Jiang, P.; Wu, Y.; Gao, F. A combined "ground support-rock modification-destressing" strategy for 1000-m deep roadways in extreme squeezing ground condition. *Int. J. Rock Mech. Min. Sci.* **2021**, *142*, 104746. [CrossRef]
19. Wang, M.; Xu, Y.; Xu, Q.; Shan, C.; Li, Z.; Nan, H.; Li, Y.; Liu, H.; Chu, T. Stability control of overburden and coal pillars in the gob-side entry under dynamic pressure. *Int. J. Rock Mech. Min. Sci.* **2023**, *170*, 105490. [CrossRef]
20. Bai, J.; Shen, W.; Guo, G.; Wang, X.; Yu, Y. Roof deformation, failure characteristics, and preventive techniques of gob-side entry driving heading adjacent to the advancing working face. *Rock Mech. Rock Eng.* **2015**, *48*, 911–926. [CrossRef]
21. Pang, D.; He, K.; Xu, Y.; Chang, J.; Niu, X.; Li, C. Stress distribution law of full-length anchorage bolt in rectangular roadway. *Front. Earth Sci.* **2022**, *10*, 885681. [CrossRef]
22. Kong, P.; Liu, C.; Yang, D.; Shihui, L.; Ruiju, J. Mechanism of Roof Cutting and Stress Relief in Coal Seams with Hard Sandstone Coverage. *Geotech. Geol. Eng.* **2024**, *42*, 5251–5267. [CrossRef]

buildings

MDPI

Article

Influence of Groundwater Level Rising on Mechanical Properties of Pile Foundations Under a Metro Depot in Loess Areas

Xuewen Rong [1,2], Mingze Li [2,*], Hongjian Liao [2], Ao Zhang [2], Tao Dang [1], Hangzhou Li [2] and Zheng Wu [1]

[1] Shaanxi Huashan Road and Bridge Group Co., Ltd., Xi'an 710016, China; rongxuewen1973@163.com (X.R.); taizi702@163.com (T.D.); wuzheng.chn@outlook.com (Z.W.)
[2] School of Human Settlements and Civil Engineering, Xi'an Jiaotong University, Xi'an 710049, China; hjliao@mail.xjtu.edu.cn (H.L.); aozhang@stu.xjtu.edu.cn (A.Z.); lihzh@xjtu.edu.cn (H.L.)
* Correspondence: lmz3122322096@stu.xjtu.edu.cn

Abstract: The span of pile foundations beneath metro depots typically ranges from 10 to 20 m, exhibiting a notably large span. This structural characteristic results in the pile foundations bearing a more concentrated upper load, while the interstitial soil between the piles bears minimal force. Concurrently, global climate change and enhanced urban greening initiatives have led to a significant increase in rainfall in northwest China, a region traditionally characterized by arid and semi-arid conditions. This climatic shift has precipitated a continuous rise in groundwater levels. Furthermore, the extensive distribution of collapsible loess in this region exacerbates the situation, as the rising groundwater levels induce loess collapse, thereby adversely affecting the mechanical behavior of the pile foundations. In light of these factors, this study utilized the pile foundations of a metro depot in Xi'an as a prototype to conduct static load model tests under conditions of rising groundwater levels. The experimental results reveal that the load–settlement curve of the pile foundations in the absence of groundwater exhibited a steep decline with distinct three-stage characteristics, and the ultimate bearing capacity was determined to be 5 kN. When the groundwater level is situated below the loess stratum, the settlement of both the pile foundations and the foundation soil, as well as the axial force, skin friction, and pile tip force, remains relatively stable. However, when the groundwater level rises to the loess stratum, there is a significant increase in the settlement of the pile foundations and foundation soil. Negative skin friction emerges along the pile shaft, and the bearing type of the pile foundation transitions gradually from a friction pile to an end-bearing pile. The influence range of the pile foundation on the settlement of the foundation soil is approximately three times the pile diameter.

Keywords: metro depot; pile foundation; groundwater; collapsible loess; model test

1. Introduction

Loess, classified as an unconsolidated quaternary aeolian sediment [1], constitutes a globally significant geological formation that occupies approximately 10% of terrestrial surfaces, predominantly within mid-latitude arid and semi-arid climatic zones [2,3]. This distinctive material exhibits a predominant granulometric composition of silt-sized particles, accompanied by notable proportions of carbonate minerals and phyllosilicate constituents including kaolinite and montmorillonite [4,5]. The pedogenic processes inherent to loess formation result in a well-developed macroporous structure, wherein interparticle voids contain not only interstitial water but also structural cementation comprising particulate aggregations and colloidal matrices-critical elements maintaining metastable fabric integrity. The synergistic combination of high void ratios and hydrophilic mineralogy predisposes loess to hydro-consolidation phenomena, characterized by disintegration of cementitious bonds under aqueous conditions, subsequent pore structure collapse, and rapid shear strength reduction [6]. Current geotechnical evaluations estimate that approximately 60% of global loess deposits demonstrate collapsible behavior [7]. Within China's northwestern territories, this problematic soil covers approximately 630,000 km^2, with the majority exhibiting metastable characteristics [8–10]. Stratigraphic investigations by Zhu et al. [11] reveal substantial thickness variations (0–350 m) in the Loess Plateau sequences, averaging 92.2 m, with spatial distribution patterns strongly modulated by topographic constraints, vegetative cover dynamics, and anthropogenic disturbances. These findings collectively establish the northwestern Chinese loess deposits as extensive yet heterogeneously stratified formations. Anthropogenic climate change and urban greening initiatives have precipitated hydrologic regime alterations in historically drought-prone northwestern China. Hydrometeorological analyses by Li et al. [12] document a progressive intensification of mean annual precipitation in fluvial basins of northwest China, escalating from 160 mm (1960s) to 190 mm (2016), with continued positive trends. This precipitation amplification has induced regional aquifer recharge, evidenced by monitoring data from Xi'an demonstrating persistent groundwater elevation trends since 2002 [13–15]. Hydrogeologic interactions attain critical significance when rising water tables saturate collapsible loess strata, triggering fabric collapse under superincumbent loads. This phenomenon induces progressive foundation settlement, culminating in substantial bearing capacity degradation and consequential geotechnical failures in pile-supported structures [16].

The progressive implementation of China's Western Development Strategy has catalyzed accelerated economic growth and urbanization in northwestern regions, accompanied by significant rural-to-urban migration [17]. This demographic shift has precipitated heightened pressure on urban transportation infrastructure. Urban rail transit systems, as sustainable mobility solutions, have gained prominence due to their operational efficiency, cost-effectiveness, and safety advantages, emerging as preferred transportation modalities in metropolitan areas [18]. Notably, while these systems demonstrate substantial societal benefits, their extensive spatial requirements and elevated capital investments necessitate innovative development approaches. The transit-oriented development (TOD) paradigm has consequently been adopted to optimize land utilization, enhance commercial potential, and ensure sustainable public transportation ecosystems [19]. This model integrates mixed-use complexes incorporating commercial, residential, and cultural facilities above metro depots, generating synergistic revenue streams to subsidize rail infrastructure development [20]. Functionally, metro depots serve as critical nodal facilities for rolling stock storage, maintenance, and operational management. Their specialized operational requirements necessitate substantial spatial footprints, with individual structures spanning 0.2–0.4 km^2 [21,22]. The architectural configuration of these integrated depot-over-development complexes imposes unique geotechnical demands, particularly regarding foundation systems. The pile-supported substructures exhibit remarkable span dimensions (10–20 m), transmitting superstructure loads through beam–slab structural systems to pile caps, ultimately distributing concentrated forces of up to 10,000 kN per pile. Contrastingly, the interstitial soil zones designated for vehicle parking and maintenance operations sustain minimal surface pressures (<10 kPa), creating pronounced differential loading conditions between structural and non-structural areas. Current academic inquiry predominantly focuses on station construction mechanics and structural vibration responses in depot facilities [23–28]. Many scholars also pay less attention to the research on the static bearing properties of metro depot pile foundations, especially in collapsible loess areas. To address this knowledge gap, this study employs scaled model testing methodologies, utilizing

Xi'an metro depot pile foundations as prototypical references, to systematically investigate load transfer mechanisms and bearing capacity evolution during groundwater elevation processes and obtain a reasonable foundation treatment range.

2. Test Materials and Instruments

2.1. Artificial Collapsible Loess

The depositional processes of loess engender distinct anisotropic structural characteristics, manifested through preferential vertical alignment of soil particles forming dense bedding planes, contrasted with relatively disorganized horizontal particle arrangements. This anisotropy induces marked variations in physico-mechanical properties along different axes, resulting in significant spatial heterogeneity of engineering parameters across depositional environments and stratigraphic depths in natural loess formations [29]. Additionally, the structure of natural loess can be destroyed during the preparations of remolded soil. To address these problems, the experimental investigation employed engineered collapsible loess specimens formulated through controlled material synthesis. The synthetic loess matrix, designed to replicate the granulometric and mineralogical characteristics of natural deposits, comprises precisely proportioned constituents: barite powder (25%), fluvial sand (35%), kaolin (30%), Portland cement (3%), sodium chloride (5%), and calcium oxide (2%) [30] (Figure 1). This formulation strategically utilizes:

1. Barite powder and fluvial sand as granular constituents regulating bulk density through particle packing density modulation;
2. Fluvial sand as shear strength modifiers controlling internal friction characteristics and deformation response;
3. Hydraulic cement as supplementary cementitious agents;
4. Kaolin forms clay cementations;
5. Calcium oxide undergoing carbonation reactions with atmospheric CO_2 in aqueous conditions to generate calcium carbonate cementation.

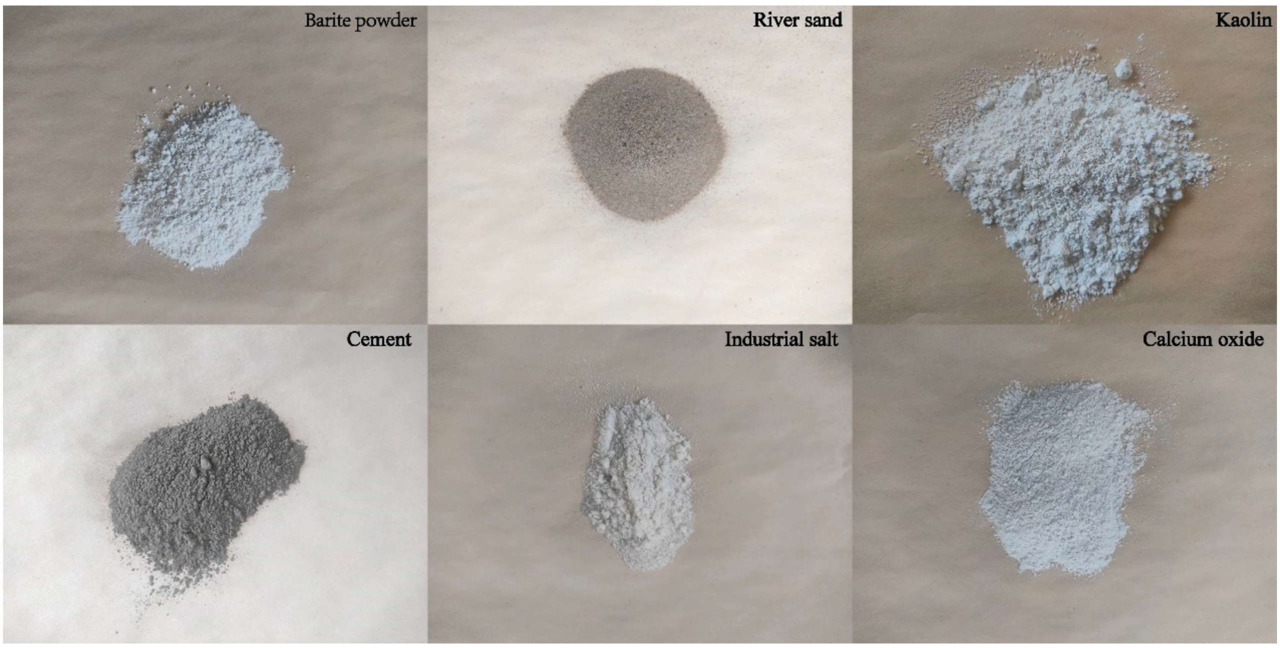

Figure 1. Materials for preparing artificial collapsible loess.

This multi-phase cementation system effectively simulates the metastable fabric of natural collapsible loess while ensuring experimental repeatability and parameter controllability—critical requirements for rigorous model testing protocols.

The interparticle contact architecture of natural loess, characterized by point-to-point particle connections, engenders an intrinsically unstable metastable fabric that fundamentally governs its collapsibility mechanisms [31,32]. This inherent characteristic necessitates rigorous replication of natural intergranular contact patterns during synthetic specimen fabrication. Building upon the methodological advancements of Assalay et al. [33,34] and Jefferson and Ahmad [35], whose Monte Carlo simulations substantiated the efficacy of the free-drop method in stimulating the deposition process of natural loess. Hence, the soil particles of the artificial loess sample prepared by the free-drop method can also form point-point contact. The specimen preparation sequence is delineated as follows (Figure 2):

(1) Precisely proportioned constituent materials were homogenously blended through mechanical mixing. A granulometric sieve (2 mm aperture) was positioned vertically at 20–40 cm above a standardized sampling ring. The composite mixture was systematically introduced onto the sieve platform, followed by continuous vibration. This methodology can simulate natural depositional processes.
(2) The prepared specimen surface was smoothed, followed by static compaction to achieve predetermined density specifications. Subsequently, specimens were subjected to isothermal desiccation in an oven maintained at 50 ± 1 °C for 24 h. Finally, a sprayer was used to sprinkle the sample with water mist and make it reach the optimum moisture content.

Figure 2. The preparation of the samples by free-drop method.

The bearing stratum was using non-collapsible loess sourced from Xianyang, Shaanxi Province (Figure 3). The physical and mechanical properties of artificial loess and non-collapsible loess are shown in Tables 1 and 2. Table 3 shows the collapsible coefficient of artificial loess. The specific gravity was determined using the hydrometer method, while the optimum moisture content was ascertained through moisture-density tests. The plastic and liquid limits were established via Atterberg limits tests. Cohesion and the angle of internal friction were derived from the direct shear tests. Void ratio and modulus of compression were acquired through standard compression tests. Finally, collapsibility coefficients were measured from wetting-induced compression tests.

Figure 3. The remolded soil of non-collapsible loess.

Table 1. Physical properties of artificial loess and non-collapsible loess.

Physical Properties	Specific Ratio	Optimum Moisture Content/%	Void Ratio	Liquid Limit/%	Plastic Limit/%
Artificial collapsible loess	2.72	12	1.12	25.5	15.4
Non-collapsible loess	2.71	16	0.63	26.8	17.5

Table 2. Mechanical properties of artificial loess and non-collapsible loess.

Mechanical Properties	Compression Modulus/MPa	Cohesion/kPa	Internal Friction Angle/°
Artificial collapsible loess	4.16	24.7	23.2
Non-collapsible loess	6.52	33.4	28.7

Table 3. Collapsible coefficients of artificial loess.

Pressure	50 kPa	100 kPa	200 kPa	300 kPa
Collapsible coefficient	0.075	0.082	0.088	0.089

2.2. Model Box and Model Piles

The experimental configuration employed a plexiglass test chamber (80 cm × 50 cm × 80 cm internal dimensions) for deformation monitoring, as illustrated in Figure 4. The parameters of the plexiglass are shown in Table 4. Structural integrity was ensured through peripheral reinforcement using hot-rolled I-beam steel sections, while a water inlet valve integrated at the lower part facilitated controlled groundwater elevation. The test chamber was rigidly mounted on a reinforced reaction frame equipped with two servo-controlled hydraulic jacks suspended from the upper crossbeam. The hydraulic system on the left side of the reaction frame can provide pressure for the actuators, and a digital pressure gauge was installed above the hydraulic system to check the loading pressure in real time.

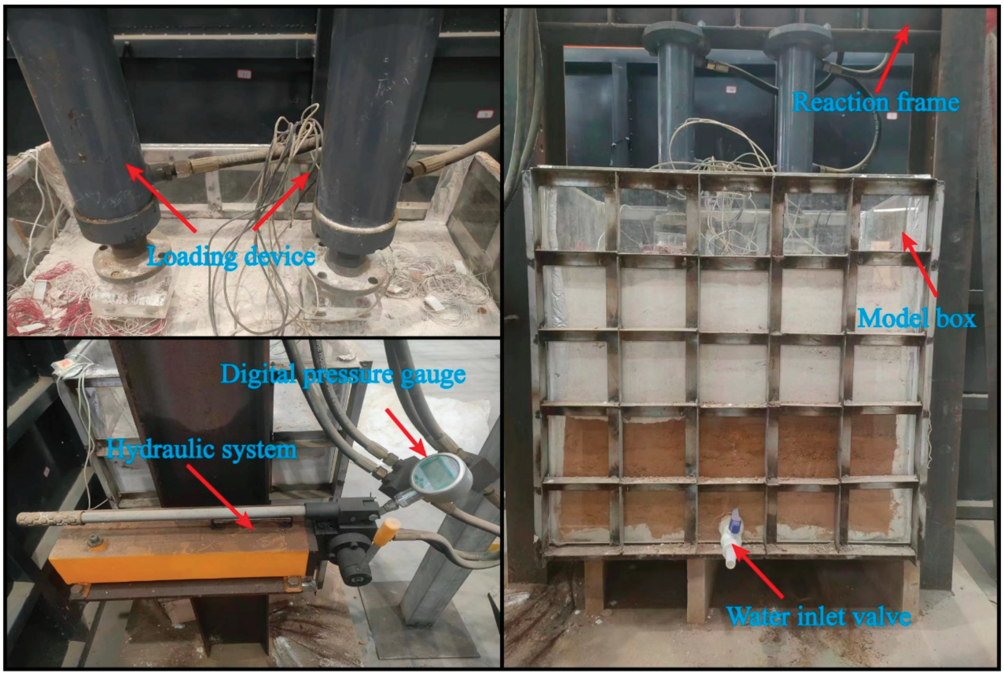

Figure 4. Model box and loading system.

In the model test, 2 × 2 pile groups with a similarity ratio of 1:50 were used. The single piles and pile caps were made of plexiglass. The pile diameter was 2 cm and the pile length was 50 cm. The pile spacing was 6 cm. The size of a pile cap size was 10 cm × 10 cm × 3 cm. The preparation processes were as follows (Figure 5):

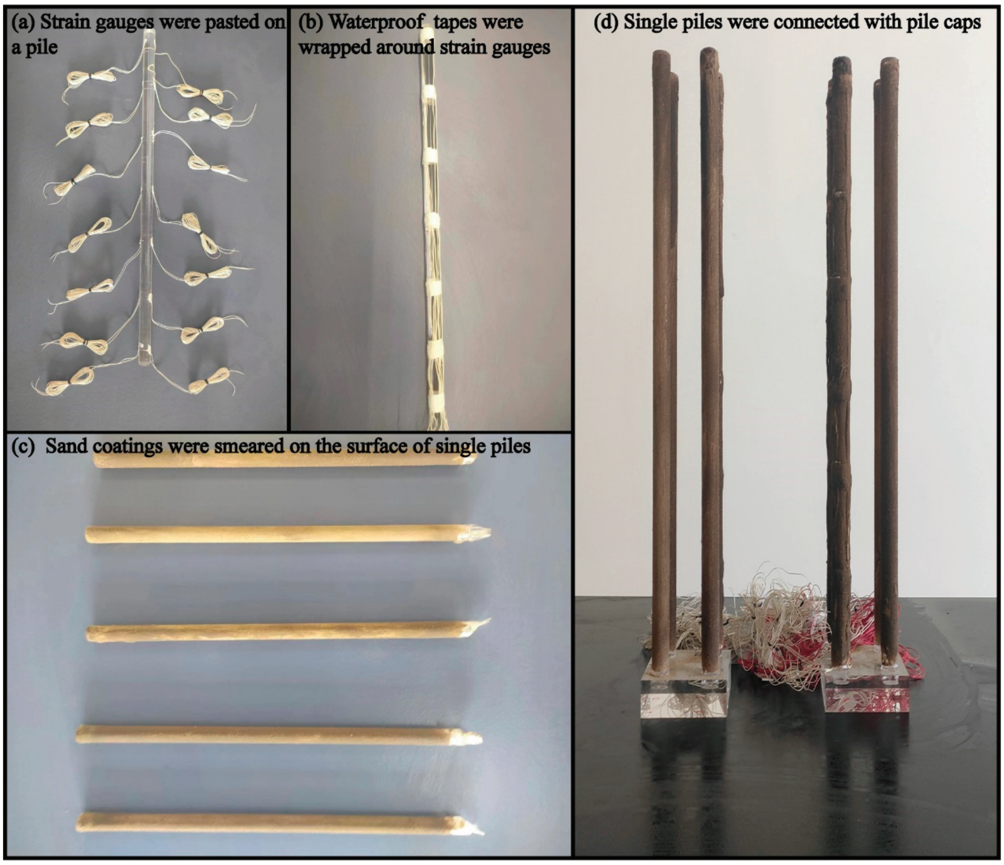

Figure 5. Preparation processes of model pile foundations.

Table 4. Material parameters of plexiglass.

Elastic Modulus/MPa	Poisson's Ratio	Gravity/(kN/m^3)
3300	0.2	12

2.3. Test Condition Setting

2.3.1. The Layout of Pile Foundations

The geometric configuration of the pile foundation, as illustrated in Figure 6, comprises a vertically embedded depth of 45 cm, with stratigraphic composition specifically divided into a 35 cm thick engineered collapsible loess stratum overlying a 30 cm compacted bearing stratum. Pile elements were positioned with a center-to-center spacing of 20 cm. Surface deformation monitoring was implemented through an array of ten settlement marks per lateral boundary. Instrumentation protocols included (Figure 7):

1. Strain Analysis: Symmetrically distributed strain gauges (120 Ω foil-type, ±1 με accuracy) along pile shafts to capture strain change;
2. Tip Resistance Monitoring: Miniaturized soil pressure transducers installed at pile tip.

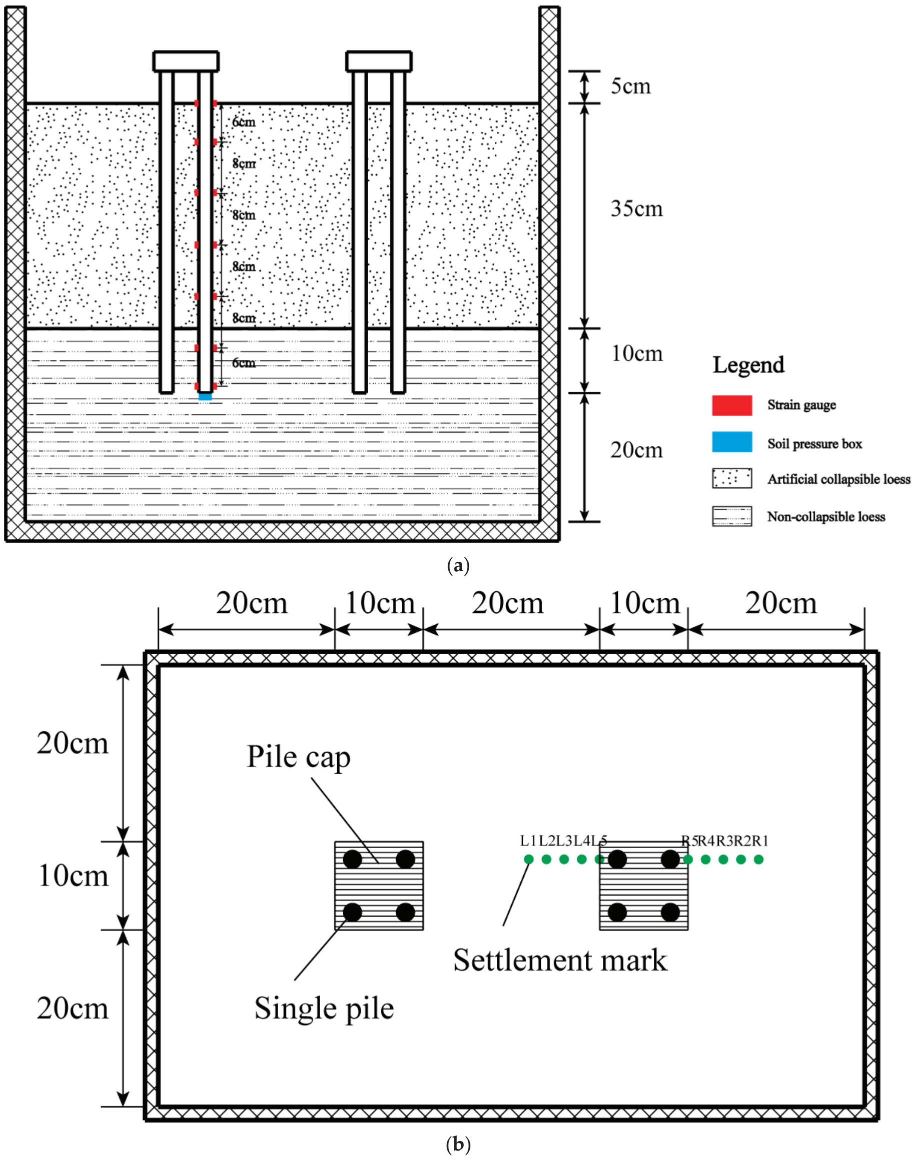

Figure 6. Layout drawing of pile foundations. (**a**) Front view. (**b**) Top view.

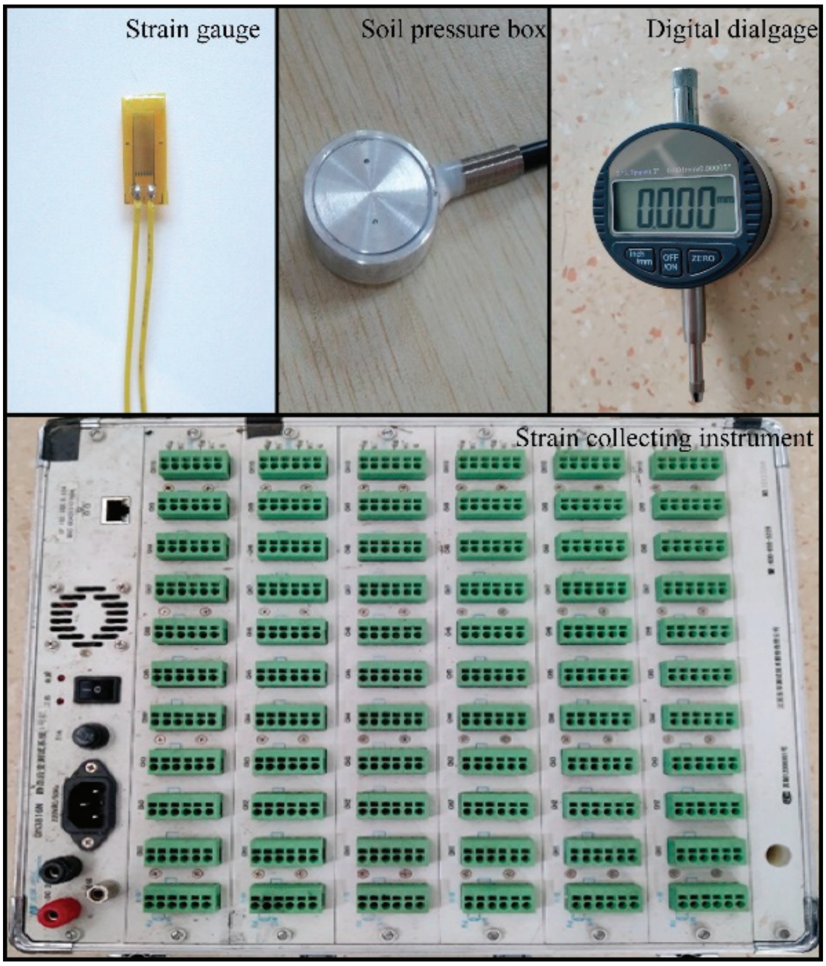

Figure 7. Data-collecting devices.

2.3.2. The Loading Process of the Without Groundwater Condition

The first testing condition is loading without groundwater. Before loading, the ultimate bearing capacity of a single pile was estimated according to the Technical Code for Building Pile Foundations (JGJ 94-2008) [36], as shown in Equation (1):

$$Q_{uk} = Q_{sk} + Q_{pk} = u\sum q_{sik}l_i + q_{pk}A_p, \quad (1)$$

where Q_{uk} is the ultimate bearing capacity of a single pile; Q_{sk} and Q_{pk} are the standard values of total ultimate skin friction and total ultimate pile tip force, respectively; u is the circumference of the pile body; q_{sik} is the standard value of the ultimate skin friction of soil layer i around the pile; l_i is the thickness of soil layer i around the pile; q_{pk} is the standard value of ultimate pile tip force; A_p is cross-sectional area of the single pile. According to the recommended value in the specification, $q_{s1k} = 25$ kPa, $q_{s2k} = 55$ kPa, and $q_{pk} = 1500$ kPa were taken. The calculated determination yielded an ultimate bearing capacity of 1.36 kN for individual model piles. Theoretical group capacity, calculated through arithmetic superposition without considering pile interaction effects, was estimated at 5.44 kN. To accommodate experimental practicality, the design bearing capacity was conservatively established at 5.5 kN. Loading protocols strictly adhered to the Technical Code for Testing of Building Foundation Piles (JGJ 106-2014) [37], implementing the following controlled sequence:

1. Load incrementation:
    a. Primary stage: 2× graded load (1.0 kN);
    b. Subsequent stages: 0.5 kN increments (1/11 of ultimate bearing capacity);
2. Stable criteria: ≤0.1 mm displacement over a consecutive 2 h monitoring period post 30 min load maintenance;
3. Termination conditions: settlement exceeds twice the preceding stage's displacement.

2.3.3. Setting of Groundwater Level and Upper Load

The other testing condition is loading while the groundwater rises slowly. Figure 8 delineates the phased elevation of the phreatic surface during hydraulic boundary condition simulations. The groundwater regime was systematically modulated through three controlled injection phases:

1. Initial phase: stabilization of the water table within the bearing stratum post-injection.
2. Second phase: groundwater rises to permeate the part of artificial collapsible loess stratum.
3. Tertiary phase: full saturation of the soil matrix through complete inundation.

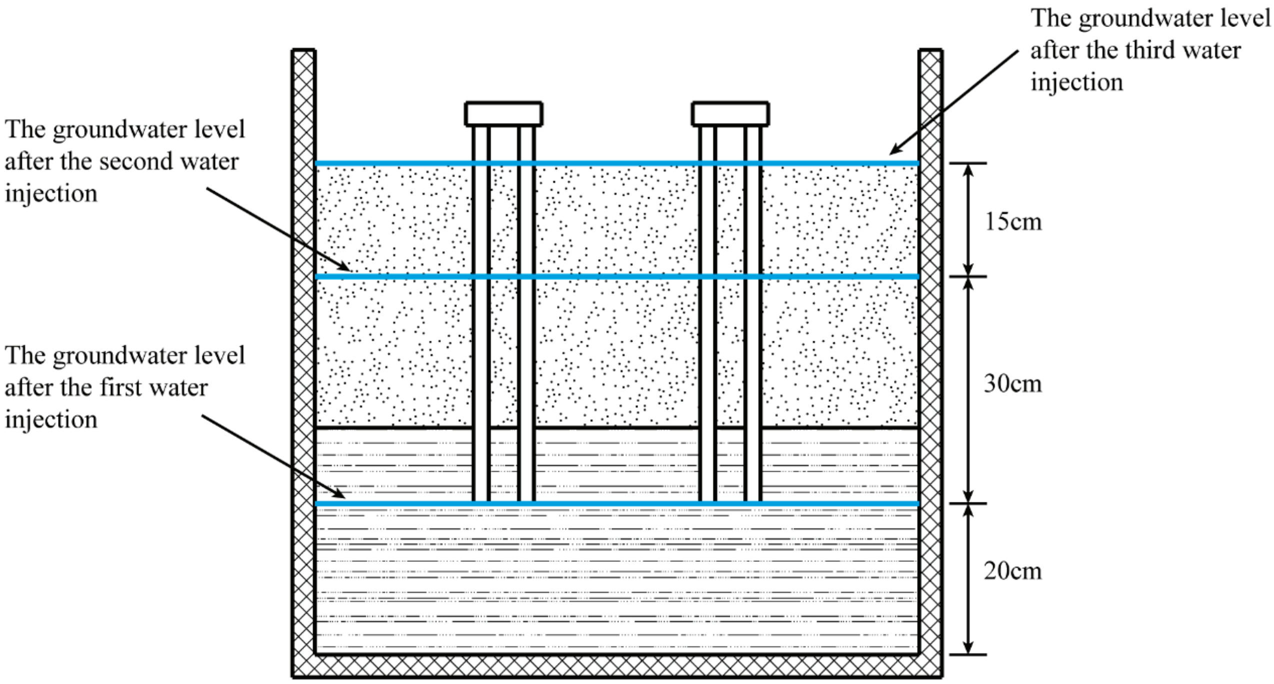

Figure 8. The setting of groundwater level.

The tests incorporated two distinct loading configurations under groundwater elevation scenarios: the upper load of 1/4 and 1/2 of the ultimate bearing capacity, respectively. Data acquisition at 8 h intervals across three sequential measurement cycles (over a cumulative 24 h observation period).

3. Static Load Test Under the Condition of No Groundwater

3.1. Change of Pile Foundations Settlement with the Applied Load

The settlement of the pile foundation is an important index to judge the bearing capacity of the pile foundation. Figure 9 delineates the load–settlement behavior of the pile foundation system, exhibiting three distinct deformation regimes demarcated by inflection points in the curve:

1. Linear elastic phase (0–4.5 kN): axial displacement demonstrated proportionality to applied load, indicative of reversible elastic strain.
2. Plastic yielding phase (4.5–5 kN): a nonlinear transition occurred, signaling the appearance of unrecoverable deformation.
3. Structural failure phase (>5 kN): displacement escalates to 15.44 mm at 5.5 kN load, exceeding the 6.55 mm displacement at 5 kN by a factor of 2.36.

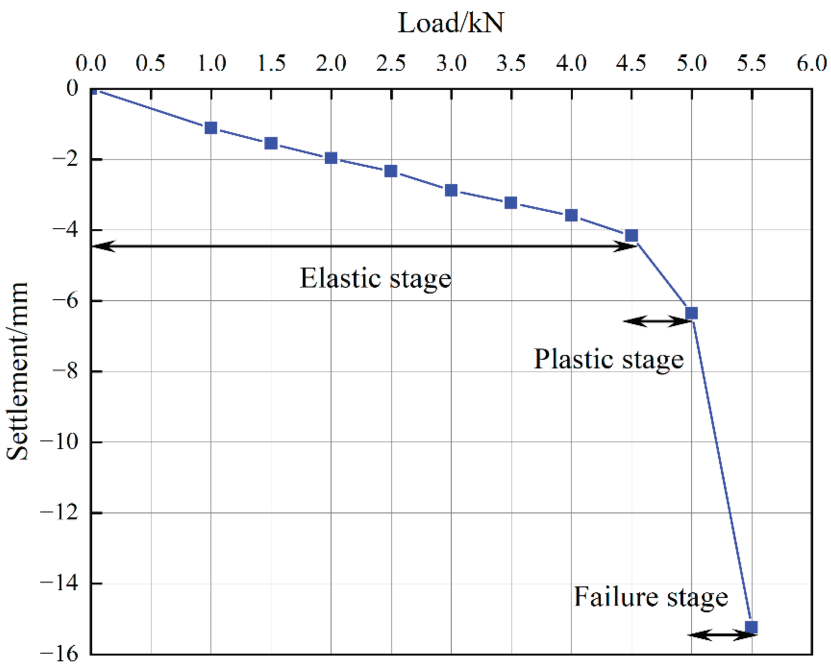

Figure 9. Load–settlement curve of pile foundations without groundwater.

The characteristic of change of settlement is in keeping with the conclusions of Chai et al. [6]. Per the Technical Code for Building Pile Foundations (JGJ 94-2008) [36], the ultimate bearing capacity Q_{ult} is defined at the load preceding a doubling of displacement under incremental loading ($s_{n+1}/s_n > 2$). Experimental validation confirmed $Q_{ult} = 5$ kN, with subsequent load increments inducing metastable collapse. Applying a conventional safety factor $K_s = 2$, the allowable bearing capacity is derived as $Q_{allow} = Q_{ult}/K_s = 2.5$ kN.

3.2. Distribution of Axial Force and Skin Friction in Pile Shafts

The interaction between the pile foundation and the soil can be revealed to a certain degree by studying the axial force and skin friction. Figures 10 and 11 delineate the axial force distribution and skin friction characteristics of the pile foundation system under non-saturated conditions. Upon application of vertical loading, the pile undergoes compressive deformation, initiating vertical displacement. The load transfer mechanism can be explained as: superstructure loads are transmitted via the pile cap to the pile shaft and subsequently redistributed to the surrounding soil matrix through interfacial shear stresses. Differential settlement arises between the pile and adjacent soil mass due to disparities in stiffness moduli, generating relative displacement at the soil–pile interface. When pile settlement exceeds peripheral soil displacement ($s_p > s_s$), positive skin friction develops, opposing the load direction and contributing to bearing capacity mobilization. As evidenced by the axial force profiles, a progressive attenuation of axial forces occurs with depth. The distribution form of axial force and skin friction in the test is similar to the results obtained by Zhang et al. [16].

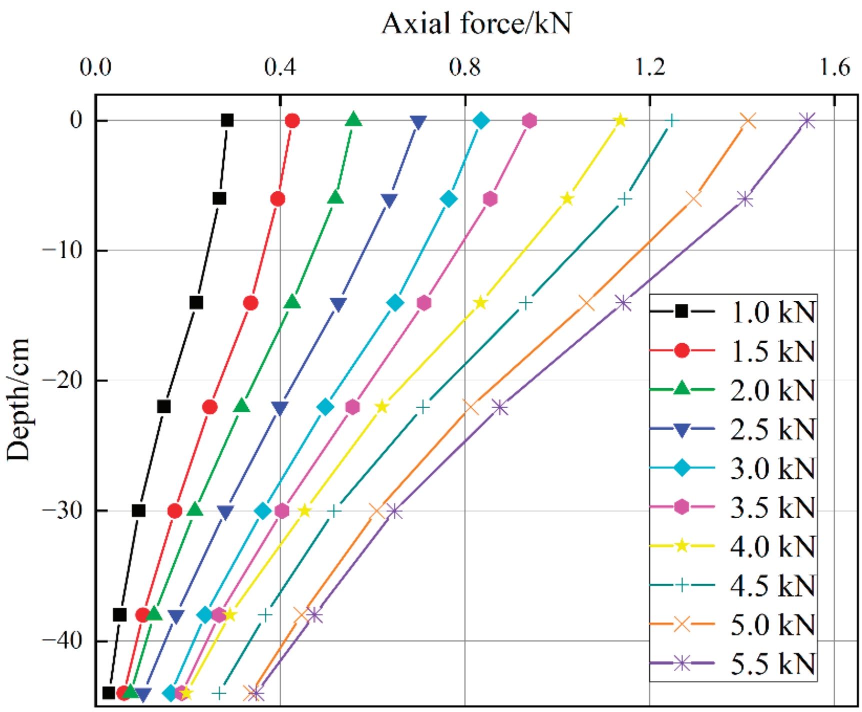

Figure 10. Axial force of the pile foundations without groundwater.

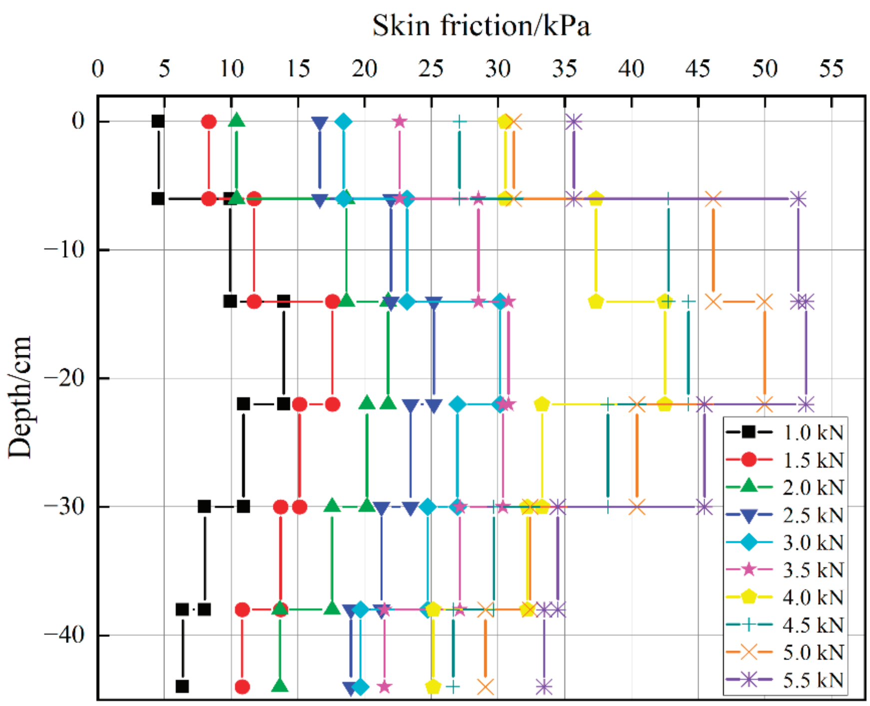

Figure 11. Skin friction of the pile foundations without groundwater.

3.3. Change of Pile Tip Force with the Applied Load

The bearing type of the pile foundation can be judged by monitoring the pile tip force. Figure 12 delineates the evolution of pile tip force under progressive axial loading. A direct proportionality is observed between the superstructure load application and the concurrent escalation of both tip force and skin friction. The load transfer efficacy is quantified through the bearing ratio r_s, mathematically expressed as Equation (2) [38]:

$$r_s = \frac{Q}{P}, \tag{2}$$

where Q is the pile tip force (skin friction) and P is the applied load. Figure 12 delineates the temporal evolution of load-bearing ratios for pile tip force and skin friction under progressive axial load. While both pile tip force and skin friction exhibit monotonic increases with applied load, proportional contributions demonstrate an inverse proportionality. This divergence becomes markedly pronounced beyond the ultimate bearing capacity threshold, which manifests in the pile foundation accelerating to the end-bearing pile (load mainly borne by pile tip force) transformation from the friction pile (load mainly borne by skin friction).

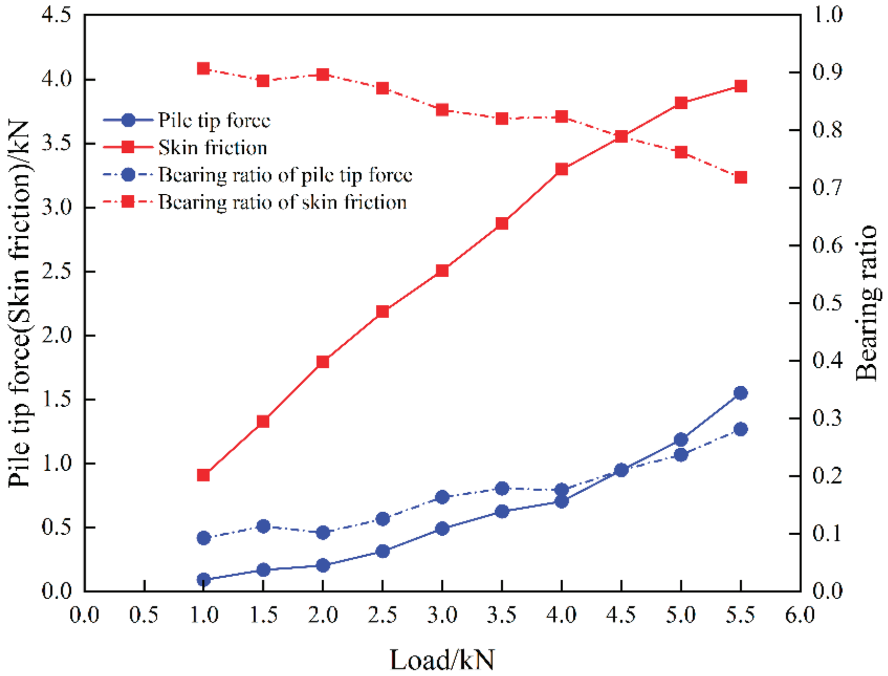

Figure 12. Change curve of pile tip force and its bearing ratio without groundwater.

3.4. Change of Foundation Soil Settlement with the Applied Load

The variation of foundation soil settlement can reveal the influence of collapsibility on foundation settlement. Figure 13 delineates the differential settlement behavior of laterally symmetric measurement nodes (L1~L5 and R1~R5) adjacent to the pile foundation. The displacement magnitudes exhibit statistically congruent evolutionary patterns across mirrored positions. The subsidence metrics follow a trajectory characterized by:

1. Initial compression phase (0–1.5 kN): progressive settlement accumulation (Δs = 0.44–1.49 mm) under linearly increasing loads;
2. Yield phase (1.5–2.5 kN): plastic deformation is generated gradually and maximum subsidence is attained finally;
3. Post-yield heave phase (2.5 kN): when the load exceeds the elastic limit of the soil, a plastic zone is formed under the pile tip. At this time, the pile tip compresses the soil, resulting in the increase of radial stress. After extension of the plastic zone, the lateral earth pressure is released, resulting in the hump of the soil.

Notably, the critical load corresponds precisely to the allowable bearing capacity derived in Section 3.1 via limit state analysis.

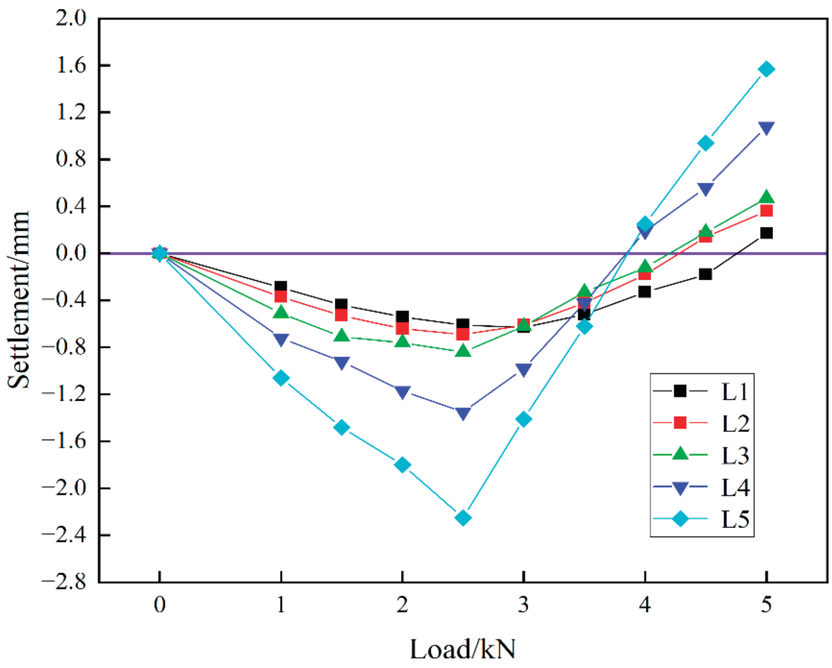

(**a**)

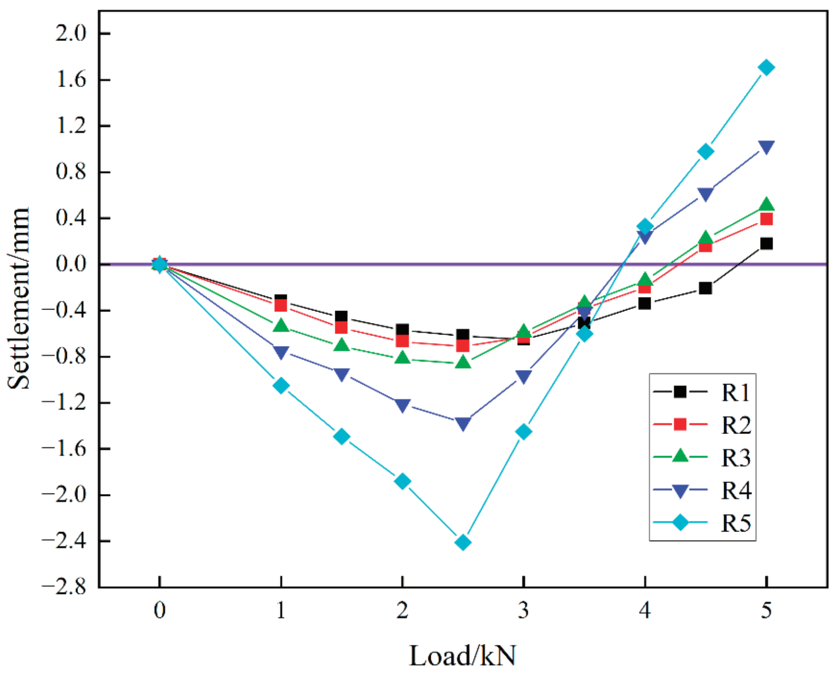

(**b**)

Figure 13. Change curve of settlement amount of foundation soil without groundwater. (**a**) L1~L5. (**b**) R1~R5.

The influence coefficient k is defined as shown in Equation (3) [38]:

$$k = \frac{s}{|r|} \tag{3}$$

where s is the vertical settlement of the foundation soil and $|r|$ is the absolute value of the radial distance from the pile axis. $k < 0$ indicates that settlement of the foundation soil has been generated and $k > 0$ indicates that the foundation soil has been uplifted. The greater the absolute value of k, the more obvious the effect of pile foundation settlement driving foundation soil settlement.

Figure 14 delineates the spatial distribution of the influence coefficient quantifying the interaction intensity between the model pile and adjacent foundation soils under unsaturated conditions. The bilateral measurement nodes (L1–L5 and R1–R5) exhibit statistically congruent influence coefficient profiles. It can be seen from the figures that the absolute value of the influence coefficient decreases rapidly, and the influence coefficient has no obvious change when it exceeds the 3D range. The test findings substantiate that under the condition of no groundwater, pile–soil interaction mechanics are governed by a confined influence zone extending radially to 3D, beyond which stress coupling diminishes asymptotically.

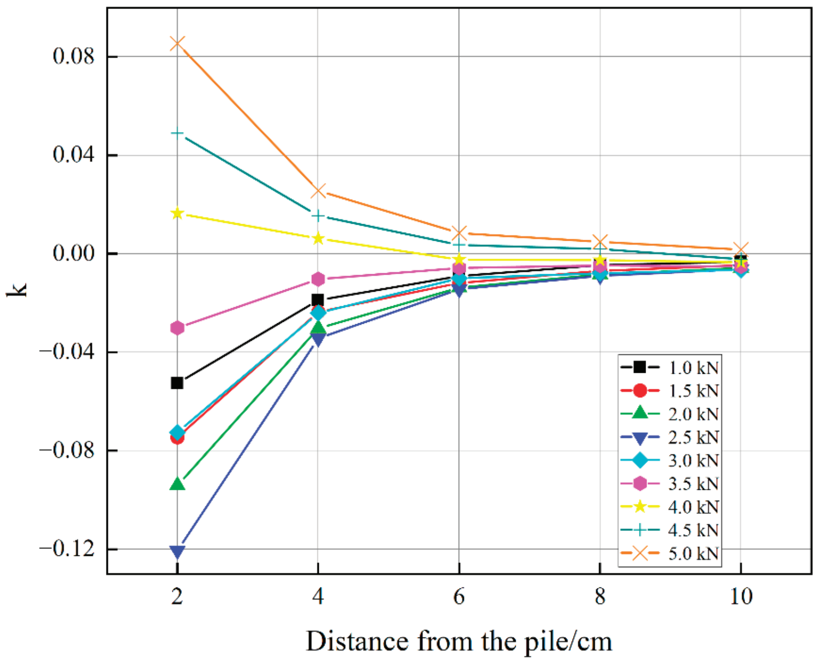

(**a**)

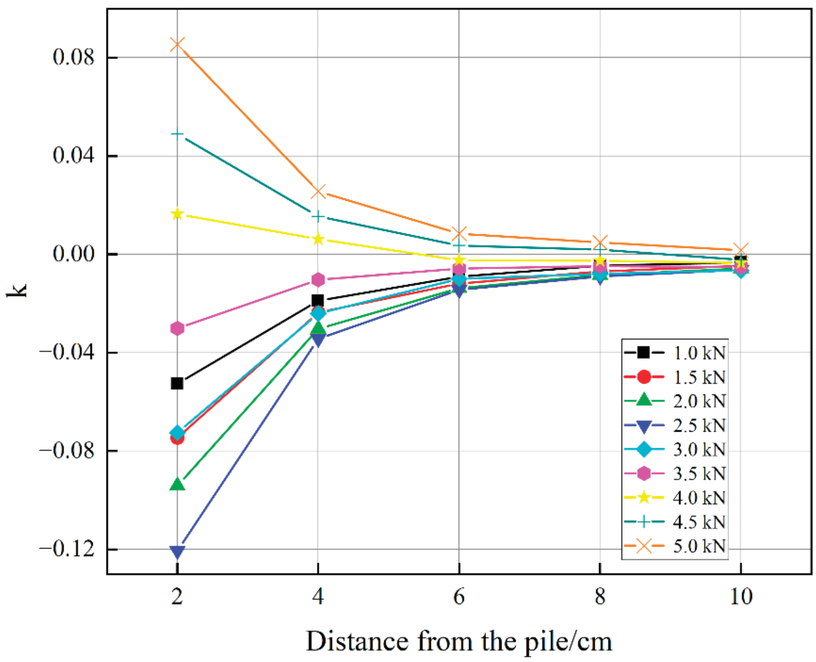

(**b**)

Figure 14. Influence coefficient of pile foundation on foundation soil without groundwater. (**a**) L1~L5. (**b**) R1~R5.

4. Static Load Test with the Condition of Rising Groundwater

4.1. Change of Pile Foundations Settlemnt with the Immersion Time

Figure 15 illustrates the variations in pile foundation settlement over time when subjected to upper loads of 1.25 kN and 2.5 kN. The data indicate that while the magnitude of settlement differs under these two loads, the overall trend in settlement follows a similar pattern. Initially, for the first 24 h following loading, the pile foundation settlement remains relatively stable due to the water level being maintained within the bearing strata, hence not impacting the collapsible loess layer. Subsequent to the second water injection, significant settlement occurs as a result of the partial collapse of the saturated artificial loess. This trend continues, albeit at a reduced rate, following the cessation of water injection, as capillary action leads to the collapse of some artificial loess above the water level. After the third injection, there is a complete collapse of the artificial loess, leading to a substantial increase in pile foundation settlement. The settlement then tends to stabilize within 24 h after stopping the water injection. Ultimately, the pile foundation settles approximately three to five times more than it would in the absence of groundwater.

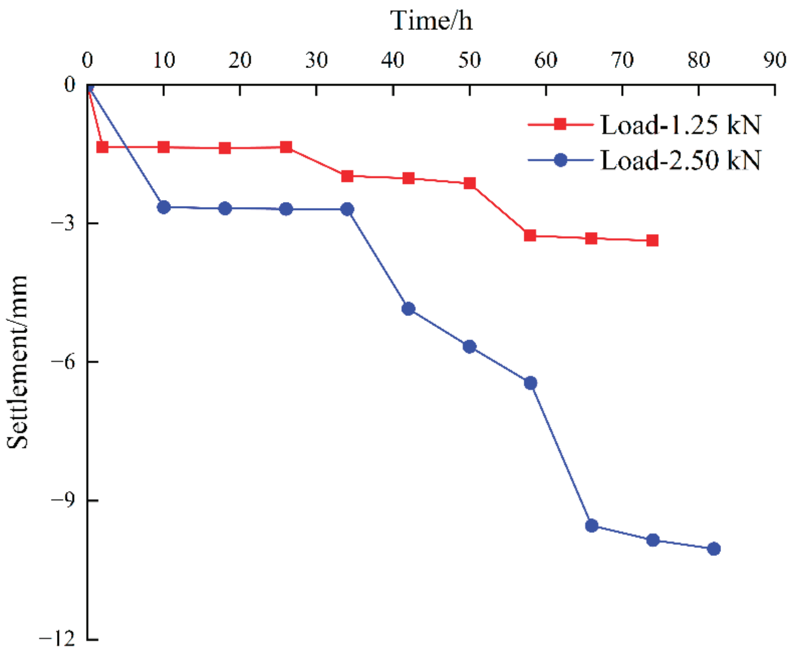

Figure 15. Settlement curve of pile foundations during groundwater rising.

4.2. Distribution of Axial Force and Skin Friction in Pile Shafts

Figure 16 depicts the axial force in the pile under applied upper loads of 1.25 kN and 2.5 kN. Under these two different vertical loads, the axial force in the pile exhibits a consistent trend. Within the first 24 h following the completion of pile foundation loading, the axial force slightly decreases due to groundwater buoyancy, although this reduction is minimal and negligible. Within 8 h subsequent to the second water injection, there is an increase in the axial force at the top of the pile, which continues to rise in the period from 8 to 24 h after injection. Following the third water injection and the complete collapse of the artificial loess, the axial force further increases, and then it eventually stabilizes.

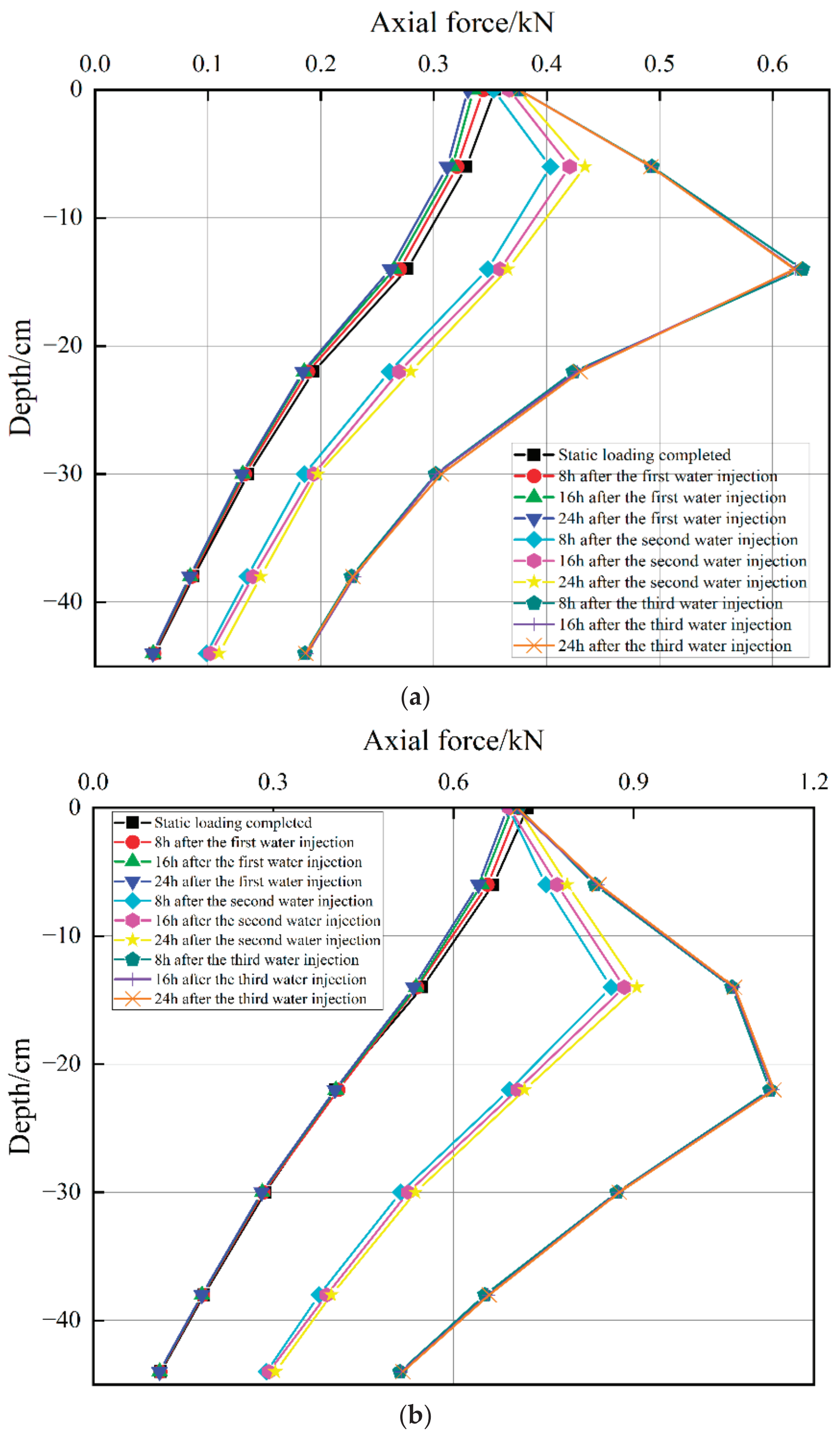

Figure 16. Axial force distribution of pile foundations during groundwater rising. (**a**) The upper load is 1.25 kN. (**b**) The upper load is 2.5 kN.

Figure 17 shows the pile skin friction under upper loads of 1.25 kN and 2.5 kN. Following loading, the pile skin friction registers as positive, aligning with the results observed in the preceding section. Within 24 h post first water injection, the presence of groundwater slightly reduces the skin friction, yet this reduction remains negligible. After the second water injection, with the partial collapse of the artificial loess layer, soil settlement intensifies and eventually exceeds that of the pile foundation. Consequently, the soil exerts a downward pull on the pile shaft, resulting in negative friction. This phenomenon also explains the continuous increase in the axial force of the pile foundations along the depth range. Once the water injection ceases, capillary action causes water to rise to the upper levels of the artificial loess layer, subsequently increasing negative skin friction resistance; however, its distribution depth on the pile does not extend. Following the third injection and the complete collapse of all artificial loess, negative friction resistance escalates, and the distribution range of negative skin friction expands, indicating that the neutral point's location descends in conjunction with the rising groundwater level. The change of skin friction and neutral point coincides with the test consequences of Zhang [38].

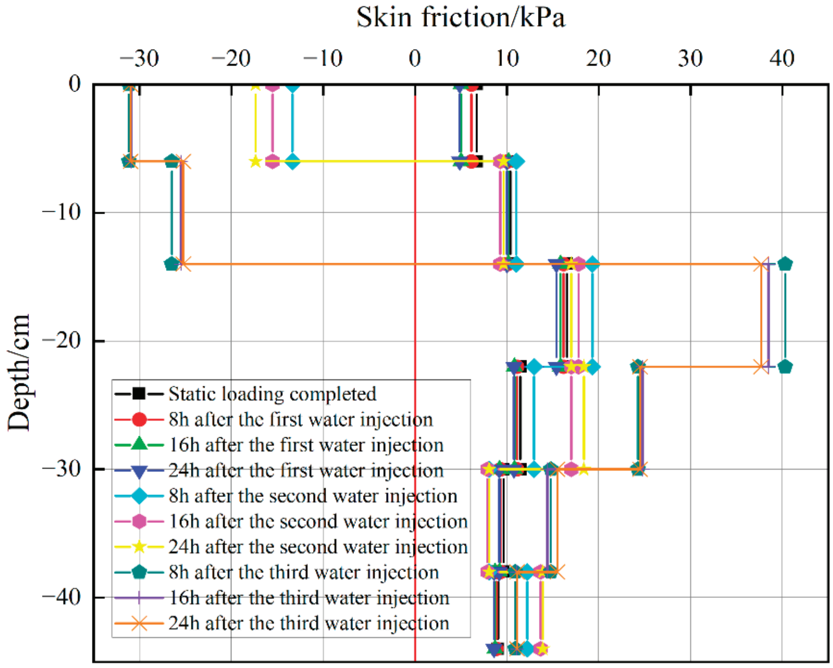

(**a**)

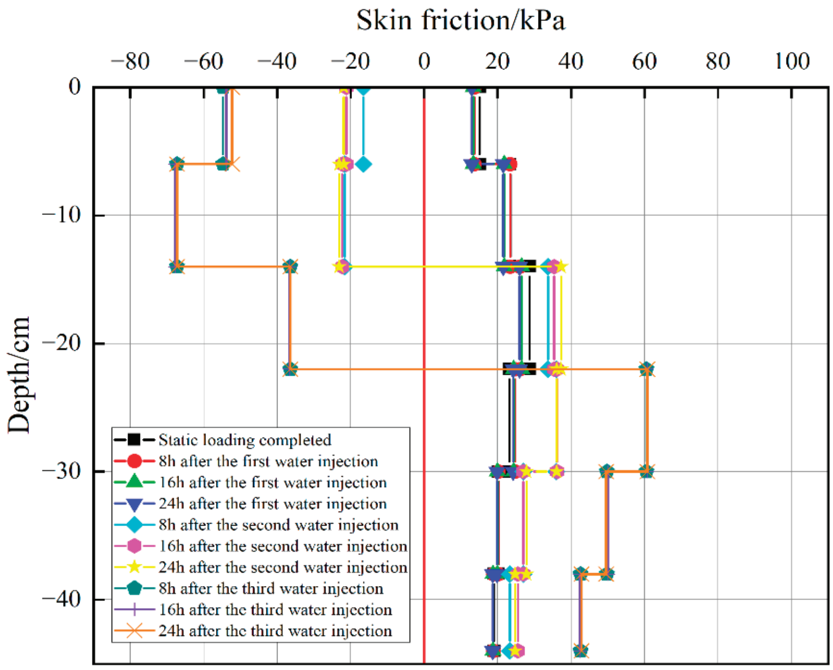

(**b**)

Figure 17. Skin friction distribution of pile foundations during groundwater rising. (**a**) The upper load is 1.25 kN. (**b**) The upper load is 2.5 kN.

4.3. Change of Pile Tip Force with the Immersion Time

Figure 18 displays the variation in pile tip force under loads of 1.25 kN and 2.5 kN. The pile tip force and skin friction remain constant from the conclusion of loading until 24 h after the initial water injection. Following the second water injection, the collapse of the artificial loess leads to reduced pile–soil relative displacement. Given that skin friction is positively correlated with the relative displacement of pile–soil, as indicated by reference [39], the skin friction diminishes substantially, while the pile tip force correspondingly increases markedly. After the third water injection, the complete collapse of the artificial loess causes a further decrease in skin friction.

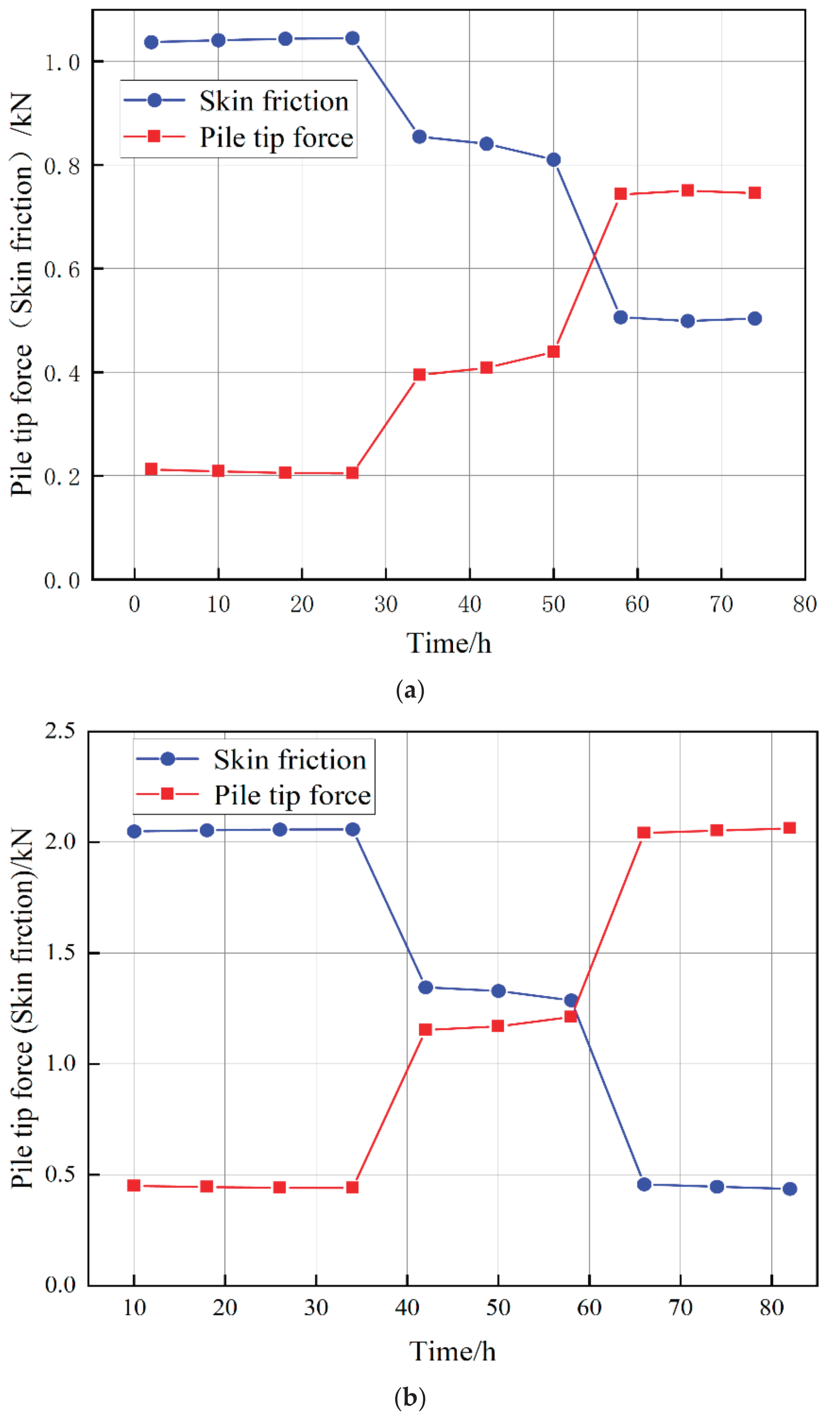

Figure 18. Changing curve of pile tip force during groundwater rising. (**a**) The upper load is 1.25 kN. (**b**) The upper load is 2.5 kN.

Figure 19 presents the bearing ratio curve of pile tip force under both load conditions as calculated by Equation (2). This figure illustrates that the pile foundation progressively transitions from a friction pile to an end-bearing pile with successive water injections.

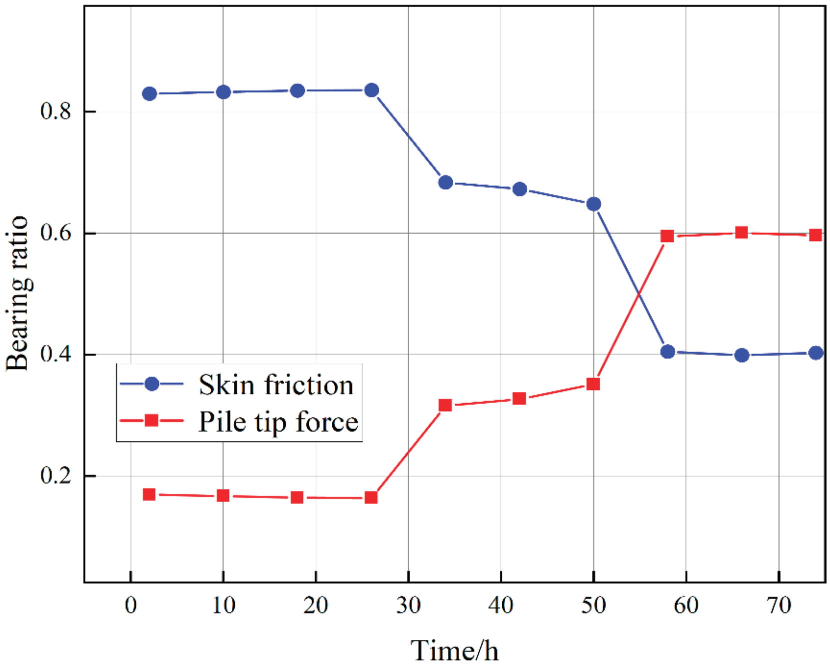

(**a**)

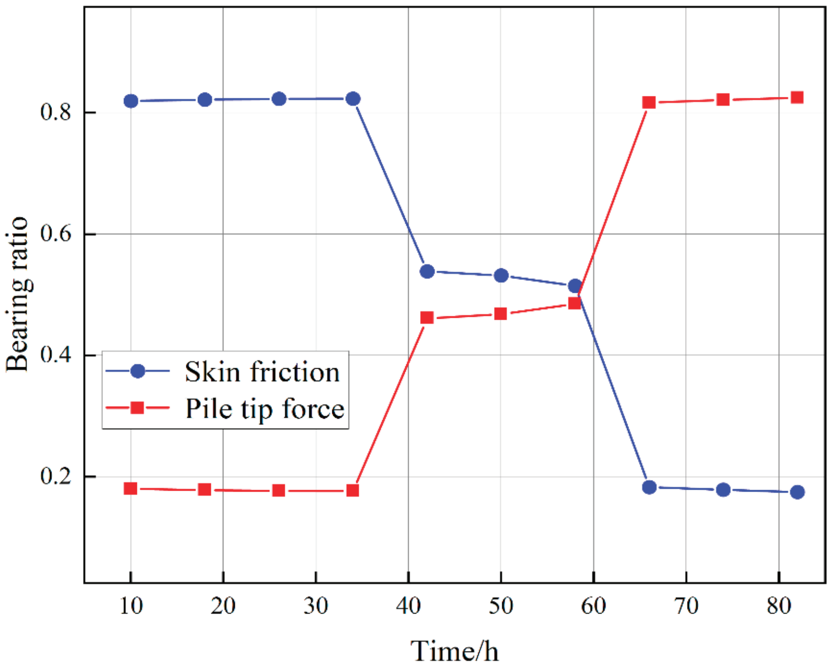

(**b**)

Figure 19. Changing curve of bearing ratio during groundwater rising. (**a**) The upper load is 1.25 kN. (**b**) The upper load is 2.5 kN.

4.4. Change of Foundation Soil Settlement with the Immersion Time

Figures 20 and 21 illustrate the settlement curves of the foundation soil around the piles under loads of 1.25 kN and 2.5 kN, respectively. Throughout the gradual rise of the groundwater, the settlement patterns of the foundation soil closely align with those of the pile foundation. During the initial phase from the completion of loading until 24 h after the first water injection, the soil settlement remains relatively constant. Following the second water injection, the collapsibility of the artificial loess leads to a marked increase in foundation soil settlement. Furthermore, capillary action prolongs this settlement even after water injection ceases. Subsequent to the third water injection, the complete collapse of the artificial loess results in the foundation soil settlement trending toward stabilization.

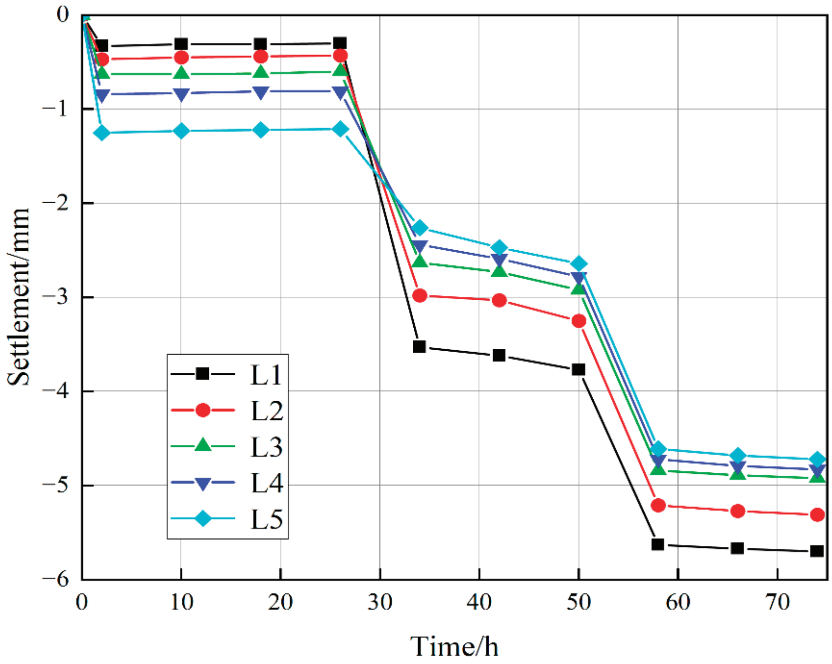

(a)

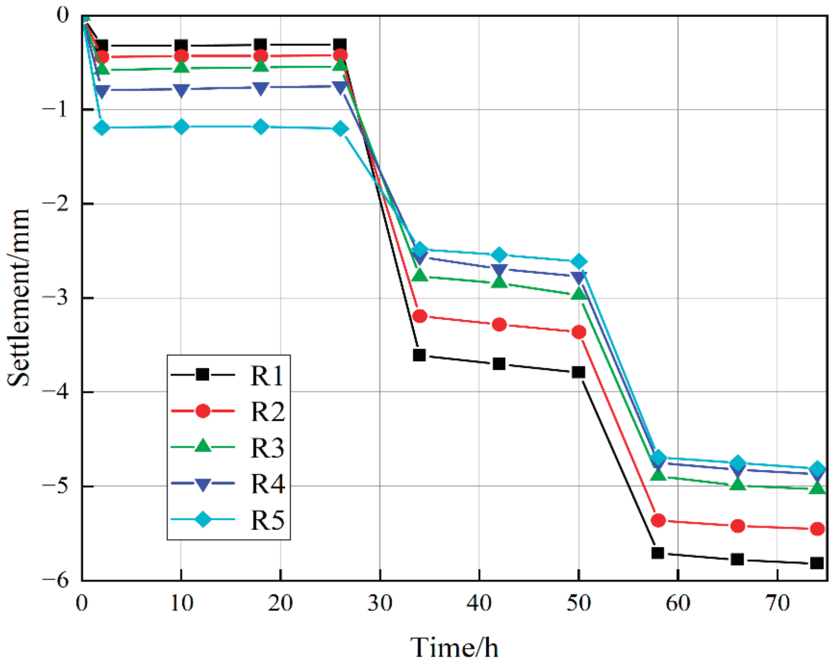

(b)

Figure 20. Foundation soil settlement under 1.25 kN load during groundwater rising. (**a**) L1~L5. (**b**) R1~R5.

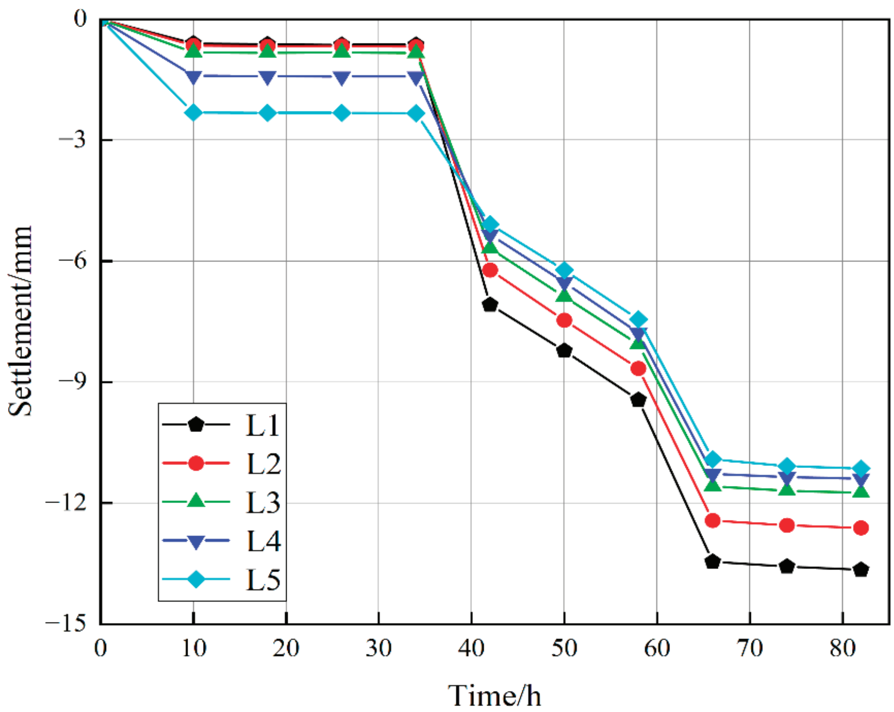

(a)

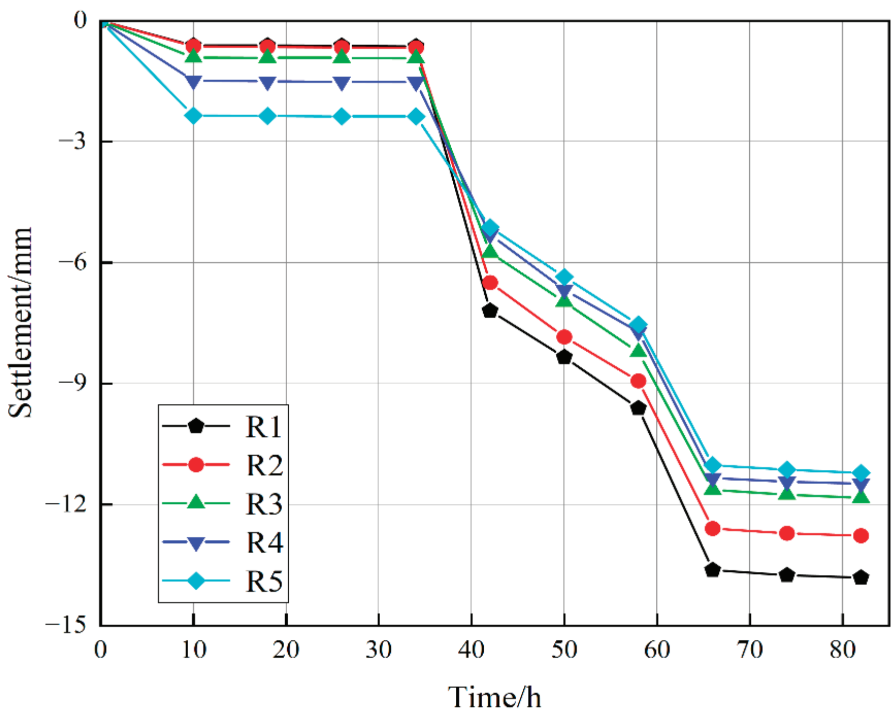

(b)

Figure 21. Foundation soil settlement under 2.5 kN load during groundwater rising. (**a**) L1~L5. (**b**) R1~R5.

Figures 22 and 23 present the change curves of the influence coefficient of the pile foundation on the foundation soil under upper loads of 1.25 kN and 2.5 kN, respectively, as calculated using Equation (3). Analogous to conditions without groundwater, the absolute value of the influence coefficient diminishes rapidly within a radial distance of D to 3D from the pile, although the rate of change is less pronounced beyond 3D. Consequently, it can be inferred that during the rise in groundwater level, the effective influence range of the pile foundation on the surrounding soil remains approximately 3D.

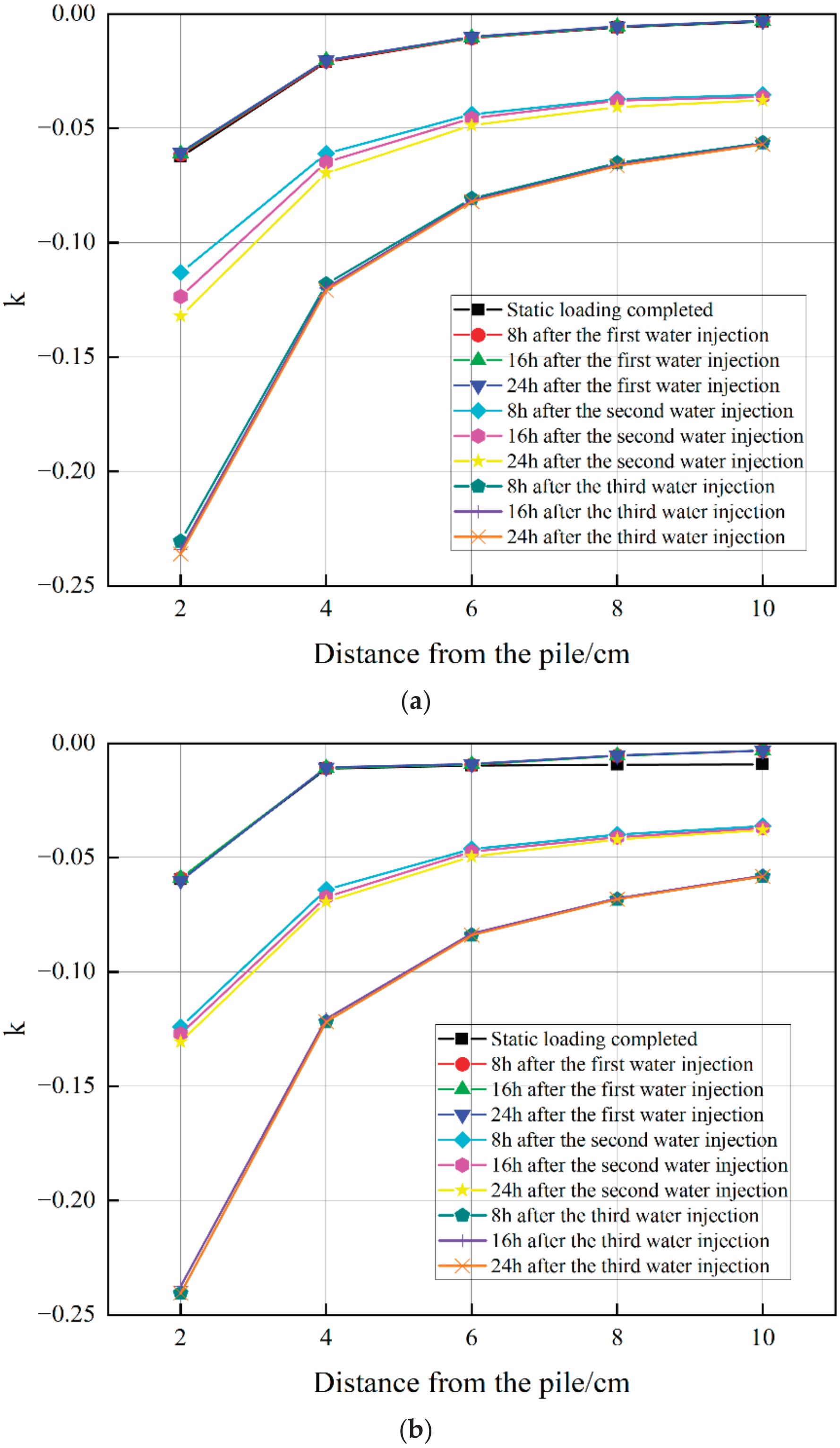

Figure 22. Influence coefficient of foundation soil under 1.25 kN load during groundwater rising. (**a**) L1~L5. (**b**) R1~R5.

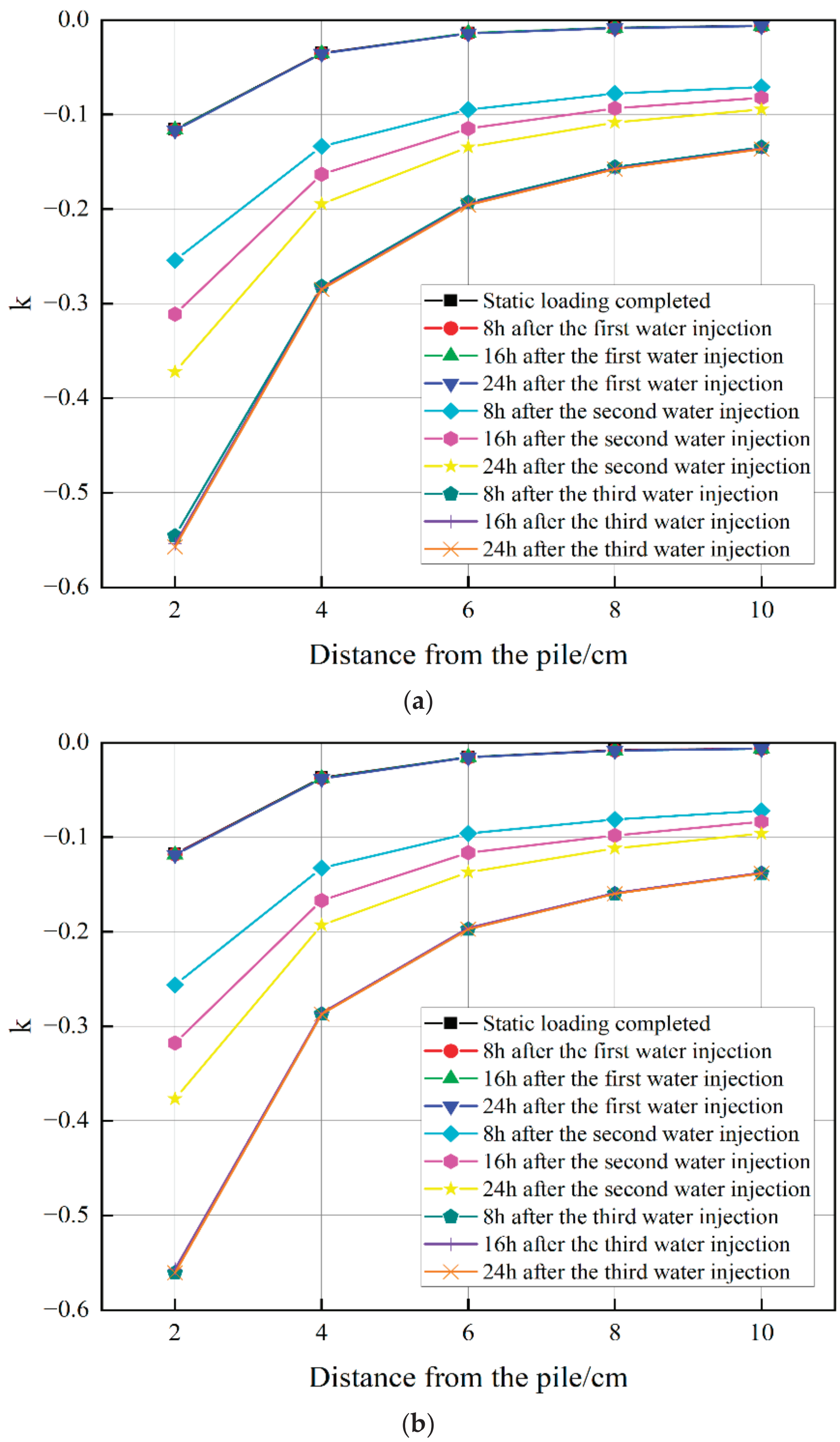

Figure 23. Influence coefficient of foundation soil under 2.5 kN load during groundwater rising. (**a**) L1~L5. (**b**) R1~R5.

5. Conclusions

In this study, static load tests on pile foundations were carried out under two distinct conditions: without groundwater and with rising groundwater levels, using artificial collapsible loess and a model pile. The research focused on exploring the impact of rising groundwater on various aspects of pile foundation behavior, including settlement, axial force, skin friction, pile tip force, and settlement of foundation soil. The key findings are summarized as follows:

(1) The load–settlement curve of pile foundations is segmented into three distinct stages: the elastic stage, rapid development stage, and failure stage, with the ultimate bearing capacity of the pile foundations being 5 kN. When the groundwater level remains within the bearing layer, the settlement of the pile foundations is essentially unchanged. However, when the groundwater level reaches the artificial collapsible loess layer, there is a significant increase in settlement. Furthermore, this settlement continues to escalate even after ceasing the water injection, due to the effects of capillary action. Ultimately, the settlement of the pile foundation peaks and gradually stabilizes once the artificial loess layer is fully saturated.

(2) In the absence of underground water, the axial force along the pile shaft decreases progressively with depth, while the skin friction remains positive. The axial force and skin friction stabilize when the groundwater level is confined within the bearing layer. However, as the groundwater ascends to the artificial collapsible loess stratum, the axial force amplifies due to increased negative skin friction at the upper part of the pile shaft. Following the cessation of water injection, the magnitude of the negative skin friction continues to escalate due to capillary action, although the neutral point remains static. As the artificial loess fully collapses, the absolute value of the negative skin friction surges significantly, and the neutral point shifts downward.

(3) The initial bearing type of the model pile is identified as a friction pile. As the upper load increases, the bearing ratio contributed by skin friction diminishes, thereby directing the evolution of the pile foundations towards an end-bearing type. When groundwater penetrates the artificial collapsible loess layer, there is a significant reduction in the load-bearing ratio of the skin friction. Once the groundwater fully saturates the soil layer, the pile foundations predominantly transition to an end-bearing pile.

(4) In the absence of groundwater, the settlement of foundation soil initially increases and then decreases as the upper load increases, reaching a turning point at the allowable bearing capacity of the foundation. The influence range of the pile foundation on the soil settlement is three times the pile diameter. After the collapse of the artificial loess due to groundwater activity, the settlement of the foundation soil begins to increase markedly, surpassing that of the pile foundation itself. Even under these conditions, the influence range of the pile foundations on the soil settlement remains consistently at three times the pile diameter. Therefore, the foundation soil within this range should be treated with an emphasis on preventing the decrease in bearing capacity. The foundation treatment methods include compaction piles, chemical consolidation, etc. The artificial loess employed in this study does not replicate the stratification, cementation, and other structural characteristics of natural loess. Moreover, the inability to scale down soil particle size leads to discrepancies in permeability, strength, and deformation when compared with natural loess. Additionally, scaling influences the stress field, which consequently affects test outcomes. Given these factors, it becomes necessary to refine the research conclusions using numerical simulations and field tests to account for potential errors.

Author Contributions: Conceptualization, X.R., M.L., H.L. (Hongjian Liao) and Z.W.; Methodology, X.R., H.L. (Hongjian Liao), A.Z. and H.L. (Hangzhou Li); Formal analysis, T.D.; Investigation, A.Z. and T.D.; Resources, X.R.; Data curation, X.R. and M.L.; Writing—original draft, M.L.; Writing—review & editing, H.L. (Hongjian Liao) and H.L. (Hangzhou Li). All authors have read and agreed to the published version of the manuscript.

Funding: This research was funded by Qin Chuangyuan Scientist-Engineer Team Construction Project of Shaanxi Province in China (grant number 2023KXJ-178), National Natural Science Foundation of China (grant number 41630639 and 51879212), Key Research and Development Project of Shaanxi Province in China (grant number 2019KWZ-09).

Data Availability Statement: The original contributions presented in this study are included in the article. Further inquiries can be directed to the corresponding author.

Conflicts of Interest: Authors Xuewen Rong, Tao Dang and Zheng Wu were employed by the company Shaanxi Huashan Road and Bridge Group Co., Ltd. The remaining authors declare that the research was conducted in the absence of any commercial or financial relationships that could be construed as a potential conflict of interest.

References

1. Weng, X.; Hu, J.; Mu, X.; Niu, H.; Huang, X. Model test study on the influence of the collapsibility of loess stratum on an urban utility tunnel. *Environ. Earth Sci.* **2022**, *82*, 32–48. [CrossRef]
2. Wang, X.; Lu, H.; Zhang, H.; Wu, J.; Hou, X. Distribution, provenance, and onset of the Xiashu Loess in Southeast China with paleoclimatic implications. *J. Asian Earth Sci.* **2018**, *155*, 180–187. [CrossRef]
3. Zhou, Y.; Yu, B.; Fan, W.; Dijkstra, T.A.; Wei, Y. 3D characterization of localized shear failure in loess subject to triaxial loading. *Eng. Geol.* **2023**, *322*, 107174. [CrossRef]
4. Shen, Y.; Yan, H.; Wang, R.; Song, P.; He, Y. Review: Progress with Functional Materials Based on Loess Particles. *Clays Clay Miner.* **2021**, *69*, 301–314. [CrossRef]
5. Munir, M.; Mujtaba, H.; Usama, K.; Khalid, F.; Zia, U. Study on Sustainable Utilization of CKD for Improvement of Collapsible Soil. *Arab. J. Sci. Eng.* **2023**, *48*, 5667–5682.
6. Chai, Q.; Chen, T.; Li, Z.; Shen, D.; Wu, C. Experimental Study on the Negative Skin Friction of Piles in Collapsible Loess. *Sustainability* **2023**, *15*, 8893. [CrossRef]
7. Li, P.; Vanapalli, S.; Li, T. Review of collapse triggering mechanism of collapsible soils due to wetting. *J. Rock Mech. Geotech. Eng.* **2016**, *8*, 256–274. [CrossRef]
8. Wang, L.; Shao, S.; She, F. A new method for evaluating loess collapsibility and its application. *Eng. Geol.* **2020**, *264*, 105376. [CrossRef]
9. Wang, M. *Study on Structure of Collapsible Loess in China*; Taiyuan University of Technology: Taiyuan, China, 2010. (In Chinese)
10. Zhang, Y.; Hu, Z.; Chen, H.; Xue, T. Experimental Investigation of the Behavior of Collapsible Loess Treated with the Acid-addition Pre-soaking Method. *KSCE J. Civ. Eng.* **2018**, *22*, 4373–4384. [CrossRef]
11. Zhu, Y.; Jia, X.; Shao, M. Thickness Variations Across the Loess Plateau of China. *Surv. Geophys.* **2018**, *39*, 715–727. [CrossRef]
12. Li, Y.; Liu, W.; Guo, X.; Pan, Z.; Li, Y. Spatial-temporal distribution and variation characteristics of precipitation in China during 1956–2016. *Adv. Water Sci.* **2025**, *36*, 1–17. (In Chinese)
13. Yao, Y.; Zhang, M.; Deng, Y.; Dong, Y.; Wu, X. Evaluation of environmental engineering geology issues caused by rising groundwater levels in Xi'an, China. *Eng. Geol.* **2021**, *294*, 106350. [CrossRef]
14. Zhang, Y.; Liang, D. Analysis of dynamic characteristics of groundwater level in Xi'an during 33 years. *Groundwater* **2018**, *40*, 66–67. (In Chinese)
15. He, X.; Tao, F.; Tao, H.; Ding, J.; Li, H. Analysis on Groundwater Level Variation Regulation of Guanzhong Plain and Its Influencing Factors. *Groundwater* **2015**, *37*, 52–54. (In Chinese)
16. Zhang, J.; Chen, X.; Li, J.; Zhang, C. Research on the Slurry Diffusion and Load-Bearing Characteristics of Postgrouted Piles in Loess Areas. *Int. J. Geomech.* **2024**, *24*. [CrossRef]
17. Xue, Z.; Zhang, Y.; Luo, J.; Yan, C.; Emmanuel, M.; Jia, X. Analysis of compressive strength, durability properties, and micromechanisms of solidified loess using industrial solid waste: Slag–white mud–calcium carbide residue. *J. Build. Eng.* **2024**, *84*, 108511. [CrossRef]
18. Qian, C.; Li, M.; Liao, H.; Zhang, C.; Li, H. Research on the Vibration Fatigue Characteristics of Ancient Building Wood Materials. *Buildings* **2024**, *14*, 2840. [CrossRef]
19. Adbullah, R.; Xavier, B.; Namgung, H.; Varghese, V.; Fujiwara, A. Managing transit-oriented development: A comparative analysis of expert groups and multi-criteria decision making methods. *Sustain. Cities Soc.* **2024**, *115*, 105871.
20. Cao, Z.; Zhang, H.; Geng, J.; Tian, Z.; Sun, Y. Research on traffic accessibility of transit-oriented development of urban high-speed beltway service area: Take Qujiang service area as an example. *J. Xi'an Univ. Archit. Technol. (Nat. Sci. Ed.)* **2023**, *55*, 827–833+839. (In Chinese)
21. He, L.; Xu, H.; Tang, B.; Liu, Q.; Tu, Q. Analysis of Vibration Test of Over-track Buildings in Different Areas of Depots. *Noise Vib. Control.* **2024**, *44*, 235–241.
22. Jin, B. *Mechanical Analysis and Optimization of Variable Mobile Trolley Bracket Based on Modular Construction of Upper Cover Plate of Metro Vehicle Section*; Shijiazhuang Tiedao University: Shijiazhuang, China, 2024.
23. Feng, Q.; Zhang, Y.; Jiang, J.; Wang, Z.; Lei, X. Field measurement and evaluation of vibration in different areas of a metro depot. *Earthq. Eng. Eng. Vib.* **2022**, *21*, 529–542.

24. Chen, Y.; Feng, Q.; Liu, Q.; Jiang, J. Experimental study on the characteristics of train-induced vibration in a new structure of metro depot. *Environ. Sci. Pollut. Res. Int.* **2021**, *28*, 41407–41422. [CrossRef] [PubMed]
25. Sun, W.; Zhu, H.; Yan, S.; Liang, Q.; Zhang, J. Seismic Fragility Analysis of Shallow-Buried Subway Station Structure in Loess Strata. *J. Southwest Jiaotong Univ.* **2025**, 1–9. Available online: https://link.cnki.net/urlid/51.1277.U.20240219.1015.002 (accessed on 12 April 2025). (In Chinese).
26. Xu, W.; Liu, Y.; Huang, Q.; Liu, X.; Zhao, C. Influence of Combination Types on Vibration Response of Superstructure of Subway Station. *J. Southwest Jiaotong Univ.* **2024**, *59*, 653–662. (In Chinese)
27. Peng, H.; Pang, F.; Li, Z.; Xiao, X.; Tang, S. Study on the Impact of a Metro Depot Cover Structure on the Existing Metro Structure and Additional Settlement of Tracks. *Buildings* **2023**, *13*, 1914. [CrossRef]
28. Ding, P.; Tao, L.; Yang, X.; Zhao, J.; Shi, C. Force Transfer and Deformation Mechanism of Single Ring Structure of Prefabricated Subway Station. *J. Southwest Jiaotong Univ.* **2020**, *55*, 1076–1084+1110. (In Chinese)
29. Mu, Q.; Dai, B.; Zhou, C.; Meng, L.; Zheng, J. A new and simple method for predicting the collapse susceptibility of intact loess. *Comput. Geotech.* **2023**, *158*, 105408. [CrossRef]
30. Liu, X.; Li, M.; Liao, H.; Huang, B.; Liu, S. Mechanical Properties of Adjacent Pile Bases in Collapsible Loess under Metro Depot. *Appl. Sci.* **2024**, *14*, 5819. [CrossRef]
31. Chen, Y.; Li, X.; Huang, R.; Huang, L.; Li, L. Micro experimental research on influence factors of loess collapsibility. *J. Eng. Geol.* **2015**, *23*, 646–653. (In Chinese)
32. Gu, T.; Wang, J.; Guo, L.; Chu, D.; Li, K. Study of Q3 loess microstructure changes based on image processing. *Chin. J. Rock Mech. Eng.* **2011**, *30*, 3185–3192. (In Chinese)
33. Assallay, A.M.; Jefferson, I.; Rogers, C.D.F.; Smalley, I.J. Fragipan formation in loess soils: Development of the Bryant hydroconsolidation hypothesis. *Geoderma* **1998**, *83*, 1–16. [CrossRef]
34. Assallay, A.M.; Rogers, C.D.F.; Smalley, I.J. Formation and collapse of metastable particle packings and open structures in loess deposits. *Eng. Geol.* **1997**, *48*, 101–115. [CrossRef]
35. Jefferson, I.; Ahamd, M. Formation of Artificial Collapsible Loess. In *Problematic Soils and Rocks and In Situ Characterization*; ASCE Press: Reston, VA, USA, 2012; pp. 1–10.
36. *JGJ 94-2008*; Technical Code for Building Pile Foundations. MoHURD: Beijing, China, 2008. (In Chinese)
37. *JGJ 106-2014*; Technical Code for Testing of Building Foundation Piles. MoHURD: Beijing, China, 2014. (In Chinese)
38. Zhang, Y. *Research on Engineering Properties of Artificial Prepared Collapsible Loess and Calculation Method of Vertical Bearing Capacity of Deep Foundation*; Lanzhou Jiaotong University: Lanzhou, China, 2017. (In Chinese)
39. Tian, J. *Research on Vertical Bearing Characteristics of Necking Pile Based on Load Transfer Method*; Henan University of Technology: Zhengzhou, China, 2024. (In Chinese)

buildings

MDPI

Article

Safety Risk Assessment of Double-Line Tunnel Crossings Beneath Existing Tunnels in Complex Strata

Bafeng Ren [1], Shengbin Hu [2], Min Hu [3], Zhi Chen [1] and Hang Lin [2,*]

[1] Nanning Rail Transit Co., Ltd., Nanning 530029, China; renbafeng@nngdjt.com (B.R.); chenz@nngdjt.com (Z.C.)
[2] School of Resources and Safety Engineering, Central South University, Changsha 410083, China; 235501008@csu.edu.cn
[3] School of Civil Engineering, Changsha University of Science and Technology, Changsha 410114, China; hum07@lzu.edu.cn
* Correspondence: hanglin@csu.edu.cn

Abstract: With the acceleration of urbanization, the development of urban rail transit networks has become an essential component of modern urban transportation. The construction of new urban rail transit lines often involves crossing existing operational lines, posing significant safety risks and technical challenges. This paper presents a comprehensive study on the safety risk assessment and control measures for the construction of new double-line shield tunnels crossing beneath existing tunnels in complex strata, using the project of Line 5 of the Nanning Urban Rail Transit crossing beneath the existing Line 2 interval tunnel as a case study. This study employs methods such as status investigation, numerical simulation, and field measurement to analyze the construction risks. Key findings include the successful identification and control of major risk sources through refined risk assessment and comprehensive technical measurement. The maximum settlement of the existing tunnel was effectively controlled at −2.55 mm, well within the deformation monitoring control values. This study demonstrates that optimized shield machine selection, improved lining design, interlayer soil reinforcement, the dynamic adjustment of shield parameters, and the precise measurement of shield posture significantly enhance the efficiency of shield tunneling and construction safety. The results provide a valuable reference for the settlement and deformation control of similar projects.

Keywords: shield tunnel; crossing; existing tunnel; numerical simulation; deformation monitoring

1. Introduction

With the acceleration of urbanization, the development of urban rail transit networks has become an essential component of modern urban transportation. The construction of new urban rail transit lines may involve crossing existing operational lines, posing significant safety risks and technical challenges [1–4]. Particularly under conditions of small clearance—when new tunnels are constructed in close proximity beneath existing ones—the construction environment can become extremely complex and hazardous. If the construction of the new tunnel is not properly controlled, it can easily induce abnormal deformation and structural damage to the existing tunnel, thereby affecting the safe operation of the existing line [5–7]. In severe cases, this may even lead to casualties and property losses. Therefore, effectively controlling the safety risks associated with the construction of new tunnels crossing beneath existing tunnels has become a core issue in urban rail transit engineering [8–11]. Gan, Yu [12] proposed a simplified two-stage analysis method to study the longitudinal response of existing tunnels with discontinuous structural stiffness to new tunnel construction and explored the influence of various factors on tunnel response. Liu, Li [13] established an internal force calculation model for a horseshoe-shaped tunnel and analyzed the impact of the construction of a new station on Line 12 of the Beijing Subway crossing beneath the existing Line 5, proposing suggestions for optimizing construction parameters. However, there is still a lack of in-depth analysis combining specific safety risk control measures with the actual construction process of crossings beneath tunnels. In terms of numerical simulation, three-dimensional finite element software has been widely used to predict the stress and deformation effects of shield tunnel construction on existing tunnels [14–17]. Yang, Zhang [18] analyzed the impact of river channel and bridge construction near Line 1 of the Changzhou Metro on existing double-line shield tunnels using three-dimensional numerical simulation and field monitoring, proposing a comprehensive protection plan. In terms of construction technology, measures such as shield machine selection, lining design, interlayer soil reinforcement, and shield parameter optimization have been proven to be effective in controlling settlement and deformation [19,20]. For example, air cushion slurry balance shield machines can effectively reduce ground settlement by precisely controlling the face pressure. Moreover, reasonable tool configuration, shield posture measurement, and the application of real-time monitoring and early warning systems also provide security for shield construction. Zhang, Liu [21] analyzed the vehicle-induced dynamic response characteristics of the existing line during the construction of Line 8 of the Chengdu Metro crossing beneath the existing Line 1 through field testing and numerical calculations. Huang, Wang [22] studied the punching shear failure mode of the pile-end-bearing stratum during shield tunneling beneath existing piles using reduced-scale model tests and PIV technology, constructing a theoretical failure mechanism based on a limit analysis. Chen, Liu [23] proposed a hybrid intelligent framework based on interpretable machine learning and multi-objective optimization for controlling the deformation of existing tunnels caused by shield tunneling beneath existing tunnels. Despite significant progress in existing research, the further optimization of shield construction parameters to enhance the safety of existing tunnels remains a current research hotspot and challenge [24–28]. Particularly under extreme conditions such as small clearance, large span, and complex strata, how to achieve safe crossing of shield tunnels still requires in-depth exploration.

This study, based on the project of Line 5 of the Nanning Urban Rail Transit crossing beneath the existing Line 2 interval tunnel, aims to address the critical issue of the safety risk assessment and control for such complex crossing projects by employing methods such as status investigation, numerical simulation, and field measurement. Through the implementation of comprehensive technical measures such as shield machine selection, lining design improvement, interlayer soil reinforcement, shield parameter optimization, and shield posture measurement, the construction parameters of the shield tunneling were dynamically adjusted, enabling the successful crossing of the new tunnel and ensuring the safe operation of the existing line.

2. Project Overview and Geological Conditions

2.1. Project Overview

The construction of Line 5 of the Nanning Urban Rail Transit crossing beneath the existing Line 2 interval tunnel is a typical example of such complex crossing projects. Located at the busy intersection of Youai Road and Mingxiu Road, the project is characterized by dense underground utilities and a complex surrounding environment. The existing Line 2 tunnel has a soil cover thickness of approximately 10.75 m, while the Line 5 tunnel has a soil cover thickness of about 18.8 m. The vertical clearance between the upper and lower tunnels ranges from 2.05 m to 2.10 m, making the construction extremely challenging. Additionally, the geological conditions of the crossing section are complex, which increases the difficulty of shield tunneling control, as shown in Figure 1. Both Line 2 and Line 5 shield tunnel sections have a lining ring outer diameter of 6.0 m, an inner diameter of 5.4 m, and a lining thickness of 0.3 m. The lining ring width is 1.5 m, and each ring consists of one cap block, two adjacent blocks, and three standard blocks. The lining concrete is designed with a strength of C50 and a water resistance grade of P12. The non-crossing section uses Type X-3 lining, while the crossing section uses Type X-4 lining. Since the minimum clearance between the newly constructed Line 5 and the existing Line 2 tunnel is about 2.0 m, the close proximity relationship is very evident; the interlayer soil between the two tunnel lines is entirely composed of water-bearing gravel; the upper half of the excavation section of Line 5 crossing beneath Line 2 tunnel is gravel, while the lower half is mudstone, forming a typical "soft-over-hard" stratum characterized by the upper gravel layer (a relatively harder material) overlying the lower mudstone layer (a softer material), which increases the difficulty of shield tunneling control.

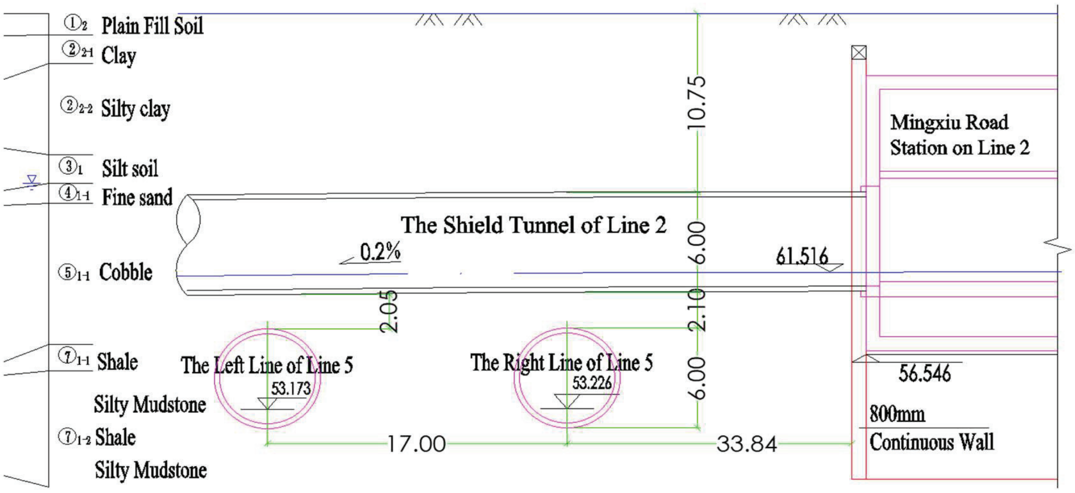

Figure 1. Location relationship of the crossing section.

2.2. Geological Conditions

The main strata of the crossing section, from top to bottom, are as follows: plain fill soil ① 2, silty clay ② 3-2, silt ③ 1, fine sand ④ 1-1, gravel ⑤ 1-1, and mudstone ⑦ 1-3. The Line 5 shield tunnel body is mainly located in the mudstone stratum, with the crown in the gravel stratum; the Line 2 shield tunnel body is mainly located in the gravel stratum, with the crown in the silt. As shown in Figure 2, the main types of groundwater in the site are upper layer stagnant water and pore water in loose rocks. The pore water in loose rocks is mainly stored in the gravel stratum, with abundant water quantity, replenished by atmospheric precipitation and underground runoff, and in hydraulic connection with the Yongjiang River, forming a mutually replenishing relationship. During the survey period, the initial water level burial depth was 8.80–13.00 m, mostly appearing at the bottom of silt or the top of sand layers; the stable water burial depth is 8.50–10.50 m, with a hydraulic gradient of about 0.17%, and the water level fluctuation amplitude is about 3.0–5.0 m.

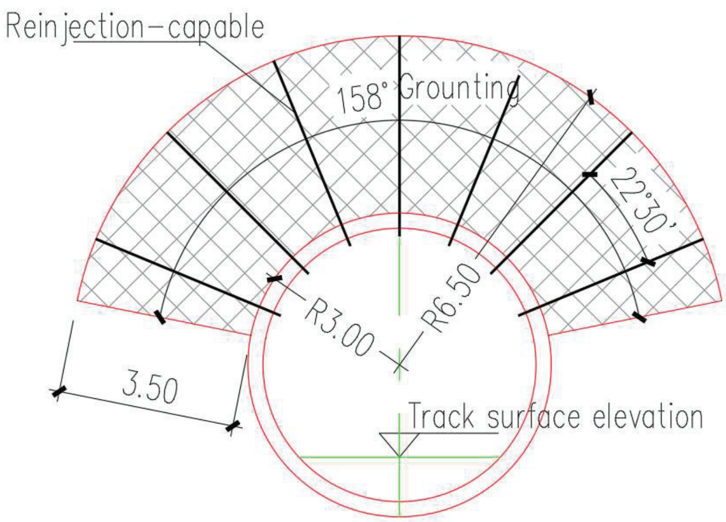

Figure 2. Improved lining segments and optimized grouting.

3. Safety Assessment of the Existing Tunnel

3.1. Reinforcement Methods for the Existing Tunnel

Field investigations revealed cracking and seepage issues in the track area of the existing line, with some tunnel segments exhibiting signs of dampness, cracking, and minor damage at the joints, although these do not currently compromise the structural safety of the existing tunnel. During the construction of the new tunnel crossing beneath the existing one, the existing tunnel structure may face several risks [29,30]. Firstly, the ground disturbance caused by the shield machine during tunneling can lead to additional deformation in the existing tunnel, thereby affecting its structural stability. Secondly, the construction of the new tunnel may alter the stress field surrounding the existing tunnel, causing a redistribution of internal forces within the existing tunnel structure and increasing the risk of structural damage. Moreover, complex geological conditions, such as water-bearing gravel and mudstone layers, further increase the uncertainty and risk associated with the construction. Therefore, reinforcing the existing tunnel can effectively enhance its structural stiffness and stability, reduce the disturbance caused by the construction process, and ensure the safety of both the construction and operation.

Grouting reinforcement within the tunnel is a key measure to improve the structural stiffness and stability of the existing tunnel. The grouting reinforcement range for the existing tunnel is 60 m in length. The grouting material primarily consists of a composite slurry with added admixtures, mainly composed of cement, sodium silicate, and anti-dispersion admixtures to enhance the stability and anti-dispersion properties of the slurry. The main design parameters for the grouting reinforcement are as follows: (1) the grouting slurry is primarily a composite type, with cement–sodium-silicate double-liquid slurry as a secondary option; (2) the grouting pipe is a Φ32 mm (t = 3.5 mm) sleeve valve pipe, with hole drilling carried out using a casing drilling rig; (3) the water-cement ratio of the slurry is between 0.6:1 and 1:1, and the grouting pressure is controlled within the range of 0.5–0.8 MPa. The patching material for the lining segments is C55 expansive concrete. The end of the sleeve valve pipe should be no less than 0.4 m away from the newly constructed tunnel, and part of the sleeve valve pipe is retained at the bottom of the tunnel, extending beyond the integral slab track, as a reserved grouting measure for the long-term stability of the interlayer soil. In the affected area of 30 lining rings in the existing tunnel, 14b-type channel steel is installed as a longitudinal tensioning strip. The newly constructed tunnel uses shield tunnel segments with 16 grouting holes per ring, and grouting is carried out based on real-time monitoring information. Grouting pipes are installed through the grouting holes into the surrounding ground, with the grouting reinforcement body formed within a 158° range of the tunnel crown, ensuring a minimum clearance of no less than 0.4 m between the existing tunnel and the newly constructed tunnel. The end of the grouting process in a single hole is controlled by combining a quantitative and pressure-based approach. The overall slurry filling rate in the gravel layer should reach above 30%. In addition to drilling 70 cm into the ground to check the permeability of the stratum during grouting drilling, a ground-penetrating radar is used to scan the density of the grouting reinforcement body. Before officially starting the grouting of the lining segments, a trial hole must be drilled. If water or sand gushing occurs, a hole mouth pipe and a water stop valve should be installed to ensure the safety and controllability of the grouting reinforcement process.

3.2. Deformation Patterns of the Existing Tunnel

In this study, MIDAS GTS NX (New eXperience of Geo-Technical analysis System, version 2019, MIDAS Information Technology Co., Ltd., Beijing, China) three-dimensional finite element software was employed to simulate the construction process of the new tunnel crossing beneath the existing tunnel. While other methods, such as the Finite Difference Method (FDM), have been successfully used in geotechnical engineering, FEM was chosen due to its superior adaptability to complex geometries and high-dimensional problems. FEM allows for the more accurate representation of the soil–structure interactions (SSIs) between the tunnel and surrounding soil [31]. This simulation aimed to analyze the stress and deformation characteristics of the existing tunnel during construction. The computational model has a width of 160 m, a length of 220 m, and a height of 42 m. The model is divided into 131,739 elements and 26,967 nodes. A soil-structure model was used for the three-dimensional modeling analysis [32–34]. In the calculations, the soil in the model was considered as an elastoplastic material, employing the modified Mohr–Coulomb (M–C) constitutive model, while the structures were all modeled as isotropic elastic materials. The M–C model is a well-established and widely used constitutive model in geotechnical engineering, particularly effective for modeling the behavior of cohesionless soils and moderately cohesive soils under monotonic loading conditions [35,36]. The new tunnel segments, existing tunnel segments, station and ventilation shaft structures, and above-ground structures were simulated using plate elements. Columns were modeled using beam elements, and the remaining parts were modeled using solid elements, as shown in Figure 3. The calculation parameters were selected according to the geotechnical investigation data, and the geotechnical calculation parameters are listed in Table 1. To accurately represent the “soft-over-hard” stratum structure in the numerical model, the geological conditions were meticulously incorporated based on detailed geotechnical investigation data. The model was calibrated to reflect the distinct mechanical properties of each stratum, with the upper gravel layer characterized by higher stiffness and lower compressibility and the lower mudstone layer by lower stiffness and higher compressibility.

To enhance the clarity and reliability of the numerical simulation, the model conditions and simplifications were explicitly defined. The geotechnical parameters used in the model were derived from detailed site investigation data and were validated against laboratory tests and field measurements to ensure accuracy. The interaction between the soil and the tunnel structures was modeled using a two-way coupling approach, where the soil was treated as an elastoplastic material and the tunnel segments as isotropic elastic materials. This simplification allows for the accurate representation of stress transfer between the soil and the tunnel structures. The model utilized a combination of plate, beam, and solid elements to represent the different components of the tunnel and surrounding soil, with finer mesh applied in critical areas such as the tunnel lining and the interface between the new and existing tunnels to balance computational efficiency and accuracy. The boundary conditions were set to simulate the actual in situ stress conditions, with vertical boundaries subjected to free boundary conditions to allow for vertical deformation, horizontal boundaries constrained to prevent horizontal movement, and the bottom boundary subjected to a fixed boundary condition to represent the underlying bedrock. The construction process was simulated in stages, with the shield tunneling load applied incrementally to reflect the actual construction sequence. The excavation face pressure and ground reaction forces were dynamically adjusted based on the excavation progress.

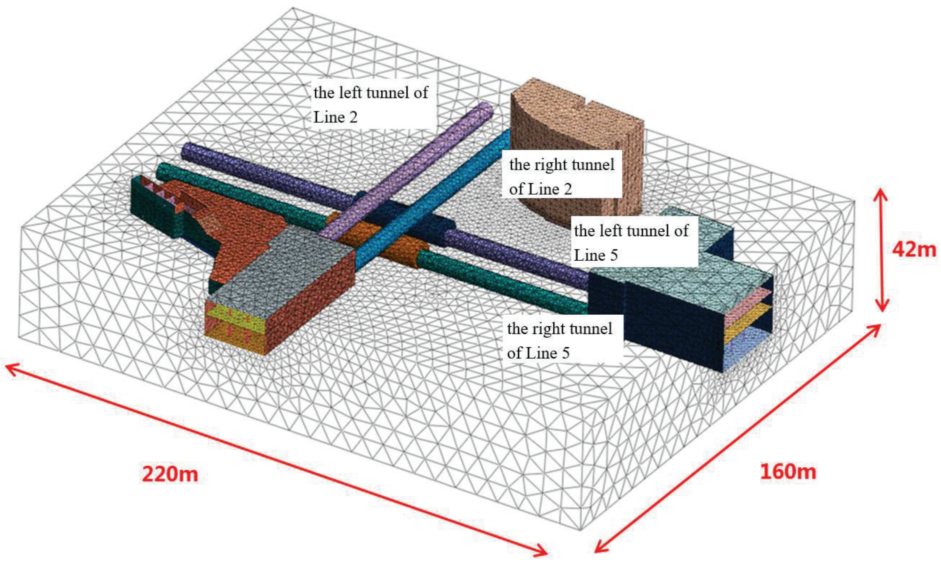

Figure 3. Three-dimensional numerical model.

Table 1. Geotechnical calculation parameters.

Stratum	Thickness (m)	Density (g/cm^3)	Cohesion (kPa)	Internal Friction Angle (°)
Plain Fill Soil	2	1.94	16	11
Silty Clay	3	2.00	25	13.5
Silt	1	2.05	6	17
Fine Sand	7	2.10	2	20
Gravel	8	2.06	0	34
Mudstone	17	2.13	85	17.5

The deformation of the existing tunnel after the right and left lines passed through is shown in Figures 4 and 5. It can be seen that, after the right line of the new tunnel passed through, the settlement of the Line 2 shield tunnel was mainly concentrated above the right line, with a maximum settlement of −1.3 mm. The vertical deformation curve presents a normal distribution, and the longitudinal influence length of the Line 2 interval is approximately twice the tunnel diameter on both sides, that is, the influence length totals 40 m. The Line 2 interval tunnel experienced a horizontal displacement towards the west, with a maximum value of 0.97 mm. After the left line of the new tunnel passed through, the settlement of the Line 2 shield tunnel increased significantly, with the maximum settlement point shifting towards the downstream direction, and a maximum settlement of −2.5 mm. The vertical deformation curve presents a “settlement trough” characteristic, with the largest settlement occurring in the middle part between the two lines of Line 2. The horizontal deformation also increased significantly, with a maximum horizontal displacement towards the west of 2.0 mm. During the construction of the new tunnel, the excavation process of the shield machine disturbs the ground, causing a redistribution of stress in the ground beneath the existing tunnel, which in turn leads to the additional deformation of the existing tunnel. In the "soft-over-hard" stratum conditions, the shield machine's cutting face experiences complex forces during excavation. Severe tool wear and cutterhead clogging with mud can easily occur, further intensifying ground disturbance and increasing the deformation of the existing tunnel. Moreover, the lining ring of the existing tunnel is surrounded by a grouting reinforcement body, which enhances the overall stiffness of the tunnel. Combined with measures such as radial grouting and secondary grouting, the deformation of the existing shield tunnel is controllable. Therefore, during the excavation process of the shield machine, the mud chamber pressure can be reasonably controlled to ensure minimal pressure fluctuations at the face, reducing ground settlement. Additionally, the shield machine's tool configuration can be optimized to improve the tools' rock-breaking capability and wear resistance, reducing the occurrence of cutterhead clogging with mud. Furthermore, the shield excavation parameters, such as thrust, torque, and excavation speed, can be adjusted in real-time based on monitoring data to ensure the safety and stability of the construction process.

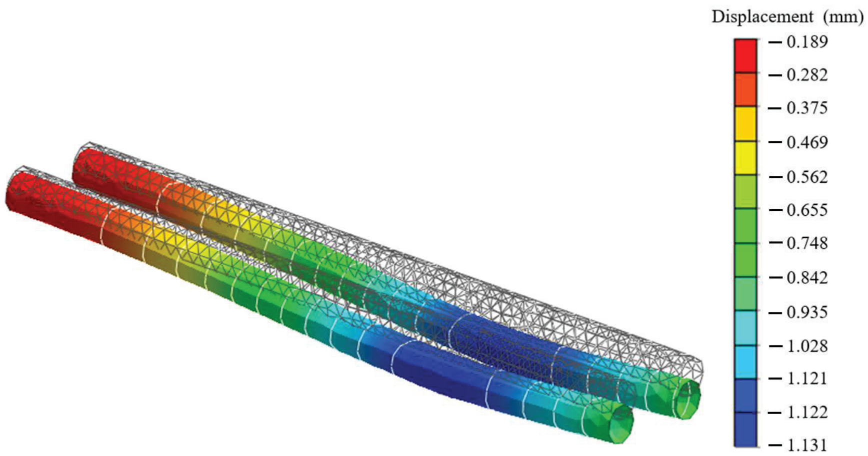

(**a**) Vertical displacement.

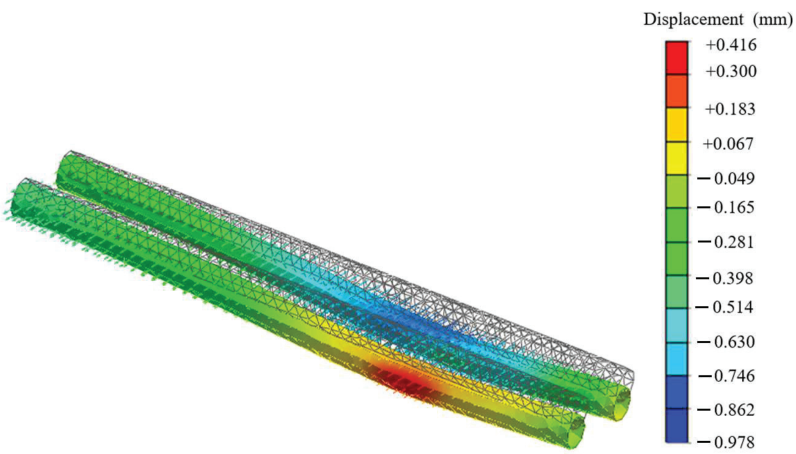

(**b**) Horizontal displacement.

Figure 4. Deformation of the existing tunnel after the right line passed through.

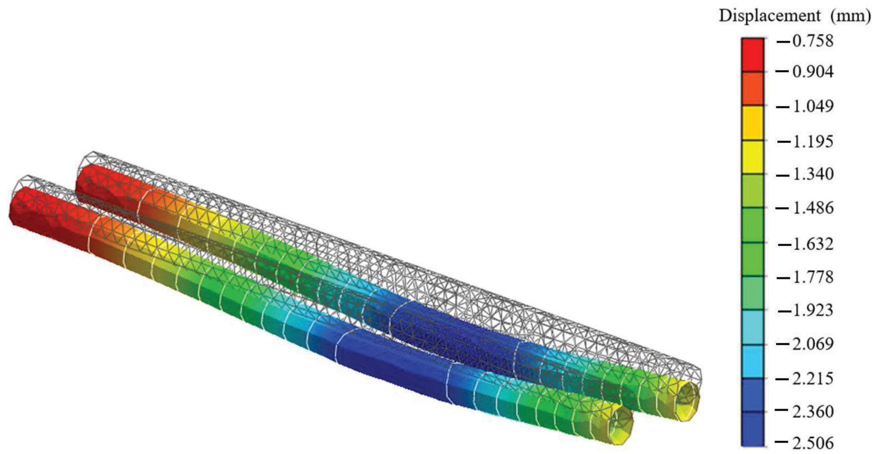

(**a**) Vertical displacement.

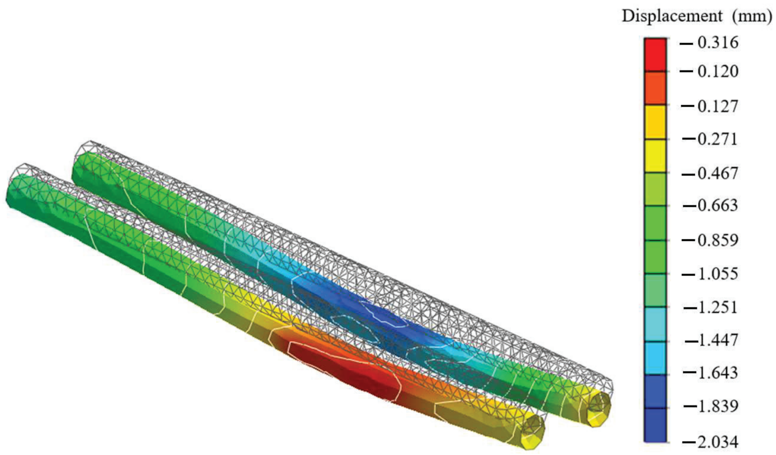

(**b**) Horizontal displacement.

Figure 5. Deformation of the existing tunnel after the left line passed through.

4. Shield Posture and Parameter Optimization for the New Tunnel

4.1. Shield Machine Selection

To ensure the smooth crossing of the new tunnel beneath the existing tunnel in complex geological conditions and to minimize the disturbance to the existing tunnel, the selection of the shield machine is of utmost importance. Considering the geological conditions and the requirements for settlement control, a pneumatic mud balance shield machine was chosen for the new shield tunnel. This machine can precisely control the pressure through the air cushion regulating chamber and the compressed air system, ensuring minimal pressure fluctuations at the excavation face. During excavation, it effectively controls ground settlement and reduces the impact on surface structures. Additionally, the shield machine's tool configuration includes a combination of tearing and scraping tools, with a cutterhead opening rate of 34%. The cutterhead is equipped with rolling cutters and replaceable tearing tools, which can be replaced from the back of the cutterhead. The main drive of the cutterhead is hydraulic, achieving true stepless speed variation and better anti-impact characteristics suitable for complex geological conditions. The tool configuration is as follows: central double-edged replaceable tearing tools: 4 pieces; front single-edged replaceable tearing tools: 20 pieces; peripheral heavy-duty toothed rolling cutters: 11 pieces; four-edged overbreak rolling cutters: 1 piece; front scraping tools: 52 pieces; peripheral scraping tool combinations (three types): 4 sets; peripheral scraping tool combinations (four types): 4 sets; welded shell tools: 12 pieces.

4.2. Characteristics of Shield Posture

The section of the newly constructed shield tunnel crossing beneath the existing line (rings 384–412) was designated as a hazardous crossing zone. After the tunnel met the measurement conditions, the posture of the segments was measured manually, and the measured data was compared and analyzed with the designed tunnel data. Figure 6 shows the deviation in the segment posture, measured twice. As can be seen from Figure 6, the horizontal and vertical deviations in the formed segments of the new shield tunnel crossing beneath the existing tunnel (rings 384–412) are both less than ±50 mm, indicating that the segment posture is generally stable and that the ring-to-ring deviation is relatively stable. However, during the first measurement, rings 401 and 402 exhibited a misalignment phenomenon. This was mainly due to the "soft-over-hard" structure of the crossing section stratum, where the mechanical properties of the upper gravel layer and the lower mudstone layer differ significantly. During the excavation process, the interaction between the shield machine and the different strata can cause slight changes in the posture of the shield machine, which in turn affects the assembly accuracy of the segments. Especially near the stratum interface, the inhomogeneity of the stratum is more pronounced, increasing the difficulty of adjusting the shield machine's posture and making it easier for segment misalignment to occur. In addition, during the crossing process, the excavation parameters of the shield machine (such as thrust, torque, and speed) need to be adjusted in real-time based on the geological conditions and monitoring data. If the adjustment of the excavation parameters is not timely or accurate enough, it may cause instability in the posture of the shield machine, thereby affecting the quality of segment assembly. Figure 7 further shows the segment posture measurement deviation in the worse cases. As can be seen from Figure 7, the vertical change value of the segment ring is between −15 mm and +10 mm, showing an overall trend of moving to the left; except for the horizontal change value of ring 402 reaching −31 mm, the horizontal change value of the other segment rings is between −25 mm and +10 mm, showing an overall trend of moving downward. This indicates that the shield excavation posture is basically consistent with the segment posture, and the segment posture meets the requirements. Through the precise measurement and control of the shield posture, potential issues such as segment misalignment and deformation caused by excessive shield machine posture deviation are effectively avoided, ensuring the quality and safety of tunnel construction.

4.3. Parameter Optimization

Based on the automated and manual monitoring data from the crossing section combined with the analysis of the shield excavation parameters from the test section, the excavation parameters of the shield machine were optimized. Mud chamber pressure: The average mud chamber pressure in the influence range of the existing line was maintained at 1.8–1.9 bar. The actual pressure also needs to be dynamically adjusted in real-time according to the monitoring data to ensure the stability of the face pressure and reduce ground disturbance. Excavation thrust: Controlled within the range of 15,000–20,000 kN. A reasonable excavation thrust can ensure the smooth advancement of the shield machine while avoiding excessive pressure on the surrounding ground, thereby reducing ground settlement. Cutterhead torque: Controlled within the range of 2500–3000 kN·m. An appropriate cutterhead torque helps the shield machine to excavate smoothly in complex geological conditions, preventing the cutterhead from being damaged due to excessive torque or being unable to effectively break the rock due to insufficient torque. Excavation speed: Controlled within the range of 5–10 mm/min. A reasonable excavation speed can ensure the continuous excavation of the shield machine while avoiding ground instability due to excessive speed or affecting the construction progress due to too slow speed. During the crossing of the existing tunnel, secondary grouting is required, using synchronous grout and sodium silicate double-liquid grout for injection. Grout is injected from the grouting pipe through the grouting holes in the segments into the gap between the segment and the ground, effectively filling the shield tail gap and reducing ground deformation. The grouting points for the multi-hole segments used in the crossing section are at the crown 1, 2, 10, and 11 points, with cross operations. In the crossing section, rings 380–420 of the crown have 40 cm of gravel, and the rest is mudstone. Since the water-bearing gravel layer has a large permeability coefficient and weak self-stability, collapse and caving-in phenomena can easily occur during excavation. Therefore, the mud pressure maintenance and synchronous grouting, as well as secondary grouting in the composite stratum during crossing, are particularly important. The grouting volume is maintained at 7.0–8.0 m^3 per ring, and the secondary grouting volume is about 1.5 m^3 per ring. Since the crossing section is in the mudstone stratum with strong mud-making ability, the configured pressure filtration system cannot meet the on-site construction requirements. To ensure the quality of the mud, when the mud viscosity index (the incoming mud viscosity reaches 30 s) reaches a level that affects the excavation parameters, mud-discarding operations need to be carried out. To ensure continuous excavation, reduce stagnation, and prevent the formation of cutterhead mud cakes, the incoming mud viscosity needs to be kept below 40 s.

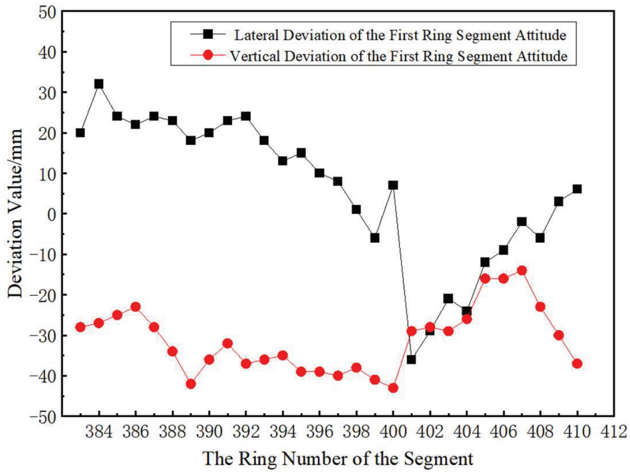

(**a**) First measurement.

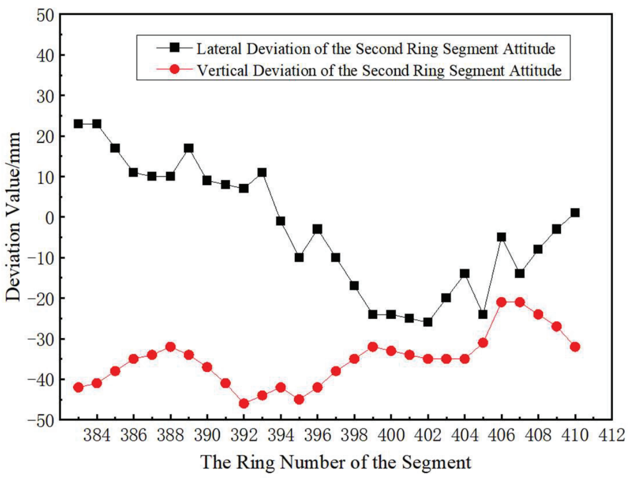

(**b**) Second measurement.

Figure 6. Segment posture measurement deviation.

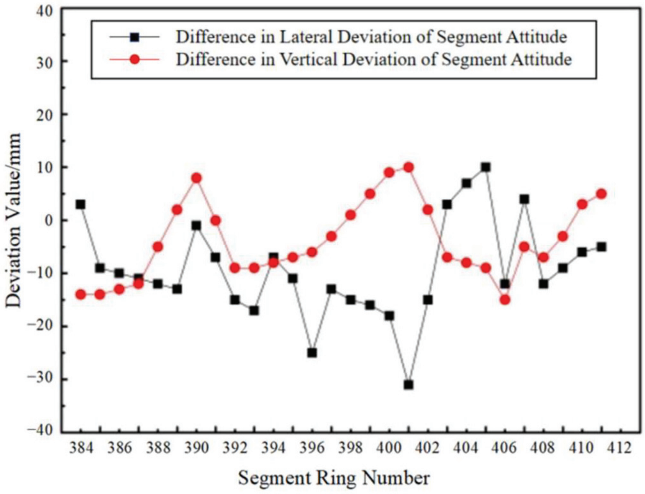

Figure 7. Segment posture measurement deviation in worse cases.

5. Safety Monitoring of the Crossing Section

5.1. Layout of Monitoring Points

The monitoring scope for this project covers a range of 45 m to either side of the center of the new tunnel lines crossing beneath the existing tunnel, corresponding to the existing tunnel section from Z(Y)DK35 + 330 to Z(Y)DK35 + 420. The safety monitoring of the existing tunnel primarily relies on automated monitoring, supplemented by manual monitoring for verification. The automated monitoring includes items such as vertical displacement, horizontal displacement, convergence of the tunnel structure, and vertical displacement of the track bed structure, while the manual monitoring verification items mainly include vertical displacement of the tunnel structure and track bed structure. The automated monitoring employs a Leica TS-60 total station system with wireless data transmission technology. Along the existing tunnel, a monitoring section is set up every 3–9 m. The left line has a total of 14 sections, and the right line has 16 sections. Each monitoring section is equipped with two prisms on either side of the track bed and two prisms at the 3 o'clock and 9 o'clock positions of the tunnel arch. Manual monitoring points are set up on the same sections as the automated monitoring, with each section having one vertical displacement monitoring point for the tunnel structure and two vertical displacement monitoring points for the track bed structure, corresponding to the automated monitoring points. During the hazardous crossing section, the frequency of manual monitoring verification is once per day. The layout of the automated monitoring points for the existing tunnel is shown in Figure 8.

Considering the characteristics of existing urban rail transit structures, operational safety requirements, deformation during construction, and local engineering experience, the settlement value, settlement rate, and differential settlement in different sections of the tunnel structure are used as monitoring and early warning control indicators. The monitoring and early warning are divided into three levels: warning value, alarm value, and control value. The warning value is set to 60% of the control value and the alarm value is set to 80% of the control value. The deformation monitoring control standards for crossing beneath the existing tunnel are shown in Table 2. As shown in Table 2, the deformation monitoring control standards are critical for ensuring the safety and stability of the existing tunnel during the construction of the new tunnel. The warning and alarm values are established to provide early detection of potential issues, allowing for the timely intervention and adjustment of the construction parameters. For instance, a warning value set at 60% of the control value allows for preemptive measures to be taken if deformation approaches the threshold, while an alarm value at 80% of the control value indicates a more urgent need for action.

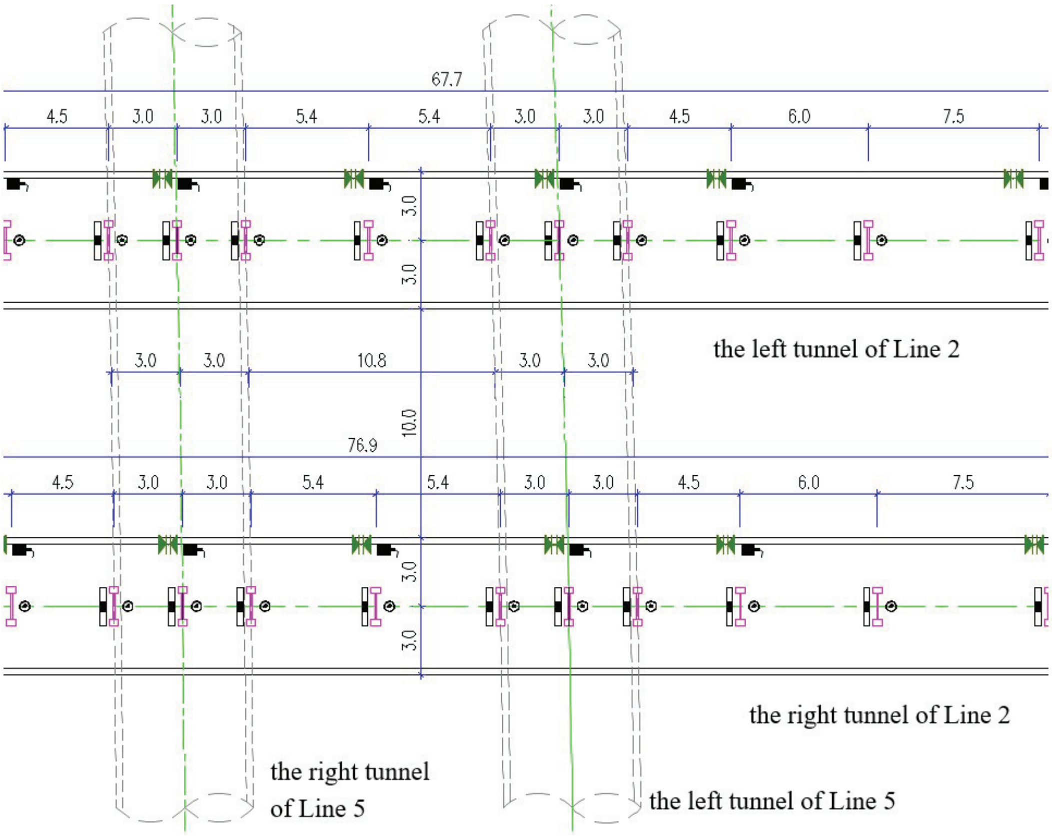

Figure 8. Layout of automated monitoring points for existing tunnel.

Table 2. Deformation monitoring control standards for crossings beneath existing tunnels.

Monitoring Item	Cumulative Control Value	Deformation Rate Control Value
Vertical Displacement of Tunnel Structure	+3mm, −5mm	±2 mm per single measurement, settlement rate reaching 1 mm/day
Horizontal Displacement of Tunnel Structure	±4mm	
Convergence of Tunnel Structure	±5mm	
Vertical Displacement of Track Bed	+3mm, −5mm	

5.2. Monitoring Results and Analysis

During the shield tunneling process of the new tunnel, the strong ground disturbance caused by the cutterhead is the main reason for the deformation of the existing tunnel. When the shield machine excavates in the "soft-over-hard" stratum, the forces on the cutterhead are complex, and severe tool wear and cutterhead clogging with mud can easily occur, further intensifying the ground disturbance. This leads to a redistribution of stress in the ground beneath the existing tunnel, causing additional deformation of the existing tunnel. Especially in the crossing section, the inhomogeneity of the stratum is more pronounced, and the difficulty of adjusting the shield machine's posture increases, making it easier for segment misalignment to occur, which in turn affects the stability of the tunnel structure. During the construction process of the new shield tunnel crossing beneath the existing tunnel, the deformation of the existing tunnel was monitored in real-time through a combination of automated and manual monitoring methods. The deformation curves of the track bed of the existing tunnel's left and right lines after the first and second crossings are shown in Figure 9. The monitoring results indicate that the deformation of the existing tunnel caused by the construction of the new tunnel is within a controllable range, but the deformation characteristics at different stages are different.

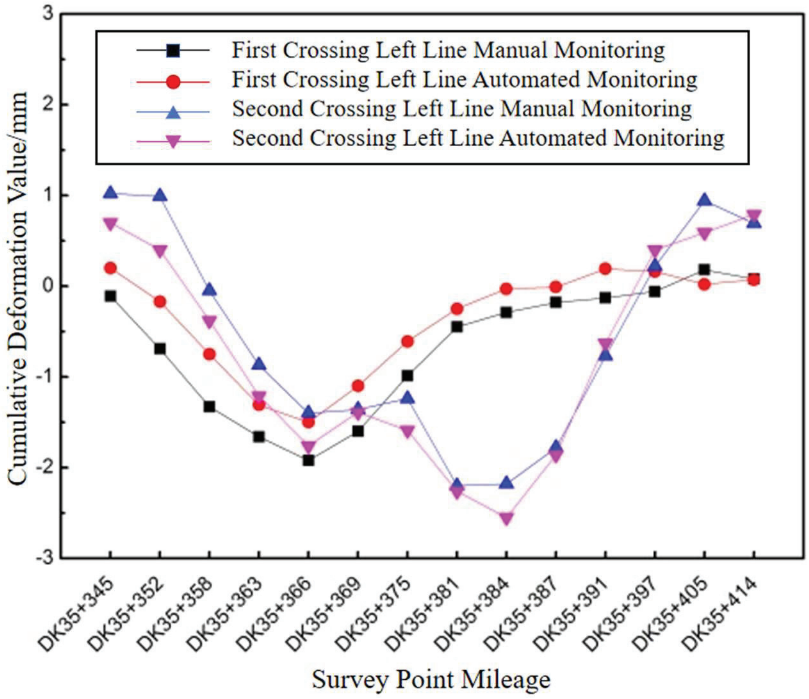

(**a**) Left line of the existing tunnel.

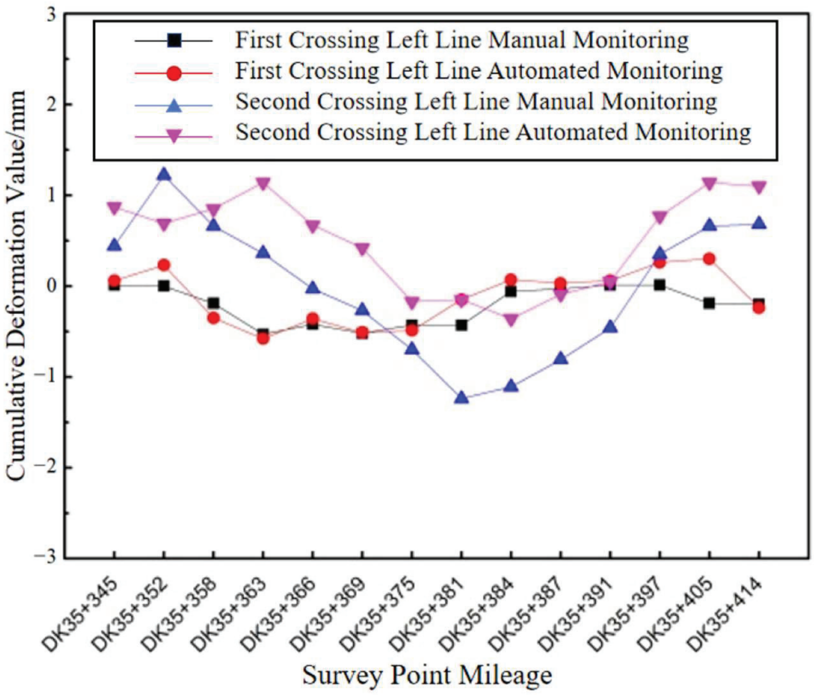

(**b**) Right line of the existing tunnel.

Figure 9. Deformation curves of the track bed of the left and right lines of the existing tunnel after the first and second crossings.

The right line of the new shield tunnel was the first to cross beneath the existing tunnel, taking 12 days. The maximum settlement of the track bed on the left line of the existing tunnel was -1.92 mm, with the maximum settlement occurring in the central crossing area and gradually decreasing towards both sides. Half a year later, the left line of the new shield tunnel crossed beneath the existing tunnel in 10 days of construction. After the second crossing was completed, the cumulative settlement of the track bed on the left line of the existing tunnel further increased, with the maximum settlement reaching -2.55 mm, showing a clear deformation superposition effect. The settlement of the track bed corresponding to the right line in the crossing center increased from -0.58 mm to -1.24 mm. However, it should be particularly noted that, between the first and second crossings, the excavation of the Phase II transfer station foundation, located about 22 m horizontally from the right line of the existing tunnel, caused a certain amount of uplift in both lines of the existing tunnel, reducing the final settlement of the left and right lines of the existing tunnel. The right line of the existing tunnel showed a more obvious uplift than the left line, but both were still within the deformation-monitoring control values. The excavation of the foundation changed the stress field around the existing tunnel, causing a redistribution of ground stress and resulting in uplift deformation of the existing tunnel. Since the excavation scope and depth of the foundation were large, the influence range on the existing tunnel was extensive, but through reasonable construction measures and monitoring control, the final deformation was still kept within the safe range.

The uplift observed in the existing tunnel during the excavation of the Phase II transfer station foundation highlights the dynamic nature of ground stress redistribution during construction activities. While the proposed measures in this paper, such as shield machine selection, parameter optimization, and monitoring, were primarily aimed at controlling settlement during the shield tunneling process, they also demonstrated adaptability in managing the complex ground-stress changes. The real-time monitoring system allowed for the dynamic adjustment of the construction parameters, which proved to be effective in maintaining the stability of the existing tunnel despite the uplift caused by the nearby excavation. This indicates that the proposed measures have a broad applicability in managing deformation risks in complex construction environments, even when unexpected ground movements occur due to adjacent construction activities.

6. Conclusions

This study provides insights into the safety risk assessment and control measures for constructing new double-line shield tunnels crossing beneath existing tunnels in complex strata. The findings are as follows:

(1) Engineering involving the construction of new tunnels at close proximity beneath existing tunnels poses extremely high safety risks, especially under complex geological conditions characterized by "soft-over-hard" strata, where construction uncertainties are significantly increased. Using refined risk assessment and control measures, major risk sources during the construction process were successfully identified and effectively managed. Comprehensive technical measures, including optimized shield machine selection, improved lining design, interlayer soil reinforcement, the dynamic adjustment of shield parameters, and the precise measurement of shield posture, enhanced the efficiency of shield tunneling and construction safety.

(2) By employing three-dimensional finite element software to model and simulate the construction process of the new tunnel crossing beneath the existing tunnel, the stress and deformation characteristics of the existing tunnel structure under various working conditions were analyzed. The numerical simulation results were validated against

on-site monitoring data, clarifying the reinforcement and monitoring scope for both the existing and new tunnels.

(3) Through the analysis of monitoring and measurement data during the shield crossing process, the maximum settlement of the existing tunnel was predicted and controlled. The actual maximum settlement measured was −2.55 mm, and all cumulative deformations were within the monitoring control values, demonstrating that the selected type of shield machine and its tunneling parameters fully met the requirements for shield tunneling construction in complex strata. This study also provides a reference for the settlement and deformation control of similar projects.

7. Future Work

In this study, the field monitoring data were limited to a specific case study, and the study focuses primarily on the construction phase without an extensive long-term operational impact analysis. Future work should conduct long-term monitoring and integrate real-time data with predictive models. The development of hybrid models combining machine learning and traditional numerical methods could also offer new insights into tunneling-induced deformations.

Author Contributions: Conceptualization, B.R.; methodology, B.R., S.H., M.H., Z.C. and H.L.; software, Z.C.; validation, B.R., S.H. and H.L.; formal analysis, B.R. and H.L.; investigation, H.L.; resources, B.R., S.H., Z.C. and H.L.; data curation, M.H. and Z.C.; writing—original draft preparation, B.R.; writing—review and editing, B.R. All authors have read and agreed to the published version of the manuscript.

Funding: This paper received funding from Project (2021) of Study on Flood Disaster Prevention Model of Nanning Rail Transit.

Institutional Review Board Statement: On behalf of all authors, the corresponding author states that there are no conflicts of interest. This article does not contain any studies with human participants or animals performed by any of the authors.

Data Availability Statement: The data used to support the findings of this study are available from the corresponding author upon request.

Acknowledgments: The authors express gratitude for the financial support extended by the organizations referenced in the funding section.

Conflicts of Interest: Author Bafeng Ren and Zhi Chen were employed by the company Nanning Rail Transit Co., Ltd. The remaining authors declare that the research was conducted in the absence of any commercial or financial relationships that could be construed as a potential conflict of interest.

References

1. Zhang, K.; Zhang, Z.; Chen, H.; Hu, Z. Experimental investigation on rheological properties and diffusion-related performance of clay shock slurry for excavation gap filling during shield tunnelling. *Tunn. Undergr. Space Technol.* **2024**, *146*, 105660. [CrossRef]
2. Jin, D.; Yuan, D.; Li, X.; Zheng, H. Analysis of the settlement of an existing tunnel induced by shield tunneling underneath. *Tunn. Undergr. Space Technol.* **2018**, *81*, 209–220. [CrossRef]
3. Shan, Y.; Wang, G.; Lin, W.; Zhou, S.; Rackwitz, F. Analytical solution of the evolution of railway subgrade settlement induced by shield tunnelling beneath considering soil stress release. *Tunn. Undergr. Space Technol.* **2025**, *162*, 106607. [CrossRef]
4. Chen, Y.; Lin, H.; Liu, B. Review of Research Progresses and Application of Geothermal Disaster Prevention on Large-Buried Tunnels. *Appl. Sci.* **2022**, *12*, 10950. [CrossRef]
5. Wu, S.; Zhang, X.; Lin, Z.; Wang, J.; Zhang, F.; Gao, H. Influence law and determination method of jack lifting load on existing station settlement. *Case Stud. Constr. Mater.* **2025**, *22*, e04180. [CrossRef]
6. Li, J.; Fang, X.; Yang, Y. Analysis of the Impact of the New Two-Lane Shield Tunnel Underpass on the Existing Tunnels. *Appl. Sci.* **2025**, *15*, 2642. [CrossRef]

7. Huang, W.; Liu, W.; Ou, M.-T.; Zhao, L. Numerical Analysis of Disturbance Control in a Four-Hole Parallel Tunnel Crossing Beneath Existing Tunnels. *Geotech. Geol. Eng.* **2025**, *43*, 75. [CrossRef]
8. Lei, M.-F.; Shi, Y.-B.; Tang, Q.-L.; Sun, N.-X.; Tang, Z.-H.; Gong, C.-J. Construction control technology of a four-hole shield tunnel passing through pile foundations of an existing bridge: A case study. *J. Cent. South Univ.* **2023**, *30*, 2360–2373. [CrossRef]
9. Pang, Y.; Lin, H.; Cao, P.; Meng, G. The Influence of Overlying High-Speed Rail Dynamic Loads on the Stability of Shield Tunnel Faces During Excavation. *Appl. Sci.* **2025**, *15*, 2567. [CrossRef]
10. Zhang, X.; Lin, Y.; Pan, Z.; Jiang, X. Risk assessment of water inrush in deep-buried karst tunnel with rich water based on combined weighting method. *Earth Sci. Inform.* **2025**, *18*, 28. [CrossRef]
11. Ter-Martirosyan, A.Z.; Anzhelo, G.O.; Rud, V.V. The Influence of Metro Tunnel Construction Parameters on the Settlement of Surrounding Buildings. *Appl. Sci.* **2024**, *14*, 6435. [CrossRef]
12. Gan, X.; Yu, J.; Bezuijen, A.; Gong, X.; Wang, C. Tunneling-induced longitudinal responses of existing tunnel with discontinuities in structure stiffness. *Transp. Geotech.* **2023**, *42*, 101113. [CrossRef]
13. Liu, B.; Li, T.; Chang, W.; Han, Y.; Fu, C.; Yu, Z. Mechanical response of horseshoe-shaped tunnel lining to undercrossing construction of a new subway station. *Tunn. Undergr. Space Technol.* **2022**, *128*, 104652. [CrossRef]
14. Guo, P.; Gong, X.; Wang, Y.; Lin, H.; Zhao, Y. Analysis of observed performance of a deep excavation straddled by shallowly buried pressurized pipelines and underneath traversed by planned tunnels. *Tunn. Undergr. Space Technol.* **2023**, *132*, 104946. [CrossRef]
15. Zhang, D.-M.; Xie, X.-C.; Huang, Z.-K.; Peng, M.-Z.; Zhu, H.-X. Observed response of maglev structure undercrossed by three shield tunnels in soft soil. *Undergr. Space* **2022**, *7*, 636–661. [CrossRef]
16. Xun, X.; Zhang, J.; Yuan, Y. Multi-Information Fusion Based on BIM and Intuitionistic Fuzzy D-S Evidence Theory for Safety Risk Assessment of Undersea Tunnel Construction Projects. *Buildings* **2022**, *12*, 1802. [CrossRef]
17. Huang, H.-W.; Gao, T.-R.; Zhang, D.-M.; Jiang, Q.-H.; Jia, J.-W. A hybrid approach for modifying tunneling-induced response in existing multi-tunnel environment. *Comput. Geotech.* **2025**, *179*, 106921. [CrossRef]
18. Yang, W.; Zhang, D.; Wang, A. Field measurement analysis of the influence of simultaneous construction of river channel and bridge on existing double shield tunnels. *Undergr. Space* **2022**, *7*, 812–832. [CrossRef]
19. Li, Y.; Zhang, Z.; Dong, J.; Wang, B.; Wang, C. Study on the Impact of Groundwater and Soil Parameters on Tunnel Deformation and Sensitivity Analysis. *Appl. Sci.* **2024**, *14*, 8196. [CrossRef]
20. Han, Y.; Xu, Q.; Cui, Y. Deformation of Existing Shield Tunnel Adjacent to Deep Excavations: Simulation and Monitoring Analysis. *Appl. Sci.* **2024**, *14*, 4153. [CrossRef]
21. Zhang, H.; Liu, G.; Liu, Q.; Chen, Z.; Wang, Z.; Niu, X. Vehicle-induced dynamic response characteristics of a new subway tunnel closely undercrossing the existing subway. *Soil Dyn. Earthq. Eng.* **2023**, *164*, 107579. [CrossRef]
22. Huang, F.; Wang, Y.; Zhang, M.; Jiang, W.; Ji, H.; Pan, Q. Model test study of punching shear failure mode of the bearing stratum induced by tunneling beneath an existing pile. *Tunn. Undergr. Space Technol.* **2025**, *158*, 106459. [CrossRef]
23. Chen, H.; Liu, J.; Shen, G.Q.; Feng, Z. Control of existing tunnel deformation caused by shield adjacent undercrossing construction using interpretable machine learning and multiobjective optimization. *Autom. Constr.* **2025**, *170*, 105943. [CrossRef]
24. Liu, W.; Chen, Y.; Liu, T.; Liu, W.; Li, J.; Chen, Y. Shield tunneling efficiency and stability enhancement based on interpretable machine learning and multi-objective optimization. *Undergr. Space* **2025**, *22*, 320–336. [CrossRef]
25. Liu, D.; Zhang, W.; Duan, K.; Zuo, J.; Li, M.; Zhang, X.; Huang, X.; Liang, X. Intelligent prediction and optimization of ground settlement induced by shield tunneling construction. *Tunn. Undergr. Space Technol.* **2025**, *160*, 106486. [CrossRef]
26. Chen, H.; Liu, J.; Shen, Q.G.; Li, T.; Liu, Y. Data-driven joint multiobjective prediction and optimization for tunnel-induced adjacent bridge pier displacement: A case study in China. *Eng. Appl. Artif. Intell.* **2025**, *142*, 109616. [CrossRef]
27. Guo, T.; Li, S.; Lu, B.; Wang, Z.; Cao, W.; Liu, S. Research on gradual optimization of slurry mixture ratio for shield tunnel backfill grouting based on fuzzy mathematics. *Constr. Build. Mater.* **2024**, *456*, 139319. [CrossRef]
28. Zhou, X.; Zhao, C.; Bian, X. Prediction of maximum ground surface settlement induced by shield tunneling using XGBoost algorithm with golden-sine seagull optimization. *Comput. Geotech.* **2023**, *154*, 105156. [CrossRef]
29. Ma, S.; Zhou, Z.; Duan, Z.; Huang, Z.; He, B.; An, P.; Li, J. Study on the Influence Characteristics of Excavation Face Instability of New Tunnels Orthogonally Crossing Existing Tunnels. *Appl. Sci.* **2024**, *14*, 10521. [CrossRef]
30. Liu, X.; Jiang, A.; Fang, Q.; Wan, Y.; Li, J.; Guo, X. Spatiotemporal Deformation of Existing Pipeline Due to New Shield Tunnelling Parallel Beneath Considering Construction Process. *Appl. Sci.* **2022**, *12*, 500. [CrossRef]
31. Cetindemir, O. Nonlinear Constitutive Soil Models for the Soil-Structure Interaction Modeling Issues with Emphasis on Shallow Tunnels: A Review. *Arab. J. Sci. Eng.* **2023**, *48*, 12657–12691. [CrossRef]
32. Mao, Z.; Ding, T.; Hu, F.; Ye, S.; Ding, L.; Zhang, X.; Li, P.; Li, N. The Impact of Different Excavation Support Structures on the Deformation and Stability of Adjacent Station and Tunnels. *Buildings* **2025**, *15*, 493. [CrossRef]
33. Zheng, F.; Li, W.; Song, Z.; Wang, J.; Zhang, Y.; Liu, N.; Xiao, K.; Wang, Y. Construction Stability Analysis and Field Monitoring of Shallowly Buried Large-Section Tunnels in Loess Strata. *Water* **2024**, *16*, 2192. [CrossRef]

34. Liu, H.; Ma, W.; Kang, M.; Fu, Y.; Yan, T.; Liu, H.; Zhao, B. Study on the Distribution Law of External Water Pressure with Limited Discharge during Shield Construction of Soft Rock Tunnel in Western Henan Province. *Appl. Sci.* **2024**, *14*, 5698. [CrossRef]
35. Robert, D.J. A Modified Mohr-Coulomb Model to Simulate the Behavior of Pipelines in Unsaturated Soils. *Comput. Geotech.* **2017**, *91*, 146–160. [CrossRef]
36. Vicente da Silva, M. Nonlinear Mohr–Coulomb yield criterion: Integration in ADMM-based finite element limit analysis formulation and application to slope stability assessment. *Comput. Geotech.* **2025**, *177*, 106897. [CrossRef]

MDPI AG
Grosspeteranlage 5
4052 Basel
Switzerland
Tel.: +41 61 683 77 34

Buildings Editorial Office
E-mail: buildings@mdpi.com
www.mdpi.com/journal/buildings

Academic Open
Access Publishing

mdpi.com

ISBN 978-3-7258-4628-3